Understanding and controlling the stability and reactivity of noble metal nanoparticles for CO oxidation

By

Chenyang Tang

A Thesis Submitted for the Degree of Doctor of Philosophy (PhD) in Chemical Engineering at Newcastle University, United Kingdom

School of Engineering

January 2020

Abstract

Heterogeneous catalysts comprising of noble metal nanoparticles (such as Pt, Pd and Rh) supported on oxides, play a key role in a wide range of important chemical transformations including automotive exhaust control. However, due to the increasing demand for these catalysts and scarce resources of noble metals, there is a pressing need to reduce the consumption of noble metals in catalysts. Sintering of nanoparticles can cause catalyst deactivation, hence stabilizing nanoparticles can be a solution to reduce the loss of noble metals. Moreover, by improving the catalytic activity of noble metal nanoparticles, the amount of noble metals in catalysts can be reduced while still maintaining the required catalytic performance. Therefore, this thesis focuses on some novel nanostructures of noble metal catalysts that can potentially lead to enhanced stability and improved activity, in order to use noble metals more efficiently. CO oxidation was chosen as the model reaction in this study, because of its importance in automotive exhaust control.

Interactions between metal nanoparticles and the support can have big influences on particle stability, as it was demonstrated in this thesis that weak particle-support interactions would lead to nanoparticle sintering under reaction conditions and hence destroy the dedicatedly designed nanostructures. In addition, the particle-support interactions may also bring some emergent functionalities that can affect the catalytic activity. Hence, different approaches were attempted to enhance the particle-support interactions, and their effects on the stability and activity of the catalysts were investigated.

In the first approach, noble metal nanoparticles (Pd) were enclosed into porous organic cages (POCs, a class of hollow, cage-like macromolecules). The POCs were able to confine the nanoparticles, which resulted in a uniform particle size distribution. However, the limited accessibility of active sites in POCs and the thermal decomposition of the POC support (~300 °C) largely restricted the activity of the resulted catalysts hence their practical applications.

The alternative approach was to partially embed (socket) noble metal nanoparticles in perovskite oxides via redox exsolution method. This has been previously demonstrated to produce highly stable transition metal nanoparticles. For the first time this thesis investigates the in situ formation of the socketed particles while at the same time

providing valuable mechanistic insight for designing more efficient exsolved materials. Experiments have been conducted in situ in a latest generation environmental transmission electron microscope (ETEM) which allowed for the direct observation of the socket formation, metal particle nucleation and growth. The socket was found to form simultaneously with the particle growth due to the rise of perovskite lattice around particles. The particle growth seemed to be limited by the availability of exsolvable ions near the perovskite surface, which highlighted the importance to reduce the perovskite grain size when attempting to exsolve from dilute compositions. All the above mechanistic insight was employed to design materials that can exsolve from dilute substitution of noble metals thus potentially allowing for more efficient use of noble metals. Parameters such as substitution levels and reduction time and temperature were used to control exsolved particle characteristics and relate them to the catalytic activity. By comparing with the state-of-the-art Rh catalyst, the exsolved Rh catalyst with the same nominal metal loading exhibited similar activity despite that only a part of Rh in the bulk of perovskite exsolved on the surface. This indicates that the activity of exsolved catalysts can be enhanced probably due to the emergent functionalities that arise from the strained particles, which could potentially reduce the amount of noble metals in catalysts if the extent of exsolution can be increased.

This thesis highlights the following design principles for noble metal catalysts. The stability of metal nanoparticles on the support must be high enough to maintain the designed nanostructures. That means that we need to have stronger particle-support interactions. Attempting to do this by full encapsulation was successful but compromised activity. Therefore, a partial embedding via the exsolution method results in a combined stabilizing effect and increased activity due to strain. Ultimately, this appeared to be the most promising method for designing efficient noble metal catalysts.

Acknowledgements

Firstly, I would like to express my sincere gratitude to my supervisor, Professor Ian Metcalfe, for providing me the precious opportunity to do research in our group and for his patient guidance during the last four years. I am also very grateful to my co-supervisors Dr Evangelos Papaioannou, Dr Dragos Neagu and Dr Kelly Kousi, for their continuous suggestion, support and encouragement throughout my PhD research.

I would like to thank all collaborators and colleagues who have ever helped me during my PhD. Dr Shan Jiang, Dr Simon Beaumont and Harrison Cox at Durham University for providing the samples in the research of metal nanoparticle pairs and porous organic cages. Dr Vasileios Kyriakou and Dr Mihalis Tsampas at DIFFER, and Dr Mimoun Aouine and Dr Philippe Vernoux at IRCELYON, for their collaboration in the experiments using the latest generation ETEM in this study. Dr Binti Wan Ramli (Nisa), for introduction to the catalytic setups in my first year before she finished her PhD. Dr Maggie White, for helping me to test hundreds of my samples in XRD. Dr Budhika Mendis at Durham University, for kindly providing SEM and TEM instruments to scan my samples. Dr Billy Murdoch, for helping me to scan my samples in HIM before he left for RMIT. Tracey Davey, for organizing the SEM instrument at Newcastle. Leonidas Bekris and Dionysios Vroulias, for the assistance for sample preparation. And all the members in our group for their helps in my study and also for organizing group activities.

I would also like to acknowledge my school for offering me the scholarship (CEAM International Postgraduate Scholarship) to support my study.

I am also very grateful to my family. I could not finish my study successfully without their huge supports and encouragements throughout my PhD period.

Table of contents

List of figures

List of tables

Nomenclature

List of abbreviations

A/F	Air-to-fuel ratio
AFM	Atomic force microscope
BSE	Backscattered electron
COF	Covalent organic framework
CNT	Carbon nanotube
EDS	Energy dispersive X-ray analysis
ETEM	Environmental transmission electron microscope
E-R	Eley-Rideal mechanism
FIB	Focused ion beam
HCs	Hydrocarbons
HIM	Helium ion microscope
IR	Infrared
L-H	Langmuir-Hinshelwood mechanism
MFC	Mass flow controller
MOF	Metal organic framework
MvK	Mars van Krevelen mechanism
NTP	Normal temperature and pressure
PEG	Polyethylene glycol
PM	Particulate matter
POC	Porous organic cage
SE	Secondary electron
SEM	Scanning electron microscope
TEM	Transmission electron microscope
TGA	Thermogravimetric analysis
TWC	Three-way catalyst
WGS	Water-gas shift
XRD	X-ray diffraction

List of key symbols

A	Pre-exponential factor
a_p	Pseudocubic cell parameter of perovskite
A_{Rh}	Atomic weight of Rh metal
d	Dimension of exsolved particle
d_{hkl}	d-spacing of reflection in XRD with Miller indices of (hkl)
D_{Rh}	Exsolution depth of Rh within the perovskite lattice
E_a	Activation energy of reaction
F_t	Total gas flow rate
f_i	Fraction of particles (per area of support, µm^{-2}) having a diameter d_i
k	Reaction rate constant
N_a	Avogadro number
n_{uc}	Number of ABO_3 units contained in the real unit cell of perovskite
N_{Rh}	Amount of Rh metal exsolved per surface area of support
P_{CO}	Partial pressure of CO
P_{O_2}	Partial pressure of O_2
r	Radius of ion
R	Gas constant
r_{CO_2}	Production rate of CO_2
t	Time
T	Temperature
T_5/T_{50}	The temperature at which 5/50% conversion of CO is achieved
tf	Tolerance factor for perovskite structure
V_{uc}	Volume of the real distorted unit cell of perovskite
X_{CO}	Conversion of CO
y_{CO_2}	Concentration of CO_2 in product
$y_{CO,inlet}$	Concentration of CO in inlet reaction mixture
ΔG	Gibbs free energy of reaction
δ	Oxygen vacancy in perovskite

τ	Time constant
ρ_{Rh}	Density of Rh metal
ζ	Degree of exsolution
η_{Rh}	Rh metal coverage

List of Publications

The publications as the results of the research included in the thesis are listed below:

- Jiang, S., H.J. Cox, E.I. Papaioannou, <u>C. Tang</u>, H. Liu, B.J. Murdoch, E.K. Gibson, I.S. Metcalfe, J.S.O. Evans, and S.K. Beaumont, *Shape-persistent porous organic cage supported palladium nanoparticles as heterogeneous catalytic materials.* Nanoscale, 2019. **11**(31): p. 14929-14936.
- <u>Tang, C.</u>, K. Kousi, D. Neagu, J. Portolés, E.I. Papaioannou, and I.S. Metcalfe, *Towards efficient use of noble metals via exsolution exemplified for CO oxidation.* Nanoscale, 2019. **11**(36): p. 16935-16944.
- Neagu, D., V. Kyriakou, I-L. Roiban, M. Aouine, <u>C. Tang</u>, A. Caravaca, K. Kousi, I. Schreur-Piet, I.S. Metcalfe, P. Vernoux, M.C.M. van de Sanden, and M.N. Tsampas, *In Situ Observation of Nanoparticle Exsolution from Perovskite Oxides: From Atomic Scale Mechanistic Insight to Nanostructure Tailoring.* ACS Nano, 2019. **13**(11): p. 12996-13005.

Chapter 1: Introduction

This chapter briefly introduces the background of noble metal nanoparticles in heterogeneous catalysis and the need to improve their stability and activity, the aim of this study and the outline of the thesis.

1.1 Noble metal nanoparticles in heterogeneous catalysis

Catalysis is one of the most important disciplines of the chemistry-related research, and a catalyst is the substance that can increase the rate of a chemical reaction without being consumed. After hundreds of years of development, catalysts have been employed everywhere in our lives nowadays, as they are widely used in about 90% of chemical processes in all fields [1] and contribute to nearly 35% of GDP all over the world [2]. There is no doubt that catalysts will continue to play a vital role in areas such as energy conversion, pollution abatement, medical applications and food production [2].

Catalysts can be generally classified into homogeneous and heterogeneous catalysts. Homogeneous catalysts stay in the same phase as the reactants (normally liquid), while heterogeneous catalysts are in a different phase from the reactants (normally a solid catalyst in liquid or gas phase). Heterogeneous catalysts are more frequently used in industry because they are easier to be recycled from the process as compared with the homogeneous counterparts, although their activity may be slightly lower than that of the homogeneous catalysts due to the lower surface area [3].

Noble metals are key materials for heterogeneous catalysts, and they play important roles in reactions such as hydrogenations, oxidations, dehydrogenations and environmental catalysis [4]. The catalysts used in automotive exhaust control are the one of the biggest consumers of noble metals, which uses roughly 34% Pt, 55% Pd and 95% Rh every year [5]. Usually, these catalysts comprise noble metal nanoparticles on a high-surface area support (normally oxides like Al_2O_3 or SiO_2). It is mainly because, as compared with the bulk counterparts, metal nanoparticles possess much higher surface area per unit volume, which could result in higher catalytic activities as heterogeneous catalytic processes are typically thought to occur on the metal surface and/or at the interface between the metal and support [6, 7]. Moreover, as the metal particle size becomes smaller, more atoms will be located at the edges and corners on the surface of particles, and these coordinatively unsaturated atoms may possess high catalytic activity as they are prone to coordinate with other species nearby such as reactants to increase their coordination number [8].

However, due to the rapidly increasing demand of these catalysts and the limited resources of noble metals, it is desired to replace noble metals or reduce their consumption in catalysts. Efforts have been made to replace or partly substitute noble metals in these catalysts with base metals or their oxides (e.g., Co_3O_4, NiO) [9, 10],

spinel materials (e.g., copper chromite, cobalt manganite) [11] or perovskites [12], but it is still challenging to achieve the same activity as noble metal catalysts. Therefore, there is a pressing need to improve the design of the catalysts to reduce the consumption of noble metals. To achieve this goal, the problem of particle agglomeration at high temperatures (known as sintering), one of the major mechanisms which cause catalyst deactivation [13], should be solved. What is worse, only small amounts of noble metals can be recycled from those deactivated catalysts [5], which results in considerable loss of noble metals. Hence, improving the stability of noble metal nanoparticles against sintering can be an effective way to reduce the loss of noble metals in catalysts. On the other hand, if the reactivity of noble metal nanoparticles can be improved, the amount of noble metals in catalysts can be reduced while still maintaining the required catalytic performance, which will also make the use of noble metals more efficiently. Some novel nanostructures for the noble metal catalysts can be designed to solve these problems. For instance, the interactions between metal particles and the support were reported to not only affect the stability of particles against sintering, but also play an important role to determine the catalytic activity [14, 15]. Therefore, this thesis studies novel catalyst systems with different particle-support interfaces, aiming to improve the stability and activity of noble metal nanoparticles.

1.2 Aim of the thesis

As introduced above, noble metal nanoparticles including Pt, Pd and Rh are intensively used in the application of automotive exhaust control. However, it is desired to improve the stability and activity of noble metal nanoparticles, in order to reduce the consumption of these noble metals in catalysts and hence to use them more efficiently, which is the primary aim of this study. CO oxidation was selected as the model reaction to test the samples in this study, because of its importance for automotive exhaust control. In order to achieve the aim of this study, efforts have been made to:

- Prepare supported metal nanoparticles with different nanostructures (e.g., nanoparticle pairs with controlled separation distance, nanoparticles encapsulated in porous organic cages, and nanoparticles partially socketed in perovskite supports via exsolution).
- Evaluate the thermal stability and activity of these resulted catalysts under CO oxidation conditions.

- Metal nanoparticles exsolved from perovskite were most promising, hence mechanistic insight into exsolution was explored for designing more efficient exsolved materials.
- Employ mechanistic insight to control the exsolution of noble metals and their particle characteristics, in order to improve catalytic activity.

1.3 Outline of the thesis

This thesis contains the chapters organized as shown below:

Chapter 2 (Background of catalyst preparation and metal nanoparticle stabilization) introduces some common preparation techniques of supported metal catalysts. Besides, as metal particle sintering is a major challenge for these catalysts, the sintering mechanisms and the parameters affecting the sintering process are also introduced, followed by some strategies for particle stabilization. The contents in this chapter aimed to provide guidance for the catalyst design to stabilize metal nanoparticles in the later studies.

Chapter 3 (Experimental) introduces the methodology employed in this study. Characterization techniques that were used to analyze materials are described as well as their working principles. The preparation methods of the perovskite-based materials are also described there. It should be mentioned that except the metal exsolution from perovskites (Chapter 7), the other two studies (Chapter 5 and 6) were both collaborative and the sample preparations were conducted by my collaborators, hence their preparation methods will be introduced briefly in the respective chapters. Moreover, the experimental setups and operation conditions for sample reduction and catalytic experiments are also briefly described in Chapter 3.

Chapter 4 (State-of-the-art noble metal catalysts in CO oxidation) introduces the application of noble metals (Pt, Pd and Rh) in heterogeneous catalysis, especially in the application of automotive exhaust control. The state-of-the-art catalysts of these metals are tested in catalytic experiments, in order to show the classic behaviors of noble metal catalysts in CO oxidation reaction and the differences between these metals. Hence, the results obtained from this chapter can help understand the catalytic behaviors of the samples designed in the later studies.

Chapter 5 (Demonstration of metal nanoparticle sintering) describes a specific example to demonstrate how the mobility of metal nanoparticles would lead to the particle sintering and hence destroy the well-designed nanostructure. In this research, efforts are made to prepare the novel nanoparticle pairs with controlled separation distance, but the stability tests indicate that the metal nanoparticles loosely dispersed on the support can easily agglomerate under reaction conditions. This emphasizes the importance of the particle stability when designing catalysts. Therefore, in the next two chapters, different catalyst systems are investigated, which can stabilize metal nanoparticles by enhancing the particle-support interactions to suppress particle migration.

Chapter 6 (Stabilizing noble metal nanoparticles via encapsulation in porous organic cages) demonstrates the approach to stabilize noble metal nanoparticles by enclosing them in porous organic cages. The sample preparation is successful, and the well-defined pore structures of porous organic cages can control the growth of metal nanoparticles and protect them from sintering under the given reaction conditions. However, the resulted catalyst demonstrates low activity for CO oxidation, probably due to the limited accessibility of active sites surrounded by the cages. Moreover, the thermal decomposition of the organic support also limits the application of this catalyst at high temperatures. Therefore, a catalyst system with both high stability and activity is desired.

Chapter 7 (Towards stabilization and high activity of noble metal nanoparticles via exsolution) demonstrates the alternative approach to stabilize noble metal nanoparticles by partially socketing them in perovskite oxides via in-situ exsolution. The modification of the preparation method for perovskites is firstly introduced, which allows for the control over the stoichiometry and microstructure of perovskites. Then the experiments conducted in environmental TEM are demonstrated to in situ study the mechanism of the formation of the socketed particles. The mechanistic insight obtained is also employed to improve the design of exsolved materials for more efficient use of noble metals. Hence, then the investigations of exsolution of noble metal (Rh) from dilute compositions are described. Different parameters are investigated to control the particle characteristics of the exsolved Rh, in order to improve catalytic activity. The exsolved Rh catalyst exhibits similar activity as the state-of-the-art Rh catalyst, despite the limited extent of exsolution, indicating the activity enhancement for the exsolved noble metal particles. Therefore, noble metals can be

used more efficiently via exsolution, considering the high stability and increased activity of the exsolved particles.

Chapter 8 (Summary and future work) summarizes the major findings in this thesis and provides some recommendations for future work.

Chapter 2: Background of catalyst preparation and metal nanoparticle stabilization

In this study, different techniques are used to prepare supported metal nanoparticle catalysts, and hence some common preparation methods in literature are summarized here and their advantages/disadvantages are also introduced. Then the mechanisms of metal particle sintering and some stabilizing strategies for metal particles are also introduced, in order to provide some guidance for the particle stabilization.

2.1 Preparation methods of supported metal catalysts

As mentioned before, nanoparticles of active metals dispersed on porous supports are extensively used as heterogeneous catalysts. There is a wide range of preparation methods for the supported metal catalysts, and these methods can have different effects on the properties of the produced metal particles (e.g., size, shape, distribution) and hence the catalytic performance (e.g., activity, selectivity, stability) [16, 17]. The two most traditional preparation methods of supported metal catalysts are impregnation and precipitation in which the metal precursor is firstly introduced onto the support followed by the dying, calcination and reduction steps [16, 18]. Apart from the traditional methods, there are also some emerging techniques being studied in recent years, such as melt infiltration, colloidal methods, chemical vapor deposition [16], etc. Here, some common preparation methods and their advantages and disadvantages will be introduced.

2.1.1 Impregnation

The one of the most widely used preparation methods for supported metal catalysts is called impregnation in which the solid support is infiltrated with a certain amount of solution containing the metal precursor (normally the metal salt) [19]. When the solution contacts with the porous support, it will enter and fill the pores of the support, and the infiltrated support will be dried, calcined and reduced in sequence. Depending on the amount of solution used with respect to the amount of the support involved, the impregnation method can be classified into two main types. The first type is called "incipient wetness" or "dry" impregnation, in which the amount of solution used is just enough to fill the total pore volume of the support without excess [16, 18], which can reduce the use of metal precursors especially when costly components are used [18]. On the other hand, the other type of impregnation is called "wet" or "soaking" impregnation where excess amount of solution is used as compared with the pore volume, which can be conducted by aging the support in the solution of metal precursor for a period under continuous stirring [20].

Although widely used due to its extensive flexibility, the impregnation method lacks the adequate control over the morphology of the resulted metal particles and large particles are usually produced due to the metal agglomeration during the heating steps [21].

2.1.2 Precipitation

Co-precipitation is also a very popular preparation method for supported metal catalysts. In this method, the precursor of the active metal and the salt precursor of the support material are mixed in the same solution, and hence they can be simultaneously precipitated as hydroxides and/or carbonates by adding a base into the mixed solution under stirring [18, 19]. The co-precipitation method is able to disperse the metal particles throughout the support and achieve high metal loadings [16], and it has been widely employed to produce catalysts in large scale for some industrially important processes, such as Ni/Al_2O_3 for steam reforming [22] and $Cu-ZnO/Al_2O_3$ for synthesis of methanol [23].

Another preparation method which is similar as co-precipitation is called deposition-precipitation, which was initially proposed by Haruta et al. [24]. In the deposition-precipitation method, the metal precursor is dissolved in the solution with the suspension of the support material in presence, and then the precipitation of the metal hydroxide is triggered normally by increasing the PH of the solution. The surface of the existing support can provide sites for nucleation, hence the metal precursor can be deposited on the surface of support.

The chemical precipitation is not a controlled process, and the nucleation and subsequent growth of particles are dependent on the precipitation reactions and hence are highly sensitive to the reaction conditions. Therefore, the catalysts prepared via precipitation methods always have a broad particle size distribution and uncontrolled particle morphology [19, 25]. Moreover, in the catalysts prepared by using co-precipitation, probably not all the active metal would be at the surface, hence this method may not be suitable for noble metals.

2.1.3 Emerging methods

As mentioned above, although traditional preparation methods like impregnation and precipitation have been used for long time, they still cannot effectively control the properties of the prepared metal particles (size, shape, distribution, etc.). Furthermore, these traditional methods also have very limited control over the interactions between metal particles and support, which would result in agglomeration and hence low stability [26]. Therefore, a range of emerging preparation techniques for supported metal catalysts have been reported over the years.

Melt infiltration, for instance, is a relatively new preparation method. In this method, the metal precursor contacts with the support and is subsequently heated above its melting point, and hence the molten metal precursor can enter the pores of the support via capillary forces [16]. Big difference between the melting point and the decomposition temperature of the metal precursor is required, otherwise the precursor will decompose before entering the pores. Hence, hydrated transition metal nitrates were reported as the most suitable precursors to be used in this method, because of their low melting points coined to dissolution in their own crystal water [27]. Melt infiltration is similar as impregnation and drying, but it is simpler and no solvent is required, which can limit the redistribution of the metal during the heating steps hence achieving a more homogeneous distribution [16]. However, currently this preparation method is only applied for a limited number of metals such as Co, Ni and Cu, because a lot of metal precursors would decompose before infiltrating the support as mentioned before [16].

Another emerging preparation method is chemical vapor deposition. In this method, a volatile metal precursor is vaporized (sublimed) and the vaporized metal precursor reacts with the support and is hence deposited onto the surface of the support, then the adsorbed precursor can be thermally treated to decompose and get reduced [19, 28, 29]. Chemical vapor deposition can produce highly dispersed metal particles on a wide range of both organic and inorganic supports under mild conditions [19]. However, the systems for chemical vapor deposition are costly, which is a big disadvantage for this preparation method.

Supported metal catalysts can also be prepared in the colloidal method. Metal nanoparticles can be prepared in colloidal sols with a well-defined particle size distribution and the produced metal nanoparticles are stabilized by some ligands or surfactants against coalescence and growth in the solution. These preformed metal nanoparticles in colloids can be then deposited onto a support with little change of the particle size [16, 30]. Hence, by controlling the parameters during the colloid preparation step such as the selection of reducing agent, stabilizer and solvent which can affect the size and shape of particles, these particle properties can also be well controlled when they are deposited on the support [30]. However, after deposition, the ligands or surfactants attached to the metal particles need to be removed, which is normally done by thermal decomposition and hence will result in changes of particle size and shape. Recent studies reported that ligands can also be removed via solvent extraction, which has little effects on the deposited metal particles [30, 31].

Apart from the methods mentioned above, there are still many other novel preparation methods for supported metal catalysts, such as sputtering [32] and flame spray pyrolysis [33], which will not be discussed further here. With the advances of the preparation methods, the control over the particle properties have been improved a lot. However, these emerging preparation methods do not improve the thermal stability of catalysts much and it is still a major problem for state-of-the-art catalysts.

2.2 Metal nanoparticle sintering and its mechanisms

As mentioned before, the nanosized particles of noble metals play vital roles in heterogeneous catalysis, but they always suffer from an inherent weakness that is the inadequate stability at high temperatures. Small metal nanoparticles will demonstrate a great tendency to agglomerate to form larger but fewer particles during reactions in order to minimize their surface energies, and this process is called sintering of nanoparticles, which is one of the major deactivation mechanisms for supported catalysts [13, 34, 35]. The problem of nanoparticle sintering is especially severe for some industrially important processes such as catalytic combustion, steam reforming, and automotive exhaust control where high temperatures are required for reactions [36]. Once the sintering happens, the surface area of the metal nanoparticles will decrease considerably, which will result in the loss of active sites hence the degradation of the catalytic activity. Moreover, for the applications which are sensitive to the particle size [37, 38] or dependent on the metal-support interface sites [39], the growth of nanoparticles also means the changes of the catalytic activity and selectivity.

According to earlier studies, the sintering of metal nanoparticles can happen via two possible mechanisms which are particle migration and subsequent coalescence (Figure 2-1(a)), and Ostwald ripening (Figure 2-1(b)), respectively [40]. In the former mechanism, two or more metal nanoparticles migrate over the support surface in the term of Brownian-like motion, which finally results in the coalescence when particles move too close to each other. On the other hand, in the Ostwald ripening mechanism, some individual metal atoms have the tendency to detach from the surface of small metal nanoparticles and subsequently migrate to join other larger particles, which is due to the lower chemical potential in larger metal particles. The detached metal atoms can be transferred either across the surface of the support or through the vapor phase, while the former is more common for supported catalysts unless the nanoparticles are composed of volatile metals. However, the real sintering process is much more

complicated as the dominant sintering mechanism may change or those two mechanisms may happen simultaneously, and more physical and chemical processes may also be involved [35, 40].
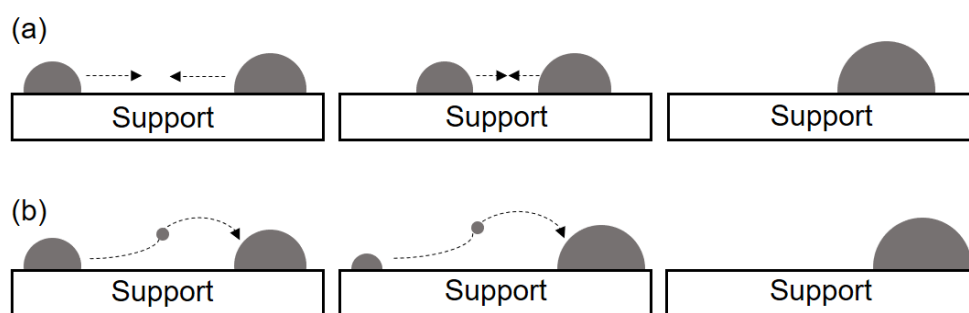
Figure 2- 1 Schematic demonstration of two possible mechanisms for nanoparticle sintering: (a) particle migration and coalescence and (b) Ostwald ripening. [40]

The nanoparticle sintering is a very complex process and it can be affected by several parameters. The first and maybe the most important parameter, of course, is the temperature. In both mechanisms introduced above for sintering, some bonds (either between the atoms within a metal particle or between the particle and the support) need to be broken, and a higher temperature can make bond breakage more facile, hence the sintering will happen more readily [41]. Apart from the temperature, sintering can also be influenced by the atmosphere which the catalyst is exposed to [42]. It was reported that the sintering of metal particles like Pt happens more easily when exposed to oxidizing atmospheres as compared with the inert or reducing atmospheres [43], and this might be attributed to the changes of the surface structure caused by the adsorbed species like H, O or OH depending on the atmosphere [42].

Sintering is also affected by the properties of metal particles. The melting point of the metal particles is one of the key parameters. The migration of species during the sintering process can be described by the so-called Hüttig and Tamman temperatures. When the Hüttig temperature ($T_{Hüttig}$) is reached, atoms at defects on the particles become mobile, while the Tamman temperature (T_{Tamman}) is related to the mobility of bulk atoms, and these two temperatures are closely related to the melting point ($T_{melting}$) according to the semi-empirical equations [41, 44]:

$$T_{Hüttig} = 0.3 T_{melting}$$

Equation 2-1

$$T_{Tamman} = 0.5 T_{melting}$$

Equation 2-2

Therefore, metal particles with higher melting points are generally more thermally stable. In addition, other parameters like particle size and shape can also affect the mobility of solids hence their stability [44-46]. For instance, Wang et al. reported that tetrahedral particles of Pt are more stable than cubic particles [45]. Lu et al. also found that the melting point hence stability of Au particles not only changes with the particle shape, but also increases with the increasing particle size [46]. Besides, the loading or dispersion of metals is also a parameter that affects the sintering process [47].

Apart from the properties of metal particles, the interaction between the metal and the support also plays an important role to determine the particle stability, as it can affect the mobility of metal atoms or particles on the support. If the support surface has a lot of defects or pores, the migration of metal on the surface will be more difficult and hence the particles will be more stable. Moreover, the effects of the particle-support interaction can be altered by the presence of some promoters or impurities [35, 42]. For instance, if Cl remains on the support when chloride precursors are used, it can increase the surface mobility of metals hence the sintering by weakening the particle-support interaction [48], and other species such as F and S also show the similar effects [42]. On the contrary, species like C, O, Ca, Ce and Ba can lower the surface mobility of metals, and hence the sintering process can be inhibited [42].

2.3 Strategies to stabilize metal nanoparticles

The sintering leads to severe deactivation of metal nanoparticles and the sintering process is usually irreversible [44], hence the deactivated catalysts have to be replaced regularly, which increases the costs for using catalysts especially the ones rely on noble metals. Additionally, the recycling of these metals from the spent catalysts is challenging. For instance, catalysts used in automotive exhaust control are the biggest consumer of noble metals which use about 60% total amount of Pt, Pd and Rh every year, but only less than 10% of these metals are recycled [5]. Therefore, in order to reduce the consumption of noble metals, the sintering process must be prevented by stabilizing the metal nanoparticles. Based on the parameters that affect the sintering process as introduced above, some strategies for particle stabilization can be proposed. Basically, the temperature and atmosphere belong to the external parameters that are determined by the conditions of specific applications, so normally they cannot be altered easily. Hence, attention should be given on the modification of

properties of metal particles and support as well as particle-support interactions [41]. Some current strategies to stabilize metal nanoparticles will be introduced below.

2.3.1 Stabilization by alloying

Since reported by Sinfelt [49], the bimetallic systems, in which two different metal species together form the individual particles, have become a hot research area for catalysis, because bimetallization can provide unique properties which the monometallic particles do not have [50]. Aside from the catalytic properties, the sintering of the bimetallic particles may also be suppressed if a metal is alloyed with a second metal which has a higher melting point [41]. Cao and Veser reported that Pt can be stabilized by forming bimetallic particles with Rh and the resulted Pt-Rh particles can stay stable at the size of ~4 nm up to 850 °C while the monometallic Pt particles sinter at 600 °C. However, the behavior of the Pt-Rh particles with the increasing temperature is dependent on the Pt/Rh ratio [51]: with high Rh amount (Pt/Rh=1), the Pt-Rh particles can remain almost unchanged up to 850 °C; with low Rh amount (Pt/Rh>3), a de-alloying process will happen, in which Pt bleeds from the Pt-Rh particles to form big Pt particles and the Rh concentration in the remaining Pt-Rh particles increases, and in this way the Pt-Rh particles can be stabilized on the sacrifice of some Pt. Moreover, it is important to choose the appropriate second metal, because the melting point of the bimetallic particles normally changes nonlinearly with the composition and the addition of a second metal may also change the activity and selectivity of the catalyst.

Also, for some bimetallic particles, phase transformation may happen to generate an outer shell to protect the core inside [41]. Unlike the normal core-shell structure that will be introduced later, this shell is grown from the bimetallic particles themselves. For instance, Liu et al. reported that by reducing the preformed bimetallic Au-Ag particles in $NaBH_4$, a core-shell nanostructure (~3 nm) with Au-Ag inside and Ag shell outside can be produced, and it is stable up to 500 °C and highly active for CO oxidation [52].

However, this phase transformation is not always beneficial in bimetallic systems. The surface segregation can happen for most bimetallic particles by increasing the temperature, and it can significantly change the composition at the particle surface, ending up with one metal accumulating on the surface or the totally reverse result in which the intended core-shell structures are converted to well-mixed bimetallic

particles [41]. This will inevitably change the catalytic properties of the sample, and how it will change is nearly unpredictable. Therefore, this particle stabilizing strategy through alloying is limited by the surface segregation phenomenon.

2.3.2 Stabilization by particle encapsulation

Another effective strategy to stabilize metal nanoparticles is encapsulation of nanoparticles in hollow porous shell materials. The basic roles of the outer shell material include physically isolating and hence protecting the core nanoparticles from coalescence [53], providing confinement and growth control to the core nanoparticles [54], and in some cases modifying the metal-support interface [55]. In order to protect the core nanoparticles, the shell material itself is required to be thermally and chemically stable, and mechanically strong enough to survive the harsh reaction conditions [41]. When used in catalytic applications, the access of reactants to the active metal surface is vital, so high porosity is also an important requirement for shell materials.

A wide range of materials have been used as the shell to encapsulate metal nanoparticles, and according to the characteristics of the final structure, they can be classified into three types including the core-shell, core-sheath and mesoporous structures [41].

The core-shell structure is the most typical and straightforward way to encapsulate metal nanoparticles by directly wrapping them with some porous oxide shells to isolate the individual nanoparticles. Porous silica is often used as the shell material to from the core-shell structure, which can provide excellent stabilization to metal nanoparticles [55-57]. Joo et al. successfully prepared the core-shell structure of Pd@SiO_2 (Figure 2-2(a)), by preparing the Pd nanoparticles first followed by coating the preformed Pd nanoparticles with the silica shell [55]. The resulted sample remained stable up to 750 °C and the particle size of Pd remained unchanged. At the same time the core-shell structure did not collapse and the sample also showed very high activity for CO oxidation and C_2H_4 hydrogenation. Apart from silica, some transition metal oxides such as Fe_2O_3, TiO_2 and SnO_2 can also be used to encapsulate noble metal nanoparticles to form the core-shell structure, which can also provide synergistic effects at the noble metal-metal oxide interface [58]. For instance, Yin et al. prepared Au@Fe_2O_3 core-shell structure by coating the preformed Au nanoparticles with Fe_2O_3,

and their sample was stable up to 700 °C and it was more active in CO oxidation as compared with Au deposited on Fe_2O_3 [59]. Moreover, it is worth mentioning that the yolk-shell structure, a variation of the core-shell ones, has also been studied a lot recently [60, 61]. Unlike the core-shell structure, the yolk-shell structure consists of a hollow shell and a core metal nanoparticle, and there is a big interstitial space between the shell and core (Figure 2-2(b)). Hence, the core nanoparticle is free in the hollow shell with homogeneous surrounding environment, and more surface area of the nanoparticle can be accessed by reactants [61]. For instance, Pablo et al. coated Au nanoparticles in turn with shells of SiO_2 and ZrO_2, and then the inner shell SiO_2 was remove by using the NaOH solution, which resulted in the Au@ZrO_2 yolk-shell structure [62]. The structure of the sample and hence its activity in CO oxidation were unchanged after being aged at 800 °C.
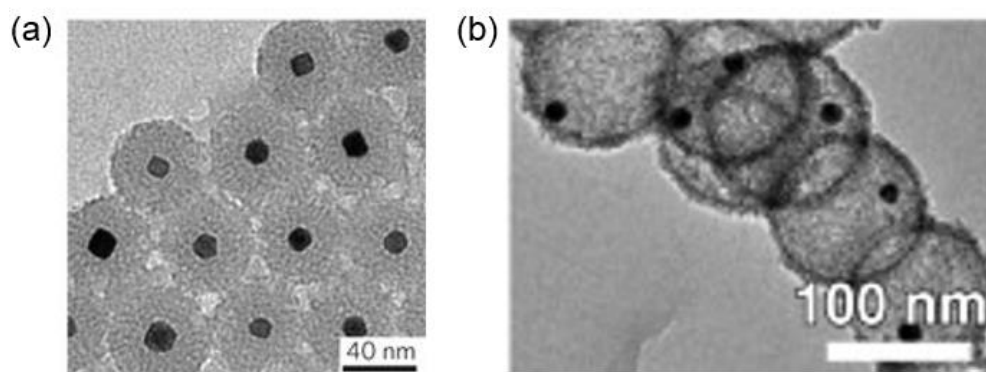
Figure 2- 2 Examples showing the (a) core-shell structure (Pt@SiO_2) [55] and (b) yolk-shell structure (Au@ZrO_2) [62].

The core-sheath concept was adopted by Cao et al. [41] for another encapsulating structure where active metal nanoparticles are confined inside tubular supports which are open from both sides. Hence, the hollow tubular support can strengthen the mass transfer of reactants, which benefits the catalytic processes. A typical support for the core-sheath structure is the carbon nanotube (CNT) which can not only control the size of metal nanoparticles but also provide unique properties and chemical reactivities to metal nanoparticles due to the interaction between the metal and interior walls of CNTs [63]. A good example is the multi-metallic nanoparticles (Rh, Mn, Li and Fe) confined in the CNTs (Figure 2-3), as reported by Pan et al. [64]. They found that the activity of the CNT confined nanoparticles was much higher (more than twice) for ethanol formation from syngas as compared to the same nanoparticles on SiO_2 support, and this high activity was maintained in the long-term experiment.
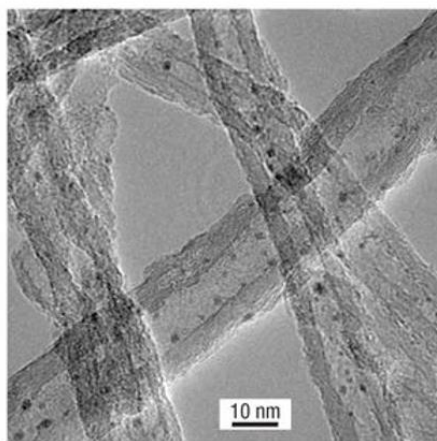
Figure 2- 3 Multi-metallic nanoparticles (Rh, Mn, Li and Fe) confined in CNT. [64]

Also, some porous materials have been widely used to stabilize metal nanoparticles. The most popular one is mesoporous silica such as MCM41 and SBA-15 which can serve as good templates to confine metal nanoparticles [65]. The advantages of silica supports include high surface area, narrow pore size distribution, tunable pore dimension and the ordered pore structure which enables the facile diffusion of both reactants and products during the catalytic processes [41, 65]. Therefore, a wide range of metal nanoparticles such as Pt, Rh, Au and Ni has been reported to be confined using mesoporous silica [66-68]. Apart from silica, mesoporous carbon can also be used as a good support, and for example, Li et al. prepared ~1.2 nm Pd nanoparticles on the ordered mesoporous carbons which showed good stability as well as enhanced activity and selectivity for hydrogenation of phenol [69]. Besides, metal nanoparticles can also be stabilized using the materials with irregular pore networks, and their high interconnectivity can allow for better mass transfer [41]. For instance, Veser and co-workers reported Pt nanoparticles embedded in the thermally stabilized alumina matrix, and the sample showed good activity and selectivity in methane partial oxidation and the sintering did not happen at 1000 °C [70].

2.3.3 Stabilization by enhancing particle-support interaction

Based on the mechanisms of metal sintering as introduced above, the sintering process can be suppressed if the mobility of the metal species on the support is reduced, which can be achieved by strengthening the particle-support interaction. As mentioned before, some elements appearing on the support can modify the particle-support interaction, which means that some species can be used as the stabilizer for nanoparticles [71, 72]. For example, CeO_2 is often added in catalysts to improve the

17

oxygen storage ability, but it is also important to stabilize the metal nanoparticles. CeO_2 can stabilize support materials by suppressing the transformation from the high-surface phase (like γ-Al_2O_3) to the low-surface phase (like α-Al_2O_3) [73], but more importantly it can provide a stronger anchoring strength to metal nanoparticles on the support by forming the metal-O-Ce bond and hence inhibiting the sintering process [71, 74]. Some other species such as CoO_x and In_2O_3 have been reported to have similar effects as CeO_2 [75, 76].

Another stabilizing method relating to the particle-support interaction was reported through modification of the support with another layer of oxides [77, 78]. For instance, Dai and co-workers reported that they prepared the $Au/Al_2O_3/TiO_2$ structure (Figure 2-4), by modifying the surface of the TiO_2 support with an extra layer of amorphous Al_2O_3 followed by deposition of Au nanoparticles on the surface-modified TiO_2 [78]. They found that Au nanoparticles could be strongly anchored to the Al_2O_3 overlayer and were more stable against sintering as compared to the Au nanoparticles deposited on the unmodified TiO_2 surface, although the mechanism for this stabilization is unclear. It is possible that the Al_2O_3 overlayer physically confines the migration of Au nanoparticles, or some chemical bonds might form between Au and the overlayer.
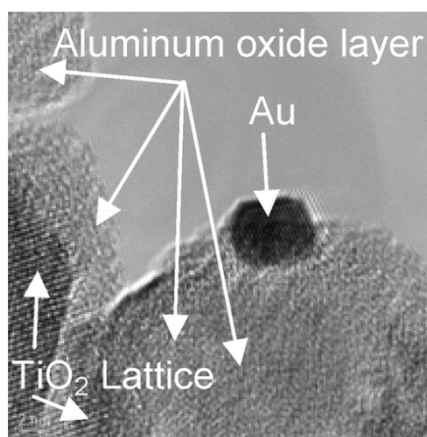
Figure 2- 4 Au nanoparticle deposited on the Al_2O_3 modified TiO_2 surface ($Au/Al_2O_3/TiO_2$). [78]

2.4 Conclusions

From this literature study, it can be found that despite the development of preparation techniques of supported metal catalysts, the metal nanoparticle sintering still remains a big challenge for these catalysts. The sintering mechanisms and the typical

stabilizing strategies described in this chapter provide valuable guidance for the catalyst design in this study. Therefore, different approaches will be demonstrated to stabilize noble metal nanoparticles, which include encapsulation of nanoparticles and modification of particle-support interface by partially socketing nanoparticles in support surface.

Chapter 3: Experimental

This chapter introduces the methodology used in this study, including the characterization techniques, sample preparation methods, experimental setups and operation conditions for reduction and catalytic experiments.

3.1 Characterization techniques

3.1.1 Powder X-ray diffraction (PXRD)

X-ray diffraction (XRD) is widely used as a non-destructive technique to analyse the crystalline phases, both qualitatively and quantitatively. This includes identification of the crystal structure, crystallite size and lattice strain, through analysing the diffraction patterns of the sample [79, 80].

When waves impinge on two adjacent slits, if the wavelength is similar to the spacing between slits, interference of the waves (constructive, destructive or partially destructive) can happen depending on the incident angle of the waves. In crystalline materials, planes of atoms are periodically ordered at a certain spacing, which can be treated as diffraction grating. In XRD, a beam of X-rays hits the sample and the X-ray waves are scattered on different planes of atoms in different directions. The wavelength of incident X-rays (~1 Å) is comparable with the distance between atoms, which fulfils the requirement for wave interference as mentioned above. Therefore, interference patterns can be generated. In most directions, destructive interference occurs, but when the path length difference of the X-rays scattered from two adjacent layers is an integral multiple of the wavelength [79, 81], constructive interference occurs, as described by Bragg's law [81] (shown in Figure 3-1):

$$2d_{is} \sin \theta = n\lambda$$
Equation 3-1

where d_{is} and θ are the interplanar spacing and incident angle of X-rays respectively, and they together determine the path length difference between the X-rays scattered by two adjacent planes to be $2d_{is} \sin \theta$. While λ is the wavelength of the X-ray, and n is the diffraction order which can be an arbitrary integer.
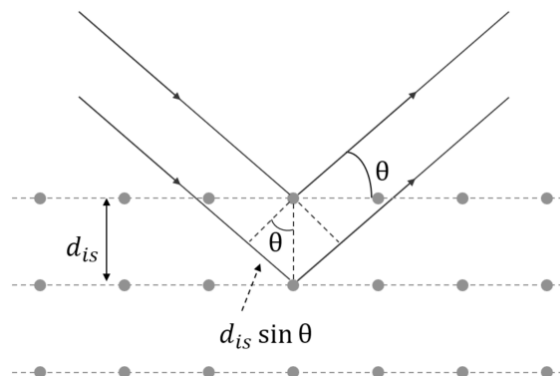
Figure 3- 1 X-ray waves scattered from adjacent planes.

In the crystal lattice, the interplanar spacing varies with the orientations of the lattice (shown in Figure 3-2). In powder XRD, fine powders serve as the diffracting target, and

X-rays can impinge all the different planes in the lattice. Hence, constructive interference can form from all the planes at their corresponding specific angles that fulfil the Bragg's equation, which can lead to the formation of diffraction cones as shown in Figure 3-3. Therefore, the diffraction pattern that contains characteristic peaks of the sample can be obtained, which provides important structural information of the sample. For instance, interplanar spacing can be calculated at different diffracting peak positions because λ and θ are known.
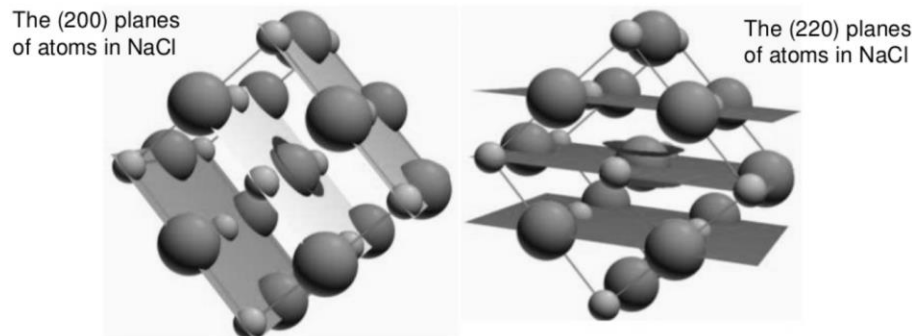
Figure 3- 2 Different lattice planes (200) and (220) in a NaCl unit cell [82].
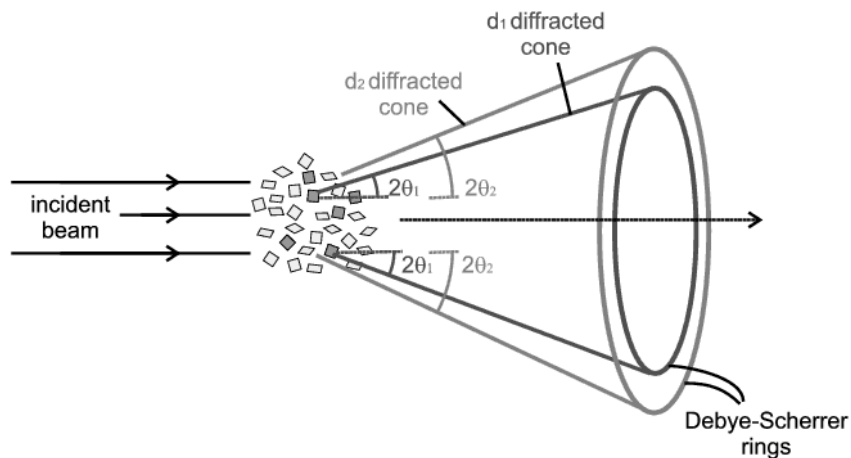
Figure 3- 3 Diffraction cones generated by illuminating powders with X-rays at different incident angles [83].

Normally, the powder XRD instrument consists of several basic components, such as X-ray generator, monochromator, goniometer, powder sample holder, and detector. Figure 3-4 shows the configuration of a typical modern Powder XRD. X-rays are normally generated by hitting a metal target (typically Cu) with electrons emitted by tungsten filament and accelerated in high voltage. In XRD, the X-rays are required to be monochromatic as the diffraction angle is related to the X-ray wavelength according to Bragg's equation, and hence the X-rays must be monochromatized to selectively

filter the Cu Kα radiation. The powder sample is packed in a sample holder that is located at the centre of the cycle of goniometer, and the X-rays illuminate the sample from different angles that will be collected by the detector finally. These basic components of XRD can be assembled in two geometries that are the reflection (also known as Bragg-Brentano) geometry and the transmission geometry respectively, as shown in Figure 3-5. The component geometry displayed in Figure 3-4 is a typical reflection geometry that is used more often than the transmission geometry.
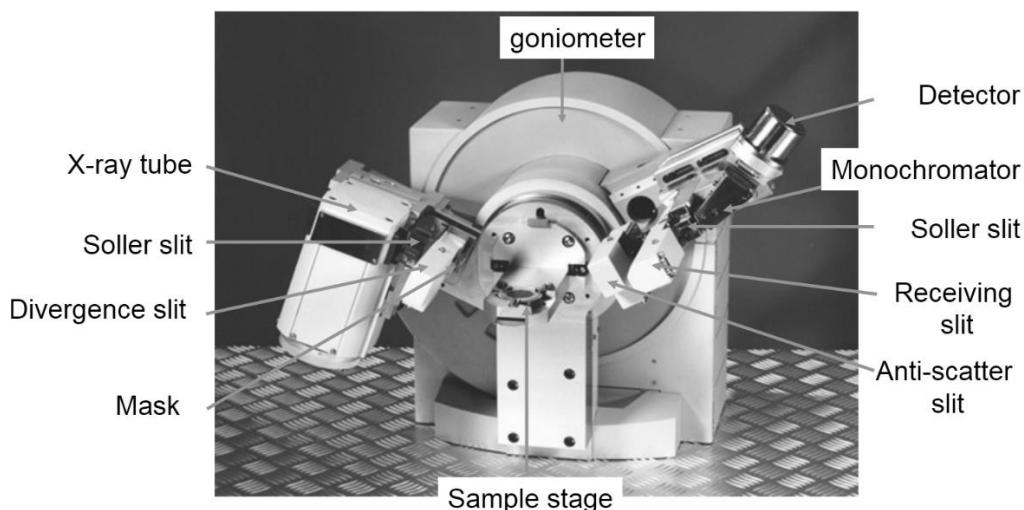
Figure 3- 4 The main components in a typical XRD [84].
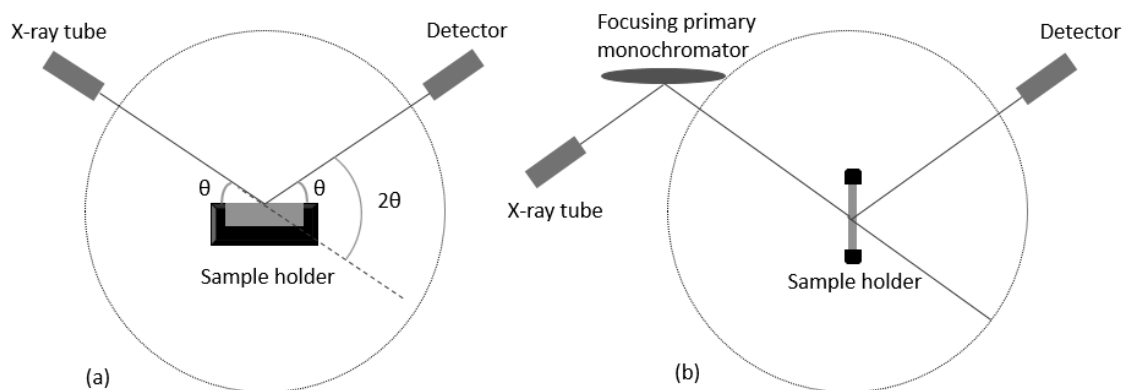
Figure 3- 5 Two XRD component geometries: (a) reflection geometry and (b) transmission geometry.

It has been mentioned above that the X-rays must be monochromatized in XRD, and the quality of this step can affect the analysis for the material purity and structure. Conventional X-ray sources contain Kα (Kα1/Kα2 doublet) and Kβ signals while the undesirable characteristic wavelength (such as Kβ) needs to be removed, which can be achieved by using a β-filter or a single crystal monochromator. A β-filter possesses an adsorption edge between Kα and Kβ, which can selectively adsorb Kβ radiation

while transmit the Kα1 and Kα2, as shown in Figure 3-6 [85]. For instance, Ni can be used as the β-filter for Cu radiation. However, the β-filter is not able to completely eliminate the Kβ signals and it will also cause a sudden change of the diffraction background near the adsorption edge. Hence, the remaining signal of Kβ and a terrace-like intensity change near the adsorption edge would be observed in the diffraction pattern (as shown in Figure 3-6(b)).
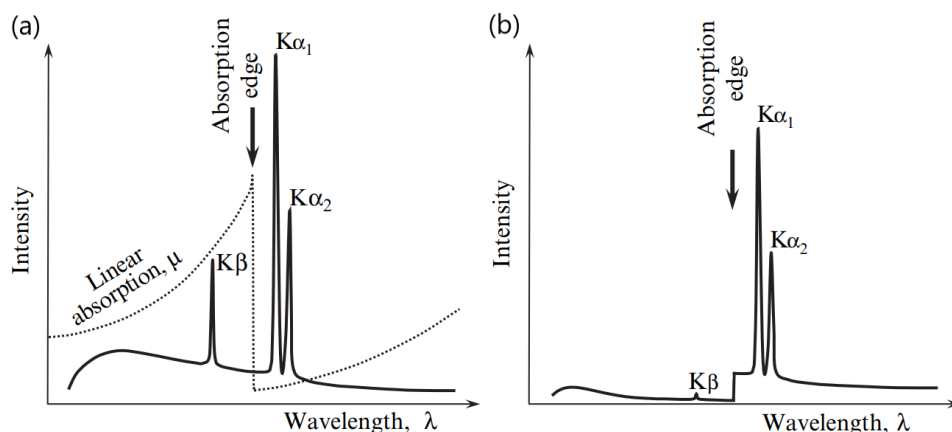
Figure 3- 6 (a) Schematic of the X-ray emission spectrum (solid line) overlapped with the schematic of the adsorption function $\mu(\lambda)$ of a β-filter material (dotted line). (b) Changes of the X-ray intensity after being filtered as a function of the wavelength. [85]

On the other hand, a single crystal monochromator would have better performance to filter the X-rays, and its basic principle is shown in Figure 3-7. When a divergent beam of X-rays reaches the crystal from a small range of angles between θ_1 and θ_2, different wavelengths λ_i will be diffracted at different angles based on the Bragg's law (Equation 3-1), and hence the spatial distribution of wavelengths becomes uneven in the reflected beam. Longer wavelengths (like the Kα1/ Kα2 doublet) will be grouped at high Bragg angles while shorter wavelengths (like Kβ) will fall into low angles, and hence Kβ can be easily removed by placing a narrow slit in the path of the reflected beam [85]. Some more complicated configurations of monochromators are also able to separate Kα1 and Kα2, and consequently eliminate the Kα2 intensity.
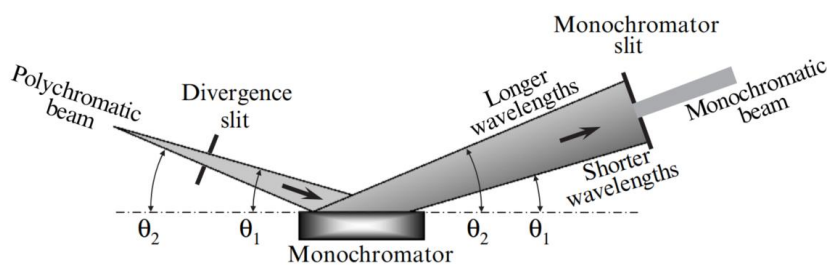
Figure 3- 7 Schematic demonstration of the principle for using a single crystal monochromator. [85]

In this thesis, XRD was used routinely to identify the composition, crystal structure and phase purity of the perovskite materials. The XRD instrument at Newcastle University is a PANalytical X'Pert Pro Multipurpose Diffractometer operating in a reflection-type geometry. The instrument is equipped with a PW1730 X-ray generator and a sample spinner stage. The diffraction patterns were generated by using Cu Kα radiation ($\lambda_{k\alpha1}$=1.540598 Å, $\lambda_{k\alpha2}$=1.544426 Å). The voltage and current employed in the X-ray tube were 40 kV and 40 mA, respectively. The samples were scanned at the range 2θ, starting from θ =20 – 90 °.

3.1.2 Scanning electron microscope (SEM)

Scanning electron microscope (SEM) is a very versatile instrument for examining the microstructure, morphology and the chemical composition of materials.

During the operation of SEM, a beam of electrons will hit the specimen, leading to various interactions between the electrons and the specimen, and the signals resulted from these interactions can be used to generate images [86]. There are two kinds of interactions between electrons and specimen in general: elastic and inelastic. Elastic scattering means that the incident electrons are deflected by the atomic nucleus or the electrons in outer shells that have similar energy, without significant energy loss. The direction of scattered electrons will be changed considerably and, for instance, electrons being elastically scattered with an angle change more than 90° are known as backscattered electrons (BSE) [86]. In inelastic scattering, incident electrons lose substantial energy that is transferred to the specimen atoms, hence the specimen atoms may become ionised and their electrons get excited. This can give rise to secondary electrons (SE) of low energies (< 50 ev) which represent the main radiation used for surface imaging. The signals from different interactions are summarised in Figure 3-8, in which we can find that, apart from BSE and SE, there are many other signals such as Auger electrons and characteristic x-rays [86].

Backscattered electrons BSE

Primary electron beam

Secondary electrons SE

Photons of visible light

X-ray photons

Auger electrons

Sample surface

Secondary electrons

Backscattered electrons

Characteristic X-rays

Continuum X-rays

Secondary fluorescence

BSE spatial resolution

X-ray spatial resolution
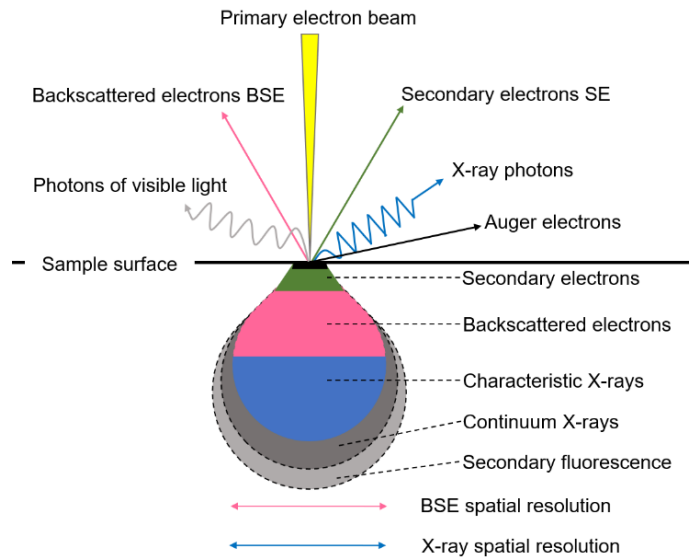
Figure 3- 8 Schematic demonstration of different signals formed by electron-specimen interactions, and the regions within specimen where these signals are generated. [87]

It is worth mentioning that the interactions do not only happen on the top-most surface of the specimen, but some electrons would penetrate in some depth into the specimen until they interact with atoms in the specimen. Therefore, a small volume near the specimen surface will be excited and produce signals, which is called primary excitation region. Depending on the voltage used for the incident electrons and the atomic number of the specimen, the shape and size of the excitation region will change as shown in Figure 3-9. When the atomic number of the atoms in the specimen increases, the shape of the excitation region will change from a "tear drop" to a hemisphere. The excitation region will be deeper when accelerating voltage increases and the specimen atomic number decreases, because higher voltage endows incident electrons with higher energy and lower specimen atomic number has less blocking effects for incident electrons. In that case, more signals from the depth in the specimen will be obtained, and details of the material surface will be compromised. Therefore, lower accelerating voltage is preferred if more surface details and high resolution are desired [86]. In SEM, specimen is irradiated with electron beams and adequate conductivity is needed for specimen to discharge the electrons. For poorly conducting specimens, electrons will accumulate on the scanning area on sample surface, which is known as charging. It would cause incident electrons to be repelled from the scanning area or result in distorted SEM images. Different methods can be used to minimise the charging effects. Coating the specimen with a conducting layer can be applied, but the relatively thick layer of the coating will mask the detailed features of

the sample surface. Besides, charging effects can also be reduced by lowering the voltage and current of incident electrons and using thinner specimen.
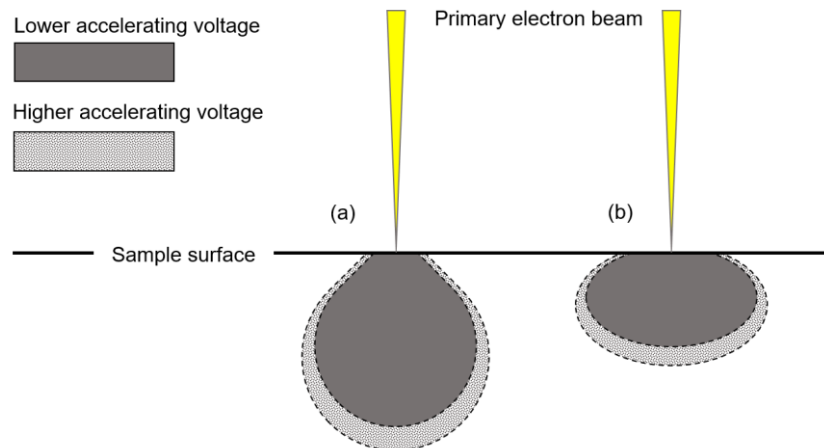
Figure 3- 9 Schematic demonstration of the excitation region changing with the accelerating voltage and the atomic number of specimen: (a) low atomic number and (b) high atomic number.

SEM images can be generated by using different signals, which can give different information of the sample. Secondary electron (SE) is the most common signal to be used in SEM. Secondary electrons are emitted from the volume within several nanometers from the sample surface, hence they are normally used to generate high-resolution images to show the sample surface texture and roughness with excellent topographic contrast. Backscattered electron (BSE) is another important signal that contains the information about sample composition and topography. Incident electrons interact with the atomic nucleus of the sample and will be deflected back as shown in Figure 3-10. Nucleus of the atoms in specimen with higher atomic numbers will have more positive charges and hence more incident electrons will be backscattered. If the material is compositionally inhomogeneous, the areas containing heavier elements will generate more backscattered electrons hence becoming brighter in the ultimate image, while other areas that contain lighter elements will be darker. Therefore, BSE images can be used to determine the compositional homogeneity of the material by checking the contrast across the surface.
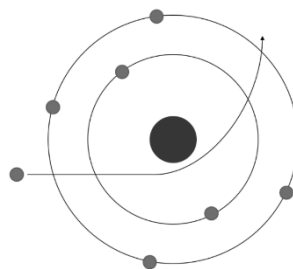
Figure 3- 10 Formation of the backscattered electron via interaction between the incident electron and the atomic nucleus of the material.

Figure 3-11 demonstrates the major components in a typical SEM instrument. Electrons are generated and accelerated by an electron gun at the top of the column. The beam of electrons is converged to a focused electron spot (1-100 nm), by passing a system of electromagnetic lenses. Then the focused electrons pass through scanning coils, and interact with the specimen placed on the sample holder. Finally, the signals generated on the specimen reach the detector. Scanning coils can deflect the electron beam, so the beam scans the specimen in a raster pattern (along x and y axes). The whole system should be operated in high vacuum to avoid electrons being scattered by air.
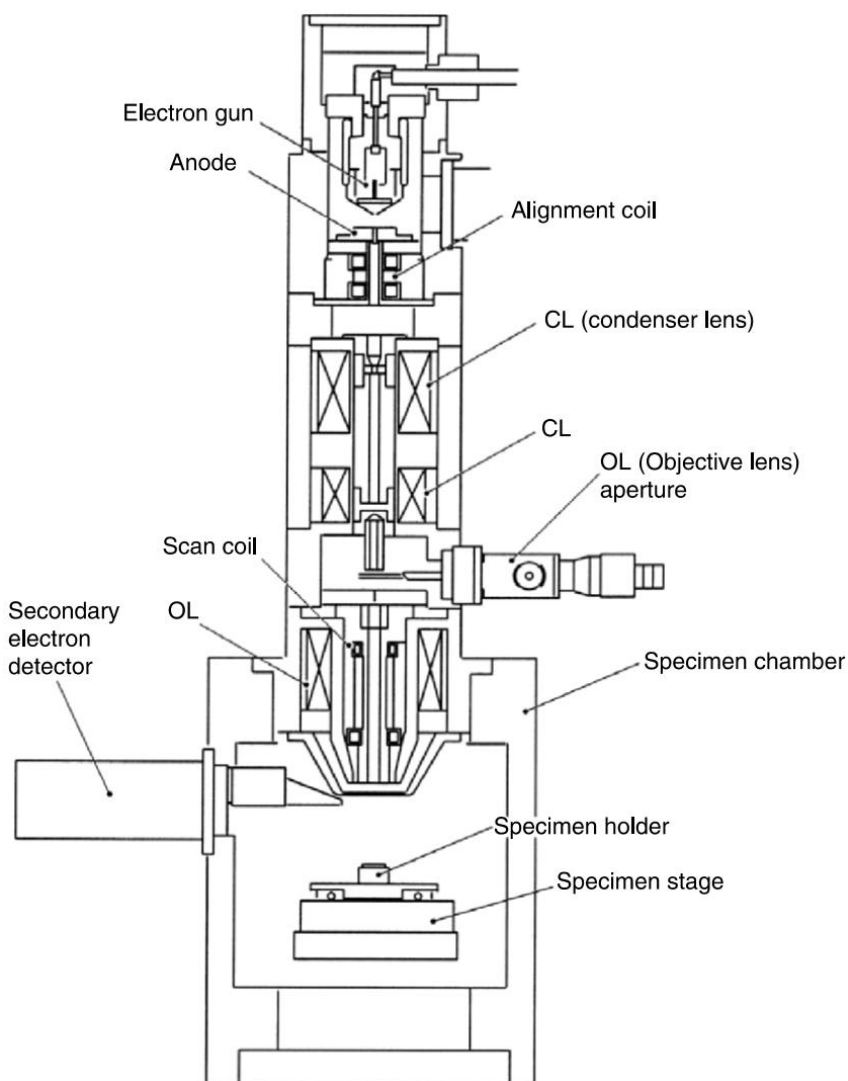
Figure 3- 11 Schematic demonstration of configuration of a typical SEM column. [86]

In this study, SEM was used as a routine technique especially for the perovskite samples. Regarding the as-prepared perovskite samples, they were scanned in BSE mode to determine the compositional homogeneity of the samples by checking the contrast across the sample surface as mentioned above. Regarding the perovskite

samples after reduction, they were scanned in the SE mode to visualize the nanoparticles grown on the surface, which could be used to determine the particle characteristics such as particle size and population. Two instruments of SEM were used: a low-resolution Tescan Vega 3LMU SEM fitted with a Bruker XFlash® 6 | 30 detector for EDS at Newcastle University, and a high-magnification and high-resolution Helios Nanolab 600 SEM from FEI at Durham University. The SEM scans were operated under high-vacuum mode and with a voltage ranging from 1 to 30 kV.

3.1.3 Helium ion microscope (HIM)

Although electron microscopes such as SEM are widely used in material study, their performance is limited by the spot size of the electron beam on the sample. The diameter d_f of the theoretical smallest focused spot of any radiation can be calculated as [88]:

$$d_f = k_f \lambda / \alpha$$

Equation 3-2

where, λ is the wavelength of the radiation; k_f is a parameter and α is the semi-convergence angle of the radiation beam. The wavelength of electrons used in SEM is in the magnitude of 0.01 nm, which sets a limit for the imaging quality. This can be improved by replacing the electrons with heavier ions that have substantially smaller wavelengths as shown in Figure 3-12. Therefore, a new microscope technique has been developed based on helium ions, which is hence called as helium ion microscope (HIM).
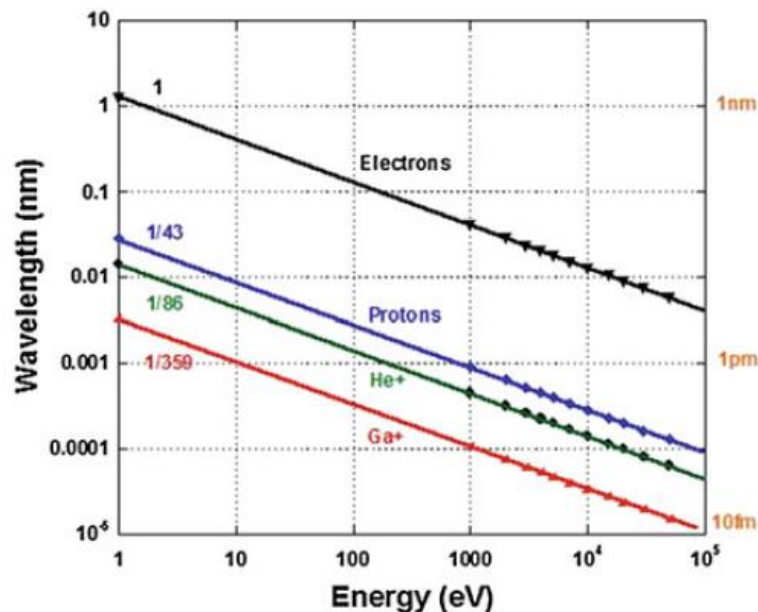
Figure 3- 12 Wavelengths of electrons and some ions as a function of energies. [88]

HIM has similar working principles as SEM, but it illuminates the specimen with helium ions instead of electrons. Interaction between the incident ions and specimen atoms leads to the formation of secondary electrons and scattered ions, and the secondary electrons are usually used to generate images [89]. HIM shows advantages in many aspects over SEM. Helium ions have smaller probe size and their interaction volume with the specimen is considerably smaller as compared with electrons, which can generate images with higher resolution, stronger topographic contrast and improved depth of focus [89, 90]. In addition, as compared with SEM, HIM can produce secondary electrons in larger quantities, which enables imaging at lower beam currents and hence reducing the damage to the sample [89, 91].

Figure 3-13 briefly describes the configuration of a HIM column, which is similar as that of an SEM. Helium ion source is a key component in HIM, and it normally consists of a single crystal metal that is fabricated in the shape of needle with a pyramidal structure at the apex. Under positive voltages, electric field will form at the apex atoms. Helium gas in the vicinity of the needle will be affected by the electric field gradient, and then be polarized and drawn towards the apex. Only those helium atoms at the tip of the apex which consists of only three atoms (trimer, as shown in Figure 3-14) can be ionised by the relatively higher electric field [92, 93]. Then the generated helium ion beams will pass through two electrostatic lens to be focused before interacting with the specimen surface. The interaction will generate different signals (e.g., secondary electrons, scattered ions, polarized photons), so there is a variety of detectors to collect these signals. Normally secondary electrons are used to generate images.

Although HIM has a lot of advantages over SEM, this technique is still in development and the availability of the instrument is limited. Additionally, samples are required to be thermally equilibrated within the microscope for long time before scanning, making HIM more difficult to use on a routine basis. Therefore, in this study, SEM was still used as a routine technique for microstructure characterization of most samples. However, in the stability test of supported metal nanoparticles in Chapter 5, clear visualisation of individual nanoparticles was required and hence the evolution of the nanoparticles could be recorded to determine their thermal stability. This required high-resolution images with excellent surface details, and because of the limited resolution of the SEM instrument at Newcastle, HIM was used instead. The HIM instrument used in this study was a Zeiss ORION NanoFab HIM at NEXUS of Newcastle University.
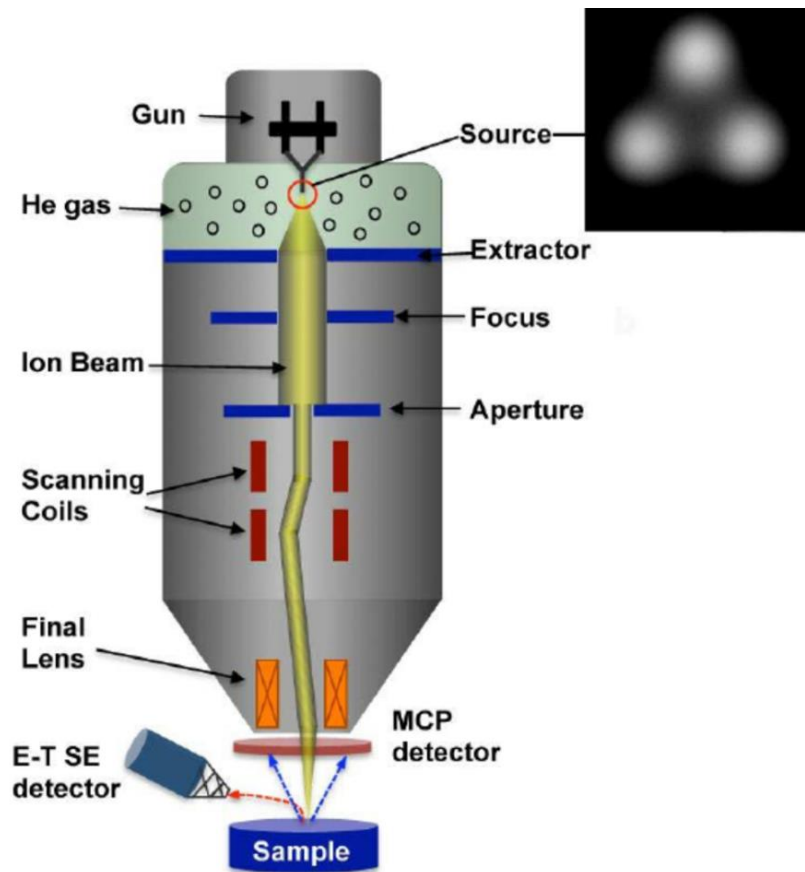
Figure 3- 13 Simplified schematic of a HIM column (Zeiss ORION HIM). [94]
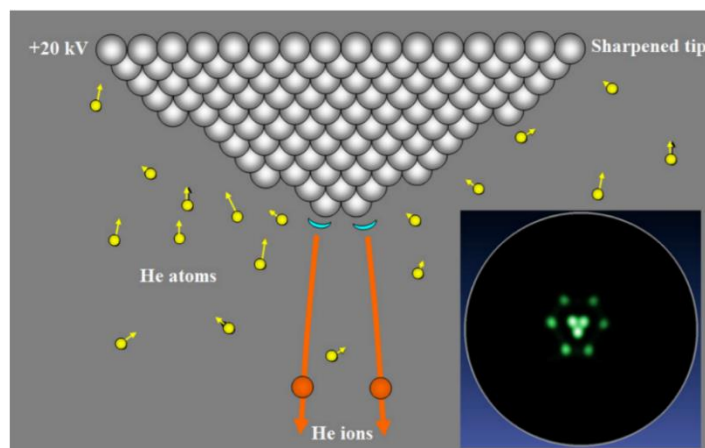
Figure 3- 14 Generation of helium ions at the tip of the emitter (trimer). [89]

3.1.4 Transmission electron microscope (TEM)

Transmission electron microscope (TEM) is also one of the main techniques for the microstructural characterization of materials in catalyst study. Unlike SEM in which the image is generated based on the scattered electrons, TEM uses the electrons transmitting through the specimen. In TEM, a high-energy electron beam (100-400 keV)

is applied to probe an 'electron transparent', thin specimen (less than 100 nm), and the electrons which pass through the specimen are collected for imaging [95, 96].

TEM resembles an optical microscope, but it uses electromagnetic rather than optical lenses to focus electron beams. A TEM instrument is typically composed of electron gun, probe-forming lenses and apertures, specimen holder, image-forming lenses and apertures, electron detectors and vacuum system (Figure 3-15) [96]. The electron gun at the top of the microscope column generates electrons and they travel in vacuum along the column. The emitted electron beam goes through a system of condenser lenses that demagnifies the beam and controls its size, and then it will transmit the specimen. In order to make the specimen electron transparent, additional preparation for TEM samples is required to control their thickness. The objective lenses can generate an intermediate magnified image, and it will be enlarged by projector lenses on the fluorescent screen, and finally the image can be exported by an operator or a camera [97].
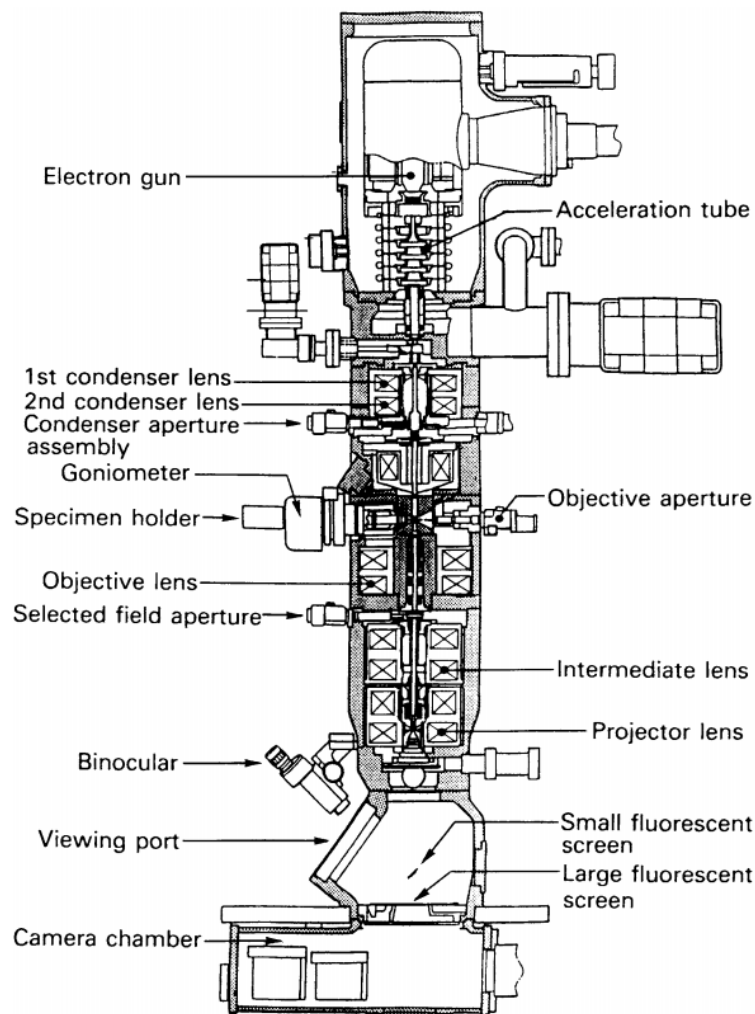
Figure 3- 15 Schematic demonstration of configuration of a typical TEM column. [98]

In this study, TEM was also used to visualise the metal nanoparticles dispersed on the supports such as Al_2O_3 and porous organic cages, and the TEM images obtained could be used to determine the particle characteristics such as size and population. The TEM instrument used in this study was a JEOL 2100F FEG TEM at Durham University, which was operated at 200 kV in scanning TEM mode. Besides, in the research of metal exsolution from perovskite, an environmental TEM was used to in situ observe the exsolution of metal particles from perovskites, which will be introduced in subchapter 3.1.5.

3.1.5 Environmental TEM (ETEM)

In heterogeneous catalysis, catalytic performance can be affected by many properties of the catalyst system, such as metal particle size, shape and interparticle interactions. However, the configuration and evolution of the system are subject to temperature, ambient atmosphere and associated gas-solid reactions. Thus development of techniques to in situ observe the evolution of nanoparticles under reaction conditions is always desired, which can provide researchers with better understanding of the behaviour of nanoparticles in reactions. To achieve this goal, conventional TEM columns can be modified to confine gas or liquid in the area around the sample and allow the sample to be heated according to a desired temperature programme, and this kind of TEM is called environmental TEM (ETEM) (also known as controlled atmosphere TEM) [99].

However, in a TEM, high-energy electrons are employed to transmit the sample and thus a high vacuum environment is required to avoid electrons being scattered by gas molecules. Therefore, in ETEM, gas must be confined in the region where the specimen holder is located (typically 10^{-3}-150 Torr), whereas the microscope column and the gun chamber still need to be maintained in high vacuum ($<10^{-6}$ Torr), to minimise the scattering from gas molecules and also extend the lifetime of the electron gun. Design of the sample region (environmental cell) is the key to fulfil this requirement, and two methods were proposed in the early developments of ETEM. The first method uses a closed cell as the sample holder, where a specially designed holder confines gas or liquid around the sample between two thin electron transparent windows of low electron scattering power (e.g., C or SiN films) [100]. This closed cell method has advantages to handle high gas pressures (depending on the thickness and strength of the window) and to be used in different instruments without further

modifications to the column [99, 101]. However, the closed cell has a big disadvantage that high-resolution images can be difficult to obtain as the windows cause additional scattering. Besides, the windows can rupture, and the holder also has less space for tilting because of its increased thickness. More importantly, the sample region cannot to heated, which limits its application in many reactions that require high temperatures. Therefore, more ETEMs nowadays use the second method which is based on a differential pumping design [102]. In differentially pumped systems, pressure difference is maintained by inserting small apertures both above and below the sample region and also applying additional pumping [99]. The typical configuration of a commercial ETEM column using differentially pumped cell can be found in Figure 3-16. Normally two pairs of pressure limiting apertures are installed, and turbo molecular and ion getter pump systems are used separately [101]. Majority of the gas leaking through the first pair of apertures is removed by a turbo molecular pump system, and the gas left in the column is further restricted by the second pair of apertures. Moreover, the most important part in TEM columns, which needs to be maintained under high vacuum, is the electron gun, so a separated pumping system is applied to evacuate above the condenser aperture [99]. By using this method, a controlled gas environment can be generated around sample region up to 3000 Pa, and all the conventional TEM sample holder can be used in the column without any modifications [101].

ETEM uses the same detectors as conventional TEM for data collection, but at a much higher rate. ETEM is often used to investigate dynamic processes, so it is required to continuously collect data with good temporal resolution to record how the process happens, which results in a huge amount of data being collected in a single experiment.
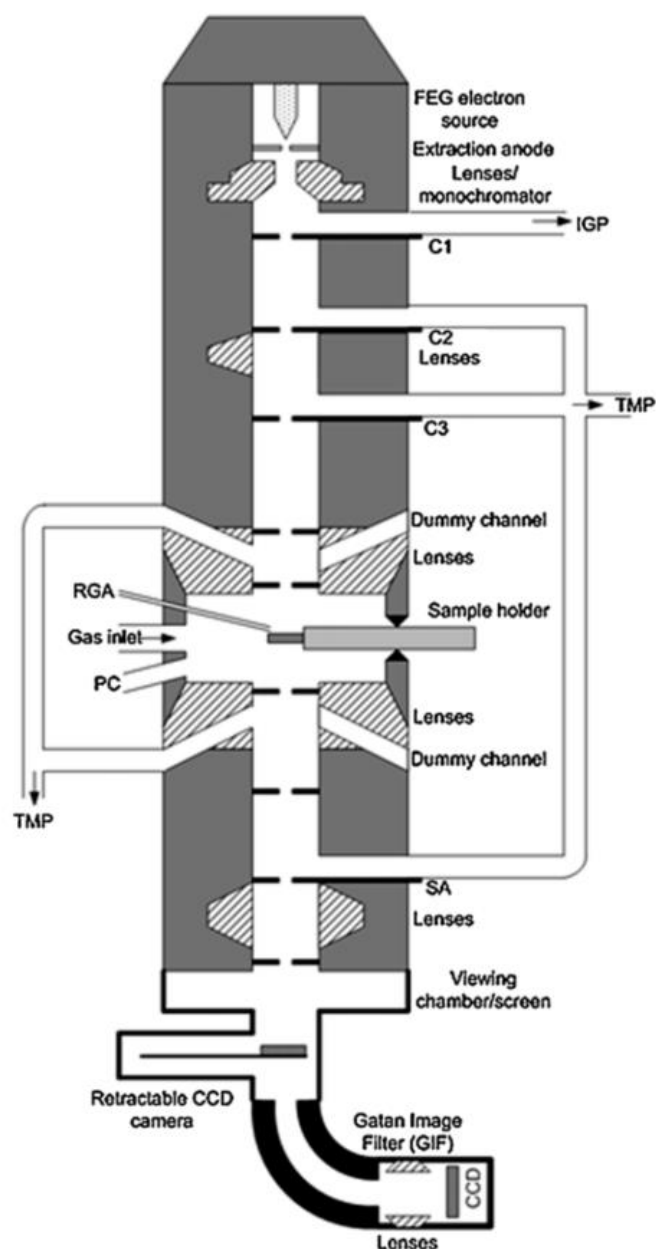
Figure 3- 16 Schematic demonstration of configuration of a typical differentially pumped ETEM column. FEG- field emission gun; IGP- ion getter pump; TMP- turbo molecular pump; RGA- residual gas analyser; PC- plasma cleaner; C- condenser aperture; SA- selected area aperture. [101]

One important application of ETEM is to investigate the transformation mechanism of nanostructures happening in gas-solid reactions. The environmental cell in an ETEM can be regarded as a tiny micro-reactor that mimics a reactor under near real conditions and allows researchers to observe the evolution of nanostructures in situ. For instance, Baker and co-workers used ETEM to study a number of metal catalysts and investigate the relationship between the transformation of particle morphology and the gaseous environment [103, 104]. Here in the research of metal exsolution from perovskite (which will be introduced in Chapter 7), experiments were conducted in situ

in ETEM to explore mechanistic insights into the exsolution process. This was conducted by my co-supervisor Dr Dragos Neagu and our collaborator Dr Mihalis Tsampas from Dutch Institute for Fundamental Energy Research (DIFFER). The instrument used was a new generation FEI TITAN G2 80-300 kV ETEM equipped with an objective Cs aberration corrector and a double tilt holder at Institute of Research on Catalysis and Environment of Lyon (IRCELYON), which allows for the operation under gas pressure up to at 20 mbar and temperature up to 1300 °C [105]. This instrument can continuously record 4K videos at a spatial resolution of 0.09 nm in TEM mode and a time resolution of ~50 ms (or equivalently 20-30 frames per second).

3.1.6 Thermogravimetric analysis (TGA)

Thermogravimetric analysis (TGA) is a technique to precisely record the mass loss (e.g., reduction, drying, desorption, decomposition) or mass gain (e.g., oxidation, wetting, adsorption) of a material versus temperature or time under a certain gas atmosphere [106]. TGA can provide a range of information about the materials depending on the temperature programme and the atmosphere applied in the testing, such as thermal stability, oxidative stability, and decomposition kinetics of materials and composition of multi-component systems. The major components in a TGA instrument include a crucible to hold samples, a balance connected with the crucible and a furnace with control over the atmosphere.

In the research of porous organic cage confined metal nanoparticles (Chapter 6), TGA was used to determine the reduction temperature and thermal stability of the samples, which was conducted by our collaborators at Durham University by using a Perkin Elmer Pyris 1 TGA. Mass change of the sample was negligible before the sample was heated to a certain temperature in reducing gas or air, and significant mass loss was observed when the temperature went higher, indicating the occurrence of the reduction of metals or the thermal decomposition of the material, respectively. Therefore, the TGA results can provide guidance for the appropriate temperature ranges to be used for the sample reduction and the catalytic tests.

3.1.7 Gas sorption analysis (BET surface area)

The BET method, pioneered by three scientists Brunauer, Emmet and Teller, is the most commonly used technique to calculate the surface area of solid materials. Based

on the BET model, the monolayer volume of the adsorbate gas can be determined and hence the sample surface area can be calculated according to the equation [107]:

$$A_s = (V_m/22414)N_a\sigma$$

<div align="right">Equation 3-3</div>

where A_s is the surface area of material; V_m is the monolayer volume of the adsorbate (N2 is normally used); N_a is Avogadro number; σ is the area covered by a single adsorbate molecule (0.162 nm^2 is usually used for N2).

V_m can be estimated from the BET model which was established by making several important assumptions [107, 108]: firstly, when forming the first monolayer of adsorbates, the heat of adsorption stays constant (the surface of the material is treated to be uniform for adsorption); secondly, there is no lateral interaction between the adsorbed molecules; thirdly, the molecules already adsorbed in one layer serve as new adsorption sites for additional molecules in the next layer; finally, the heat of adsorption of the first layer is E_1, while all other layers have the same heat of adsorption which equals the heat of liquefaction ($E_2 = E_3 = \cdots = E_n = E_L$).

Based on these assumptions, the adsorbed volume of molecules (V_{ads}) at a given pressure can be expressed by BET equation as [107-109]:

$$V_{ads} = V_m \frac{cp/p_0}{1-p/p_0} \frac{1-(n+1)(p/p_0)^n+n(p/p_0)^{n+1}}{1+(c-1)(p/p_0)-c(p/p_0)^{n+1}}$$

<div align="right">Equation 3-4</div>

where p/p_0 is the relative pressure; n is the number of layers; c is a constant which is related to the energy of adsorption:

$$c \approx exp\left(\frac{E_1-E_L}{RT}\right)$$

<div align="right">Equation 3-5</div>

Equation 3-4 can be simplified if $n \to \infty$:

$$V_{ads} = V_m \frac{cp/p_0}{(1-p/p_0)(1+(c-1)p/p_0)}$$

<div align="right">Equation 3-6</div>

$$\frac{(p/p_0)}{V_{ads}(1-(p/p_0))} = \left(\frac{c-1}{V_m c}\right)(p/p_0) + \frac{1}{V_m c}$$

<div align="right">Equation 3-7</div>

This simplified form of BET equation is valid for $n > 4$ and for $p/p_0 < 0.35$. A BET plot can be generated by plotting $\frac{(p/p_0)}{V_{ads}(1-(p/p_0))}$ versus p/p_0. In the linear region of the BET plot, the values of $\frac{c-1}{V_m c}$ and $\frac{1}{V_m c}$ can be found as the slope (S) and the intercept (I), respectively, and hence the values of V_m and c can be determined:

$$V_m = \frac{1}{S+I}$$

Equation 3-8

$$c = \frac{S}{I} + 1$$

Equation 3-9

Normally, the linear region appears between $0.05 < p/p_0 < 0.35$, but a lower p/p_0 range may be used for microporous materials [108]. Then the BET surface area per unit mass of the material can be determined:

$$S_{BET} = \frac{A_S}{m} = \frac{V_m N_a \sigma}{22414m}$$

Equation 3-10

where m is the mass of the material.

In this study, the adsorption and desorption of nitrogen (at 77.3 K) was employed to determine the surface area of materials relating to porous organic cages. The nitrogen adsorption and desorption experiments were conducted by our collaborators at Durham University by using a Micromeritics ASAP 2020 volumetric adsorption analyzer. The samples were degassed at offline (100 °C, 15 h) under dynamic vacuum prior to the experiments, and they were then degassed on the analysis port also at 100 °C.

3.1.8 X-ray photoelectron spectroscopy (XPS)

X-ray photoelectron spectroscopy (XPS) is one of the most commonly used techniques for surface chemical analysis, which is based on the principle of photoelectric effect. In XPS, the surface of a material is irradiated by X-ray with a characteristic energy hv. The X-ray interacts with electrons in the core level and also transfers energy to these electrons, hence some of these electrons will be emitted from the surface of the material as photoelectrons that have a kinetic energy E_k. The relationship between hv and the kinetic energy of the emitted photoelectrons E_k can be found as [110]:

$$hv = E_k + E_b + \emptyset$$

Equation 3-11

where E_b is the binding energy of a core-level electron (with reference to the Fermi level), and $\emptyset$ is the work function of spectrometer. Since the energy of X-ray used in experiments is known and the work function is constant, the kinetic energy measured can be used to determine the binding energy of electrons. Therefore, the intensity of photoelectrons measured can be plotted as a function of the binding energy, which forms XPS spectra. The binding energies obtained can be used to determine the surface composition as well as the oxidation states and chemical environments of the

elements appearing at the sample surface. The energy of the X-ray used in commercial XPS instruments is usually low (<1.5 keV), hence XPS is only sensitive for a shallow depth (~10 nm) from the surface of materials.

In this study, XPS was used to analyse the oxidation states of elements on the surface of perovskites, which was conducted by using a Thermo Scientific KAlpha photoelectron spectrometer using monochromatic Al X-ray sources. The software CasaXPS was used for data analysis.

3.2 Preparation of perovskite materials

In this thesis, different techniques are investigated to prepare supported noble metal catalysts as mentioned before, where the metal exsolution from perovskites has been mostly studied. Efforts have been made to modify the preparation method for perovskites to precisely control the stoichiometry and tailor the microstructure. The procedures that have been attempted to modify the preparation method are introduced here.

3.2.1 Conventional solid-state method

The preparation of perovskites was firstly attempted by using the conventional solid-state method as shown in Figure 3-17. For example, to prepare $La_{0.8}Ce_{0.1}Ni_{0.4}Ti_{0.6}O_3$, high-purity metal precursors including La_2O_3, CeO_2, $Ni(NO_3)_2 \cdot 6H_2O$ and TiO_2 were used. The metal oxides were dried at different temperatures (400 °C for CeO_2 and TiO_2, 800 °C for La_2O_3) for 3 hours before they were cooled down to approximately 300 °C, and then they were weighed while hot into a beaker. $Ni(NO_3)_2 \cdot 6H_2O$ was also weighed in the same beaker at room temperature. All the metal precursors were weighed according to the desired stoichiometric ratios. The powders in the beaker were mixed before being transferred into a cup of the planetary ball mill, in which small amounts of acetone and dispersant (ATLOX LP-1, from CRODA) were added as well as the milling media (zirconia balls). The mixed powders were milled at 400 rpm for 2 hours, and then acetone was evaporated at room temperature and subsequently in a drying oven. The dried powder was transferred into an alumina crucible and calcined in air at 1000 °C for 12 hours (5 °C min^{-1} ramp rate). The powder after the calcination was ball milled again using the same procedure as mentioned above (400 rpm, 2 hours). The powder obtained was pressed into dense pellets that were moved into an alumina boat

and sintered in air at 1400 °C for 14 hours (5 °C min^{-1} ramp rate) to form the perovskite phase. The sample prepared in the method above was referred to as the 1st batch sample which was found to contain secondary phases (impurities). Hence, the resulted sample was grounded and ball milled into fine powder, and then pressed into pellets to be sintered again (1400 °C, 6 hours) as demonstrated by the red arrows in Figure 3-17, attempting to facilitate more solid-state reactions to get rid of secondary phases. Hence, the 2nd batch sample was obtained. However, the purity of the 2nd batch sample did not seem to be improved a lot as secondary phases were still seen. Therefore, the solid-state method was modified a lot as introduced below.
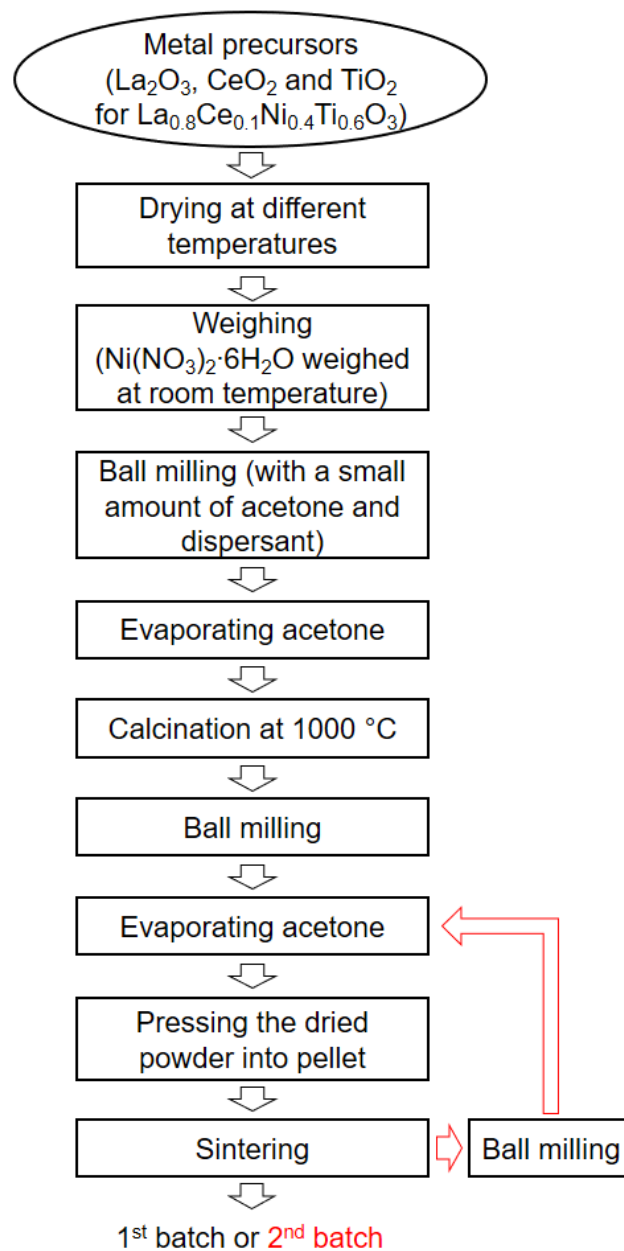
Figure 3- 17 Flow diagram demonstrating the procedures in the conventional solid-state method for perovskite synthesis (exemplified by $La_{0.8}Ce_{0.1}Ni_{0.4}Ti_{0.6}O_3$).

3.2.2 Modified solid-state method

In order to avoid the secondary phases hence to precisely control the stoichiometry of perovskites, the solid-state method was modified as shown in Figure 3-18. The metal precursors were dried and weighed in the same way as used in the conventional solid-state method above. However, instead of being mixed in the ball mill, the solids of precursors were mixed directly in the beaker where they were initially weighed under sonication (Figure 3-18(b-d)): small amounts of acetone and dispersant were added into the beaker and then an ultrasonic probe (Hielscher UP200S) was used to break down the agglomerates and consequently homogenize precursors in acetone to form a fine and stable dispersion. The mixing performance achieved by sonication would be better as compared to the ball milling that was used previously, which could lead to better homogeneity of the final product. The property of the dispersant could also affect the dispersion of precursor solids in acetone, hence two different types of dispersant were tried, namely ATLOX LP-1 (from CRODA, with low solubility in acetone) and Hypermer KD1 (from CRODA, with high solubility in acetone), which gave rise to the 3rd and 4th batch of $La_{0.8}Ce_{0.1}Ni_{0.4}Ti_{0.6}O_3$, respectively. After sonication, acetone was evaporated under continuous stirring (Figure 3-18(e)), which resulted in the homogeneous mixture after drying (Figure 3-18(f)). The following steps were similar as described in the conventional solid-state method. The mixture was transferred into a crucible (Figure 3-18(g)) and calcined at 1000 °C for 12 hours (Figure 3-18(h)), followed by ball milling (400 rpm, 2 h). Finally, after the acetone was completely evaporated, the resulted powder was pressed into dense pellets that were subsequently sintered in air at 1100-1400 °C for 14-24 hours. As exemplified by $La_{0.8}Ce_{0.1}Ni_{0.4}Ti_{0.6}O_3$, this modified solid-state method (by using dispersant Hypermer KD1) could produce highly pure perovskite without secondary phases, hence it was also used to prepare other perovskites in the study. Additionally, the conditions of the final sintering step could be further modified in order to prepare the Rh-substituted perovskites and also to modify the microstructure of the perovskite, which will be demonstrated in detail in subchapter 7.2.
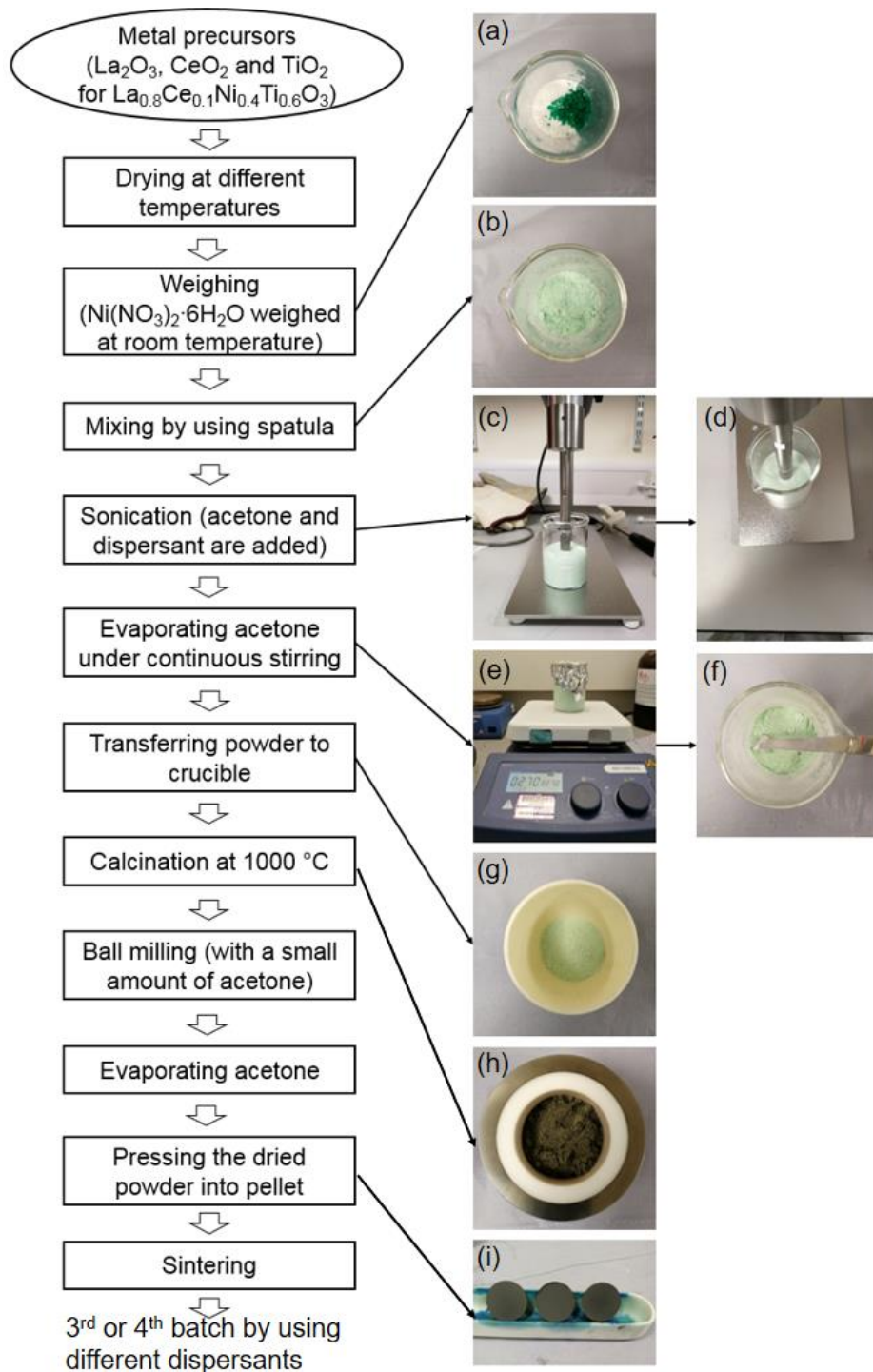
Figure 3- 18 Flow diagram demonstrating the modified solid-state method. Some pictures are added to show the status of the sample at different stages: (a) precursors weighed after drying; (b) precursors mixed by using spatula; (c and d) precursors being mixed under sonication to form homogenous dispersion; (e) acetone being evaporated under continuous stirring; (f) powder obtained after acetone was evaporated; (g) dried powder before calcination; (h) powder after calcination and was transferred into the ball mill cup; (i) powder being pressed into dense pellets before sintering.

3.2.3 Impregnated catalyst

An impregnated sample, 0.6 wt% Rh on commercial γ-Al$_2$O$_3$ (Rh/Al$_2$O$_3$), was also prepared to compare with the exsolved Rh catalyst from perovskite. The support material was added into the dilute Rh(NO$_3$)$_3$ aqueous solution under continuous stirring, followed by evaporation of water and drying in oven (90 °C) overnight. The dried material was calcined at 500 °C for 4 hours (10 °C min^{-1} for heating and cooling). After calcination, the material was sieved to get powders with particle size between 80-160 μm. Then the sample was reduced in 5% H$_2$/Ar at the flow rate of 25 mL min^{-1} (flow rates in all experiments are given at normal temperature and pressure, NTP, which will not be stressed again henceforth) at 550 °C for 4 hours (5 °C min^{-1} for heating and cooling).

3.3 Reduction setup

Some samples in this study need to be reduced to convert the metal oxides to metallic nanoparticles, especially for the perovskite samples as reduction is highly important to trigger the exsolution of metal nanoparticles from perovskites. The setup used for the sample reduction is schematically described in Figure 3-19.
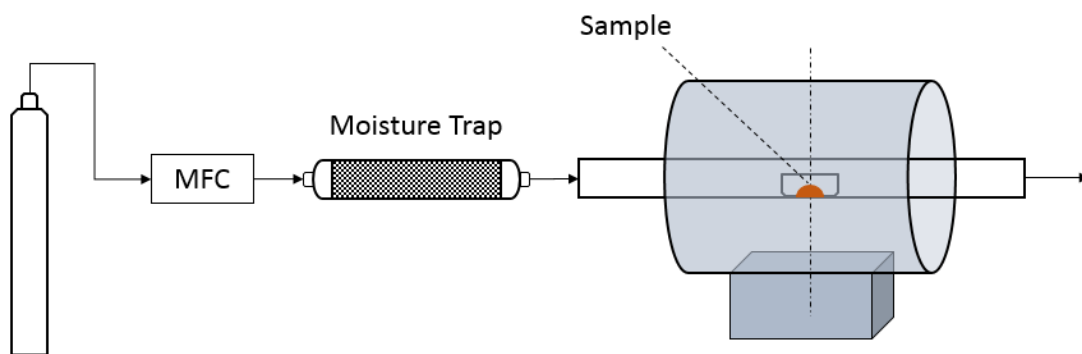
Figure 3- 19 Experimental setup for sample reduction.

As shown in the figure, samples were reduced in a control atmosphere furnace that consists of a tubular furnace and an alumina tube going through the furnace. Samples were placed in a small alumina boat and located at the centre of the furnace. The reducing gas was supplied from a cylinder (5% H$_2$/Ar, from BOC), and the flow rate (25 mL min^{-1}) was regulated by a mass flow controller (MFC). However, the gas from the cylinder could not be used directly for reduction, as the cylinder contained a small amount of moisture that could increase the oxygen partial pressure in the reducing gas.

Hence, a moisture trap was installed before the reduction furnace in order to remove the moisture from the gas. Prior to reduction, the system needed to be purged with the reducing gas (~250 mL min^{-1}) for 1 hour to remove the air from the system. Then the reducing gas was flowed at 25 mL min^{-1}, and the furnace could be set to the desired temperature for reduction (5 °C min^{-1} for heating and cooling).

3.4 Catalytic experimental setup

3.4.1 Experimental system

The catalysts in this study were designed for the application of automotive exhaust control, and CO oxidation was selected as the model reaction to evaluate the activity of these catalysts as mentioned before.

$$CO + \frac{1}{2}O_2 = CO_2$$
<div align="right">Equation 3-12</div>
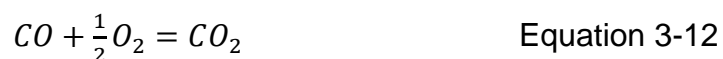
In this study, different catalyst systems were investigated and their thermal stability and activity were evaluated in catalytic experiments. All the samples were tested in CO oxidation conditions by using a setup as schematically described in Figure 3-20 (different reactors were used for powder and pellet samples, respectively).
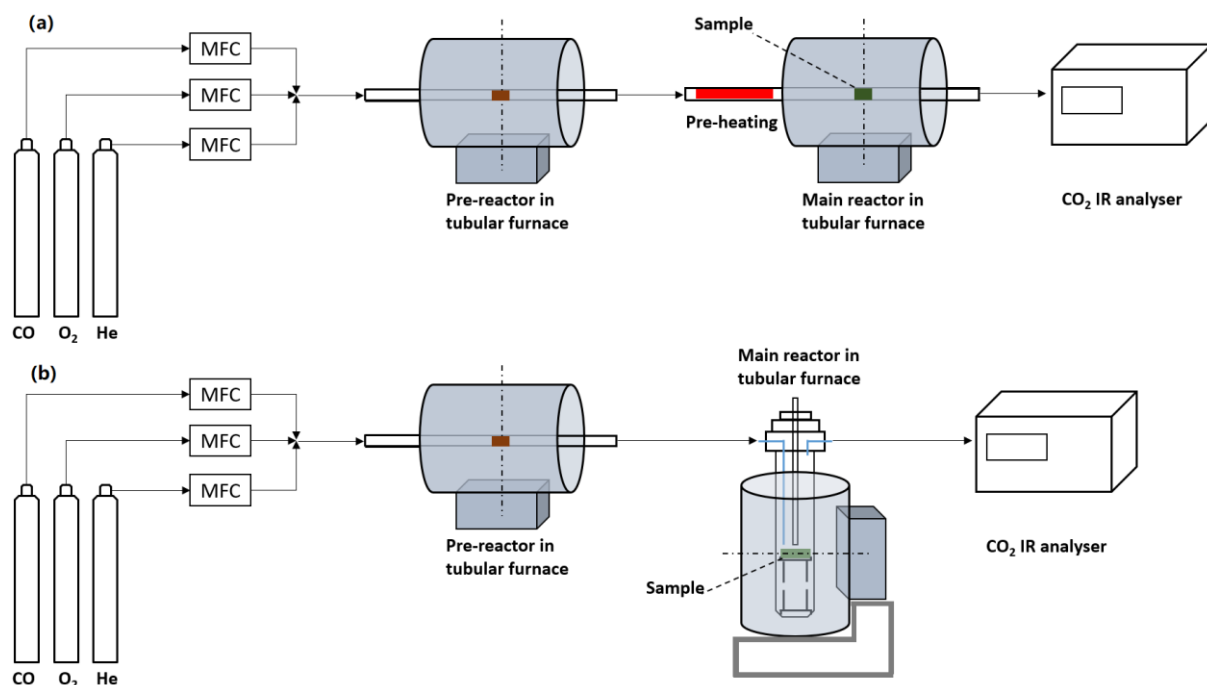
Figure 3- 20 Experimental setup for catalytic experiments with: (a) reactor for powder samples and (b) reactor for pellet samples.

Gases used in the catalytic experiments were supplied by cylinders as summarized in Table 3-1. The reaction mixtures were supplied from 20% CO/He, 20% O_2/He and the balance gas (helium) by varying their flow rates. Apart from these three gas cylinders, a 1% CO_2/He cylinder was also used to calibrate the gas analyser. The gas flow rate from each cylinder was regulated by a mass flow controller (MFC), depending on the desired composition of the reaction mixtures. The mixed reaction gases first entered a pre-reactor consisting of a quartz tube containing inert alumina inside, which was used to remove metal carbonyls (iron carbonyl for instance) that may exist in gas cylinders. Since metal carbonyls normally start decomposing at temperatures ranging from 35 to 80 °C [111], the pre-reactor was heated to 90 °C to remove the possible metal carbonyls. Then the mixed reaction gases were directed into the main reactor in which the samples were placed. Reaction took place in a conventional continuous flow reactor, and depending on the form of the samples, a horizontal or a vertical reactor was used for powder or pellet sample, respectively, which will be introduced in the following subchapter. Finally, the outlet gases from the main reactor were directed into an IR CO_2 analyser (Rosemount™ X-STREAM from Emerson), which could measure the concentration of CO_2 in the outlet gases with a minimum value of 1 ppm.

Table 3- 1 Summary of gas cylinders used for catalytic experiments.

Gas cylinders	Vendor	Usage
CO/He (20%)	BOC	To form reaction mixture
O_2/He (20%)	BOC	To form reaction mixture
He (99.996%)	BOC	To blend reaction mixture and for IR analyser calibration
CO_2/He (1%)	BOC	For IR analyser calibration

3.4.2 Experimental reactors

Two types of reactors were used for catalytic experiments. For powder samples, a horizontal fixed-packed bed reactor was used, which is schematically described in Figure 3-21 below. The powder reactor was a quartz tube with an inner diameter of 7 mm. The sample region of the quartz tube was held inside a tubular furnace, and the sample was placed at the centre of the furnace (8.0 cm away from each side of the furnace). The powder sample was closely packed between two pieces of quartz wool of equal amount (25 mg), so the powders did not move in the gas flow. Catalytic tests for powder samples were conducted normally by using a total gas flow rate (F_t) of 450

mL min^{-1}, however the flow rate might be changed according to the requirements for specific tests. The flow rate was checked both before and after each experiment at the outlet of the gas analyser by using a Varian digital flow meter (1000 series). The part of the quartz tube reactor prior to the furnace was wrapped with heating tapes and insulation, to provide pre-heating to the gases and ensure that the temperature of the gases could increase fast to reach the required reaction temperature around the sample region. The furnace used for the main reactor was a tubular furnace from Vecstar that was calibrated prior to the catalytic experiments by measuring the temperatures at different positions in the furnace, and the temperature distribution profile obtained is shown in Figure 3-22. If an isothermal zone in the furnace was defined as the region in which the temperature variation was less than 5 °C as compared with the temperature measured at the centre of the furnace, it can be found that the length of the isothermal zone was around 1 cm (0.5 cm to the centre of the furnace from both sides). It is important to control the reaction temperature accurately during the catalytic experiments to obtain the correct kinetic data. Therefore, the sample in every catalytic experiment was placed precisely at the centre of the furnace to ensure that the whole sample is in the isothermal zone. It is worth mentioning that a thermocouple (type K) was placed in proximity to the catalyst bed to measure the sample temperature during the reaction.
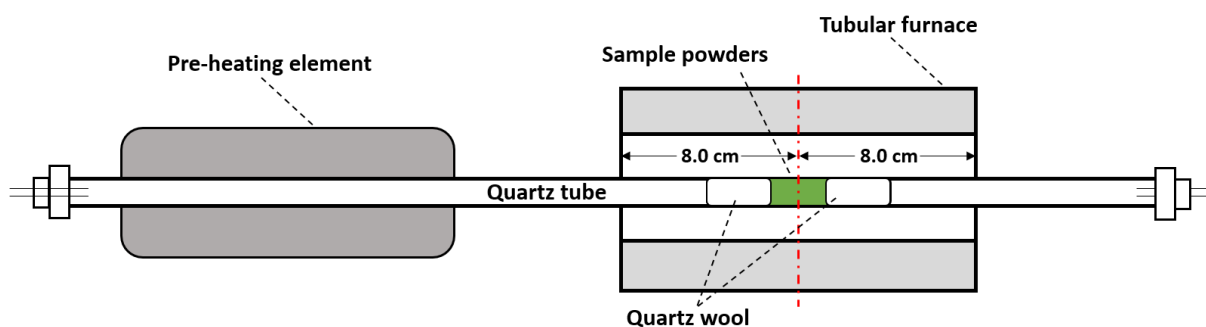
Figure 3- 21 Schematic drawing of the single chamber reactor for powder samples.
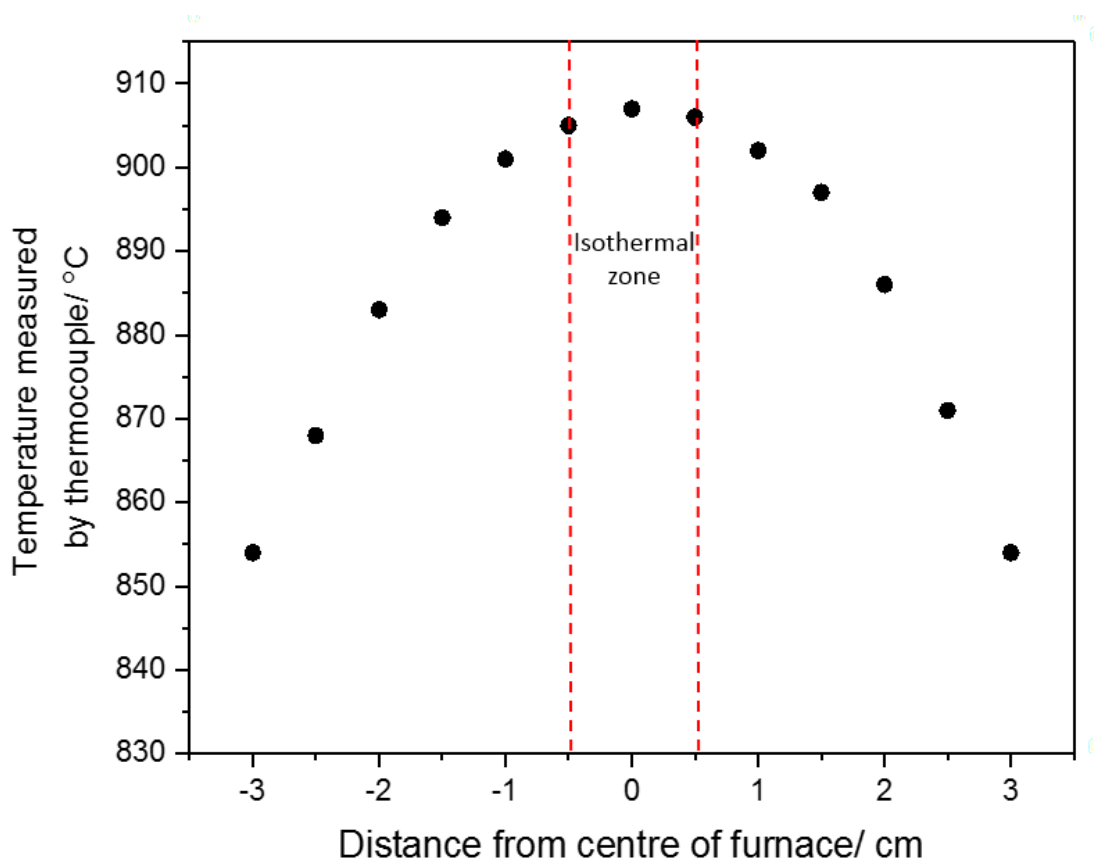
Figure 3- 22 Temperature distribution profile in the tubular furnace for main reactor, with isothermal zone labelled between two red dashed lines.

Pellet samples were tested in the other reactor that was designed in a vertical form, as schematically presented in Figure 3-23. The pellet reactor mainly consisted of a quartz tube reactor with one end closed, and Swagelok Ultra-Torr fittings to seal the reactor and avoid leaking from the air. The pellet sample was placed on a dedicated quartz holder in the reactor, and the height of the reactor was adjusted to ensure that the sample was located in the isothermal zone at the centre of the furnace. The inlet gas tube was inserted in proximity (5 mm above) to the surface of the sample to ensure the adequate contact between reaction gases and the sample surface. A thermocouple (type K), in a thin quartz tube with one end closed, was also placed close to the surface of the sample, which measured the sample temperature during experiments. Total gas flow rate used for the pellet sample tests was 150 mL min^{-1}. The total flow rate was checked before and after the catalytic experiments at the outlet of the gas analyser by using the digital flow meter.
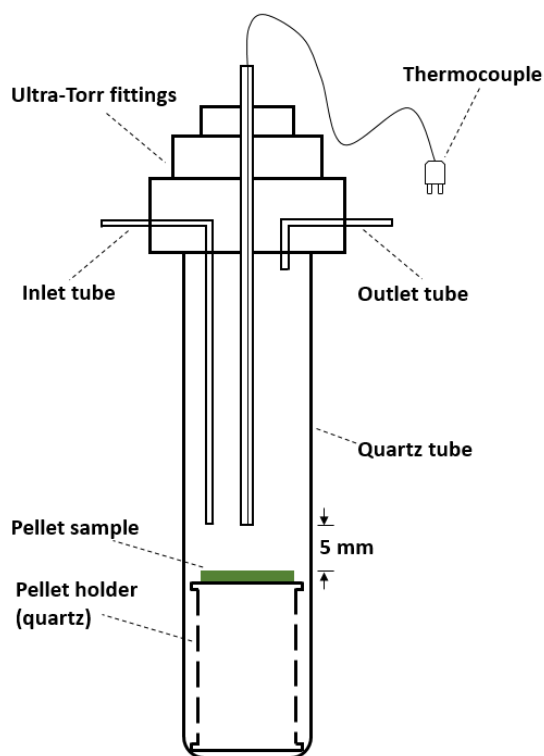
Figure 3- 23 Schematic drawing of the single chamber reactor for pellet samples.

3.4.3 Gas analyser (Infrared measurement)

The concentration of CO_2 in the gases in the outlet of the reactor was measured by using an infrared CO_2 analyser (IR analyser, Rosemount™ X-STREAM from Emerson) which could measure the minimum detectable CO_2 mole fraction of 1 ppm. The working principle of an IR analyser is based on the adsorption of IR radiation by the sample gas. Different gases have their own distinguishing spectrum for IR adsorption, hence the wavelength of the IR adsorption can be used to characterize the gas component and the intensity of adsorption can be used to determine the concentration [112]. IR analyser utilizes an analysis cell with two separated sides. One side of the analysis cell is flowed with the gas to be measured (sample side), and the other side is filled with either inert gas such as N_2 or reference gases (reference side), as shown in Figure 3-24(a). IR light would irradiate both sides of the analysis cell alternately with the same intensity. Then the light leaving the analysis cell passes a filter cell and reaches an opto-pneumatic detector that is shown in Figure 3-24(b). The detector consists of an adsorption chamber, a compensation chamber, and a flow channel connecting these two chambers in which a micro flow detector is installed. The gas to be measured is filled in the detector chambers, so it is only sensitive to the characteristic wavelength

band of this specific gas. The IR transparent CaF_2 window is used to seal the adsorption chamber. When the IR radiation from the reference side reaches the detector, gas in the adsorption chamber will adsorb the radiation of the characteristic wavelength and be heated, hence the gas will expend and flow towards the compensation chamber, which produces a voltage signal by the micro flow detector. However, the radiation of the characteristic wavelength would lose some intensity when passing through the sample side. Hence, when it reaches the detector, temperature of the gas in the adsorption chamber decreases and the gas flows back from the compensation chamber, which produces a reverse voltage signal. Therefore, alternating voltage signals can be produced, and the intensity change of the signals is proportional to the concentration of the sample gas [112]. In this way, the concentration of a certain gas can be measured.
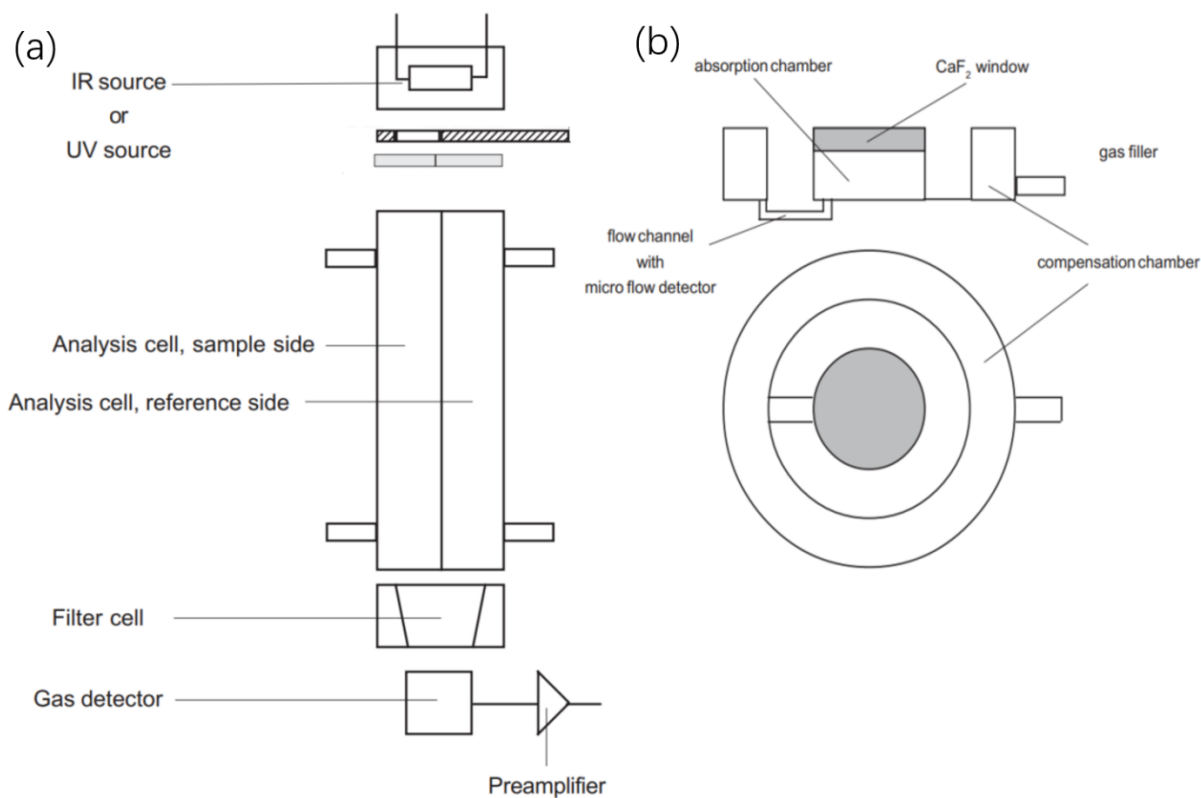
Figure 3- 24 (a) Configuration of IR analyser. (b) Opto-pneumatic detector design principle. [112]

3.4.4 Conditions of catalytic experiments

The activities of the catalysts in this study were mainly tested in the model reaction of CO oxidation as a function of temperature (referred to as light-off experiment henceforth). During the catalytic tests, the reaction temperature was increased

stepwise from the room temperature to a desired temperature depending on samples, and at each temperature, enough time was given for the reaction rate to stabilize (i.e. changes of CO_2 concentration in the product are less than $\pm 5\%$ within 60 min). Hence the stable reaction rate in term of CO_2 production (r_{CO_2}) as well as the conversion of CO (X_{CO}) can be calculated as:

$$r_{CO_2}(mol\ s^{-1}) = \ y_{CO_2} F_t \ \times \ 10^{-6} \qquad\qquad \text{Equation 3-13}$$

$$X_{CO} = \ \frac{y_{CO_2}}{y_{CO,inlet}} \times 100\% \qquad\qquad \text{Equation 3-14}$$

where y_{CO_2} is the CO_2 concentration (in ppm) in the product measured by the IR analyser, F_t is the gas total flow rate (in mol s^{-1}), and $y_{CO,inlet}$ is the CO concentration (in ppm) in the inlet of reaction mixture. Prior to experiments, the system would be flown with reaction mixture without being heated, in order to detect the CO_2 level in the inlet hence to be subtracted from the measurements in experiments. The calculations shown above are only accurate by using the data from differential conditions (low CO conversion, i.e. <20%) as the conditions (such as temperature and pressure) under which the data are measured are known, while the data from the integral conditions (high CO conversion) should not be over-interpreted. The CO_2 production rate can be further normalised on different bases such as the weight of catalyst, the amount of active metals and the metal coverage (surface area of metal per surface area of support, μm^2 μm^{-2}).

Table 3-2 below shows the gas compositions of the automotive exhaust used in literature. Compositions of the automotive exhaust vary with the ratio of air and fuel, and normally the conditions of the exhaust are slightly oxidising or stoichiometric. In this study, different catalyst systems were investigated, and depending on the nature of these catalyst systems, different compositions of the reaction mixture were selected for the catalytic experiments.

Table 3- 2 Gas compositions of automotive engine exhausts reported in literature.

Components	Concentrations
Hydrocarbons*	350 ppm [113], 1000-5000 ppm [114], 0.062/0.052/0.040%** [115], 0.1067% [116], 900 ppm [117]
NO_X	900 ppm [113], 100-1000 ppm [114], 0.099/0.10/0.10%** [115], 0.1% [116], 900 ppm [117]
CO	0.5% [113], 0.05-0.5% [114], 1.3/0.6/0.28%** [115], 0.7% [116], 1.60/0.40%*** [117]
H_2	0.17% [113]
CO_2	10% [113, 115-117]
O_2	0.5% [113], 0.5-5% [114], 0.28/0.58/1.1%** [115], 0.78% [116], 0.465/1.26%*** [117]
H_2O	10% [113, 115-117]

* only C3 is considered.

** under air/fuel ratio of 14.1, 14.6 and 15.1, respectively.

*** with air/fuel ratio changing between 14.13 and 15.17.

In the study of spatially controlled metal nanoparticle pairs (Chapter 5), metal nanoparticles were dispersed on silicon wafer substrate and experiments were conducted to evaluate their thermal stability. Hence, the experiments were carried out in the pellet reactor as introduced before, and stoichiometric CO oxidation conditions were selected where the partial pressures of CO (P_{CO}) and O_2 (P_{O_2}) were 1.0 kPa and 0.5 kPa, respectively, and F_t=150 mL min^{-1} (1 x 10^{-4} mol s^{-1})).

For the sample of metal nanoparticles stabilized by porous organic cages (Chapter 6), different experimental conditions were used. The sample was in the powder form, so the experiments were carried out in the powder reactor as introduced before. Because it is a relatively new catalyst system which has not been studied much before, stoichiometric CO oxidation conditions (P_{CO}=1.0 kPa, P_{O_2}=0.5 kPa and F_t=450 mL min^{-1} (3 x 10^{-4} mol s^{-1})) were selected first, which could provide a preliminary activity for the sample without concerning the effects of CO and O_2 ratio. However, the activity of the sample obtained under stoichiometric conditions was not good, hence the effect of O_2 partial pressure was investigated in order to make the sample present its best activity. This was conducted via the "O_2 kinetics" experiments where CO partial pressure was kept constant (P_{CO}=1.0 kPa) while O_2 partial pressure P_{O_2} was increased stepwise from 0.5 to 7.5 kPa. Based on the results from O_2 kinetics experiments, the new oxidising

reaction conditions (P_{CO}=3.0 kPa, P_{O_2}=15.0 kPa and F_t=60 mL min^{-1} (4.5 x 10^{-5} mol s^{-1})) were employed to test the activity of the sample, which also allowed for the comparison with other samples that were tested under similar conditions in literature.

For the exsolved catalysts from perovskites (Chapter 7) and the conventional alumina supported catalysts, they have been studied a lot previously in literature. Hence, the slightly oxidising CO oxidation conditions (P_{CO}=0.6 kPa, P_{O_2}=1.0 kPa and F_t=450 mL min^{-1} (3 x 10^{-4} mol s^{-1})) were selected for these samples to mimic the real working conditions for the catalysts which are used for automotive exhaust control. These samples were all in the powder form, so the experiments were carried out in the powder reactor as introduced before.

It is worth mentioning that for the determination of kinetic parameters, only the data measured under "gradientless" conditions where the reactor was operated under differential conversion (low CO conversion, i.e. <20%) should be used. Otherwise, the reactor would be considered to operate under integral conditions at high conversions, where the conditions such as temperature and pressure would vary across the reactor. Hence, the rates measured under such conditions are averaged values, and analysis based on these values would be unreliable.

Chapter 4: State-of-the-art noble metal catalysts in CO oxidation

In this chapter, the application of noble metals of Pt, Pd and Rh as three-way catalysts for automotive exhaust control is introduced first. CO oxidation is one of the most important reactions in automotive exhaust control and it is also the most extensively studied reaction in heterogeneous catalysis, hence it was chosen as the model reaction to evaluate the catalysts in this study. Previous study of CO oxidation on noble metal catalysts in literature is summarized, and the most commonly used noble metal catalysts (Pt, Pd and Rh on alumina) were tested to understand their catalytic behaviors in CO oxidation as well as their differences, which could provide some guidance for this study in the following chapters.

4.1 Introduction to noble metal catalysts

4.1.1 Origin of activity for noble metal catalysts

Noble metals especially Pt, Pd and Rh are widely used in state-of-the-art catalysts in oxidations, hydrogenations, dehydrogenations, catalytic reforming, environmental catalysis, and so on [4, 118]. The origin of their catalytic activity for a wide range of reactions could be attributed to the appropriate adsorption/desorption properties of different reactant/product molecules on the surface of these metals [119, 120]. In most heterogeneous catalytic processes, reaction steps include adsorption of reactants on the catalyst surface, surface reaction between the adsorbed reactants, and desorption of the products, giving the vacant sites back to reactants. Therefore, the adsorption/desorption of reactants and products is a very important property for a catalyst. If the adsorption strength of either reactant or product on catalyst surface is too strong, the adsorption equilibria will be partial to the adsorbed state, which will lead to a slow reaction rate. Conversely, if the adsorption strength of reactant is too weak, there will be insufficient reactant molecules adsorbed on the active sites and the reaction rate will be slow as well. Hence, the relative adsorption strength of both reactant and product molecules on a metal surface is critical to determine the catalytic activity of this metal, and a high activity is normally achieved only if the metal surface provides intermediate adsorption strength for reactants but lower adsorption strength for products [120, 121]. Noble metals adsorb many reactant molecules of interest with moderate strengths, which makes them favourable candidates for a variety of catalytic processes as compared to other metals which are cheaper and more abundant in reserve [120].

Therefore, the unique catalytic property of noble metals makes them nearly irreplaceable in many important applications. For example, automotive exhaust control is the most important catalytic application of noble metals and a lot of efforts have been made to replace them with base metals [9-12], but this replacement without compromising activity is still challenging. Automotive exhaust control by using noble metals is also chosen as a topic of this study, and it will be introduced below.

4.1.2 Application of noble metals in three-way catalysts

The past few decades have witnessed the explosive growth of the number of vehicles on the road, and the majority of these vehicles still rely on traditional internal combustion engines rather than electric power motors. According to the forecast from

the International Energy Agency (IEA), the number of total vehicles around the world will increase from 1.1 billion in 2015 to 2 billion between 2035 and 2040, while only 220 million of them will be electric cars [122]. The fuels used for internal combustion engines come from crude oil (hydrocarbons). If the hydrocarbons are completely combusted, only H_2O and CO_2 will be generated, but in reality, the combustion of fuels is always incomplete in engines and also the temperature in engines can be very high (up to 1100°C), which gives rise to the formation of many harmful substances in the exhausting gases from the engine [123]. People started to be aware of the impact of automotive emission long time ago but the situation is becoming worse with the rapid growth of car ownership, hence a series of regulations have been announced by governments over the years to set the threshold limits on different pollutants in the automotive exhausts. The first official regulation for automotive emission was put forward in 1970 when the Clean Air Act was agreed in the U.S. Congress [124], and today all regions have their own regulations. For instance, the European emission standards have come to the 6th edition (Euro 6) in 2015 (shown in Table 4-1), and it has become much more stringent than the older editions. Therefore, automakers must develop their technologies for emission abatement to fulfill the requirements of new emission standards.

Table 4- 1 Emission standards (g/km) of different pollutants for passenger cars regulated by Euro 6. [125]

	Petrol engine	Diesel engine
CO	1.0	0.50
HCs	0.10	-
NO_x	0.06	0.08
HCs + NO_x	-	0.17
Particulate matters	0.005	0.005

The composition of the exhaust gases varies a lot with the type of engines, and the common exhaust compositions from typical petrol engines and diesel engines can be found in Table 4-2. For a typical petrol engine, the major harmful substances in the exhausts are unburned hydrocarbons (HCs), CO (from incomplete combustion of HCs) and NO_x (NO and NO_2, from high-temperature reaction between N_2 and O_2), together with some small amount of SO_x. If the exhaust gases from engines do not go through any purification before emitting, the amount of the harmful substances entering the atmosphere will be far higher than the threshold limits regulated by standards like the one listed in Table 4-1, which will pose highly negative impacts on our environment.

Table 4- 2 Compositions and conditions of exhausts from typical petrol and diesel engines, respectively. [126]

Exhaust substances and conditions	Four-stroke spark ignited-engine (Petrol)	Diesel engine
CO	0.1-6%	300-1200 ppm
HCs (ppm C)	500-5000	50-330
NO_x (ppm)	100-4000	350-1000
O_2 (%)	0.2-2	10-15
H_2O (%)	10-12	1.4-7
CO_2 (%)	10-13.5	7
SO_x (ppm)	15-60	10-100
PM (mg m^{-3})	-	65
Temperatures (°C)	1100	650
Gas hourly space velocity (h^{-1})	30,000-100,000	
A/F	~14.7	~26

In order to eliminate the environmental impacts of the automotive exhausts, catalytic converters are used to simultaneously transform the major pollutants to less harmful substances through either oxidation or reduction reactions depending on the nature of the pollutants. Therefore, a range of reactions can occur in the catalytic converter and the main reactions are shown in Table 4-3, although there can be many other undesirable reactions.

Table 4- 3 Major reactions taking place in the catalytic converter to transform the harmful substances in automotive exhausts. [123, 126, 127]

Oxidations	$CO + 1/2\ O_2 \rightarrow CO_2$
	$C_xH_y + (x + y/4)\ O_2 \rightarrow x\ CO_2 + y/2\ H_2O$
Reductions/three-way	$CO + NO \rightarrow 1/2\ N_2 + CO_2$
	$2(x + y/4)\ NO + C_xH_y \rightarrow (x + y/4)\ N_2 + y/2\ H_2O + x\ CO_2$
	$NO + H_2 \rightarrow H_2O + 1/2\ N_2$
WGS	$CO + H_2O \rightarrow CO_2 + H_2$
Steam reforming	$C_xH_y + 2x\ H_2O \rightarrow x\ CO_2 + (2x + y/2)\ H_2$

In the first generation of catalytic converters, only the two oxidation reactions listed in Table 4-3 were promoted by the automotive catalysts because there was much catalytic knowledge towards the oxidation reactions at that time, and hence these catalysts are referred to as "two-way" catalysts [128]. Nevertheless, the two-way catalysts could only transform CO and HCs, but the stricter regulations required the removal of NO_x as well. This led to the new generation of automotive catalysts, which can simultaneously transform CO and HCs via oxidation reactions and NO_x via reduction reactions, hence the new generation catalysts are termed as "three-way" catalysts (TWCs). The performance of TWCs highly depends on the operating conditions of engines, especially the air-to-fuel ratio (A/F), because of the corresponding variation of the exhaust compositions as summarized in Figure 4-1. The stoichiometric condition means that the amount of O_2 in air that enters the engine is just enough to react with all the fuels, where the A/F value is ~14.6 (wt/wt) for petrol. It is obvious that the oxidations of CO and HCs are favoured under lean burn conditions (excess air, A/F>14.6), while the reduction of NO_x is favoured under rich conditions (excess fuel, A/F<14.6). Only near the stoichiometric conditions, the ratio between reducing and oxidizing agents present in the exhausts is appropriate for TWCs to transform CO, HCs and NO_x to less harmful substances simultaneously and efficiently (as shown in Figure 4-2) [126]. Therefore, TWCs are only applied for those engines that are operated under stoichiometric conditions, and it is important to maintain the stoichiometric A/F ratio during the operation.
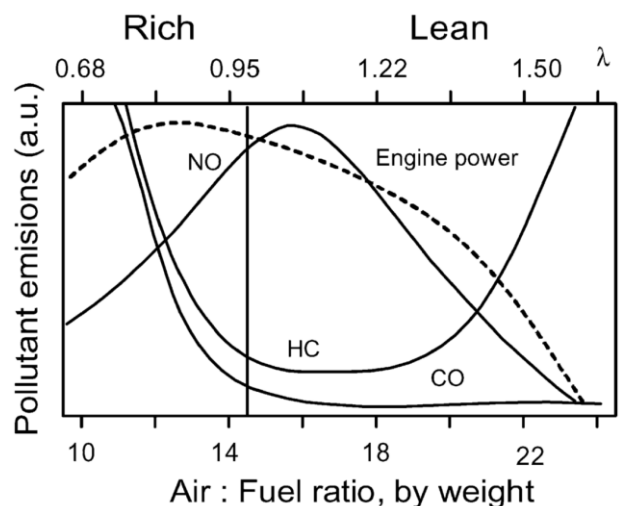
Figure 4- 1 Compositions of engine emissions vary with A/F ratio (wt/wt). λ is the air/fuel equivalence ratio which shows the ratio of the actual A/F to the stoichiometric A/F value. [126]
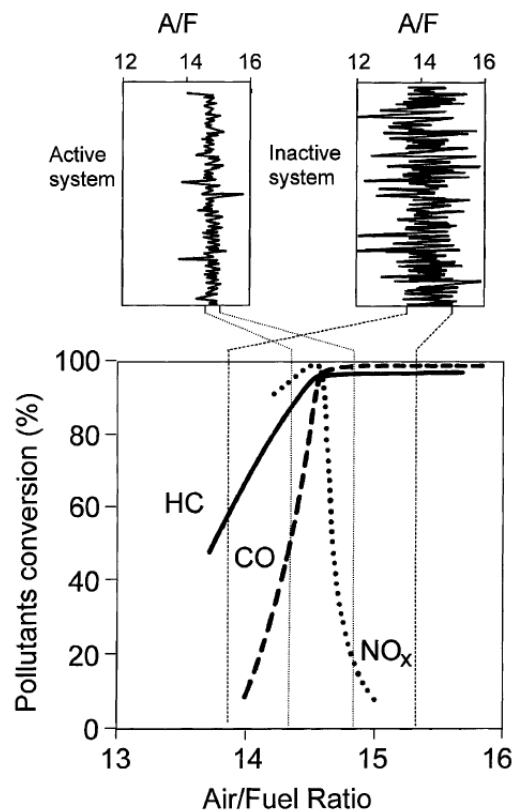
Figure 4- 2 Conversion of pollutants catalysed by TWCs at different A/F ratio. [126]

The structure of a common three-way catalytic converter can be found in Figure 4-3. In general, the converter is a stainless steel container in which a ceramic honeycomb monolith is mounted. An oxygen sensor is also installed near the inlet of the catalytic converter and it gives feedback to the injection control loop of the engine to maintain the A/F ratio within the narrow operating window around 14.6, which allows for the optimum operation of TWCs as mentioned above. A washcoat containing active catalysts is supported on the monolith. The active catalysts comprise of noble metals (Pt, Pd, and Rh) supported on high surface area alumina. In addition, some mixed oxides of CeO_2 and ZrO_2 are added in the washcoat to improve the oxygen storage, and BaO and/or La_2O_3 are also included to stabilize the structure and avoid degradation which leads to the loss of surface area of the alumina support against the varying temperatures during operation [126].

The noble metals Pt, Pd and Rh have been used in TWCs since 1974 [129, 130], and it is clear that they play the most critical role among all the components in TWCs to determine the performance for the abatements of CO, HCs and NO_x. Rh is included in TWCs mainly to promote the reduction of NO_x [126, 129, 131], as Rh was found to be active for NO_x dissociation [132, 133]. On the other hand, Pt and Pd are used to

promote the oxidation reactions of CO and HCs, although Rh has high catalytic activity for oxidation reactions as well [126]. Different combinations of these three metals have been used in TWCs over the years, and nowadays the most common combination is Pd/Rh, mainly due to the lower price of Pd as compared to Pt in recent years [129]. However, this combination will keep changing in the future. Normally there is only a small fraction (0.1-0.15%) of noble metals in the TWC, and the common Pd/Rh or Pt/Rh ratio is ~5 [134].
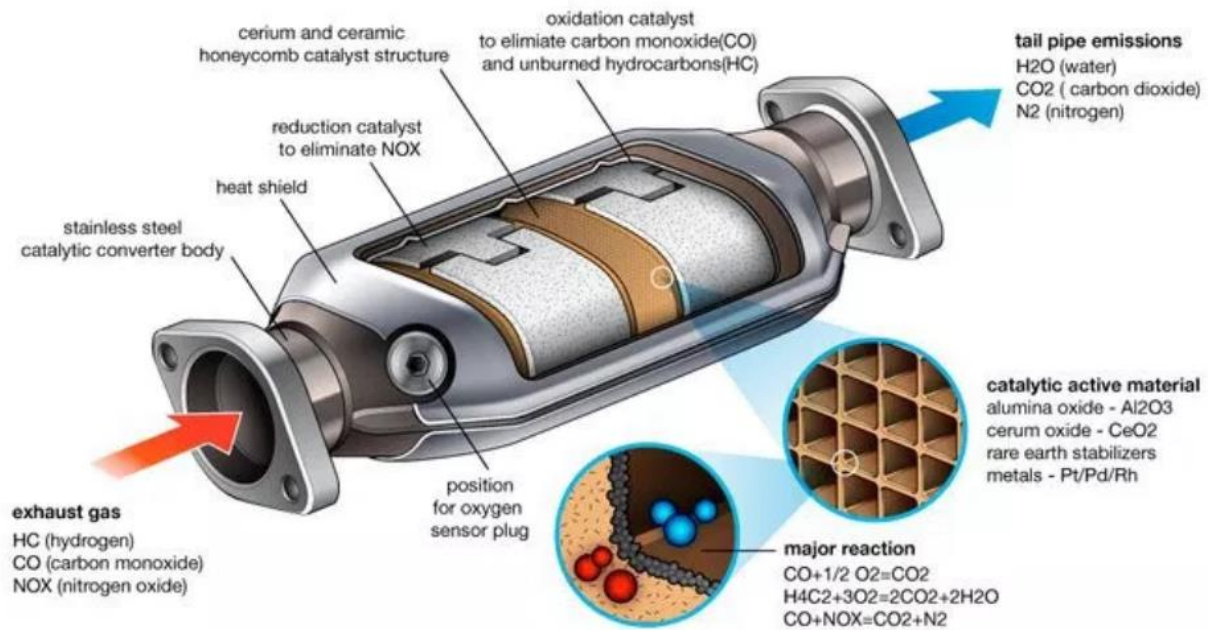
Figure 4- 3 Typical design of a three-way catalytic converter for petrol engines. [135]

However, the deactivation of TWCs during the vehicle operation can happen mainly via the thermal and chemical mechanisms. Firstly, the sintering of noble metal particles, resulting in the loss of active sites, is the main pathway for deactivation of TWCs, as the temperature of a stoichiometric petrol engine can reach ~1100 °C [126]. Secondly, TWCs can also be chemically poisoned by some substances such as phosphates [136], sulphur compounds [137, 138] and some other elements like zinc [139]. Moreover, the sintering of Al_2O_3 support and oxygen storage promoter CeO_2-ZrO_2 can also contribute to the deactivation of TWCs [126]. Once a TWC is deactivated, the regenerating work can be very challenging, and the best method to extend the service life of the TWC is preventing the deactivation by improving the thermal stability and the poisoning resistance for the catalysts. What is more, in consideration of the high price and the limited reserve of these noble metals, more efficient use of these metals is extremely desirable.

4.1.3 CO oxidation over noble metals

The oxidation of CO is one of the principal reactions taking place in the three-way catalytic converter, and it is one of the most investigated reactions for heterogeneous catalysis over the years. CO oxidation is always used as a model reaction for the test of catalysts because of its simplicity, which makes the measurement and interpretation of kinetic results relatively straightforward [140]. Therefore, CO oxidation was also selected as the model reaction here to evaluate the performance of the catalysts involved in this study as mentioned before.

CO oxidation taking place over transition metal catalysts has been widely studied and researchers tried to explain this catalytic process by several different reaction mechanisms. The two main kinetic mechanisms for CO oxidation reaction proposed earlier are called Langmuir-Hinshelwood (L-H) mechanism and Eley-Rideal (E-R) mechanism, respectively (Table 4-4) [141-144].

Table 4- 4 Elementary steps of catalytic CO oxidation reaction, according to Langmuir-Hinshelwood and Eley-Rideal mechanisms, respectively.

	Langmuir-Hinshelwood	Eley-Rideal
Adsorption	$CO_{gas} \rightarrow CO_{ads}$	$O_{2\,gas} \rightarrow 2\,O_{ads}$
	$O_{2\,gas} \rightarrow 2\,O_{ads}$	
Reaction	$CO_{ads} + O_{ads} \rightarrow CO_{2\,ads}$	$CO_{gas} + O_{ads} \rightarrow CO_{2\,gas}$
Desorption	$CO_{2\,ads} \rightarrow CO_{2\,gas}$	

According to the L-H mechanism (as shown in Figure 4-4(a)), CO and O_2 molecules in the gas phase are firstly absorbed onto the surface of active metals, and dissociation of O_2 also takes place on the metal surface. Then the surface reaction between the chemisorbed CO molecules and oxygen atoms happens, which gives rise to the CO_2 as the product, and finally the produced CO_2 molecules desorb from the metal surface and enter the gas phase.

On the other hand, the E-R mechanism (as shown in Figure 4-4(b)) suggests that the reaction does not happen between the two chemisorbed surface species. Instead, the CO molecules in the gas phase directly strike the dissociatively adsorbed oxygen atoms, and the collisions have chances to generate CO_2, which escapes directly from the metal surface into the gas phase.
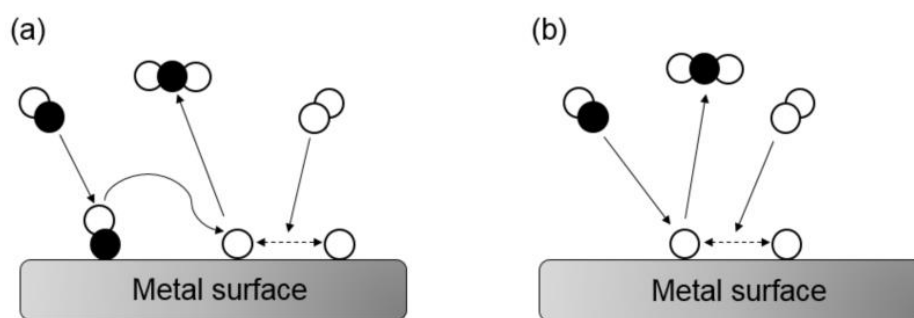
Figure 4- 4 Schematic demonstration of elementary steps of CO oxidation on metal surface, according to (a) the Langmuir-Hinshelwood and (b) the Eley-Rideal mechanisms, respectively. The white balls and black balls represent oxygen atoms and carbon atoms, respectively.

Furthermore, there are also some other reaction mechanisms trying to explain the CO oxidation reaction. For instance, Mars van Krevelen (MvK) mechanism (as shown in Figure 4-5) was initially proposed to explain the CO oxidation over reducible metal oxides [145, 146], but recently some researchers claimed that the MvK mechanism also applies for metallic surfaces such as Pt and Pd. They observed that the metal catalyst can switch between the metallic and oxide states [147, 148]. Basically, the MvK mechanism emphasizes the participation of the catalyst as an intermediate in the reaction, in which the metal catalyst is firstly oxidized under O_2-rich conditions and the oxygen from the metal oxides can react directly with the chemisorbed CO molecules to generate CO_2 which then desorbs. The oxygen vacancies left on the catalyst surface will absorb oxygen from the gas phase hence being refilled.
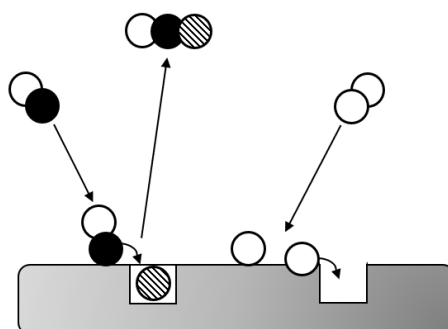
Figure 4- 5 Schematic demonstration of elementary steps of CO oxidation according to the Mars van Krevelen mechanism. The white balls, black balls and textured ball represent oxygen atoms from gas phase, carbon atoms and the oxygen atom from metal oxides, respectively.

Although there is some debate on the mechanisms of CO oxidation reaction, it is widely accepted by most of researchers that the CO oxidation on noble metal catalysts follows the L-H mechanism [149-156]. Goodman et al. have published a series of articles that

adequately showed that the CO oxidation kinetics over Pt, Pd and Rh in a wide range of pressures follows the L-H mechanism [149, 157, 158]. According to the L-H mechanism, CO and O_2 need to competitively adsorb on the metal surface, and the reaction only takes place between the chemisorbed CO and oxygen, therefore the adsorption/desorption behavior of CO and O_2 on the metal surface will become a key factor to determine the reaction rate. In fact, it is well known that CO can exhibit inhibiting effect on the CO oxidation reaction at low temperatures by predominantly adsorbing on noble metal surface, whereas the active surface for CO oxidation was proved to be the one with less CO occupied but more O_2 adsorbed. This was clearly shown by the works from Goodman et al. in which they found that the increase of the reaction probability corresponded well with the decrease of CO coverage on metal surface by using the polarization modulation infrared reflection absorption spectroscopy (PM-IRAS), as shown in Figure 4-6 [149].
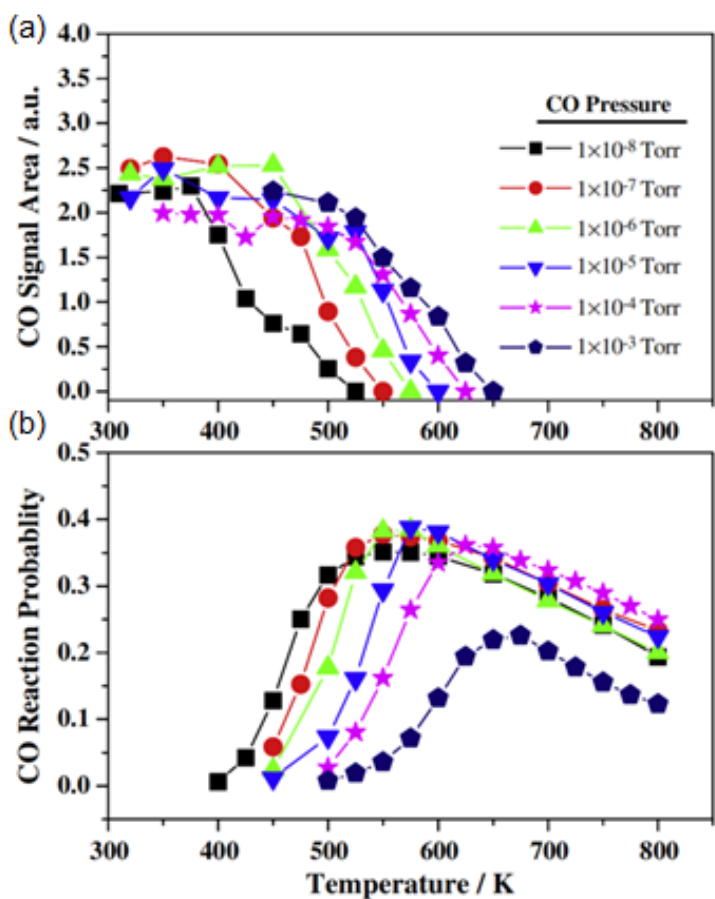
Figure 4- 6 (a) CO PM-IRAS signal area and (b) the corresponding reaction probability over Pd(100) at different temperatures, indicating CO oxidation reaction rate increases when CO coverage decreases. [149]

Three different kinetic regimes for CO oxidation on the surface of Pt, Pd and Rh can be summarized as a function of temperature [149, 150], which is illustrated in Figure 4-7. The first regime is CO-inhibited regime at low temperatures, and the reaction activation energy obtained in this regime is ~110 kJ mol^{-1} that is similar as the corresponding desorption energy of CO. The adsorption and dissociation of O$_2$ are inhibited in this kinetic regime and the reaction rate is limited by the desorption of CO. As the temperature increases, the second kinetic regime begins. This is a transient regime where the reaction rate would increase rapidly (known as light-off), as predominantly CO chemisorbed surface changes to the oxygen chemisorbed surface which is highly active. Finally, the reaction rate becomes invariant with the temperature as the reactants at the metal surface can be readily consumed and the mass transfer becomes the limiting factor for the reaction in the third kinetic regime. However, under some oxidizing conditions, the reactivity decrease might happen at high temperatures [149, 157, 159], probably due to the metal oxidation or O$_2$ inhibition in the third regime. Moreover, the transition of the inactive surface (CO-dominant) to the highly active surface (oxygen-dominant) is dependent on the relative adsorption energies of CO and O$_2$. The CO adsorption energies on Rh, Pd and Pt surfaces are similar, which are 130, 142 and 138 kJ mol^{-1}, respectively [160, 161]. However, the O$_2$ dissociative adsorption energies vary for these metals that 234, 230 and 188 kJ mol^{-1} were reported for Rh [162], Pd [163] and Pt [164], respectively. Therefore, it is easiest to form the active surface on Rh, followed by Pd and Pt. This manifests in some aspects that, for instance, at a given temperature, the activation of catalyst can be motivated by increasing O$_2$/CO ratio to a critical value, and the critical O$_2$/CO ratio needed for these three metals ranks in the order: Rh < Pd < Pt [150, 165].
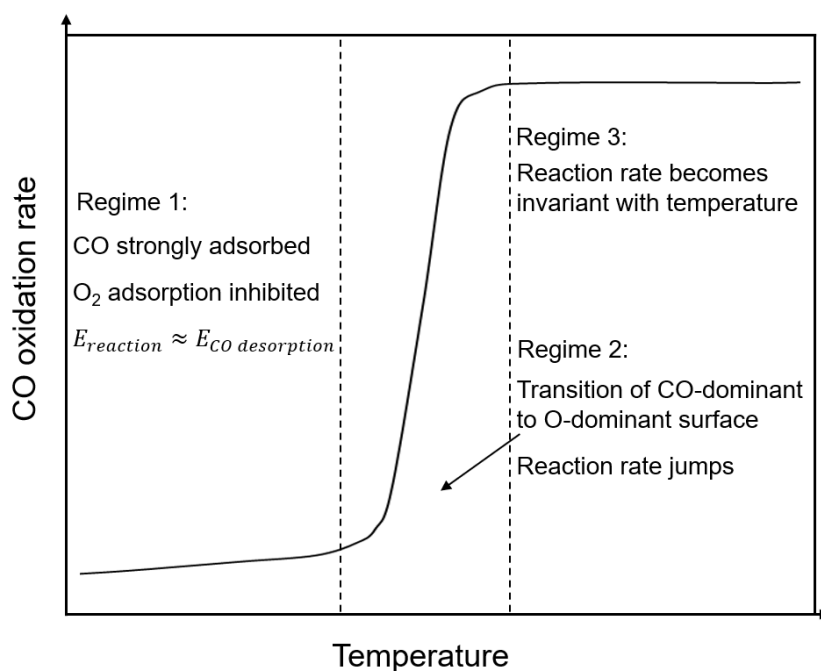
Figure 4- 7 Schematic demonstration of three kinetic regimes of CO oxidation reaction on noble metal catalysts, with some brief description of the features in each regime.

As aforementioned, the state-of-the-art TWCs use different combinations of Pt, Pd and Rh as the active metals and they play different roles in the pollutant abatement. The catalysts in this study are designed for the application of automotive exhaust control and CO oxidation is used as the model reaction. Therefore, before starting to design catalysts, the commercially available catalysts of these three metals were tested first in CO oxidation, in order to get an insight into catalytic behaviors of these three metals and also their differences. The results of these experiments were expected to provide guidance for the catalyst design in the later studies.

4.2 Investigation of catalytic behavior of noble metals in CO oxidation

4.2.1 Activity of individual noble metals (Pt, Pd and Rh)

As mentioned before, the major active components in state-of-the-art TWCs consist of Pt, Pd and Rh dispersed on Al_2O_3 support. In order to investigate the catalytic behaviors of these noble metal catalysts, the commercially available catalysts (Pt/Al_2O_3, Pd/Al_2O_3 and Rh/Al_2O_3, all from Alfa Aesar) were tested in CO oxidation. These commercial catalysts are similar as those that are used in the conventional TWCs. They have the same nominal amount (1 wt%) of respective noble metals, which allowed for the comparison of the activities for these three metals. TEM images of the

commercial catalysts are shown in Figure 4-8, and the particle sizes of Pt, Pd and Rh were estimated to be ~1.9±0.2, ~2.5±0.3 and ~1.8±0.2 nm, respectively.
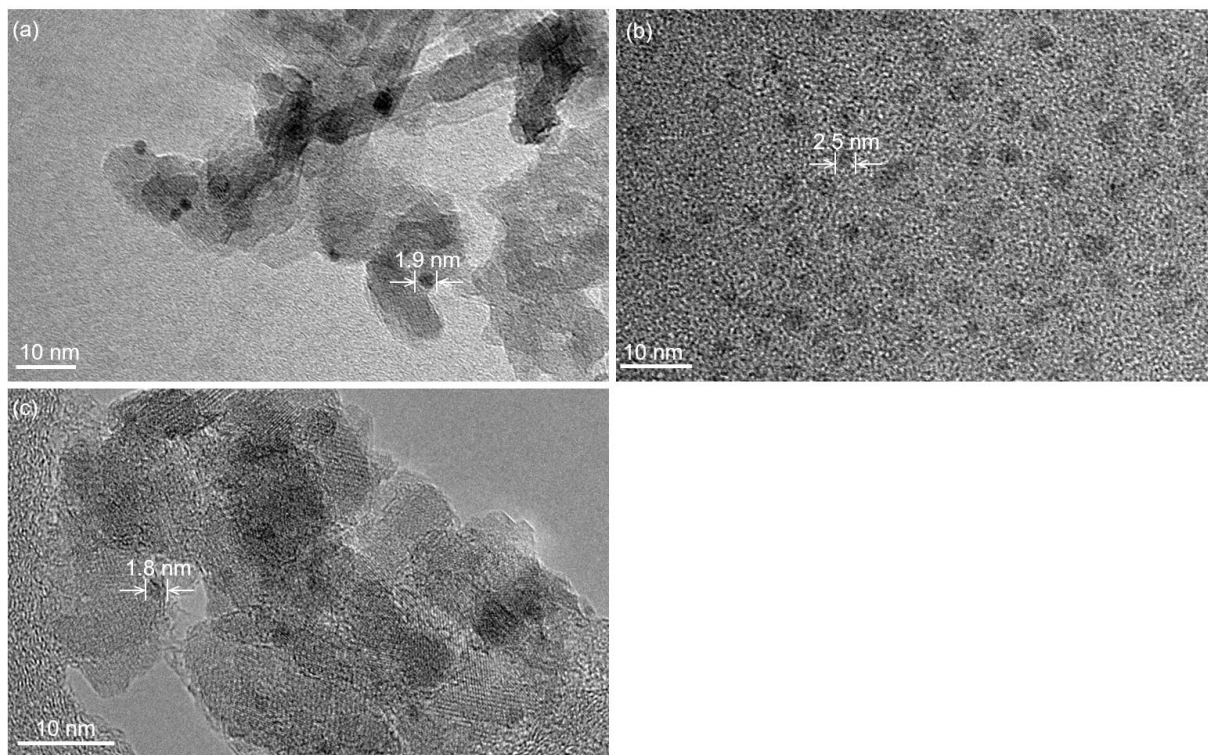
Figure 4- 8 TEM images of commercial catalysts of (a) 1 wt% Pt/Al_2O_3, (b) 1 wt% Pd/Al_2O_3 and (c) 1 wt% Rh/Al_2O_3.

The assumption was made that there is no synergistic effect among these three metals when they are employed together in TWCs, therefore the activity obtained for the individual metals can be treated as the same activity as they exhibit in real TWCs. The light-off experiments (Figure 4-9(a)) of these commercial noble metal catalysts (10 mg) were conducted in CO oxidation under slightly oxidizing conditions (P_{CO}=0.6 kPa, P_{O_2}=1.0 kPa and F_t=450 mL min^{-1}) to mimic the real working conditions of TWCs as introduced in Chapter 3. Figure 4-9(a) shows that the catalytic behavior of these catalysts was similar and it was also consistent with the characteristic behavior of noble metal catalysts where three kinetic regimes can be observed as introduced in Figure 4-7. Their activities can be compared based on the temperatures at which they achieve 5% and 50% CO conversion (referred to as T_5 and T_{50}, respectively). Taking Pt/Al_2O_3 as an example, its activity for CO oxidation increased slowly in the first kinetic regime with T_5 of ~225 °C, as the metal surface was predominately occupied and inhibited by CO. As the temperature increased, the second kinetic regime started where the reaction rate increased suddenly, with the value of T_{50} to be around 240 °C. The

sudden activity increase is likely to be ascribed to the rapid decrease of CO bound to the metal surface due to the faster CO desorption and the formation of the oxygen-dominant surface that is much more active as compared with the CO-dominant surface [149, 150, 157, 158]. Finally, the CO conversion reached 100% in the third kinetic regime and the reaction rate became invariant with temperature. Pd/Al_2O_3 and Rh/Al_2O_3 also showed the similar catalytic behavior in the experiments, while as compared to Pt/Al_2O_3, their T_5 and T_{50} values were lower (Pd/Al_2O_3 showed T_5 and T_{50} of 190 and 205 °C, while Rh/Al_2O_3 showed T_5 and T_{50} of 160 and 180 °C).

Moreover, the relation between the activation energy and the reaction rate can be found from Arrhenius equation:

$$k = Ae^{-\frac{E_a}{RT}} \qquad\qquad \text{Equation 4-1}$$

$$ln\, k = -\frac{E_a}{R}\left(\frac{1}{T}\right) + ln\, A \qquad\qquad \text{Equation 4-2}$$

where k is rate constant, A is pre-exponential factor, E_a is activation energy, T is temperature, and R is gas contant. Therefore, the Arrhenius plots can be generated as shown in Figure 4-9(b), and the activation energies can be estimated by using the data measured in the low temperature range of activity. For Rh/Al_2O_3, a good linear relation can be found in low temperature regime, while for Pd/Al_2O_3 and Pt/Al_2O_3, inspite of some slope changes occuring at 161 and 163 °C respectively, their Arrhenius plots can still be reasonably fitted with straight lines. Hence the activation energies (E_a) calculated for Rh, Pd and Pt catalysts are 120, 104 and 77 kJ mol^{-1}, respectively. In addition, a big step change of Arrhenius plots happened for all these catalysts at the temperatures near T_{50}, which also suggested a sudden change of the active surfaces.
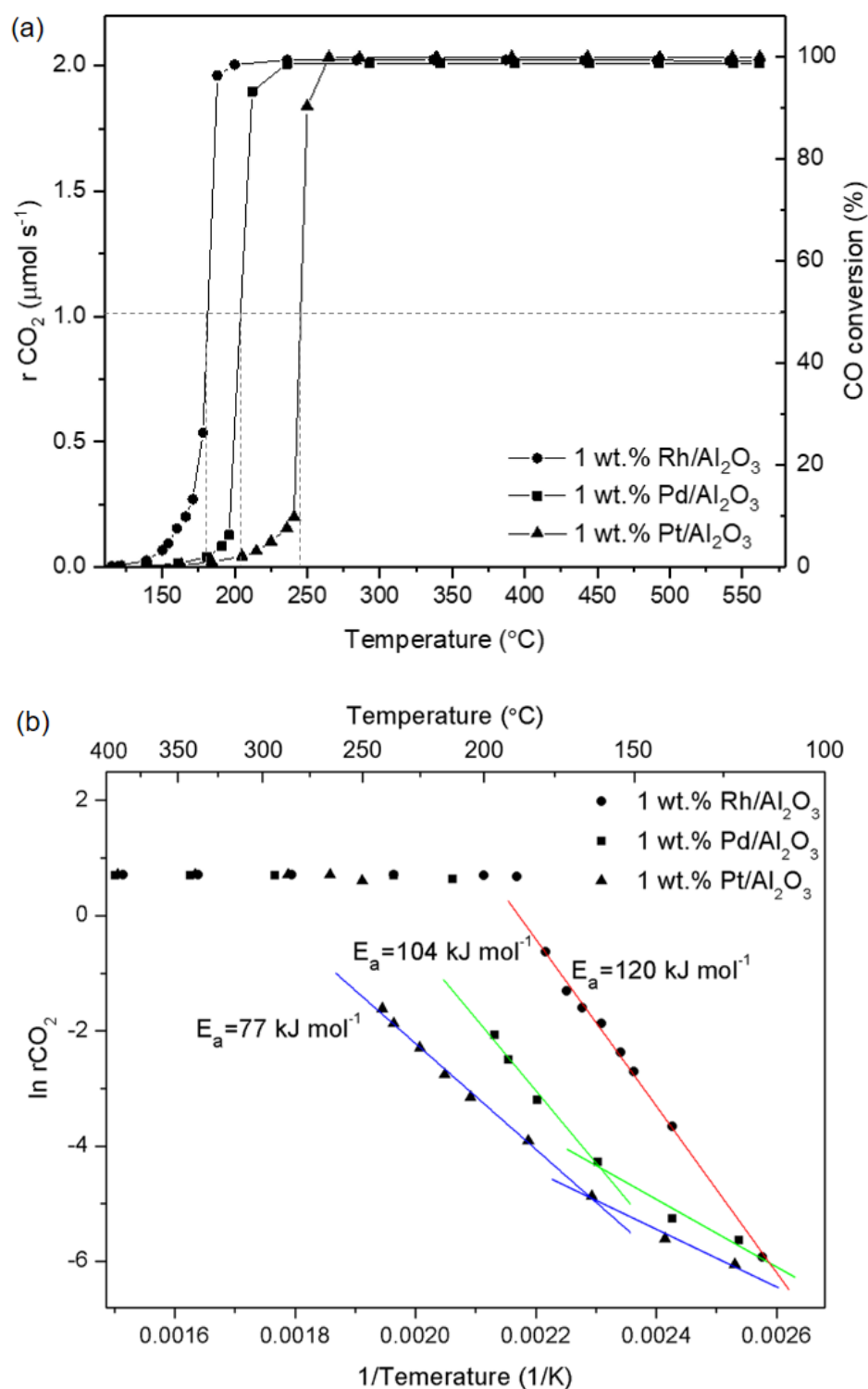
Figure 4- 9 (a) Light-off experiments over commercial catalysts of 1 wt% Rh/Al₂O₃, 1 wt% Pd/Al₂O₃ and 1 wt% Pt/Al₂O₃ in CO oxidation reaction under conditions of P_{CO}=0.6 kPa, P_{O_2}=1.0 kPa and F_t=450 mL min^{-1}. (b) Corresponing Arrhenius plots for each catalyst.

Furthermore, the values of T₅₀ for these three metals were in the sequence of Rh < Pd < Pt as shown in Figure 4-10, and this sequence is also consistent with the results reported previously in literature [156, 159, 166, 167]. This indicates that Rh is most

active among these three metals followed by Pd, while Pt is least active. To explain the difference in the activity of these metals, the reaction steps of CO oxidation in L-H mechanism (listed in Table 4-4 above) must be examined one by one. Firstly, the CO adsorption energies on these three metals are similar as discussed in subchapter 4.1.3 above, therefore the CO adsorption step does not account for the activity difference for these metals. On the other hand, the adsorbed CO reacts very fast with the adsorbed oxygen on the surface of all noble metals, so it is not the reason for activity difference either. However, it is shown in Figure 4-10 that these metals have quite different energies for O_2 dissociative adsorption that indicates obvious correlation with T_{50}, so the step of O_2 dissociative adsorption is believed to be the reason for the activity difference. In the low temperature regime, when CO and O_2 need to competitively adsorb onto the metal surface, higher O_2 dissociative adsorption energy means more efficient formation of adsorbed oxygen on the vacant sites on the metal surface, which leads to faster subsequent generation of new vacant sites via the reaction between oxygen and CO adsorbed on adjacent sites [156, 159]. Hence, the reaction is easier to occur on Rh surfaces at low temperatures and the values of T_{50} (as well as T_5) for these metals were found as Rh < Pd < Pt from the experiments.
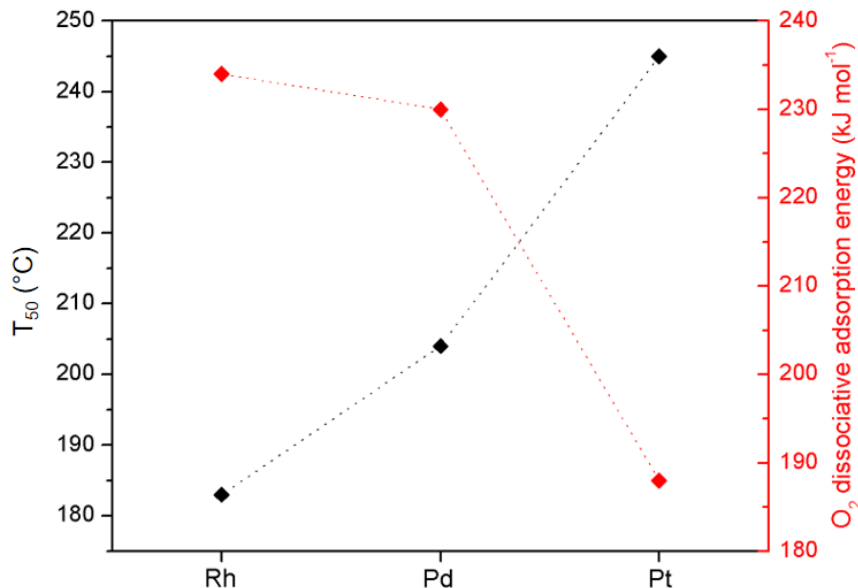
Figure 4- 10 T_{50} of CO oxidation reaction and O_2 dissociative adsorption energy on Pt, Pd and Rh.

4.2.2 Effect of amount of noble metal on catalytic activity

For noble metal supported on an inert support, such as Al_2O_3 here, it is well known that the majority of the catalytic activity is contributed by the noble metal particles on which the active sites locate [168, 169], so the amount of noble metals in the catalyst is expected to affect the activity. On the other hand, in order to use noble metals more efficiently, their amount in the catalyst is desired to be reduced and it is also one of the objectives in this thesis to use dilute noble metal systems. Therefore, here experiments were conducted to investigate how the amount of noble metals would normally affect the catalytic activity, by using the commercial catalyst. The commercial Rh/Al_2O_3 sample was chosen to be tested, because Rh-based samples would be mostly investigated in the later studies as shown in Chapter 7. The noble metal can be treated, to some extent, to be uniformly dispersed on Al_2O_3 support in commercial samples, hence the amount of noble metal in each test can be controlled by directly controlling the total amount of the sample used (as Al_2O_3 can be treated inert). Figure 4-11(a) shows the light-off experiments over 1 wt% Rh/Al_2O_3 sample of different amounts (10, 5 and 2.5 mg, respectively) in CO oxidation reaction by using the same experimental conditions as shown above in subchapter 4.2.1. If we assume that the amount of sample used in these three experiments was always 10 mg (the 5 and 2.5 mg experiments can be treated to be balanced by extra 5 and 7.5 mg inert Al_2O_3, respectively), the apparent metal loading of Rh in these experiments would be 1, 0.5 and 0.25 wt%, respectively. It can be found that their light-off curves under low CO conversion conditions (<~5%) were similar (Figure 4-11(a)) and the activation energies calculated under these conditions were also very close (Figure 4-11(b)), while the sample with higher metal loading exhibited relatively higher reactivity because of more active sites. However, the light-off curves started to diverge at higher conversions, and the value of T_{50} increased gradually with the decreasing metal loading as shown in Figure 4-12. The shift of T_{50} might be mainly ascribed to the heat transfer effect. CO oxidation is an exothermic reaction and a big amount of heat would be released at high reaction conversions. The heat cannot be dissipated to the environment quickly, and the actual temperature of the active sites might be higher than the average temperature of the catalyst bed or gas measured by thermocouple [170]. Hence, as mentioned before, the data obtained at high conversions (integral conditions) should not be over-interpreted, but it still shows that the sample with higher metal loading can achieve high conversions earlier.
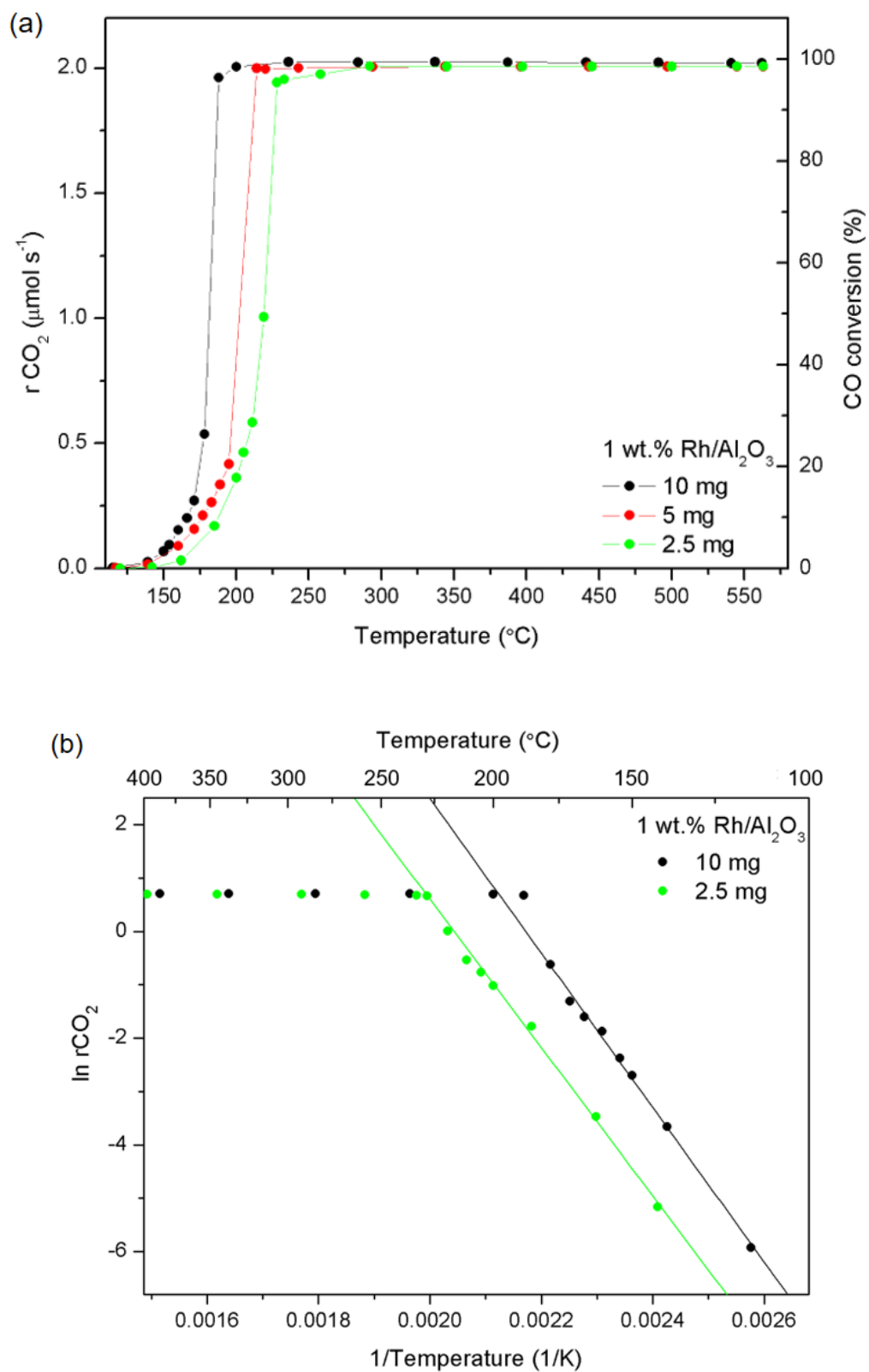
Figure 4- 11 (a) Light-off experiments over commercial catalyst 1 wt% Rh/Al₂O₃ of different amounts (10, 5 and 2.5 mg, respectively) in CO oxidation reaction under conditions of P_{CO} =0.6 kPa, P_{O_2} =1.0 kPa and F_t =450 mL min⁻¹. (b) Corresponding Arrhenius plots for 10 and 2.5 mg samples showing the activation energies.
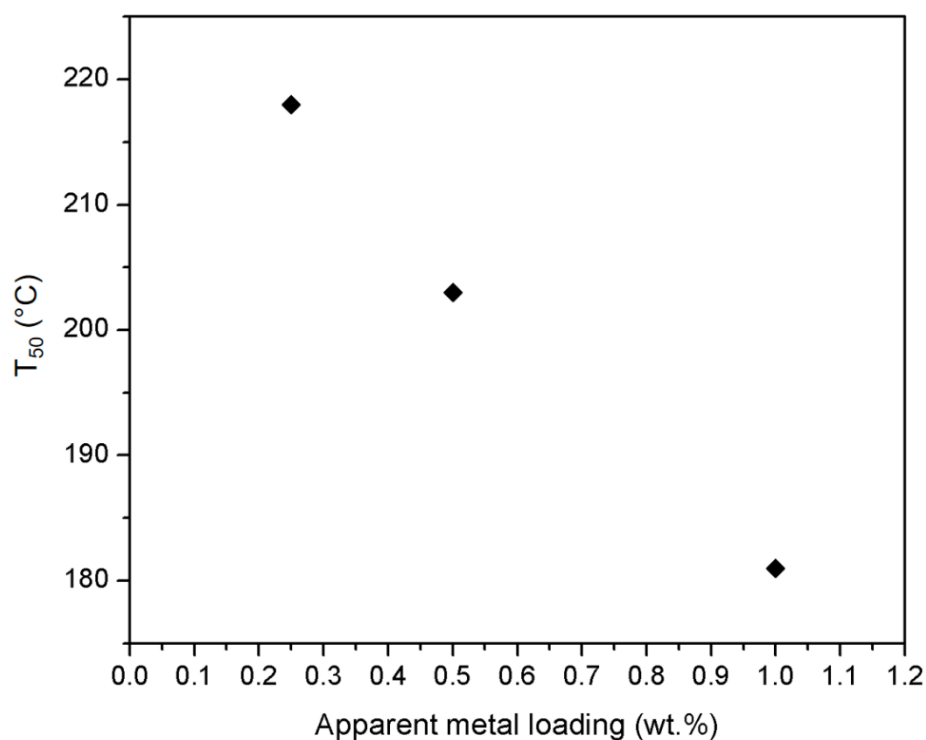
Figure 4- 12 T_{50} of CO oxidation reaction as a function of apparent loading of Rh.

4.3 Conclusions

In this chapter, the application of noble metals in catalysis especially in automotive exhaust control was introduced. The commercial noble metal catalysts (Pt, Pd and Rh on Al_2O_3, respectively) were tested in the model reaction of CO oxidation, and the results indicated:

- All these three metals exhibited excellent activity for CO oxidation.
- There were three kinetic regimes in which noble metal catalysts had different behaviors (CO inhibited, activity rapid increase and highly active regimes, respectively), which followed the L-H reaction mechanism.
- Rh was the most active one among these three metals as it showed the lowest T_5 and T_{50} values, despite that Rh is normally regarded as the active component for the conversion of NO_x in TWCs.
- Catalyst with higher amount of noble metals would exhibit higher reactivity.

These results revealed the classic catalytic behaviors of noble metal catalysts in CO oxidation, which could help to understand the behavior of the catalysts designed in the later studies. Reduced amount of noble metal in catalyst could result in lower activity, but attempts could be made to find a way to enhance the activity, probably by

controlling the particle characteristics and particle-support interactions. More importantly, as introduced in literature, particle sintering is a big problem for these noble metal catalysts, and a specific example will be given in the next chapter to demonstrate how a novel catalyst system can be destroyed by sintering, hence the importance of particle stabilization will be highlighted in the later studies.

Chapter 5: Demonstration of metal nanoparticle sintering

In this chapter, a specific example is given to demonstrate how the mobility of metal nanoparticles can lead to agglomeration. A well-defined system of spatially controlled metal nanoparticle pairs was attempted to be produced, but the movement of the particles under reaction conditions at high temperatures could cause agglomeration and hence the failure of the system.

5.1 Design principles of spatially controlled nanoparticle pairs

Purposefully designed catalysts can be used as model systems for the investigation of the mechanisms of reaction processes on the surfaces of catalysts. For instance, surface diffusion of reacting and/or intermediate species can occur during some catalytic processes and the hydrogen spillover is a well-known example, but this phenomenon is often overlooked mainly due to the lack of well-defined systems in which the catalytic functions can be clearly separated to probe the surface diffusion phenomenon [171]. However, for catalyst systems where sites of different activities exist, the surface diffusion may have big influence on the catalytic performance (e.g., activity and selectivity), hence a well-defined system is desired to understand this process. The spatially controlled nanoparticle pairs seem to be promising, where pairs of two metals with fixed separation distance can be formed as illustrated in Figure 5-1. Hence, the diffusion length between the particles can be controlled and its effects on the catalytic performance can be studied. To prepare the particle pairs with controlled separation distance, the method pioneered by Dong et al. [172] could be used, which will be introduced in detail together with the preparation steps in subchapter 5.2.2.

In this study, nanoparticle pairs of Au and Pt were attempted to be prepared, and they were subsequently deposited on the support. Silicon wafer was selected to be the support as its flat surface can allow the controlled distance between particles to be maintained when introduced onto the support. Moreover, the mobility of metal nanoparticles on the support surface should also be considered, as it could lead to the failure of the system if particles move and agglomerate. Hence, preliminary experiments were conducted to test the thermal stability of the supported nanoparticles under reaction conditions of CO oxidation. The results of nanoparticle pair preparation and the preliminary stability test will be demonstrated in the following subchapters.
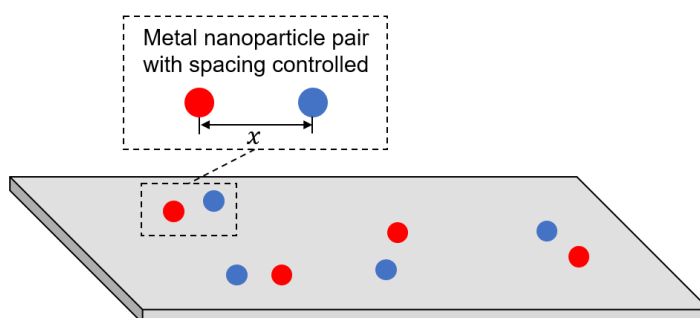
Figure 5- 1 Schematic demonstration of spatially controlled metal nanoparticle pairs. Red and blue balls represent two different metal species, respectively.

5.2 Sample preparation

This project was collaborative, and the preparation work for the samples was conducted by collaborators Dr. Shan Jiang and Dr. Simon Beaumont from Chemistry Department at Durham University. The principles of their preparation process as well as some characterization information of the samples will be presented here.

5.2.1 Synthesis of metal nanoparticles

Pt nanoparticles were synthesized by using the Schlenk method [173] under N_2 flow. Platinum(II) 2,4-pentanedione ($Pt(acac)_2$, 0.13 mmol) was added to a 3-neck round bottom flask, which was evacuated and refilled with N_2 for three times. Then oleylamine (15 mL) was added and the flask was heated to 100 °C and stirred for 20 minutes, which allowed $Pt(acac)_2$ to get fully dissolved. Borane triethylamine (200 mg) in oleylamine (2 mL) was added into the solution resulted from previous steps, which changed the colour of solution from yellow to dark brown. The solution was then heated to 120 °C and held for 60 minutes before it was cooled down to room temperature. Hexane (5 mL) and ethanol (30 mL) were added to the suspension, followed by centrifugation. Add another 60 mL of ethanol to the resulting suspension before centrifugation. The produced nanoparticles were re-dispersed in hexane (4 mL) for storage.

Au nanoparticles were synthesized using a different method [174]. $HAuCl_4$ (0.1 g) was dissolved in tetralin (10 mL) and oleylamine (10 mL) at 45 °C under N_2 flow and stirring. Dissolve borane tert-butylamine complex (0.5 mmol) in tetralin (1 mL) and oleylamine (1 mL) by applying sonication, and the solution obtained was added into the $HAuCl_4$ solution previously made, followed by stirring at 45 °C for 1 hour. Then add acetone (40 mL) in the solution and collect the Au nanoparticles by applying centrifugation. The solid obtained was dispersed in hexane (20 mL), precipitated by adding ethanol (40 ml) and centrifugation. Finally, the nanoparticles were re-dispersed in hexane for storage.

5.2.2 Fabrication of nanoparticle pairs

In this study, the method proposed by Dong et al. [172] was used to fabricate the pairs of metal nanoparticles, which can be schematically summarized as Figure 5-2. Firstly, hetero-bifunctional polyethylene glycols (PEG) of COOH-PEG-SH and BOC-NH-PEG-SH are crystallized to form the single crystals. Metal nanoparticles can be adsorbed

onto these single crystals by covalently bonding to the thiol (-SH) groups excluded on the surface of crystals. Some capping agents such as dodecanethiol can be used to cap the free surface of the nanoparticles. Then, by dissolving the crystals, the metal nanoparticles are detached from the crystal surface with linking polymers selectively attached to only one side of these nanoparticles [172]. The linking polymers attached to metal nanoparticles have different terminal groups (-COOH and -NH2), which allows for the directional linking of two nanoparticles. Finally, the linked metal nanoparticles can be deposited onto the support.
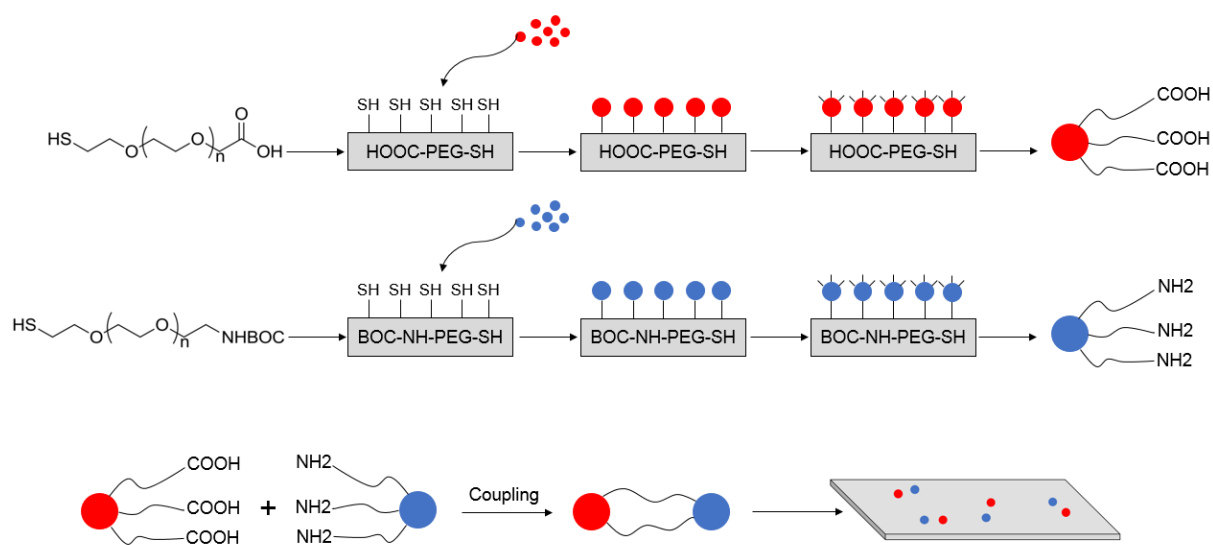
Figure 5- 2 Schematic demonstration of preparation route for metal nanoparticle pairs.

Crystallizations of COOH-PEG-SH and BOC-NH-PEG-SH were both carried out in the self-seeding process [172]. For COOH-PEG-SH, 4-5 mg of it was dissolved in pentyl acetate (10 mL) at 60 °C for 10 minutes, before the solution was cooled down to 4 °C for 2 hours. The solution was heated to 35 °C (seeding temperature) and held for 10 minutes, and then it was crystallized at 22 °C (crystallization temperature) for 2 days. Similarly, BOC-NH-PEG-SH (8 mg) was dissolved in pentyl acetate (10 mL) at 60 °C for 10 minutes, before the solution was cooled down to 4 °C for 2 hours. Then the solution was heated to 33 °C for 10 minutes and crystallized at 17 °C for 2 days. SEM images of the obtained single crystals of COOH-PEG-SH and BOC-NH-PEG-SH are shown in Figure 5-3(a) and (b), respectively. Then Au and Pt nanoparticles were separately adsorbed onto these two crystals, and the TEM images of nanoparticle adsorbed crystals can be found in Figure 5-3(c-f). The crystals were then dissolved to obtain the metal nanoparticles with different linking polymers, and finally the pairing of nanoparticles was attempted for Au via reactions between -COOH and amine groups.

The resulted Au nanoparticle pairs were deposited on the support, which can be seen in Figure 5-4. Generally, the pairs of Au nanoparticles were formed, but the distance between the nanoparticle pairs was not well controlled as some pairs were too close to each other. Moreover, the pairing of Au and Pt nanoparticles still needs to be studied further.
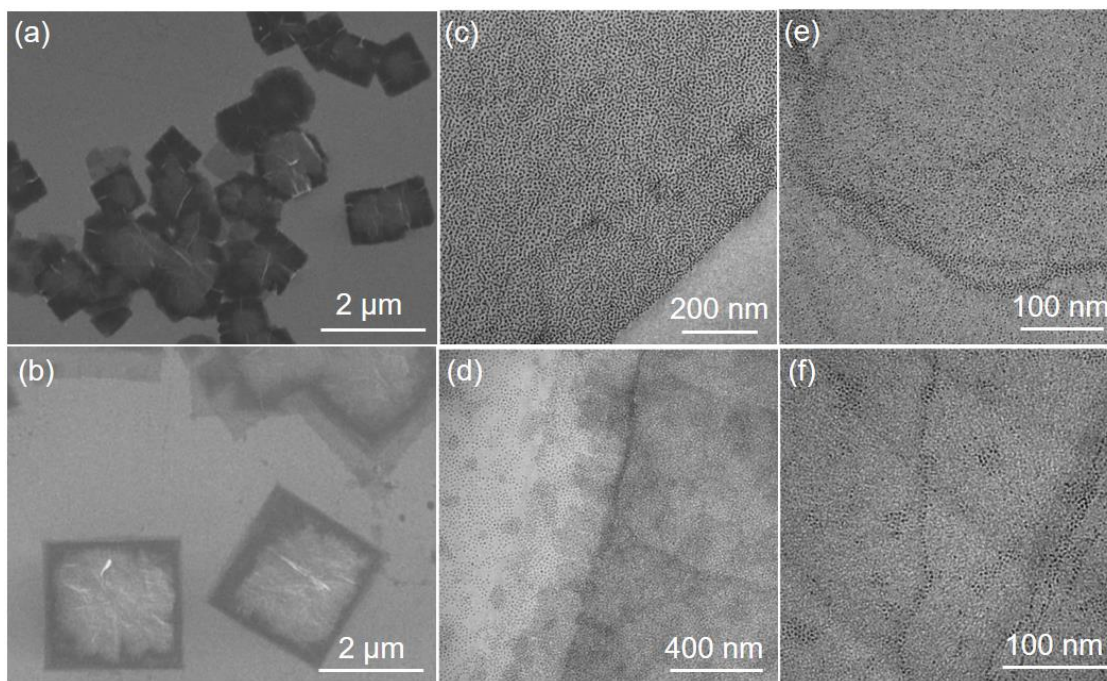
Figure 5- 3 SEM images showing single crystals of (a) COOH-PEG-SH and (b) BOC-NH-PEG-SH. TEM images of (c) Au nanoparticles adsorbed on COOH-PEG-SH, (d) Au nanoparticles adsorbed on BOC-NH-PEG-SH, (e) Pt nanoparticles adsorbed on COOH-PEG-SH, and (f) Pt nanoparticles adsorbed on BOC-NH-PEG-SH. Images were collected by collaborators at Durham University.
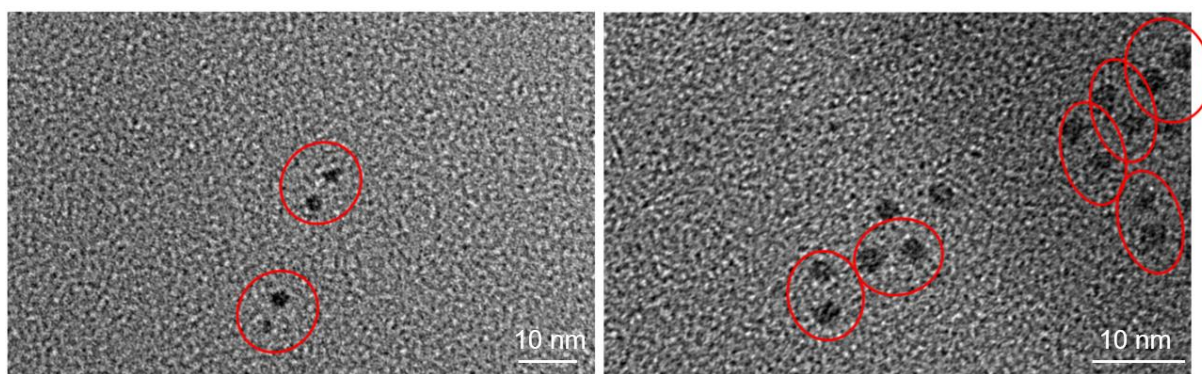
Figure 5- 4 Au nanoparticle pairs on support. Images were collected by collaborators at Durham University.

5.3 Thermal stability test of the supported nanoparticles

In the meantime, experiments were conducted to test the thermal stability of the supported metal nanoparticles. Because the preparation technique for nanoparticle pairs was not mature at the time of the study, discrete nanoparticles were used instead of pairs for the preliminary thermal stability tests. Nanoparticles were deposited onto the silicon wafer support via the drop casting method, where a small amount of dilute solution of nanoparticles was dropped on the support and the solvent was evaporated at room temperature to leave nanoparticles on the support. If preliminary tests show that these metal nanoparticles will not move and agglomerate, then the experiments can be continued to test the nanoparticle pairs.

The thermal stability tests were carried out for supported Au nanoparticles (as Pt nanoparticles have not been successfully prepared at that time), by tracking groups of nanoparticles when they were subjected to a series of temperature treatments, which therefore will be referred to as "particle tracking" experiments henceforth. The supported Au sample would be heated under mixtures of CO and O_2 (to mimic real reaction conditions) to a series of temperatures (gradual increase), and the sample would be scanned in helium ion microscope (HIM) before and after the heat treatment at each temperature to track the groups of nanoparticles that were selected before the treatment and check if these nanoparticles coalesced at the corresponding temperature. HIM, which could provide higher resolution images as compared to the conventional SEM, enabled the visualization of individual nanoparticles and it was crucial for the particle tracking. Prior to the experiments, some groups of metal nanoparticles needed to be selected to be traced throughout the experiments. Therefore, the as-prepared sample was scanned first in HIM. However, the HIM images of the as-prepared sample (Figure 5-5(a)) were very blurry, due to a thin layer of impurities covering the surface of the sample. That was probably due to some organic residue originated from the Au solution that was not completely evaporated at room temperature. Hence the sample was treated in 20% O_2/He flow (90 mL min^{-1}) at 150 °C for 3 hours, aiming to remove the organic residue and expose the Au nanoparticles underneath (as shown in Figure 5-5(b)). Then a cross-shaped mark (shown in Figure 5-5(c)) was made on the surface of the support by using the focused ion beam (FIB), and a small area in the vicinity of the mark was selected as the target area for observation. The cross-shaped mark was used to help search for the target

area in HIM. Several groups of metal nanoparticles were selected in the target area to be tracked before and after each temperature treatment.
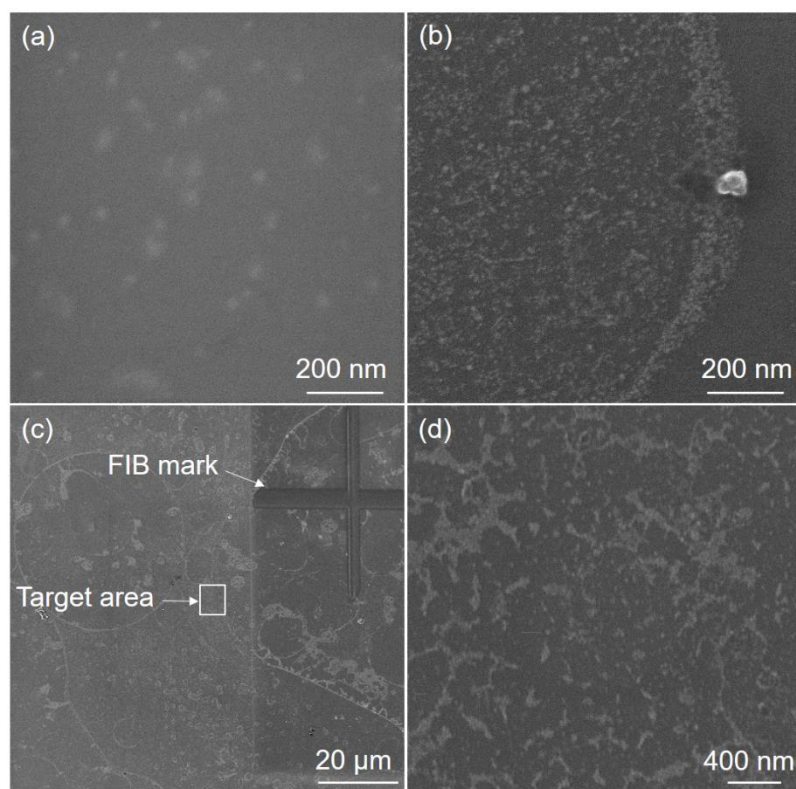
Figure 5- 5 HIM images of (a) as-prepared sample of Au nanoparticles on silicon support, (b) after being treated in 20% O₂/He at 150 °C for 3 hours, (c) with cross-shaped mark made on the support and a small target area was selected, and (d) close view of the target area for particle tracking.

Then the marked sample was treated in CO oxidation reaction and the experiments were carried out in the pellet reactor introduced in Chapter 3, using the stoichiometric reaction conditions (P_{CO} =1.0 kPa, P_{O_2} =0.5 kPa and F_t =150 mL min^{-1}). In each experiment, the sample was heated from room temperature to a certain temperature and was then cooled down back to room temperature once the reaction rate was stabilised. The sample was scanned in HIM before and after the experiment to obtain the status changes of the selected groups of nanoparticles (such as particle size, number and dispersion) happening at the corresponding temperature of experiment. Then the temperature of the experiment was increased gradually, and a series of HIM images were collected from all the experiments (as shown in Figure 5-6). Therefore, the evolution of the selected groups of nanoparticles with the increasing temperature could be observed directly, which was used to determine whether and at which temperature the nanoparticles would start to agglomerate under the CO oxidation reaction conditions.

The rate of CO_2 production (r_{CO_2}) was measured as a function of temperature as it can be found in Figure 5-6(a), and the numbers (1 to 6) shown in the graph highlight the stages at which the sample was taken out from the reactor and scanned in HIM for particle tracking. Two groups of nanoparticles were selected to present the evolution of nanoparticles with the temperature, as shown in Figure 5-6 (b) and (c), respectively (the numbers on the top left corner of HIM images correspond to the stages highlighted in Figure 5-6(a)). Although the sample has been heated in 20% O_2/He at 150 °C before, the temperature might not be high enough to burn out all the organic residue as the images of the sample treated at low temperatures were still blurry. It can be found that, as the reaction temperature increased, the nanoparticles in HIM images became sharper, and individual nanoparticles could be visualized clearly after the sample was treated at 350 °C. By observing the HIM images which show clear nanoparticles, changes can be easily noticed: the number of nanoparticles decreased when reaction temperature went higher, and some small particles disappeared; Also, the size of nanoparticles grew larger and the distance between these nanoparticles became bigger as well. For instance, detailed particle analysis was conducted for one of the selected nanoparticle groups, and the changes of the size and number of Au nanoparticles with the temperature of treatment (from 350 to 500 °C) can be found in Figure 5-7. All these results indicate that agglomeration of Au nanoparticles happened on the silicon support at elevated temperatures and small nanoparticles in vicinity coalesced to form larger particles. Unfortunately, clear images of the sample that was treated at the temperatures below 350 °C could not be obtained, so it was difficult to tell at which temperature the nanoparticle agglomeration initiated. However, the changes of nanoparticles were already seen between the images of 350 and 400 °C, but it is also possible that the agglomeration started at a lower temperature. Therefore, the Au nanoparticles that were loosely dispersed on the support did not have enough thermal stability to survive the high-temperature processes. When turning to the production rate of CO_2 as shown in Figure 5-6(a), no reaction rate was observed at low temperatures (below around 300 °C) as nanoparticles were covered by the impurities and the metal surface could not be accessed by reactants. When temperature went higher, as the impurities were removed gradually, the reaction rate increased despite some loss of metal surface as nanoparticles agglomerated to get larger particle size but smaller particle number as shown in Figure 5-7. However, if particle agglomeration keeps occurring, it can be expected that the activity will decrease at some point.

The particle tracking experiments indicate that, even though the spatially controlled particle pairs could be prepared, their mobility on the support would lead to agglomeration at high temperatures and hence they could not act as the model system to study the surface diffusion process. Therefore, this study was not carried out further.
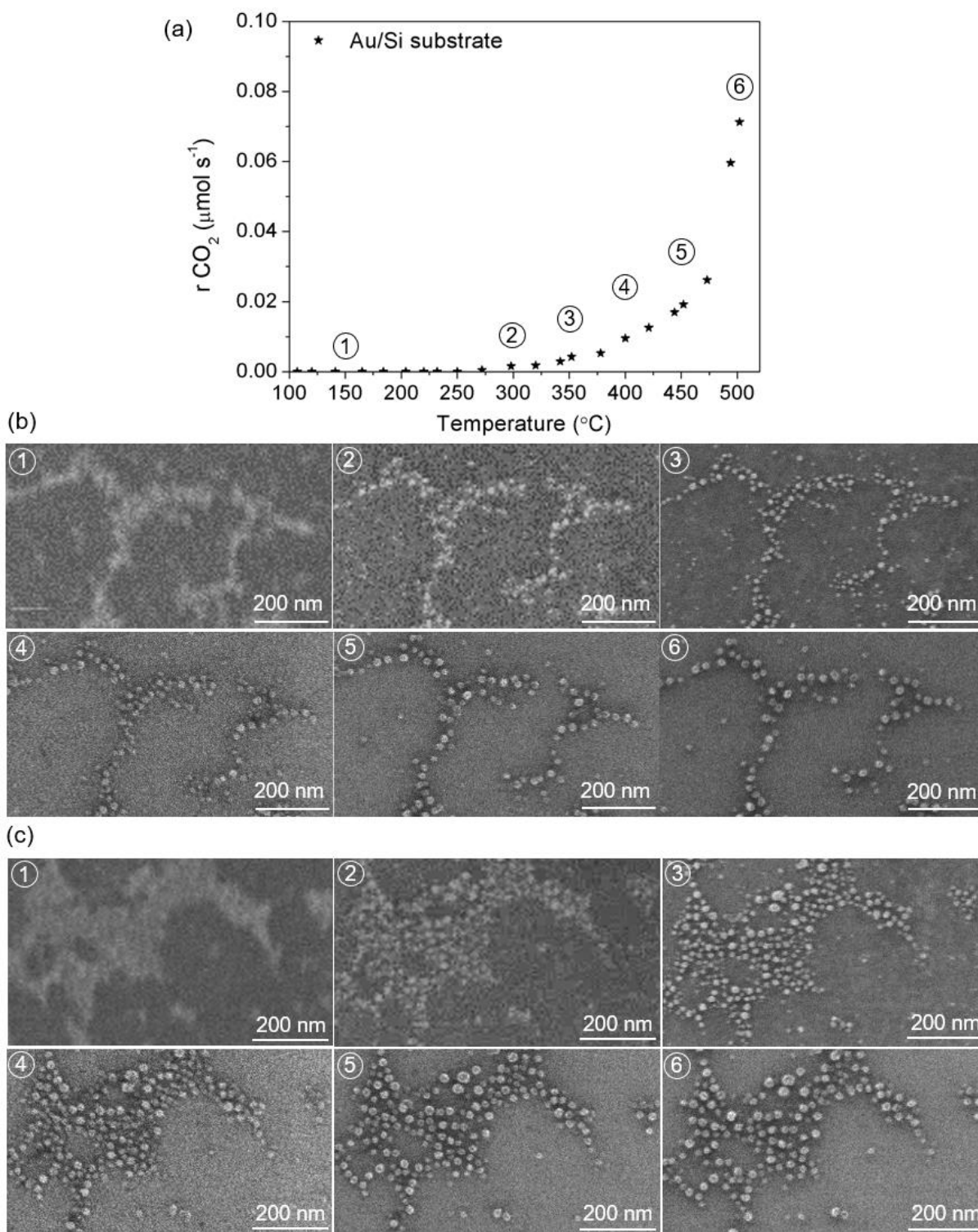
Figure 5- 6 (a) CO_2 production rates achieved by Au/silicon sample as a function of temperature under stoichiometric CO oxidation conditions (P_{CO}=1.0 kPa, P_{O_2}=0.5 kPa and F_t=150 mL min^{-1}). (b) and (c) show the HIM images of two groups of Au

nanoparticles, respectively, after being tested at different temperatures and the corresponding temperatures are labelled in (a).
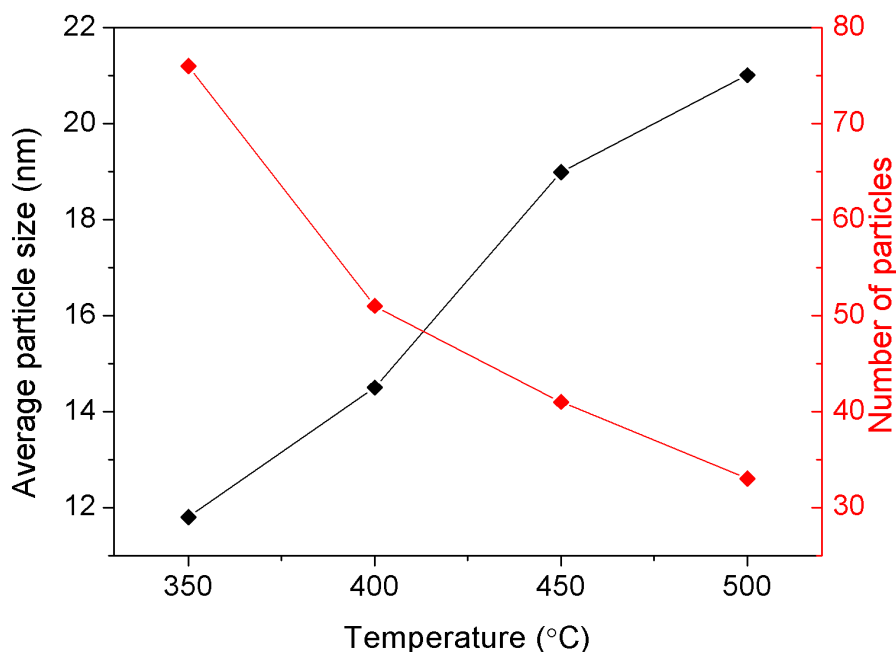
Figure 5- 7 Changes of the size and number of Au nanoparticles in the selected group with the increasing temperature, indicating the agglomeration of Au nanoparticles.

5.4 Conclusions

In this chapter, it was proposed to prepare a novel catalyst system of spatially controlled metal nanoparticle pairs. Indeed, some progress has been made for the preparation of nanoparticle pairs:

- Metal nanoparticles were successfully adsorbed onto the PEG crystals of COOH-PEG-SH and BOC-NH-PEG-SH, in order to attach different linking polymers.
- Metal nanoparticles with different functional polymers could be linked together, which resulted in nanoparticle pairs as exemplified by Au-Au pairs.

However, preliminary thermal stability tests showed that discrete metal nanoparticles on silicon support could agglomerate under CO oxidation conditions from 350 °C or even lower temperatures. This could indicate that the metal nanoparticles that are only loosely dispersed on the support surface can move easily at high temperatures, which would cause agglomeration and hence destroy the purposefully designed system. Therefore, the stability of metal nanoparticles should always be highlighted when designing novel catalyst systems. The results in this chapter also indicate that, in order

to stabilize metal nanoparticles, the particle-support interactions should be enhanced to suppress the particle migration. Therefore, two different approaches for metal nanoparticle stabilization are investigated in the later studies, and firstly encapsulation of metal nanoparticles is attempted as demonstrated in the next chapter.

Chapter 6: Stabilizing noble metal nanoparticles via encapsulation in porous organic cages

It has been demonstrated in the last chapter that metal nanoparticles loosely dispersed on the support would suffer from sintering, so stronger particle-support interactions might be required to enhance the thermal stability. In this chapter, attempts are made to stabilize noble metal nanoparticles by enclosing them into a type of hollow and cage-like molecules (porous organic cages). The porous organic cages can control the size of metal nanoparticles by limiting their growth, and the stability and activity of the resulted catalyst are evaluated under CO oxidation conditions.

6.1 Introduction to porous organic cages

6.1.1 Porous organic cages and their applications in catalysis

It has been introduced in Chapter 2 that encapsulation of metal nanoparticles in some porous materials such as mesoporous silica, carbon, alumina as well as metal organic frameworks (MOFs) [175] is an effective strategy for nanoparticle stabilization. Porous materials exhibit appealing features to act as catalyst supports, such as high surface areas and tunable porosity which can enhance the catalytic performance, as well as the ease of recycling as compared with the homogenous counterparts. Therefore, porous materials like silica and alumina have been employed as important catalyst supports for metal nanoparticles. Moreover, encapsulation of metal nanoparticles by using new classes of porous materials like MOFs has attracted considerable research attention in the past two decades [176-178]. The well-defined pore structure can confine the growth of metal nanoparticles, which can provide good control over the particle size and hence brings some potential benefits such as the improved surface area and selectivity and also the enhanced stability of metal nanoparticles. Nevertheless, despite the rapid progress achieved in this field, the effective controls over the particle size, composition, spatial distribution, confinement and accessibility of metal nanoparticles within the pores and the resulting effects on catalytic properties still remain big challenges [7, 179].

Conventional organic porous solids such as MOFs and covalent organic frameworks (COFs) are all extended frameworks or networks in which individual molecules are linked by covalent or coordinative bonds [180]. On the contrary, it is difficult to find discrete covalent organic molecules that can maintain permanent porosity, because most molecules have the tendency to pack together with minimal spacing in the solid state in order to obtain maximum attractive intermolecular interactions [181, 182]. Therefore, molecular crystals with open channels or voids are usually unstable when guests, such as solvents, are removed from the pores [183]. However, there are some exceptions that a diversity of "porous organic molecules" were reported in recent years, which show some unique properties as compared to the extended porous framework analogues.

Porous molecule is the term used to describe those molecules that can be packed in solid state with extrinsic or intrinsic porosity. Extrinsic porosity locates between adjacent molecules, which is caused by the loose packing of molecules because of rigid molecule structures, or the directional intermolecular interactions such as

hydrogen bonds [182]. In contrast, intrinsic porosity locates inside the molecule itself. For instance, porous organic cages (POCs), unlike the extended networks like MOFs, comprise individual molecular building blocks (the cages) that pack together with noncovalent intermolecular interactions to form the porous structure. POCs have permanent cavity inside the molecules (cages) due to their rigid structure, and their cavity is open to the outside atmosphere through cage windows [182]. Although the study of porous molecules started decades ago, the POC is a relatively new class of material and the first POC with intrinsic permanent porosity was reported by Cooper et al. in 2009 [181]. According to their study, a series of tetrahedral organic cages can be generated through cycloimination reactions of trialdehydes with diamines [181, 184, 185]. The porosity of these cage materials is a result of both intrinsic molecular voids inside the cages and the extrinsic voids resulted from the inefficient molecule packing. POCs show some potential advantages over the extended networks like MOFs in the following aspects: POCs can be dissolved to form discrete molecules in solvents and then they can be re-assembled into solids, and even to cast membranes or thin films [186]. The "mix and match" strategies can also be applied to mix cage molecules of different types to generate porous organic alloys [187], which provides a potential method to fabricate well controlled bimetallic or multicomponent systems in the context of nanoparticle and catalyst syntheses. POCs have been widely studied for applications in molecular separation [188-190], gas storage [191, 192], and recently the potential of POCs for metal nanoparticle stabilization and confinement has been considered.

Initially, soluble POC molecules were studied as stabilizers for metal nanoparticles (like Rh or Pd), which allowed for the homogenization of heterogeneous metal nanoparticles in solutions to achieve not only enhanced catalytic activity but also easier recovery and recycling. For instance, Sun et al. reported that POC stabilized Rh nanoparticles (~1.1 nm) showed the highest TOF value (215.3 mol of H_2 per mol of Rh per min) among all other studies reported in literature for the reaction of methanolysis of ammonia borane [179]. Similarly, POC stabilized Pd nanoparticles prepared by Zhang et al. (as shown in Figure 6-1) exhibited higher activity as compared to the commercial catalyst Pd/C in carbonylation of aryl halides under mild conditions [193].
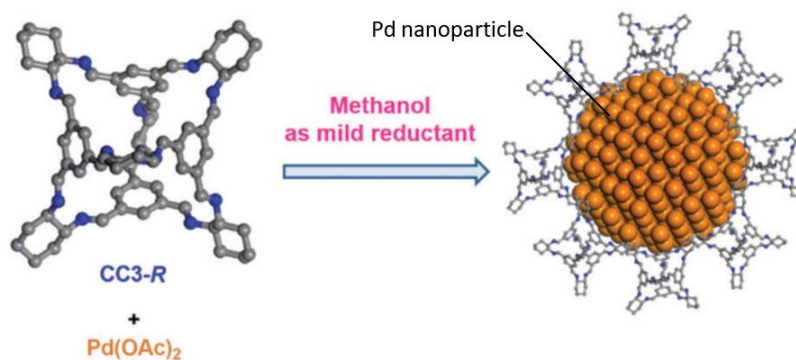
Figure 6- 1 Schematic demonstration of Pd nanoparticle stabilized by CC3-R cages. [193]

On the other hand, efforts have also been made to enclose metal nanoparticles inside the cavity of the POC molecules (as shown in Figure 6-2) [194-197]. According to the study from Mukherjee's group, Pd nanoparticles with narrow size distribution (1.8 ± 0.2 nm) could be embedded into POCs which had internal cavity size of ~2.0 nm and the cage-embedded Pd nanoparticles showed higher catalytic activity for cyanation of aryl halides as compared to some commercial Pd catalysts [194]. In addition, Zhang's group also reported that they embedded ~1.9 nm Au nanoparticles [195] and ~1.8 nm Pd nanoparticles [196] into organic cages, respectively, and the resulted catalysts showed good activity and stability in the Suzuki-Miyaura reaction. Moreover, Xu's group also reported recently that ultrafine Pd nanoparticles (~0.72 nm) were encapsulated in POCs and were examined in different liquid-phase reactions such as methanolysis of ammonia borane, hydrogenation of nitroarenes, and reduction of organic dyes, which showed that the Pd nanoparticles in POCs have promising catalytic activity and stability [197].
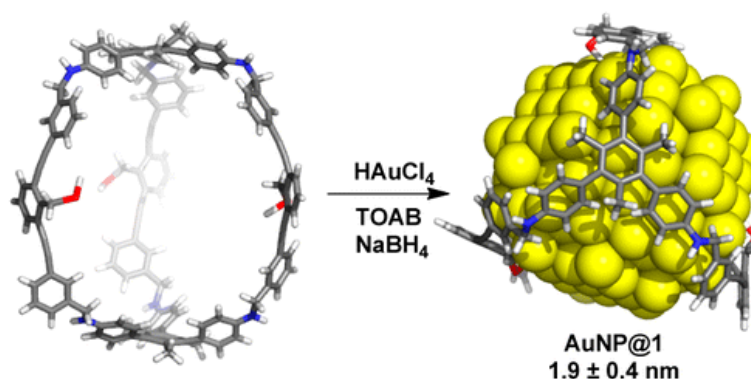
Figure 6- 2 Schematic demonstration of the encapsulated Au nanoparticle in cage molecule. [195]

Enclosing metal nanoparticles in POCs is appealing, as it can provide many advantages for catalytic applications in aspects of controlling the growth hence the size of metal nanoparticles, suppressing particle aggregation, and creating synergistic effects between metal nanoparticles and porous supports [197]. Nevertheless, this is still an emerging research area. The issues such as maintaining the pore structure and crystallinity of POCs as well as the accessibility of active metals in POCs still need to be further studied.

6.1.2 Controlling the porous properties of POCs

As mentioned above, Cooper's group reported a series of POCs with permanent porosity for the first time in 2009 [181]. Imine-linked tetrahedral organic cages were synthesized via [4+6] cycloimination of 1,3,5-triformylbenzene with vicinal diamine linkers. They reported three types of cages (CC1-CC3) which were prepared by using different diamine linkers: 1,2-ethylenediamine, 1,2-propylenediamine and (R,R)-1,2-diaminocyclohexane for CC1, CC2 and CC3, respectively (as shown in Figure 6-3). All the three cages show tetrahedral symmetry and they have four approximately triangular windows through which the intrinsic pores in cages can be accessed [181]. It can be noticed that CC1-CC3 have different steric groups on their vertices, depending on the types of diamines used. CC1 has unfunctionalized groups on the vertices, while methyl groups and cyclohexyl groups can be found on the vertices of CC2 and CC3 molecules, respectively. These vertex steric groups were found to have pronounced effects on the packing motif of cages and hence the porous properties of the resulting materials [181, 182]. For instance, two adjacent cages of CC1 would pack in a window-to-arene motif, which results in the isolated voids in individual cages without inter-cage window connectivity (as shown in Figure 6-4(a)). Cages of CC2 would pack in a similar way as CC1 but, thanks to the methyl groups on vertices, the packing of stacks is slightly frustrated, which gives rise to an 1D pore channel running between the CC2 cages as shown in Figure 6-4(b). However, as the windows of CC2 cages do not face towards the channel, the voids in these cages do not connect with the channel and they are still isolated. On the contrary, CC3 shows a window-to-window packing motif resulted from the interlocking of three vertex cyclohexyl groups on two adjacent CC3 cages. The alignment of windows allows for the connection between the voids in adjacent cages and, combined with the tetrahedral symmetry of cages, a 3D diamondoid pore network is established as shown in Figure 6-4(c) [181].
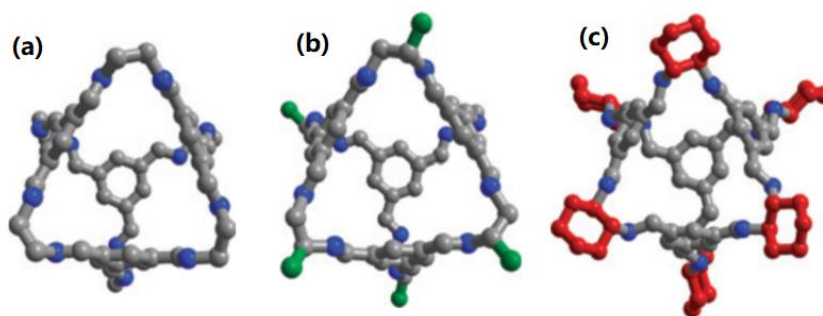
Figure 6- 3 Structures of (a) CC1, (b) CC2 and (c) CC3 molecules. Blue balls represent nitrogen atoms and grey balls represent carbon atoms, while hydrogen is omitted for clarity. Methyl groups on CC2 and cyclohexyl groups on CC3 are displayed in green and red, respectively. [181]
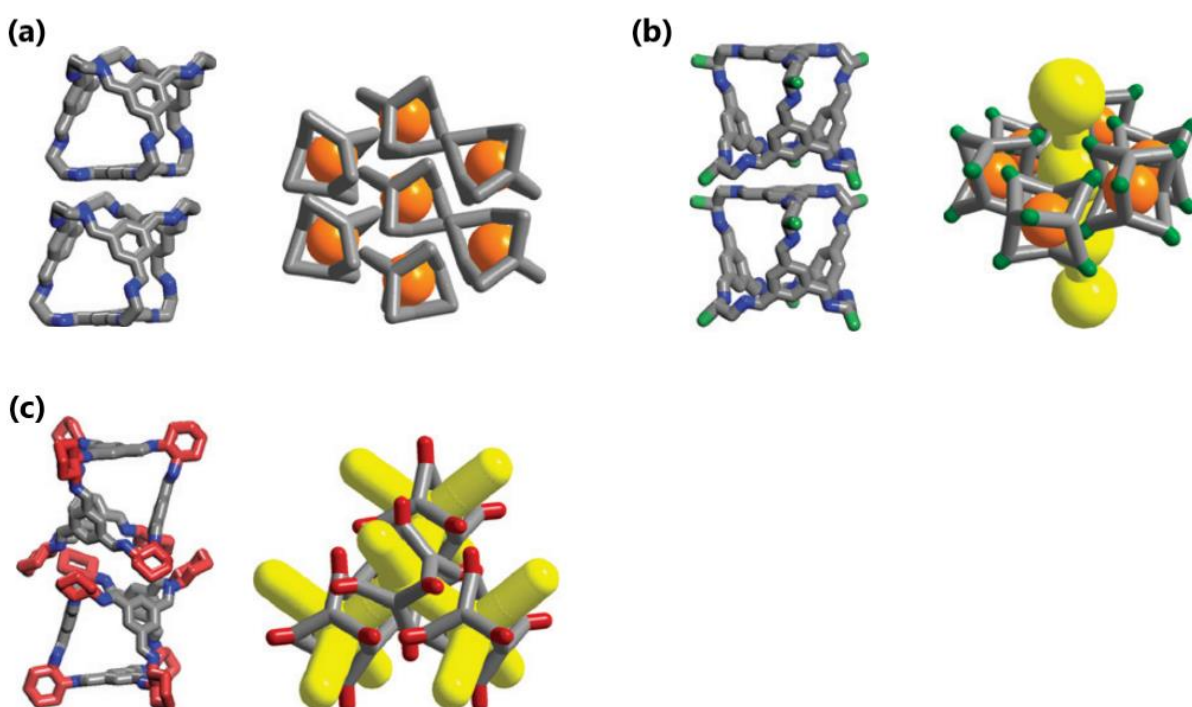
Figure 6- 4 Packing methods of adjacent cage molecules. (a) Window-to-arene packing for CC1, which gives rise to isolated void volume in individual molecules (orange areas). (b) Similar window-to-arene packing hence isolated void for CC2, while 1D pore channel (shown in yellow) exists in the interstice between molecules because of the interactions between methyl groups (green). (c) Window-to-window packing for CC3 interlocked by cyclohexyl groups (red), which results in 3D diamondoid channels (yellow) getting through individual cages. [181]

All the cages discussed above can be used to accommodate metal nanoparticles to control particle size and prevent particle agglomeration. However, gas diffusion through the cages should also be taken into consideration, as the reactant molecules must access the metal surface in heterogeneous catalysis. As shown above, CC3 has good interconnected pore channels and this would allow for better diffusion of gases

through the cages, hence it was selected as the support material in this study. Pd nanoparticles would be incorporated into CC3 and the activity of the resulted catalyst was tested in CO oxidation reaction.

6.2 Preparation of Pd nanoparticles in CC3

In this study, 0.5 wt% Pd nanoparticles in CC3 (referred to as Pd@CC3 henceforth) was prepared and then tested in CO oxidation reaction. The preparation of the Pd@CC3 sample was conducted by our collaborators Harrison Cox, Dr. Shan Jiang and Dr. Simon Beaumont from Chemistry Department at Durham University, and the principles of their preparation processes are briefly described here.

The synthesis of CC3 cages was conducted through the [4+6] cycloimination reaction between 1, 3, 5-triformylbenzene and (*1R, 2R*)-(-)-1, 2-diaminocyclohexane (Figure 6-5(a)), as described by Cooper et al. [181]. 1, 3, 5-triformylbenzene (100 mg, 0.62 mmol) was dissolved in dichloromethane (8 mL), and (*1R, 2R*)-(-)-1, 2-diaminocyclohexane (106 mg, 0.93 mmol) was also dissolved in dichloromethane (8 mL), and then the former solution was added to the latter in an oven-dried round bottomed flask. The flask was sealed and left at room temperature for 7 days without stirring. After 7 days, the solvent was removed in vacuum, and the obtained crude product was filtered and then washed with methanol, which resulted in the final product of CC3 that appeared as a white powder (112 mg, 0.11 mmol, 71%). The resulted product consisted of CC3 molecules in tetrahedral symmetry with intrinsic voids and four windows that allow gases to diffuse through (Figure 6-5(b)). It is worth mentioning that most CC3 cages would pack in the window-to-window arrangement (known as CC3α) [184] which has 3D diamondoid pore channels (as shown in the left of Figure 6-5(c)). CC3α is the thermodynamically favored form for CC3, which has been confirmed in previous studies. However, another frustrated packing motif (CC3β) might also exist at a small amount, and it has 2D layered pore structure with formally disconnected voids (as shown in the right of Figure 6-5(c)) [198]. As the quantity of CC3β is very low, it will not be discussed further here.

The incorporation of Pd into CC3 was conducted through cocrystallization of Pd precursor ($Pd(NO_3)_2$ here) and CC3, and the subsequent reduction step transformed Pd precursor into Pd nanoparticles, which is briefly illustrated in Figure 6-5(d). The CC3 product (10 mg, 8.95×10^{-3} mmol) was dissolved in dichloromethane (2 mL), and

a solution of $Pd(NO_3)_2$ in acetone (3 mg mL^{-1}) was prepared. The CC3 solution was then mixed with the $Pd(NO_3)_2$ solution, and hence the $Pd(NO_3)_2$@CC3 cocrystals could be formed. The mixed solution was stirred for 1 hour, and then the solvent was evaporated slowly. The sample vial of the solution was covered by a lid, but not fully sealed, hence the solvent could escape. The solution was left under ambient conditions to let the solvent evaporate. After all the solvent disappeared, the sample was moved into an oven operating at 70 °C to get further de-solvated under vacuum overnight. Once the product of $Pd(NO_3)_2$@CC3 was obtained, the reduction was carried out in the environment of H_2 (10% H_2/N_2, 30 mL min^{-1}) to reduce $Pd(NO_3)_2$ into Pd nanoparticles. To find the appropriate reduction temperature for $Pd(NO_3)_2$@CC3 without decomposing the cage structure itself, TGA was used to investigate the changes of both CC3 and $Pd(NO_3)_2$@CC3 samples upon heating in both the inert atmosphere (N_2) and the reducing atmosphere (10% H_2/N_2), which was conducted at Durham University, as shown in Figure 6-6. It can be observed that, for CC3 cage only, there was no significant mass decrease until the temperature reached ~400 °C under 10% H_2/N_2 atmosphere (initial mass loss of solvent and/or physisorbed water was excluded), and the mass loss above 400 °C can be attributed to the thermal decomposition of cages. For $Pd(NO_3)_2$@CC3 under N_2 atmosphere, its weight did not decrease significantly until 300 °C at which the decomposition started. On the other hand, for $Pd(NO_3)_2$@CC3 under 10% H_2/N_2 atmosphere, slow mass loss was seen to initiate at ~150 °C, and the material decomposed eventually at ~400 °C. This implied that the reduction of $Pd(NO_3)_2$ might start from 150 °C. Therefore, our collaborators at Durham University attempted to run the reduction of $Pd(NO_3)_2$@CC3 at several different temperatures above 150 °C, and they found that when the sample was reduced in 10% H_2/N_2 flow at 200 °C for 1 hour (5 °C min^{-1} during heating and cooling), $Pd(NO_3)_2$ could be effectively reduced to metallic nanoparticles. The resulted Pd nanoparticles can be potentially located both inside and between the CC3 cages as shown in Figure 6-5(e).
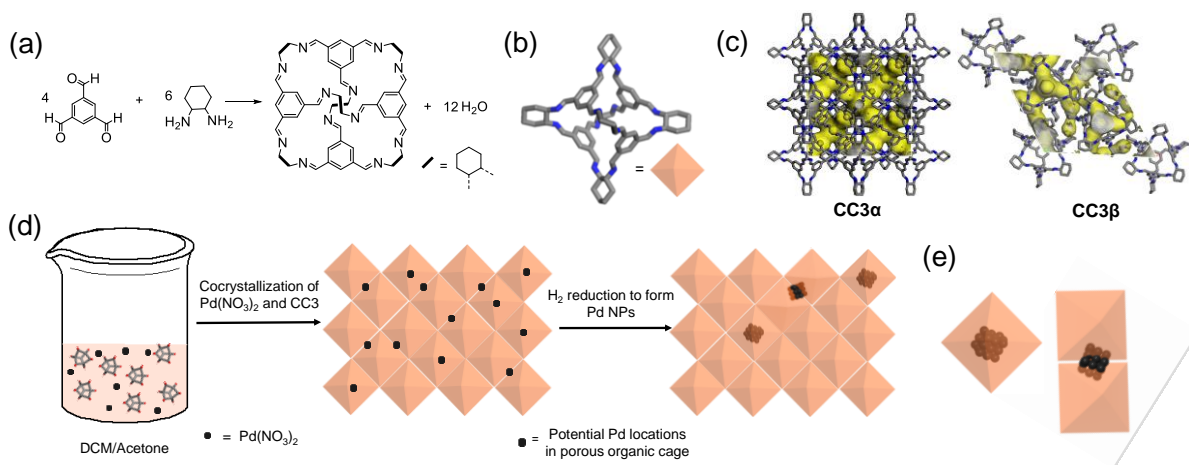
Figure 6- 5 Preparation of Pd@CC3. (a) Synthesis of CC3 through [4+6] cycloimination between 1, 3, 5-triformylbenzene and (1R, 2R)-1, 2-diaminocyclohexane. (b) Structure of the CC3 molecule. (c) Packing motifs of CC3 molecules and the pore connectivity. The yellow surfaces show the interconnected 3D pore structure for CC3α (left), and 2D layered pore structure for CC3β (right), respectively. (d) Steps to incorporate Pd into CC3 hence to form Pd@CC3. (e) Pd nanoparticles are potentially located either inside or between the cages.
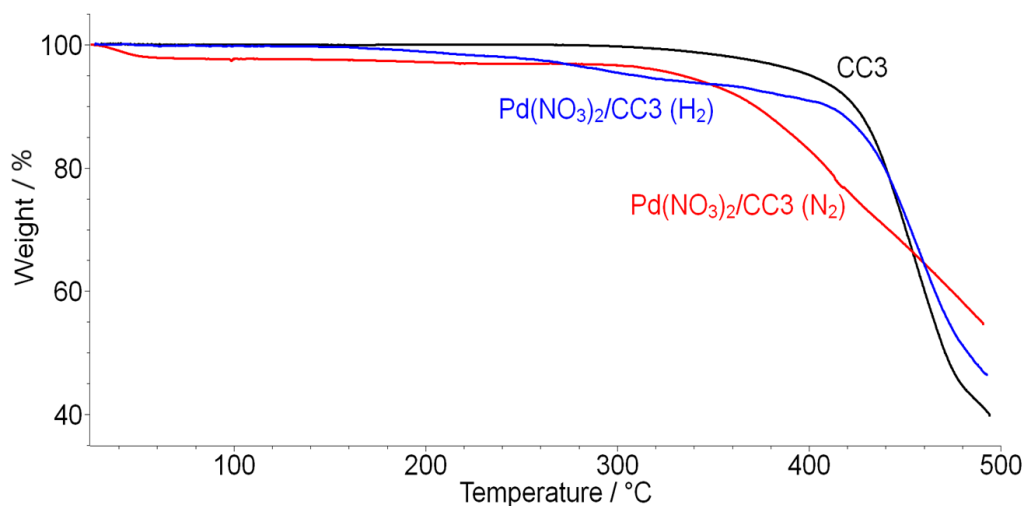
Figure 6- 6 TGA results for both CC3 and Pd(NO3)2@CC3 samples. Pd(NO3)2@CC3 was tested in both inert (N2) and reducing (10% H2/N2) atmospheres, while CC3 was only tested in 10% H2/N2 atmosphere as a reference.

6.3 Characterization of Pd@CC3

Prior to the catalytic experiments for Pd@CC3, the as-prepared sample was characterized to investigate the morphology of cage crystals and the distribution of metal nanoparticles (the characterization experiments were done by our collaborators at Durham University).

The SEM image in Figure 6-7 shows the morphology of the crystals formed by Pd@CC3 cages. It was found that discrete crystals (~15 μm diameter) were formed with an octahedral crystal morphology. It has been confirmed computationally and experimentally that the octahedron is the ideal crystal morphology for metal-free CC3 crystals [186, 199-201]. Here the octahedral crystal morphology was preserved, which indicated that the incorporation of 0.5 wt% Pd into the cage crystals did not affect their packing motif.
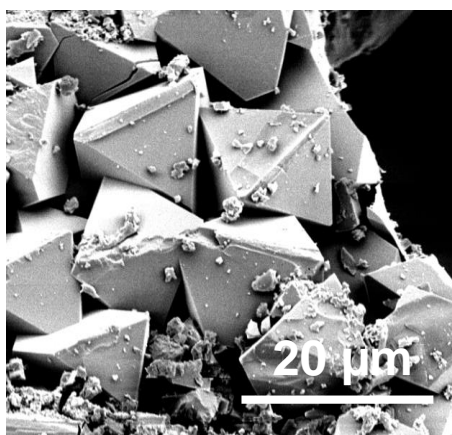
Figure 6- 7 SEM image of crystals of as-prepared Pd@CC3, showing the octahedral crystal morphology.

Also, both CC3 and Pd@CC3 samples were tested in gas sorption experiments. The N_2 sorption isotherms for both samples (Figure 6-8) indicate that the gas adsorption capacity of CC3 is slightly higher than that of Pd@CC3. The BET surface area for CC3 was found to be ~400 m^2 g^{-1}, and it was consistent with the BET surface area reported for CC3 sample (409 m^2 g^{-1}) in literature [198]. On the other hand, the BET surface area for Pd@CC3 was found to be ~350 m^2 g^{-1}, and the slightly lower BET surface area of Pd@CC3 as compared to CC3 might imply that some pores were blocked by Pd nanoparticles.
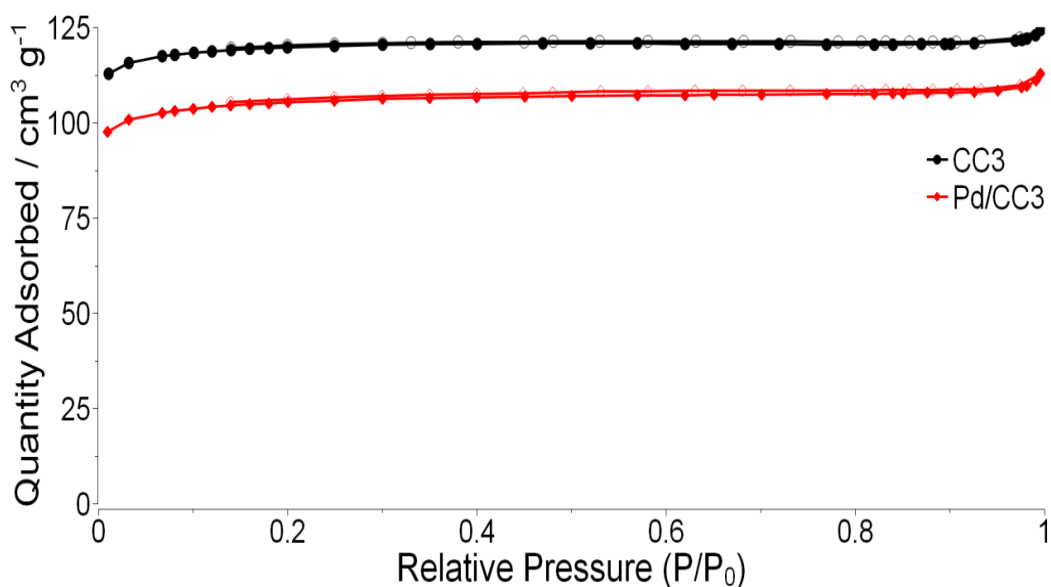
Figure 6- 8 N_2 sorption isotherms for CC3 and Pd@CC3 samples. Black plots and red plots represent CC3 and Pd@CC3, respectively. Solid circles and empty circles represent adsorption and desorption, respectively.

The Pd@CC3 sample after reduction at 200 °C was also scanned in STEM (shown in Figure 6-9) in order to visualise the Pd nanoparticles. It can be observed that small and near monodispersed Pd nanoparticles were embedded in the crystals of CC3. The corresponding size histogram showed a narrow particle size distribution of Pd nanoparticles and most particles are in the range between 1.0 and 2.0 nm with the average particle size being 1.6 ± 0.3 nm in diameter.
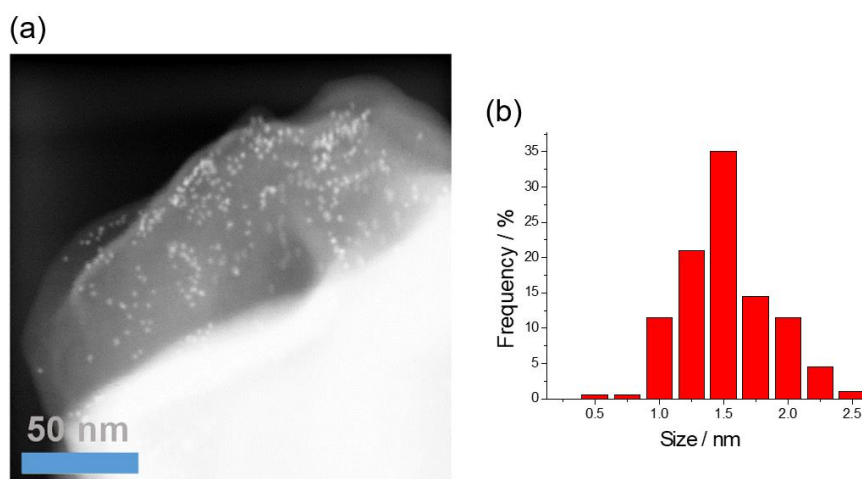
Figure 6- 9 (a) STEM image of Pd@CC3 sample showing the distribution of Pd nanoparticles and (b) its corresponding size histogram for Pd nanoparticles.

The results above indicate that discrete cage crystals were formed and Pd nanoparticles with controlled particle size and distribution were observed to disperse

in the cage crystals. Therefore, the preparation of Pd@CC3 was successful and this sample would be tested in CO oxidation reaction to evaluate its catalytic activity.

6.4 Investigation of catalytic activity of Pd@CC3

6.4.1 Pd@CC3 vs Pd/Al₂O₃

The Pd@CC3 sample was tested to evaluate its catalytic activity. Prior to the catalytic experiments, the temperature operating window for the sample should be determined, hence the TGA experiment of Pd@CC3 in air was conducted (by our collaborators at Durham University). From the TGA experiment in air (Figure 6-10), sharp weight decrease can be seen above the temperature of ~300 °C, which indicates that the cages were stable only up to ~300 °C in air and thermal decomposition of the cage material would happen when the temperature went above this limit. Therefore, the reaction temperature in the catalytic experiments must be monitored by the thermocouple and carefully controlled to prevent destroying the sample by overheating to above 300 °C (assuming that the sample and the gas phase are always thermally equilibrated).
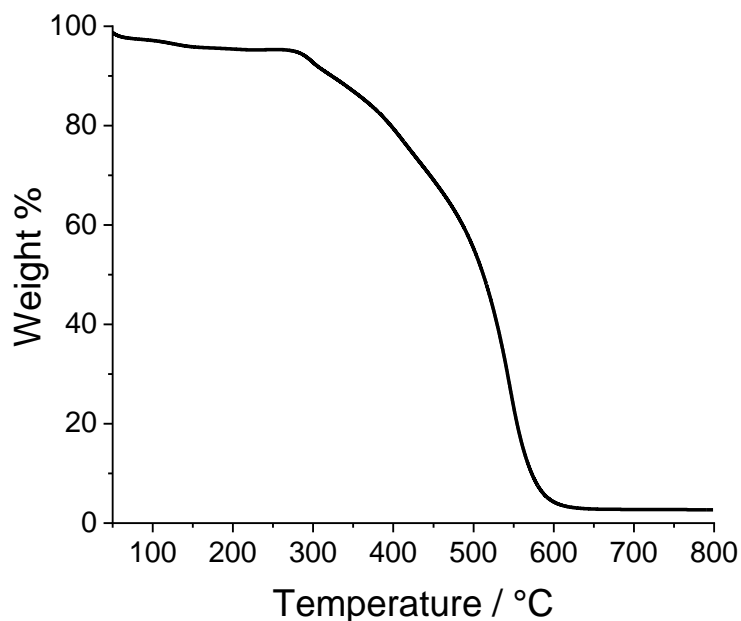
Figure 6- 10 TGA result of Pd@CC3 in air.

The 0.5 wt% Pd@CC3 sample (23 mg) was firstly tested in the light-off experiment of CO oxidation by using the stoichiometric conditions (P_{CO}=1.0 kPa, P_{O_2}=0.5 kPa and F_t=450 mL min⁻¹) as mentioned in Chapter 3. The commercial catalyst 1 wt% Pd/Al₂O₃

(26 mg) was also tested by using the same experimental conditions for comparison. Both samples were in the powder form but they had different nominal loadings of Pd, hence the CO_2 production rates (r_{CO_2}) were normalised with respect to the amount of Pd metal involved in the tests. The results of light-off experiments for both 0.5 wt% Pd@CC3 and 1 wt% Pd/Al_2O_3 samples in terms of r_{CO_2} and CO conversion are presented in Figure 6-11. It was found that the Pd/Al_2O_3 sample started to produce minimum measurable CO_2 (1 ppm, which corresponds to CO_2 production rate of 3 x 10^{-10} mol s^{-1}) at 151 °C, and it achieved 5% and 50% CO conversion at around 205 °C and 210 °C, respectively. However, the catalytic activity shown by the Pd@CC3 sample was much lower as compared with Pd/Al_2O_3, where minimum CO_2 production was measured at 200 °C and the highest CO conversion achieved was still below 1% within the given temperature range (<240 °C).
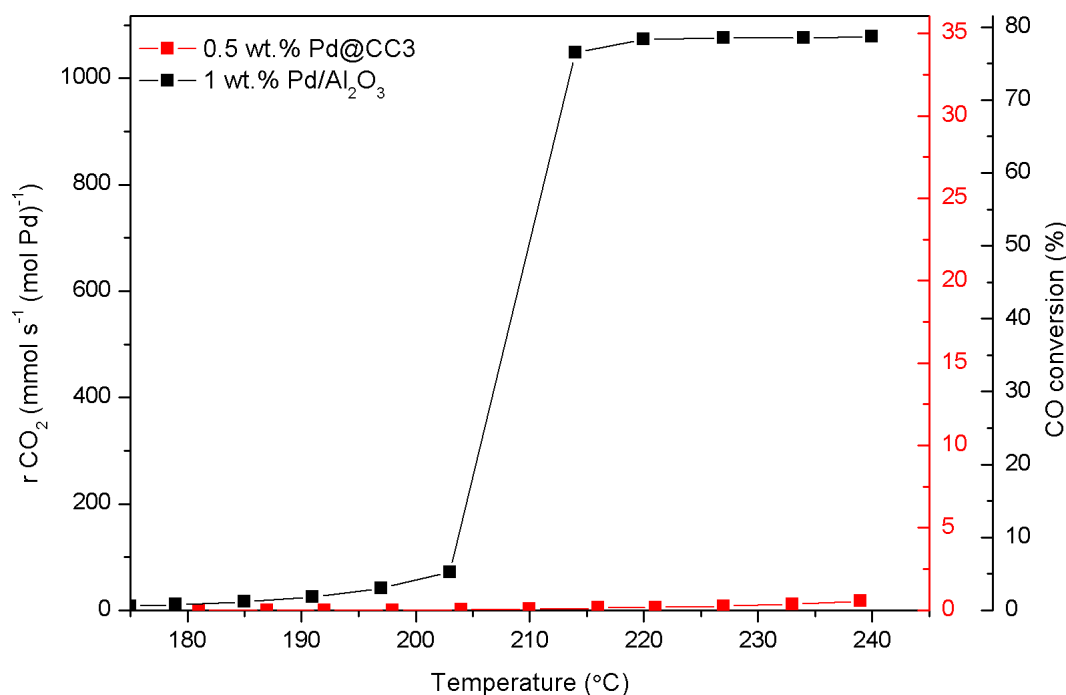
Figure 6- 11 Light-off experiments over 0.5 wt% Pd@CC3 and commercial 1 wt% Pd/Al_2O_3 catalyst in CO oxidation reaction under conditions of P_{CO}=1.0 kPa, P_{O_2}=0.5 kPa and F_t=450 mL min^{-1}. The CO_2 production rates are normalised with respect to the amount of Pd metal. Two Y axes on the right of the graph show CO conversion for the two samples, which are labelled in the same colours as the corresponding samples.

To investigate the difference in the catalytic activity between the Pd@CC3 and the Pd/Al_2O_3 samples, Arrhenius plots (in low temperature regime under differential conditions) for both samples (Figure 6-12) were generated. It was calculated that the activation energy of CO oxidation over 0.5 wt% Pd@CC3 was 139 kJ mol^{-1} and it was

almost the same as the one obtained for 1 wt% Pd/Al_2O_3 sample (135 kJ mol^{-1}). The similar activation energy could indicate the same active sites in these two catalysts, but the much lower activity exhibited by Pd@CC3 might imply that many active sites are inaccessible in its system. The Pd particle size in Pd@CC3 (~1.6 nm) was even smaller than that in commercial Pd/Al_2O_3 (~2.5 nm, as mentioned in Chapter 4), but the particles in Pd@CC3 are enclosed by rigid frameworks of cages, so the access to some sites on these particles might be hindered by cage structures, which could probably result in the low activity.
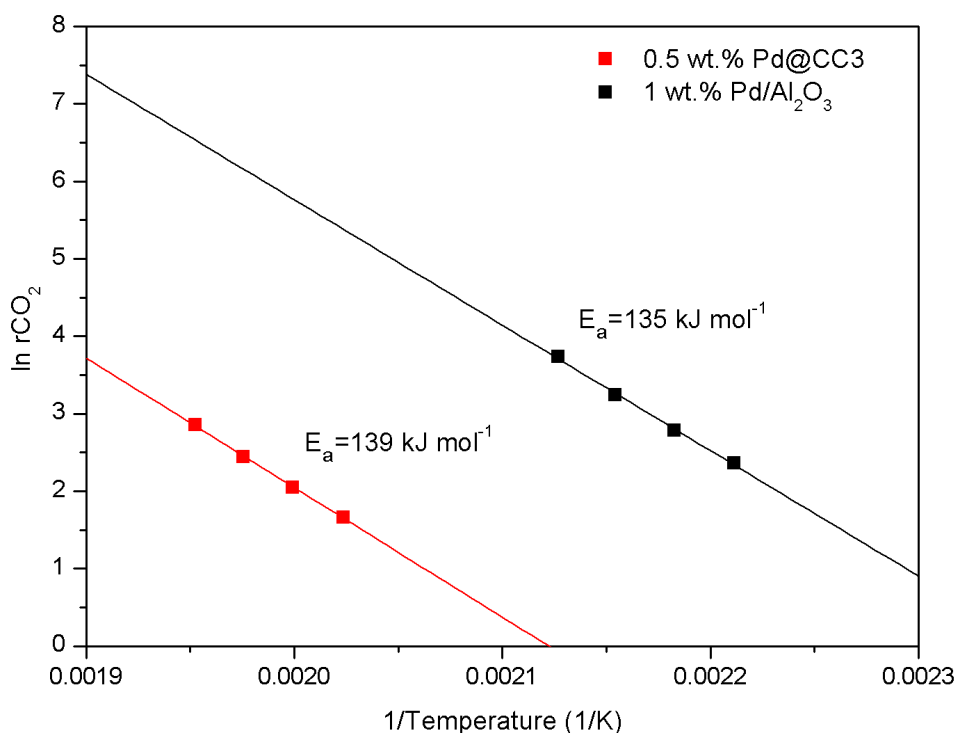
Figure 6- 12 Arrhenius plots for CO oxidation over 0.5 wt% Pd@CC3 and commercial 1 wt% Pd/Al_2O_3 catalyst, respectively, under the reaction conditions of P_{CO}=1.0 kPa, P_{O_2}=0.5 kPa and F_t=450 mL min^{-1}.

Moreover, to investigate if there were any mass transfer effects along the reactor, the same Pd@CC3 sample was tested in another light-off experiment by using the same P_{CO} and P_{O_2} (1.0 and 0.5 kPa, respectively) but a different total flow rate (150 mL min^{-1}). By comparing two light-off experiments of Pd@CC3 sample using different total flow rates (Figure 6-13), it was found that the CO_2 production rates obtained in the two experiments were very close and the ratio between the CO conversion values in the two experiments was close to 3:1 whilst the ratio between the total flow rates was 1:3. This implies that there was no significant mass transfer effect along the reactor.
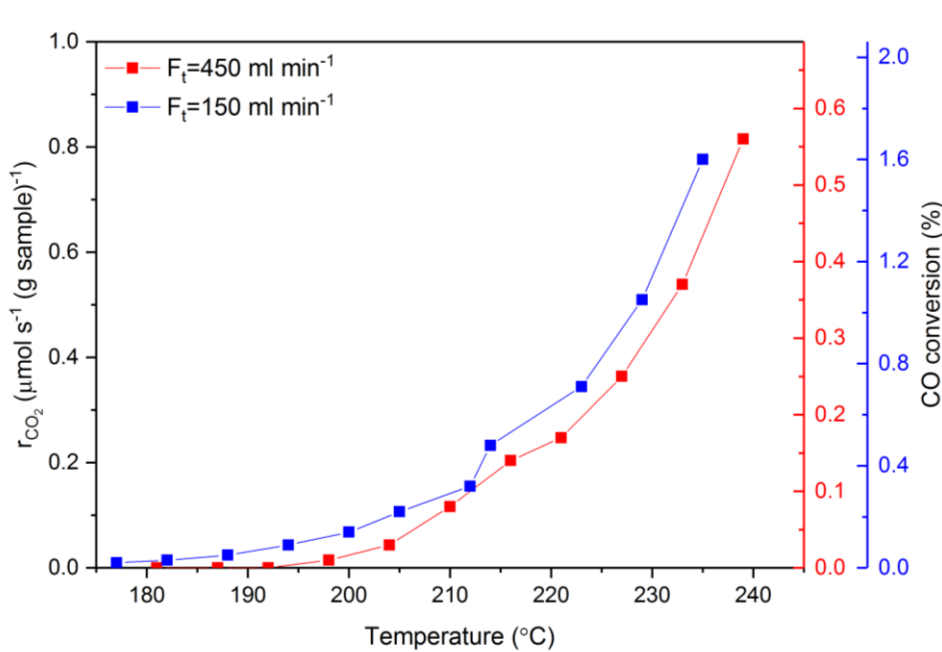
Figure 6- 13 Light-off experiments over 0.5 wt% Pd@CC3 sample in CO oxidation reaction by using P_{CO}=1.0 kPa, P_{O_2}=0.5 kPa and two different total flow rates of 450 mL min⁻¹ and 150 mL min⁻¹, respectively. The CO_2 production rates are normalised with respect to the mass of sample. Two Y axes on the right of the graph show CO conversion in these two experiments, which are labelled in the same colours as the corresponding flow rates.

Therefore, the catalytic results shown above indicate that the activity of Pd@CC3 was much lower as compared with the conventional Pd/Al₂O₃, which might be ascribed to the limited accessibility of active sites on Pd nanoparticles when they were enclosed in POC crystals.

6.4.2 Catalytic activity of Pd@CC3

The effect of O_2 partial pressure on the CO_2 production rate over the Pd@CC3 sample was investigated, and this experiment will be referred to as O_2 kinetics (as explained in Chapter 3). In O_2 kinetics experiment the CO partial pressure and reaction temperature were kept constant while the partial pressure of O_2 was varied. Therefore, the O_2 kinetics experiment was conducted by using the conditions of P_{CO}=1.0 kPa, F_t=80 mL min⁻¹ and reaction temperature of 200 °C, with P_{O_2} varying from 0.5 to 7.5 kPa (increase by 0.5 kPa intervals). The reaction temperature of 200 °C was selected, because this is the temperature at which the reaction was seen to initiate from the light-off experiment shown above and it was away from the decomposition temperature of the sample (~300 °C). More importantly, this low temperature could allow the reaction to occur under differential conditions (low conversion, <20%) hence making the kinetic

data more reliable. The CO_2 production rate as a function of O_2 partial pressure over the Pd@CC3 sample can be found in Figure 6-14(a), and it indicates that the r_{CO_2} hence the CO conversion initially increased with the O_2 partial pressure, but when O_2 partial pressure increased above ~6 kPa the r_{CO_2} didn't rise further and showed a plateau. In order to determine the effect of O_2 partial pressure (reaction order), the kinetic relation between the CO_2 production rate and the partial pressures of reactants can be expressed as shown below by assuming that the power rate law applies:

$$r_{CO_2} = k \, P_{CO}{}^m \, P_{O_2}{}^n$$
Equation 6-1

where k is the rate constant; m and n are the apparent reaction orders for CO and O_2, respectively. By simply transforming the equation, the reaction order of O_2 can be determined by finding the slope of the plot of $\ln r_{CO_2}$ against $\ln P_{O_2}$, as shown in Figure 6-14(b). As it was discussed in Chapter 4 that according to L-H reaction mechanism, CO and O_2 need to competitively adsorb onto the catalyst surface and higher O_2 partial pressure can promote the formation of the active oxygen covered surfaces, therefore the reaction orders for O_2 shown in Figure 6-14(b) were generally positive. When P_{O_2} increased to ~6 kPa, a saturation condition was reached where CO_2 production rate did not increase any further with P_{O_2}, so the reaction order for O_2 became almost zero.
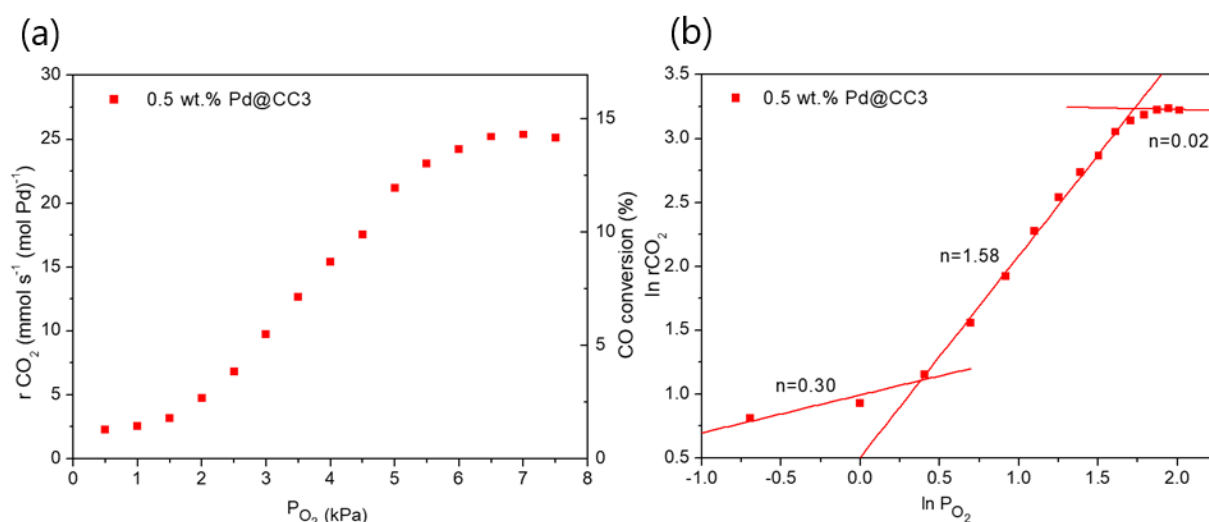
Figure 6- 14 (a) O_2 kinetics experiment over the 0.5 wt% Pd@CC3 sample in CO oxidation reaction by using P_{CO}=1.0 kPa, F_t=80 mL min^{-1} and reaction temperature of 200 °C with P_{O_2} varying from 0.5 to 7.5 kPa. (b) Determination of the reaction order for O_2 based on the kinetic results from (a).

From the O_2 kinetics experiment, it was found that the r_{CO_2} is highly dependent on the O_2 partial pressure. Therefore, new reaction conditions of P_{CO}=3.0 kPa, P_{O_2}=15.0 kPa

and F_t=60 mL min^{-1} were selected for the light-off experiment, which could make the Pd@CC3 sample to show better performance in the CO oxidation reaction. Despite changing the reaction conditions, they were still of interest as similar CO/O_2 ratios are frequently reported in other studies of Pd-based catalysts in literature and could allow for better comparison. The light-off experiment of the Pd@CC3 sample by using the new reaction conditions can be found in Figure 6-15. The reaction catalysed by Pd@CC3 achieved the CO_2 production rate of 23.8 mmol s^{-1} (mol Pd)$^{-1}$ (equivalent 6.3% CO conversion) at 200 °C, which was much higher as compared to the results of the previous light-off experiments under stoichiometric gas conditions (<1% CO conversion). Moreover, the r_{CO_2} reported for other similar Pd-based catalysts in literature are also shown in Figure 6-15 for comparison (in low temperature regime and with CO conversion lower than 20%), and the details of these catalysts (including the experimental conditions under which the data were collected) can be found in Table 6-1. It is clear that the catalytic activity of Pd@CC3 is broadly comparable to other Pd-based catalysts reported in literature (normalised to the amount of Pd), and Pd@CC3 even exhibited higher activity than those catalysts employing other organic supports. Also, to demonstrate the thermal stability of the Pd@CC3 system, the light-off experiment was repeated for several cycles over the same Pd@CC3 sample (Figure 6-16). No significant change of catalytic activity was observed, which indicates that Pd@CC3 catalyst was thermally stable in the temperature regime <200 °C, and it was also consistent with the results of TGA in air (Figure 6-10) which showed that the sample was stable up to ~300 °C.
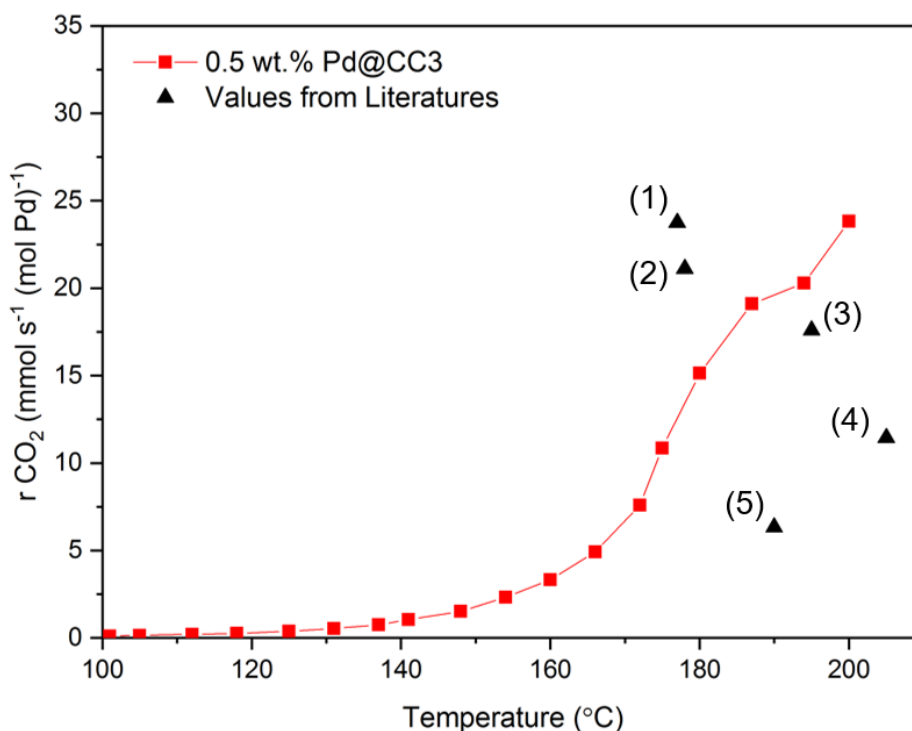
Figure 6- 15 Light-off experiment over the 0.5 wt% Pd@CC3 sample in CO oxidation reaction under conditions of P_{CO}=3.0 kPa, P_{O_2}=15.0 kPa and F_t=60 mL min^{-1}. The CO_2 production rates are normalised with respect to the amount of Pd metal. CO_2 production rates obtained from other Pd-based catalysts reported in literature were also marked in the graph for comparison, and all these values were obtained under conditions where CO conversion was lower than 20%. Samples from the literature are: (1) 2 wt% Pd/ZnO [202]; (2) 3 wt% Pd/Ce-based MOF [203]; (3) 0.9 wt% Pd/triptycene-based microporous polymer [204]; (4) 3.6 wt% Pd/Ni-based MOF [205]; (5) 1 wt% Pd/Cu-based MOF [206].

Table 6- 1 Comparison of activity of 0.5 wt% Pd@CC3 with other Pd-based catalysts in the literature for CO oxidation reaction.

Sample	% Pd[a]	m_{cat}[b] (mg)	F_t (ml min^{-1})	P_{CO} (kPa)	P_{O_2} (kPa)	T_{ref}[c] (°C)	X_{CO}[d] (%)	r_{CO_2} (mmol s^{-1} (mol Pd)$^{-1}$)
Pd/ZnO [202]	2	20	100	4	20	177	3	23.8
Pd/Ce-based MOF [203]	3	25	100	4	20	178	5	21.1
Pd/triptycene polymer [204]	0.9	50	50	1	21	195	20	17.6
Pd/Ni-based MOF [205]	3.6	60	52	3	8.5	205	20	11.4
Pd/Cu-based MOF [206]	1	50	20	1	20	190	20	6.3
Pd@CC3 (this work)	0.5	71.5	60	3	15	200	6.1	23.8

[a] Pd loading on the catalyst. [b] Mass of catalyst used in experiment. [c] Temperature of reference, at which the CO conversion and CO_2 production rate in the table were obtained. [d] CO conversion.
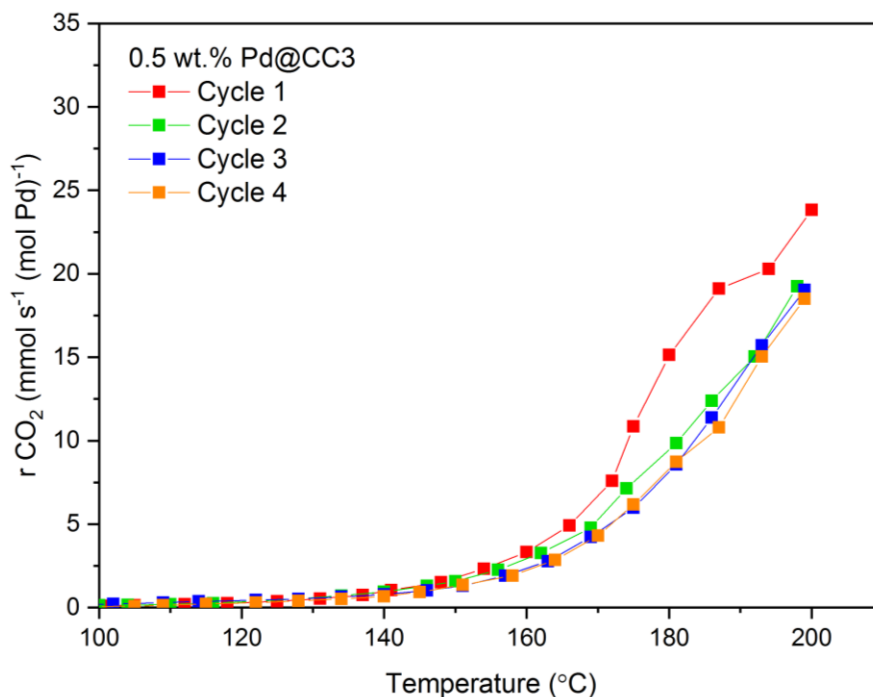
Figure 6- 16 Repeating the light-off experiments over the 0.5 wt% Pd@CC3 sample in CO oxidation reaction (4 cycles in total), under conditions of P_{CO}=3.0 kPa, P_{O_2}=15.0 kPa and F_t=60 mL min^{-1}.

6.5 Conclusions

In this chapter, noble metal nanoparticles were stabilized through encapsulation in POCs crystals, and the results indicated:

- Uniform and small (~1.6 nm) Pd nanoparticles could be dispersed in the CC3 crystals.

- The resulted catalyst could stay stable (with no activity change) under the given reaction conditions below ~250 °C.

- The POCs stabilized Pd catalyst was much less active than the state-of-the-art Pd catalyst, despite that its activity was comparable with some other Pd-based catalysts reported in literature.

- The low catalytic activity might be due to the limited accessibility of active sites in POCs crystals.

The results above indicate that, although the noble metal nanoparticles could be stabilized via encapsulation in POCs, their activity was heavily compromised. This highlights the balance between the confinement for metal nanoparticles and the accessibility of these nanoparticles, which can lead to good stability and activity at the

same time. Additionally, the POCs support would decompose at temperatures above 300 °C, which limits the resulted catalysts in high temperature applications such as automotive exhaust control, hence the stability of the support itself is very important as well. Therefore, in the next chapter, a more stable ceramic support (perovskite) is used and metal nanoparticles are partially embedded in the support via redox exsolution, which can result in both enhanced stability and activity.

Chapter 7: Towards stabilization and high activity of noble metal nanoparticles via exsolution

The previous chapter demonstrated that full encapsulation of metal nanoparticles would compromise the catalytic activity. Therefore, an alternative system will be introduced in this chapter, in which the metal nanoparticles are grown (exsolved) directly from the perovskite host and are partially embedded (socketed) in the perovskite. Due to the strained nature of exsolved metal nanoparticles, they demonstrate excellent stability and activity.

The in-situ experiments on the Ni-based perovskites in environmental TEM provided insight into the exsolution process, revealing the mechanisms of the socket formation, metal particle nucleation and growth. The socket was observed to form because of the rise of perovskite lattice around metal particles during the particle growth period. Moreover, the growth of metal particles was likely to be limited by the availability of exsolvable ions near perovskite surface, which indicated the importance to reduce the grain size of perovskites for later studies when noble metal was attempted to be exsolved from dilute compositions.

The mechanistic insight obtained was used to design the material that allowed for the exsolution of a noble metal (Rh) from a dilute substituted system. Particle characteristics of exsolved Rh could be controlled by different parameters, and the correlations between particle characteristics and catalytic activity were also investigated. Despite the limited extent of exsolution, exsolved Rh catalyst still showed promising activity in CO oxidation as compared with the state-of-the-art Rh catalyst, indicating enhanced activity probably due to the strained nature of exsolved particles.

7.1 Introduction to the metal exsolution from A-site deficient perovskites

7.1.1 Stoichiometric perovskite

The perovskite-type materials were originated from a mineral with the formula of $CaTiO_3$ which was firstly discovered by Gustav Rose, and it was named after the Russian mineralogist Lev Perovski [207]. Having been extensively studied for decades, perovskite-type materials have developed into a big range of compositions sharing a common formula of ABO_3, where the A-sites can be occupied by alkali (e.g., Na, K), alkaline earth (e.g., Ca, Sr) or lanthanide (e.g., La, Ce) cations, and the B-sites are occupied by smaller cations such as transition metal cations. The ideal structure of a stoichiometric perovskite is shown in Figure 7-1 (exhibited by $SrTiO_3$) [208]. It can be visualized as a cubic structure in Figure 7-1(a), where the twelve-fold A-site cation and the six-fold B-site cations occupy the center and the corners of the cubic cell, respectively, while oxygen anions lie at the midpoint of the edges of the cube. Alternatively, the perovskite structure can also be visualized in another way as shown in Figure 7-1(b), where the B-site cations are located in the corner-sharing oxygen octahedra (TiO_6), while the A-site cation is situated at the center of the cuboctahedral cavity formed by eight BO_6 octahedra. The geometric relationship between the radii of different ions in the unit cell of an ideal perovskite can be found from Figure 7-1(a) as:

$$r_A + r_O = \sqrt{2}(r_B + r_O) \qquad \text{Equation 7-1}$$

where r_A, r_B and r_O are the ionic radii of A-site, B-site and oxygen ions, respectively. However, perovskites can still be formed if the equation above is not strictly satisfied. The tolerance factor (tf) was introduced by Goldschmidt [209] to describe the geometric relationship of ionic radii for a common perovskite:

$$tf = \frac{r_A + r_O}{\sqrt{2}(r_B + r_O)} \qquad \text{Equation 7-2}$$

The ideal perovskite structure is generally formed when $tf \approx 1$, while the perovskite structure can still remain stable when $0.8 \leq tf \leq 1$ in spite of some lattice distortion resulted by the tilting of BO_6 octahedra and lowering of symmetry [207, 210]. Nevertheless, $tf > 1$ means that the A-site cations are too big and hence the formation of the perovskite structure might be hindered, whereas when $tf < 0.8$, alternative structures might be formed because the A-site cations are too small to fit the perovskite structure [210]. Therefore, the structure of perovskite has some level of flexibility according to the Goldschmidt tolerance factor, which allows for the accommodation of almost 90% of the metal species from the periodic table of elements in the perovskite

lattice [211]. Moreover, the original A-site and/or B-site cations in perovskite lattice can be partially substituted with a small amount of other metallic elements, to generate new perovskites with the formula of $A_{1-x}A'_xB_{1-y}B'_yO_3$ [212-216]. The partial substitution can lead to the changes of the oxidation state of metallic cations and even the vacancies (non-stoichiometry) on A-, B- or oxygen sites according to the electroneutrality principle [217, 218]. Therefore, the design of perovskite-type materials is convenient and a wide diversity of perovskites have been investigated in areas such as heterogeneous catalysis and material science.
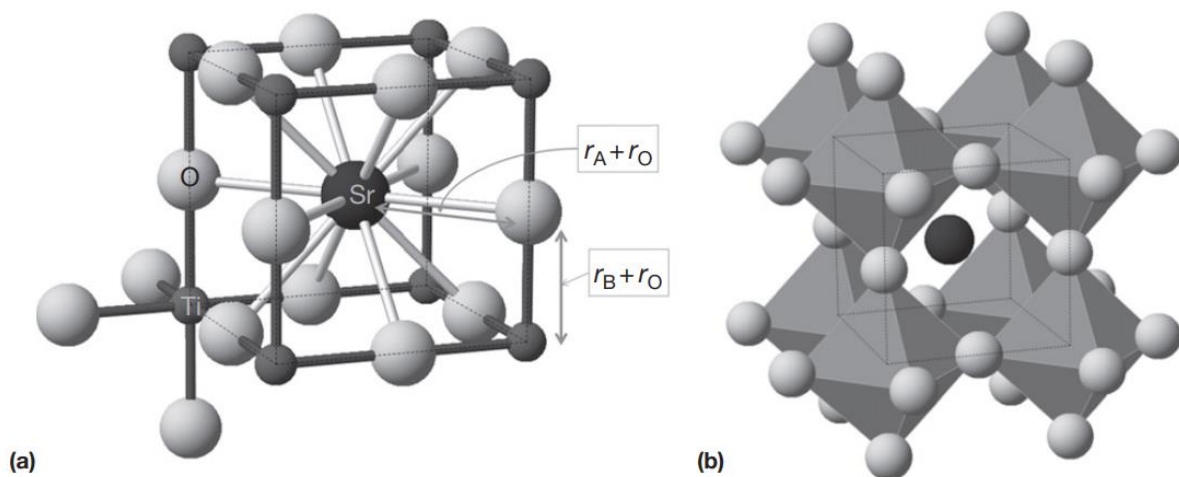
Figure 7- 1 Ideal structure of perovskites (exhibited by $SrTiO_3$), viewed by: (a) focusing on the unit cell and the coordination number of cations; (b) emphasizing the corner-sharing BO_6 octahedra. [208]

7.1.2 Nonstoichiometry in perovskites

As mentioned above, a perovskite is able to accommodate some defects in its structure, and the type and concentration of the defects can be controlled by doping/substituting the original cations in the perovskite with other cations exhibiting similar size but different oxidation states. Because of the electroneutrality principle, the increase or decrease of the charge in the perovskite structure induced by cation substitution must be compensated and there are several possible mechanisms of charge compensation as summarized in Figure 7-2. In Figure 7-2, nonstoichiometric perovskites deviated from the ideal perovskite ABO_3 are presented, as well as the specific examples originated from the archetype perovskite $SrTiO_3$ through the cation substitutions. Theoretically, the nonstoichiometry can exist individually or simultaneously on all the A-, B- and oxygen sites. Nevertheless, because of the strong interactions between the B- and oxygen ions in the corner-sharing BO_6 octahedra as shown in Figure 7-1(b),

the nonstoichiometry on B-sites is energetically more difficult to happen as compared with the other two sites [219]. Therefore, the cations on the B-sites are usually stoichiometric, despite some exceptions of B-site deficient compositions such as a series of hexagonal $A_nB_{n-1}O_{3n}$ perovskites [220, 221]. On the other hand, there is a variety of perovskites with different combinations of nonstoichiometry on the A- and/or oxygen sites. Depending on the nature of the nonstoichiometry, the perovskites can be generally classified into two types which are super-stoichiometric (or excess) and sub-stoichiometric (or deficient) perovskites, as shown in Figure 7-2.

Different nonstoichiometric perovskites can be exemplified based on deviations from $SrTiO_3$. In stoichiometric $SrTiO_3$, the oxidation states of Sr and Ti cations are +2 and +4, respectively. If some Sr^{2+} cations are substituted by trivalent cations like La^{3+}, the resulted excess charge can be compensated in different ways [208]. Firstly, extra oxygen ions can be incorporated into the structure, hence the perovskite formula becomes $La_xSr_{1-x}TiO_{3+x/2}$ (namely oxygen excess stoichiometry). Secondly, the formation of vacancies on the A-sites is also possible, which changes the perovskite formula into $La_xSr_{1-3x/2}TiO_3$ (A-site deficient stoichiometry). Alternatively, the oxidation state of the B-site cations can be partially decreased if the lowered oxidation state can be stabilized, and for instance, perovskites with formula of $La_xSr_{1-x}Ti_x^{3+}Ti_{1-x}^{4+}O_3$ can be prepared under reducing conditions. If the cation substitution takes place on the B-sites and, for instance, if some Ti^{4+} are substituted by foreign cations M^{m+} ($m \neq 4$), the perovskite with nonstoichiometric oxygen sites ($SrM_xTi_{1-x}O_{3-(4-m)(x/2)}$) can be generated: oxygen vacancies will be formed if $m<4$; inversely oxygen interstitials will be formed if $m>4$. Moreover, if the cation substitution takes place on both A- and B-sites, perovskites with vacancies on both A- and oxygen sites ($La_xSr_{1-3x/2}M_yTi_{1-y}O_{3-(4-m)(y/2)}$) may be generated, which is dependent on the nature of M and the concentration of overall vacancies. On the other hand, the charge compensation could also be achieved between A- and B-sites, which gives rise to the perovskites with deficient A-sites but stoichiometric oxygen sites ($La_{0.4+(4-m)x}Sr_{0.4-(4-m)x}M_xTi_{1-x}O_3$). Besides, when perovskites are treated in reducing atmospheres (such as in H_2) to a high temperature (normally above 900 °C), the oxygen ions in perovskites are allowed to migrate and might be stripped out of the structure, which leaves oxygen vacancies and some electrons as shown [208]:

$$2Ti_{Ti}^x + O_O^x \leftrightarrow 2Ti_{Ti}' + V_O^{\bullet\bullet} + \frac{1}{2}O_2 \qquad \text{Equation 7-3}$$
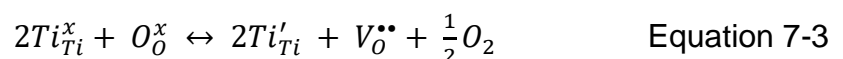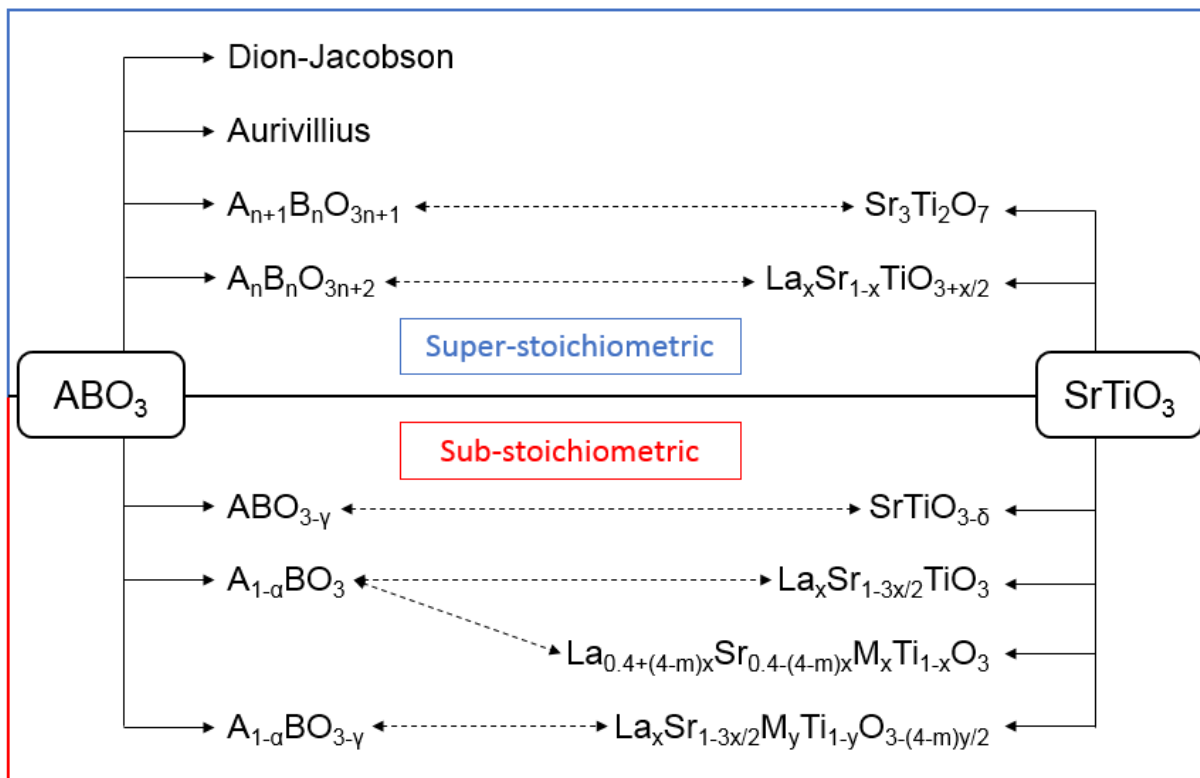
Figure 7- 2 Different types of perovskite nonstoichiometry and some corresponding examples derived from $SrTiO_3$. This figure was modified from Neagu et al. [208].

Perovskites accommodating different types of nonstoichiometry will show distinct behaviors for the metal exsolution that is the topic studied in this chapter. The concept of metal exsolution and the effects of perovskite nonstoichiometry will be introduced below.

7.1.3 Self-regeneration of metals from perovskites

The potential of perovskites in catalysis has been extensively investigated for various applications such as water-gas shift, fuel cells and automotive exhaust purification [222-225], due to the high thermal stability and good activity for oxidation reactions of perovskites. More importantly, the flexible composition, partial substitution of A- and B-site cations, and even the nonstoichiometry of lattice as discussed above, provide multiple possibilities to tailor the properties of perovskites and hence to change their catalytic activity [207, 226]. It is generally agreed that catalytic activity of perovskite is mainly dependent on the transition metals on the B-sites [207, 227], as shown in Figure 7-3. On the other hand, the A-site cations might influence the perovskite activity more indirectly. Hence, the focus of the research of perovskite catalysts stayed on the selection of B-site cations [207, 228-230]. For instance, since Libby reported the

potential of the perovskite $LaCoO_3$ for automotive exhaust purification in 1971 [231], perovskites substituted with other transition metals such as Mn, Fe and Ru have also been investigated and they showed appealing performance in reactions like CO oxidation and NO_x reduction [232-235].
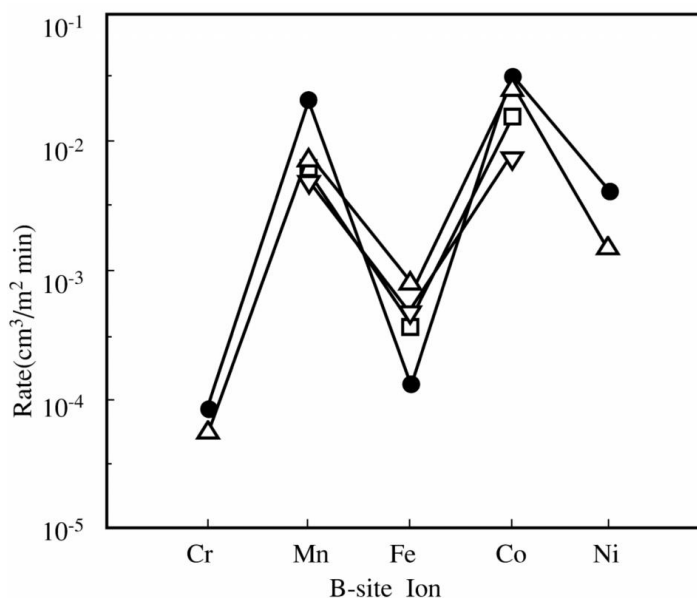
Figure 7- 3 Effects of B-site cations on the catalytic activity of perovskites in the reaction of propane oxidation at 227 °C. ●-oxides of B-site metals; △-$LaBO_3$; □-$SmBO_3$; ▽-$GdBO_3$. [207]

However, the "self-regeneration" phenomenon of metals from perovskites reported by Nishihate et al. in 2002 led the research of perovskite-based catalysts to a new direction [236]. It was reported that, for perovskite $LaFe_{0.57}Co_{0.38}Pd_{0.05}O_3$, Pd substituted on the B-sites was able to reversibly dissolve into and segregate from the perovskite structure as the response to the reactant composition that fluctuates between oxidizing and reducing conditions, respectively. They called this kind of perovskites that allow for the metal self-regeneration as "intelligent" catalysts, and it was found that they had higher thermal stability as compared to traditional Al_2O_3 supported catalysts, which was attributed to the suppressed agglomeration tendency of metal particles due to the reversible movements of metal into and out of the perovskite [236]. Apart from the higher thermal stability, Tanaka et al. also reported that intelligent perovskites containing Pd had higher catalytic activity as compared with Pd/Al_2O_3 containing the same amount of Pd as that in perovskites, hence the intelligent perovskites can reduce the use of noble metals in catalysts [237]. They also found that the self-regenerative property could be extended from Pd to other noble metals such as Pt and Rh, and the resulted catalysts were regarded as promising candidates for

the application of automotive exhaust purification [238, 239]. Nevertheless, the observations from Katz et al. towards the metal diffusion into and out of perovskite were different from the conclusions of Nishihata et al. [240, 241]. They found that the formation of Pd particles on the perovskite surface upon reduction was quite limited that only a very small fraction of Pd which initially sits a few nanometers within the perovskite can segregate out of the surface and form particles [240], while most of the noble metals remain within the bulk phase of parent perovskites [241]. Besides, instead of dissolving back into the perovskite lattice upon oxidation, the metal particles formed on the perovskite surface were found to react with the oxide support and only sink slightly into the support [240].

Not only that, in the earlier stage of this research, only the perovskites with the stoichiometric compositions were studied, and only a few metal cations (such as Ni^{2+}, Pd^{4+}, Rh^{4+} and Ru^{2+}) were found to be able to diffuse out of the perovskite to form metal particles [239, 242, 243], because this process was thought to be mainly determined by the reducibility of the metals. Moreover, the formation of the active metal clusters was found to occur mainly in the bulk phase of the perovskite [240, 241], which is a big disadvantage for heterogeneous catalysis as the most of metal clusters cannot be accessed by reactants. Because of the limited formation of metal particles on the material surface as discussed above, the self-regeneration technique in catalysis had not made big breakthroughs for long time.

7.1.4 Metal exsolution from A-site deficient perovskites

In the past few years, the in-situ growth of metal nanoparticles from perovskite supports has become a hot topic again, thanks to the works from John Irvine's group at St Andrews University. They proposed the concept of exsolution, in which the catalytically active metals are substituted on the B-sites in perovskite lattice under oxidizing conditions during synthesis and then these metals can be partly segregated from the perovskite to form metal nanoparticles upon reduction [244, 245]. Unlike the self-regeneration phenomenon mentioned before, the exsolution is irreversible and the exsolved metal nanoparticles will not re-dissolve into the perovskite host under oxidizing conditions. More importantly, Neagu et al. have done comprehensive investigations of the B-site exsolution from perovskite and the parameters controlling the exsolution process, and they reported that nonstoichiometry of the perovskite has significant effects on exsolution [26, 245]. They found that abundant Ni nanoparticles

could be exsolved on the surface of the A-site-deficient perovskite (Figure 7-4(b)) while no particle was observed on the oxygen-excess perovskite (Figure 7-4(a)), in spite of the same amount of Ni in both perovskites and the same reduction conditions. Besides, Neagu et al. also reported that some metals which are normally thought to be insufficiently reducible could also be exsolved from perovskites by controlling the A-site deficiency [245]. Therefore, the A-site deficiency in the perovskite seems to be a very important driving force to promote the exsolution of B-site species.
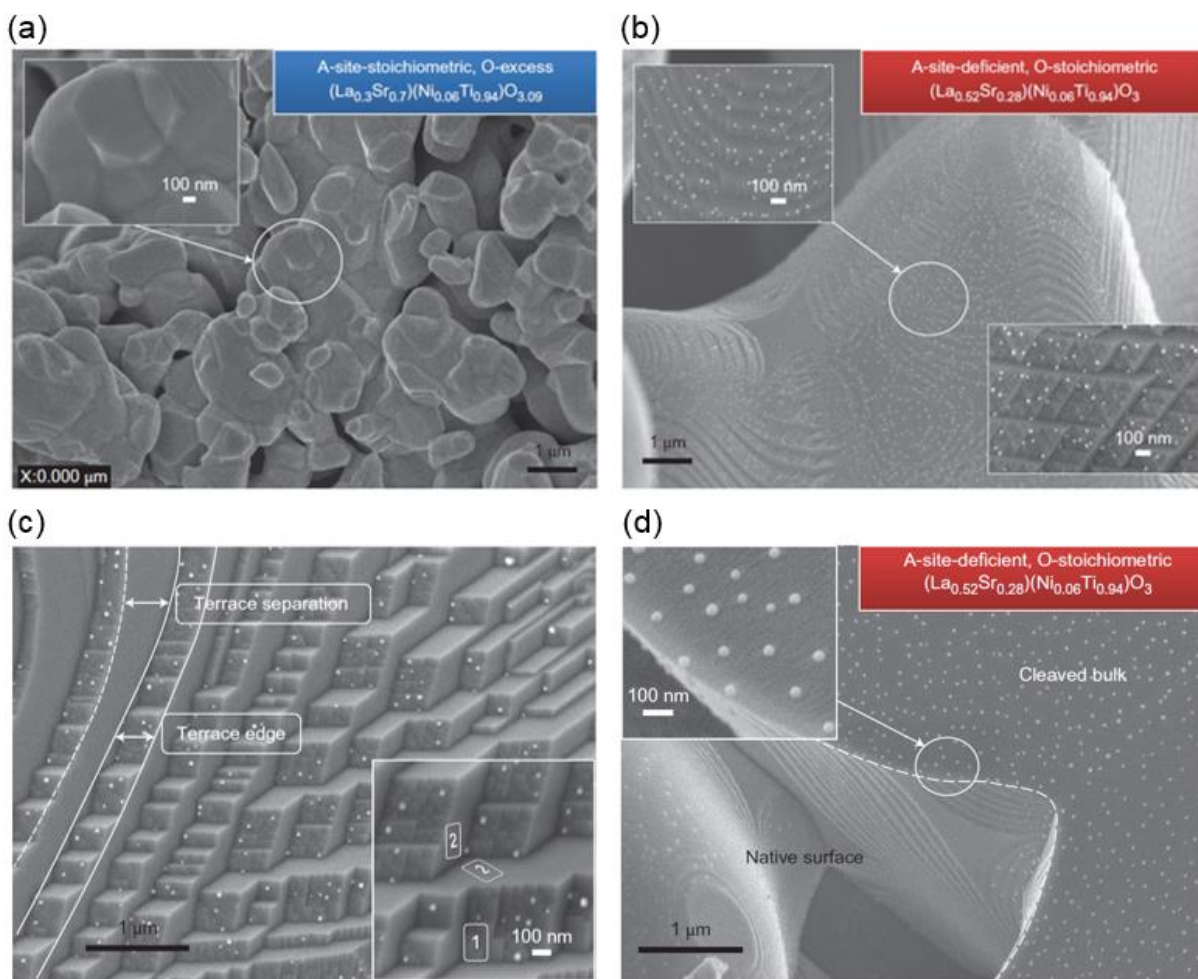
Figure 7- 4 Effects of perovskite nonstoichiometry and surface properties on exsolution. (a) A-site-stoichiometric, oxygen-excess perovskite ($La_{0.3}Sr_{0.7}Ni_{0.06}Ti_{0.94}O_{3.09}$) shows no metal exsolved after being reduced in 5% H_2/Ar at 930 ˚C for 20 h. (b) A-site-deficient, oxygen-stoichiometric perovskite ($La_{0.52}Sr_{0.28}Ni_{0.06}Ti_{0.94}O_3$) is decorated with a lot of exsolved nanoparticles on the surface after being reduced under the same conditions as in (a). (c) The native surface of perovskite ($La_{0.4}Sr_{0.4}Ni_xTi_{1-x}O_{3-y}$) shows a terraced morphology with nanoparticles preferentially exsolved on the edge of terraces. (d) Abundant and uniformly distributed metal nanoparticles are exsolved on the bulk surface of A-site-deficient perovskite ($La_{0.52}Sr_{0.28}Ni_{0.06}Ti_{0.94}O_3$). [245]

For an A-site-deficient perovskite $A_{1-\alpha}BO_3$, oxygen vacancies can also be generated upon reduction and hence the perovskite lattice becomes unstable to hold vacancies on two of its three primitive sites. Eventually the spontaneous B-site exsolution would happen when the concentration of oxygen vacancies is built up to a sufficiently high level (δ_{lim}), and hence the stoichiometry of perovskite can be re-established locally [245]:

$$A_{1-\alpha}BO_{3-\delta_{lim}} \xrightarrow{Exsolution} (1-\alpha)ABO_{3-\delta} + \alpha B \qquad \text{Equation 7-4}$$

From another point of view, the perovskite with high deficiency on both A- and oxygen sites can be treated as the B-site-excess composition, so the B-site species would be highly prone to exsolve. The process of B-site exsolution from A-site-deficient lattice can also be presented as Figure 7-5 [245]: oxygen can be easily stripped from the unit cell which accommodates the A-site vacancy, hence locally segregating the BO_n part (the purple group) out of the main perovskite structure, and by further reducing the perovskite, the segregated B-site cation would lose all the oxygen initially coordinated to it and hence shows great tendency towards exsolution.
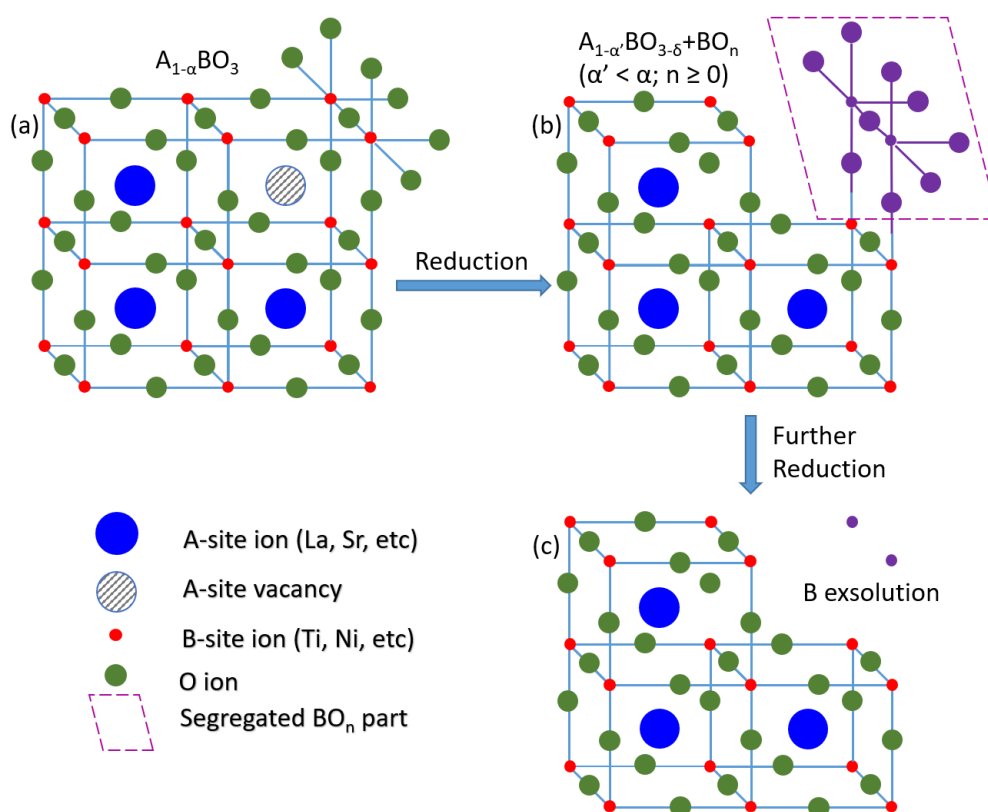
Figure 7- 5 Schematic demonstration of B-site exsolution process from A-site-deficient perovskite. (a) Some oxygen atoms are stripped out of the unit cell which contains A-site vacancy, making the BO_n part be locally segregated from the perovskite lattice as shown in the purple dashed area in (b). (c) Further reduction removes all the oxygen coordinated with B in BO_n to generate metallic B-site exsolution. Modified from Neagu et al. [245]

The exsolution is also controlled by the stoichiometry and morphology on the surface of perovskite. By annealing the material under oxidizing conditions during the synthesis of perovskite, the surface of the as-prepared perovskite ("native surface") usually evolves to a different stoichiometry from the nominal bulk. The phenomenon of A-site enrichment is often seen on the surface of perovskite where the native surface of perovskite possesses a stoichiometry with higher A/B ratio as compared to the nominal bulk stoichiometry [246, 247], and this might even happen for the perovskite with an A-site-deficient nominal stoichiometry [245]. The excess stoichiometry on the surface is detrimental for the B-site exsolution as the deficiency on A- and oxygen sites is important to destabilize the perovskite lattice to trigger the exsolution as explained above. Besides, it is also known that some perovskites will develop terraced native surfaces as shown in Figure 7-4(c), and the B-site exsolution would happen preferentially on edges of the terraces, indicating the spatial inhomogeneity on the native surface of perovskite [26, 245]. On the contrary, the "bulk surface", revealed by cleaving through the grains, shows the nominal stoichiometry of the perovskite and is much smoother than the native surface, hence more abundant and uniformly distributed metal nanoparticles would be formed on the bulk surface through exsolution as shown in Figure 7-4(d) [26, 245]. The migration of B-site cations in the bulk of the perovskite was found to possibly follow a curved path between the adjacent B-sites, where the trajectory of the B-site cations is in the (110) planes (as shown in Figure 7-6(a)). This process can be significantly promoted by the vacancies on the neighboring A-sites because of the reduced electrostatic repulsion for cation migration [26, 248], which again explains the promoting effect of the A-site deficiency on exsolution. Moreover, it was found that under reducing conditions, the B-site cations can diffuse from a depth of ~100 nm in the bulk of perovskite to get exsolved on the surface, and the diffusion of B-site cations is likely to be coupled with the diffusion of A-site cations (Figure 7-6(b)). Therefore, the A-site cations in the bulk diffuse in parallel with the B-site cations to the surface where the A-site vacancies are filled by the migrating A-site cations, which gradually lowers the driving force for the cation diffusion and hence limits the exsolution [26]. This can explain why the bulk surface with nominal stoichiometry is favored for exsolution as compared with the native surface that is enriched with A-site cations.
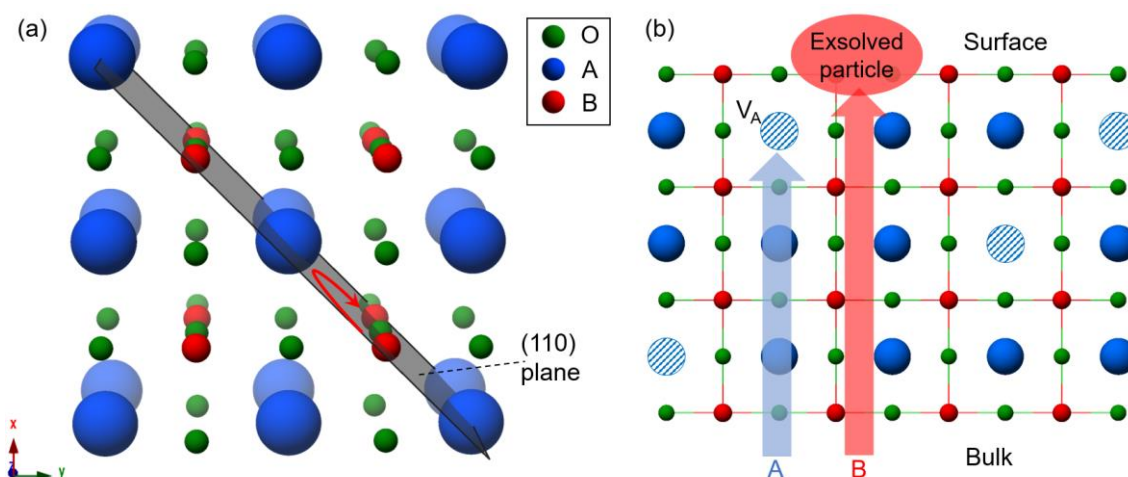
Figure 7- 6 (a) Migration of B-site cations between the adjacent B-sites follows the curved trajectory (shown as the red arrow) in the (110) plane [26, 248]. (b) Schematic of cation diffusion in bulk perovskite in which A- and B-site cations diffuse in parallel towards the surface where B-site cations get exsolved to form nanoparticles while A-site cations fill the A-site vacancies near the surface gradually [26].

Therefore, by controlling the stoichiometry of the perovskite and its surface properties, numerous and evenly distributed metal nanoparticles can be produced via exsolution. The strong anchorage of particles on the parent perovskite is one of the most important and appealing features for the exsolved materials, as it was reported by Neagu et al. that the exsolved particles are partially socketed in the surface of the parent perovskite (with ~30% diameter of the particle immerged in perovskite) as shown in Figure 7-7(a) [26]. They also discovered that the lattices of the perovskite and the exsolved metal particles were well aligned at their interface (Figure 7-7(b)), which implies that the particles could be epitaxially exsolved from perovskite. Not only that, the inter-diffusion between the two phases is possible as the exsolved particles are actually formed by the B-site cations diffusing from the perovskite lattice, which could also enhance the anchorage of particles to the support due to the stronger interaction between these two phases [26, 249]. However, the catalysts prepared via the traditional deposition techniques do not possess this socketed interface between the metal particle and the support (as shown in Figure 7-7(d)), which implies much weaker particle-support interactions as compared with the exsolved counterparts.
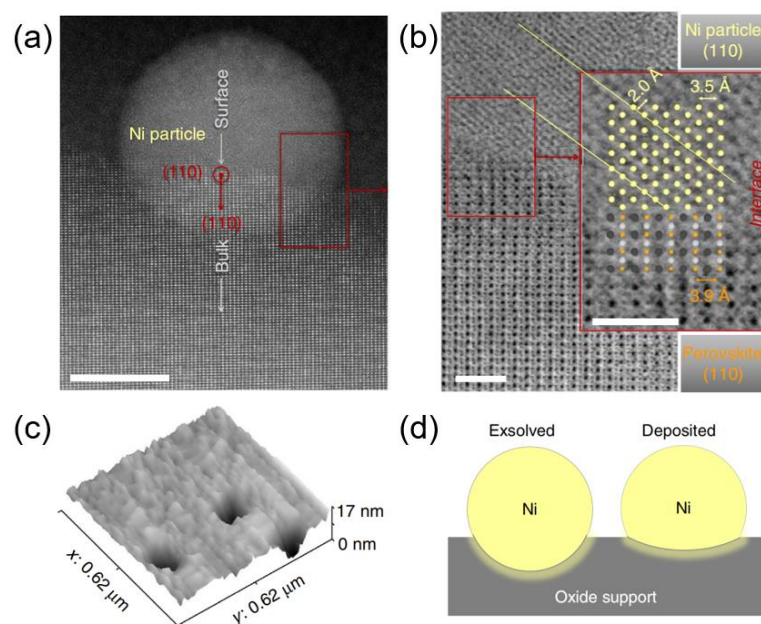
Figure 7- 7 (a) TEM image shows that the exsolved Ni particle is partially socketed in the parent perovskite. (b) Detail of metal-perovskite interface as shown in (a), shows the alignment between the lattices of Ni and perovskite. (c) 3D AFM of perovskite surface after the exsolved metal nanoparticles were etched in nitric acid, confirming the deep anchorage of exsolved particles in perovskite. (d) Schematic of different interface structures of exsolved and deposited Ni particles with the support. [26]

The strong particle-support interaction is a very important advantage for the exsolved materials, which brings the enhanced stability (resistance to sintering, coking and poisoning) to the exsolved nanoparticles. As Neagu et al. reported that, by thermally aging the exsolved and deposited Ni nanoparticles of the similar initial particle size, the exsolved nanoparticles did not sinter at 900 ˚C while severe agglomeration was observed for the deposited counterparts [26]. Besides, the exsolved nanoparticles are less likely to suffer from coking. As presented in Figure 7-8(a and c), the deposited Ni nanoparticles produced a large amount of carbon fibres covering the sample surface after being treated in the 20% methane atmosphere, while only few carbon fibres were observed on the exsolved nanoparticles [26]. The resistance of the exsolved nanoparticles to coking can be attributed to the strong particle-support interaction as it suppresses the lifting of nanoparticles from the support and hence the growth of carbon at the metal-support interface in the "tip-growth" mechanism for carbon growth as shown in Figure 7-8(b) [250]. Only very small amount of short carbon fibres can form on the exsolved nanoparticles, which probably follows another growth mechanism ("base-growth") as shown in Figure 7-8(d) [251], and this mechanism would happen only when a strong interaction exists between the metal particles and the support. What is more, many metal catalysts (especially Ni based) can be poisoned by sulphur

compounds. However, Papaioannou et al. reported that the exsolved metal nanoparticles have higher tolerance to sulphur poisoning as compared to their deposited analogues and the reduced activity of the exsolved nanoparticles caused by sulphur poisoning could get largely recovered after the sulpher compound was removed from the environment [252].
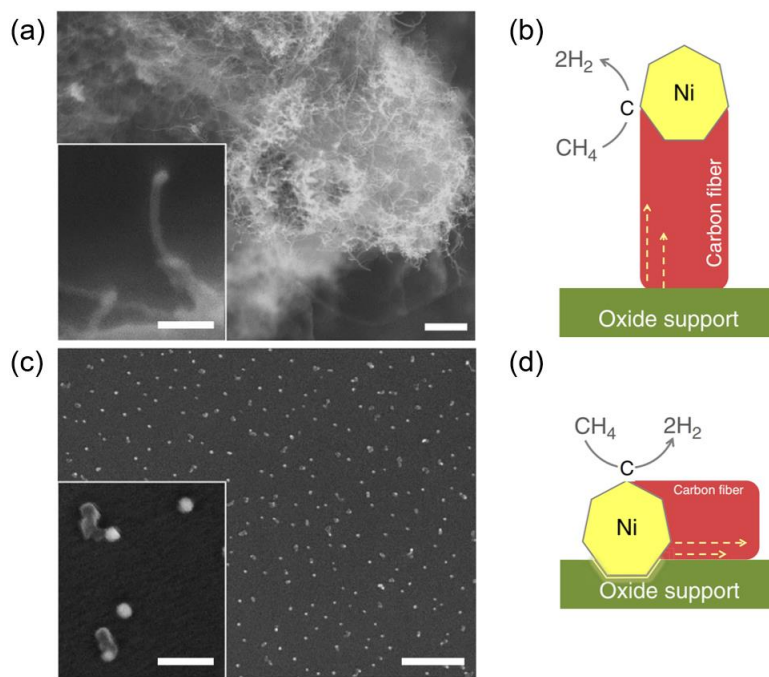
Figure 7- 8 Growth of carbon fibres under the coking conditions (20% CH_4/H_2, 800 ˚C, 4 h): (a) deposited nickel particles (~20 nm) produce a big amount of carbon fibres; (c) exsolved nickel particles (~25 nm) show very limited growth of carbon fibres. The "tip-growth" mechanism (b) and "base-growth" mechanism (d) can explain the carbon fibre growth in (a) and (c), respectively. [26]

To sum up, by controlling the nonstoichiometry (especially the A-site deficiency) of perovskites, the B-site metal exsolution can be significantly promoted, which can produce abundant, well distributed and compositionally diverse nanoparticles on the perovskite support. The unique interactions between the metal nanoparticles and the oxide substrate would cause strong anchorage of the exsolved nanoparticles, which results in the enhanced thermal stability, resistance to coking and poisoning. Due to the emerging functionalities introduced above, the exsolved materials have been widely studied in applications such as catalysis of CO and NO oxidation [253], fuel cells [254-256], hydrogen production via chemical looping [257], hydrocarbon reforming [258] and CO_2 reduction [259], etc. However, the mechanisms of exsolution (such as the formation of the socketed interface and the particle nucleation and growth) have not been understood yet, mainly due to the difficulties of observing the exsolution

process at atomic scale. Mechanistic insights can not only help us understand the functionalities (like stability and activity) which arise from exsolution, but also allow for the more advanced design of the exsolved materials to control the exsolved particle characteristics, increase the exsolution extent or even generate new exsolved nanostructures. Therefore, in this study, the mechanisms of exsolution have been investigated by using the latest generation ETEM, and the mechanistic insights obtained are used to design the noble metal (Rh) based exsolved materials.

7.2 Controlling the perovskite stoichiometry and microstructure by modifying the solid-state method

7.2.1 Design principles of perovskite stoichiometries

Generally, there are two basic principles to design the composition of the perovskite. Firstly, the relationship between the radii of different ions in the perovskite must meet the requirement restricted by the Goldschmidt tolerance factor ($0.8 \leq tf \leq 1$, shown in Equation 7-2 above), otherwise the perovskite structure would be unstable. If the original cations (mainly at the B-sites) in the host perovskite need to be partially substituted with some other cations of interest, the radius of the substituting cations should be similar as the original cations, so the substituting cations can be inserted in the perovskite lattice without distorting the structure too much. Secondly, the charges on the three primitive sites of the perovskite must be balanced to fulfill the electroneutrality principle. For instance, if the B-sites are partially substituted with some cations of different oxidation states, the change of the overall charges on the B-sites must be compensated via nonstoichiometry on the A- and/or oxygen sites or changes of the oxidation states.

First of all, two compositions of perovskites containing different substitution levels of exsolvable ions (Ni) were selected to be used for the mechanistic investigation of the exsolution process in ETEM, because exsolution of Ni has been widely studied previously [26, 245]. The perovskite with relatively low Ni content was derived from Ca-based titanate $La_xCa_{1-3x/2}TiO_3$, where the oxidation states of La, Ca and Ti are +3, +2 and +4, respectively, hence the charge was balanced. The value of x was designed to be 0.4 and the perovskite became $La_{0.4}Ca_{0.4}TiO_3$, so there would be a high degree of A-site vacancies (20%). By substituting 6% Ti^{4+} with Ni^{2+}, the decrease of charges can be compensated by the change of A-site oxidation state (the ratio between La^{3+} and

Ca^{2+}) and oxygen vacancies simultaneously. Therefore, the Ni-doped composition was La$_{0.43}$Ca$_{0.37}$Ni$_{0.06}$Ti$_{0.94}$O$_{3-\gamma}$ (γ=0.045, the low degree of oxygen vacancies will not be shown in formulas henceforth for simplicity) [260], where both the retained A-site vacancies (20%) and the small amount of oxygen vacancies can promote the ion diffusion and subsequently exsolution. Moreover, the Ca-based titanate is also important for the design of noble metal (Rh) doped perovskites, which will be introduced in the next paragraph. On the other hand, for the perovskite with high Ni content (40% on the B-sites), the substantial decrease of charges should be compensated by the increase of A-site oxidation state, hence La$_{0.8}$Ce$_{0.1}$Ni$_{0.4}$Ti$_{0.6}$O$_3$ from previous studies [245] was chosen. These two compositions with vastly different substitution levels of Ni can cover the currently reported range of exsolved materials, and they can allow for the investigation of metal exsolution behaviors from different concentrations of exsolvable ions.

Perovskites with dilute amounts of Rh were also designed for catalytic measurements in CO oxidation reaction and, as mentioned above, the Ca-based titanate was also used where Ni in La$_{0.43}$Ca$_{0.37}$Ni$_{0.06}$Ti$_{0.94}$O$_3$ was replaced by different levels of Rh, which resulted in a series of Rh-doped perovskites La$_{0.43}$Ca$_{0.37}$Rh$_x$Ti$_{1-x}$O$_3$ (x=0.01, 0.03 and 0.06). The design of La$_{0.43}$Ca$_{0.37}$Rh$_x$Ti$_{1-x}$O$_3$ was based on several reasons as listed below. Firstly, the solid-state method used for perovskite synthesis normally requires high reaction temperatures (>1200 °C), but the Rh precursor (Rh$_2$O$_3$) would decompose at a relatively lower temperature, which poses a challenge to incorporate Rh$_2$O$_3$ in the perovskite. Secondly, high reaction temperatures would also result in large grains of perovskite, which might limit the ion diffusion to the perovskite surface and hence exsolution. Ca is known to promote the perovskite formation at lower temperatures and ion diffusion [261], so the challenges above would be solved by employing the Ca-based compositions. Moreover, in order to use Rh more efficiently, it is desired to exsolve from perovskites with dilute concentrations of Rh although this might be challenging. The presence of the high concentration of A-site vacancies as well as a small amount of oxygen vacancies in La$_{0.43}$Ca$_{0.37}$Rh$_x$Ti$_{1-x}$O$_3$ might allow for the dilute exsolution of Rh, due to the ease of ion diffusion as mentioned above. Also, La$_{0.43}$Ca$_{0.37}$Rh$_x$Ti$_{1-x}$O$_3$ is similar as La$_{0.43}$Ca$_{0.37}$Ni$_{0.06}$Ti$_{0.94}$O$_3$, so the exsolution of Ni and Rh from these perovskites might be governed by the similar mechanisms and the knowledge obtained from the mechanistic study of Ni exsolution might be useful to control the exsolution of Rh. As the perovskites La$_{0.43}$Ca$_{0.37}$Rh$_x$Ti$_{1-x}$O$_3$ have not been

reported before, the tolerance factor of these perovskites was checked. Rh can be incorporated as Rh^{3+} (0.665 Å) and/or Rh^{4+} (0.6 Å) in $La_{0.43}Ca_{0.37}Rh_xTi_{1-x}O_3$ (details about Rh oxidation states will be discussed later), hence the tolerance factor is about 0.96 and 0.98, respectively, indicating that the perovskite structure can be stable. More details about perovskite design will be discussed in the result parts later.

Phase purity of the prepared perovskites is very important. If secondary phases exist in the final product, the stoichiometry of the perovskite will deviate from the desired ones as designed, which will cause uncertain effects on the subsequent metal exsolution. The solid-state preparation method was used and the conventional procedures were modified to produce the single-phase perovskites. The steps to modify the solid-state method will be presented in this subchapter, and the determination of the phase purity and the structure of the prepared perovskites will also be discussed.

7.2.2 Determination of the phase purity and crystal structure of perovskites

The determination of the phase purity and structures of the prepared perovskites is conducted in the method based on indexing the XRD pattern of the perovskite on a double cubic cell and checking the splitting (or broadening) of the peaks in XRD [245, 262-264]. The structure of an ideal perovskite such as $SrTiO_3$ is cubic, but by accommodating ions of different sizes or charges, the structure can be distorted to show a lower symmetry. The perovskite structure can be distorted in different ways including octahedral tilting, B-site cation displacement and the distortion of octahedra [262], and the octahedral tilting is most commonly seen [265]. Glazer proposed to treat the octahedral tilting as different component tilts around the pseudocubic axes (x, y and z), and the successive octahedra may tilt in the same or opposite direction around one of axes, which is referred to as in-phase or out-of-phase tilting, respectively [265, 266]. Hence, the octahedral tilting can be described by using the symbols of $a^\#b^\#c^\#$, where a, b, c represent the magnitudes of the tilts around the x, y and z axes, respectively, and the superscript # can be +, - and 0 to show in-phase tilting, out-of-phase tilting and no tilting around that axis, respectively. Letters can be identical when the magnitudes of the tilts around two axes are the same. For instance, $a^0b^+b^+$ means in-phase tilts with equal magnitude around the y and z axes and no tilt around the x axis.

The octahedral tilting may cause the doubling of the unit cell parameter along certain axes [262]. As shown in Figure 7-9, the tilting of octahedra occurs around the axis that is perpendicular to the plane of the paper, and it can be found that two neighboring octahedra tilt in opposite directions, which results in the doubled unit cell parameter perpendicular to this axis. This can happen for all the three axes of tilting.
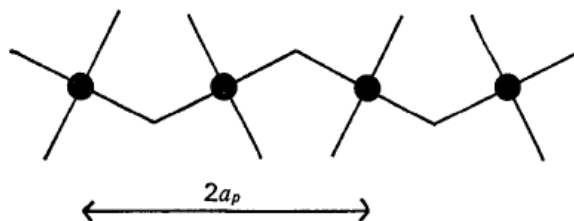
Figure 7- 9 Schematic demonstration of octahedral tilting around the axis perpendicular to the plane of paper, with the black points representing B-site cations. [262]

Therefore, for perovskites with different types of tilting, the analysis of the structure is conducted by defining the double pseudocubic cell parameters $(2a_p \times 2a_p \times 2a_p)$, where a_p is a pseudocubic cell parameter of a hypothetical cubic cell that contains a single ABO_3 unit:

$$a_p = \sqrt[3]{\frac{V_{uc}}{n_{uc}}}$$

Equation 7-5

where V_{uc} is the volume of the real distorted unit cell, and n_{uc} is the number of ABO_3 units involved in it. Typically, the cell parameter can be estimated according to its relationship with the d-spacing value:

$$d_{(hkl)}^2 = \frac{a^2}{h^2+k^2+l^2}$$

Equation 7-6

where d_{hkl} is the d-spacing at a certain reflection in the XRD pattern with the Miller indices to be (hkl). The reflection (220) usually has the strongest intensity among all the reflections in the XRD pattern of a perovskite, and hence it is always used to calculate the value of estimated pseudocubic cell parameter (a_p^*):

$$d_{(220)}^2 = \frac{(2a_p^*)^2}{2^2+2^2+0^2}$$

Equation 7-7

so

$$a_p^* = \sqrt{2}d_{(220)}$$

Equation 7-8

Therefore, the value of a_p^* is obtained, which enables indexing the diffraction pattern of the double pseudocubic cell ($2a_p^* \times 2a_p^* \times 2a_p^*$) as mentioned before and by assuming the cubic $Pm\bar{3}m$ structure, in the software STOE Win XPOW, and hence the Miller indices can be assigned to the corresponding peaks in the diffraction pattern. The octahedral tilting will result in the splitting (or broadening) of the X-ray diffraction lines at the primitive perovskite peaks and the presence of extra (superlattice) reflections, and they can be used to determine the structure of the perovskite [245, 262, 264], which has been comprehensively summarized in the work from Dragos Neagu [267]. For instance, primitive perovskite peaks possess Miller indices consisting of all even numbers (eee), and the splitting (or broadening) of these peaks can be used to determine the overall structure of the perovskite as shown in the red box in Figure 7-10, where the perovskite structure can be selected from rhombohedral, monoclinic, orthorhombic or tetragonal symmetry, respectively, depending on the appearance of splitting (or broadening) on different primitive peaks. For example, if (hhh) such as (222) shows splitting (or broadening), while (h00) like (200) is a single peak, the perovskite is most likely to have a rhombohedral structure. On the other hand, the presence of the superlattice reflections, which have Miller indices containing odd numbers, can be checked to determine whether the in-phase or/and out-of-phase tilting exists, as shown in the blue box in Figure 7-10. The intensities of superlattice reflections are usually very low, hence they need to be examined carefully.
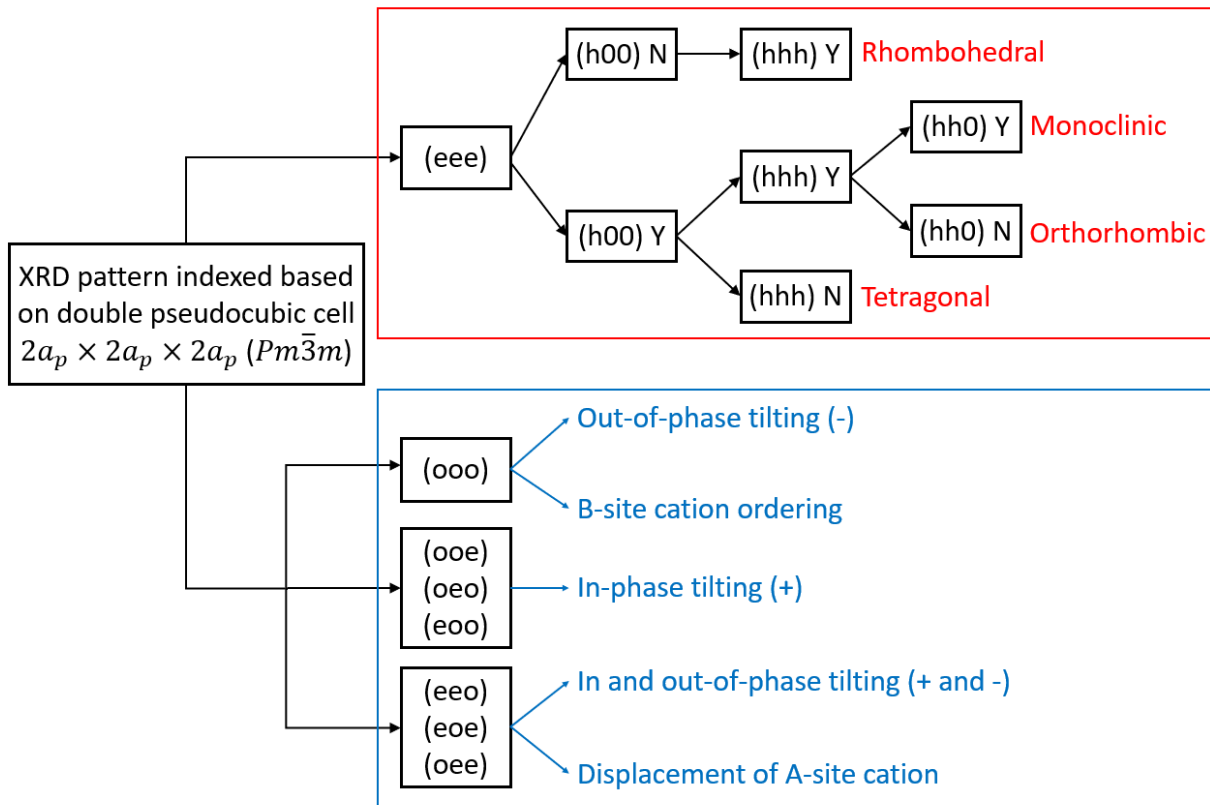
Figure 7- 10 Diagram showing the algorithm to determine the crystal structure of a perovskite based on the corresponding XRD pattern. Modified from Neagu [267].

Once the overall structure and the tilting types of the perovskite crystal are estimated from the diffraction pattern, the corresponding space group can be selected from Figure 7-11 as summarized by previous researchers [263]. Also, the XRD pattern of the perovskite will be analyzed via Rietveld refinement which can further confirm the space group as selected.

Moreover, if extra reflections other than the primitive or superlattice reflections of the perovskite exist, it probably indicates the presence of impurities (secondary phases) in the sample and these secondary phases must be avoided by modifying the preparation procedures. Therefore, based on the methodology introduced here, the phase purity and the structure of the perovskites prepared in this study can be determined.
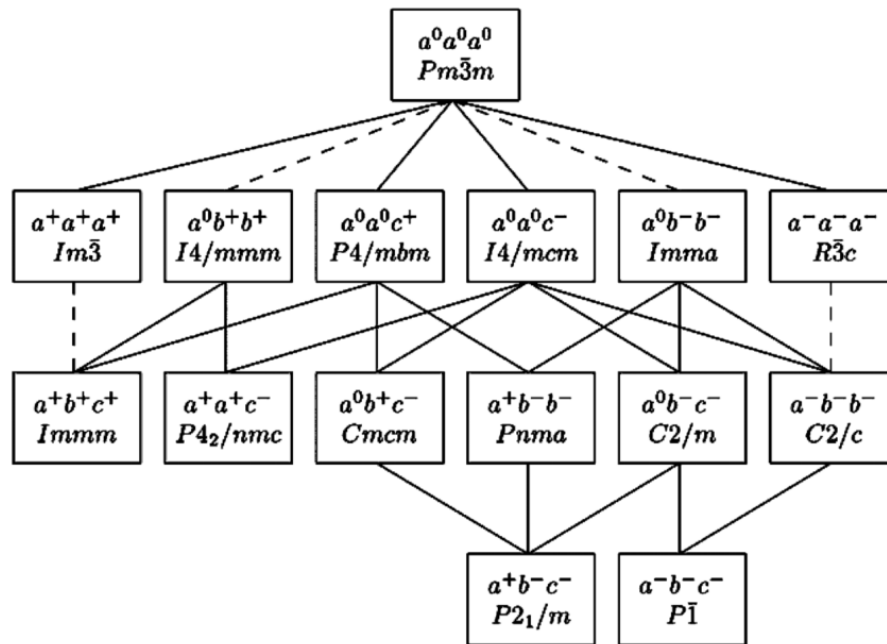
Figure 7- 11 Diagram showing the symbols for tilting proposed by Glazer and the corresponding space group symmetries. [263]

7.2.3 Preparation of La$_{0.8}$Ce$_{0.1}$Ni$_{0.4}$Ti$_{0.6}$O$_3$ by modifying solid-state method

The perovskite La$_{0.8}$Ce$_{0.1}$Ni$_{0.4}$Ti$_{0.6}$O$_3$ was prepared first to serve as an example that helped to modify the preparation method to produce single-phase perovskites without impurities.

The 1st batch of La$_{0.8}$Ce$_{0.1}$Ni$_{0.4}$Ti$_{0.6}$O$_3$ sample was prepared by using the conventional solid-state method as described in subchapter 3.2.1, and the as-prepared sample was scanned in XRD (shown as black line in Figure 7-12) to determine its phase purity. By indexing the diffraction pattern of the 1st batch sample using the methodology as described in subchapter 7.2.2, it can be found that most of the peaks came from the perovskite phases, however, some extra reflections (for example, at the positions of 29.2 °, 31.3 °, 37.3 ° and 62.9 °) were also observed. According to the position and shape of the reflections appearing at 29.2 ° and 31.3 °, they were likely to be the remaining Kβ signal and the terraced-like intensity change near the adsorption edge of β-filter (as previously introduced in Figure 3-6), respectively, as a Ni filter was used in the XRD instrument at Newcastle to monochromatize the Cu radiation. However, the appearance of the other two extra reflections (at 37.3 ° and 62.9 °) could not be attributed to the Ni filter, but instead they could imply the presence of some impurities (secondary phases). This was confirmed by searching the database in the software

HighScore Plus (v 4.8), which indicated that these extra reflections belong to some mixed oxides of La and Ni (e.g., $La_8Ni_4O_{16}$) that were formed separately from the main perovskite phase during the preparation.
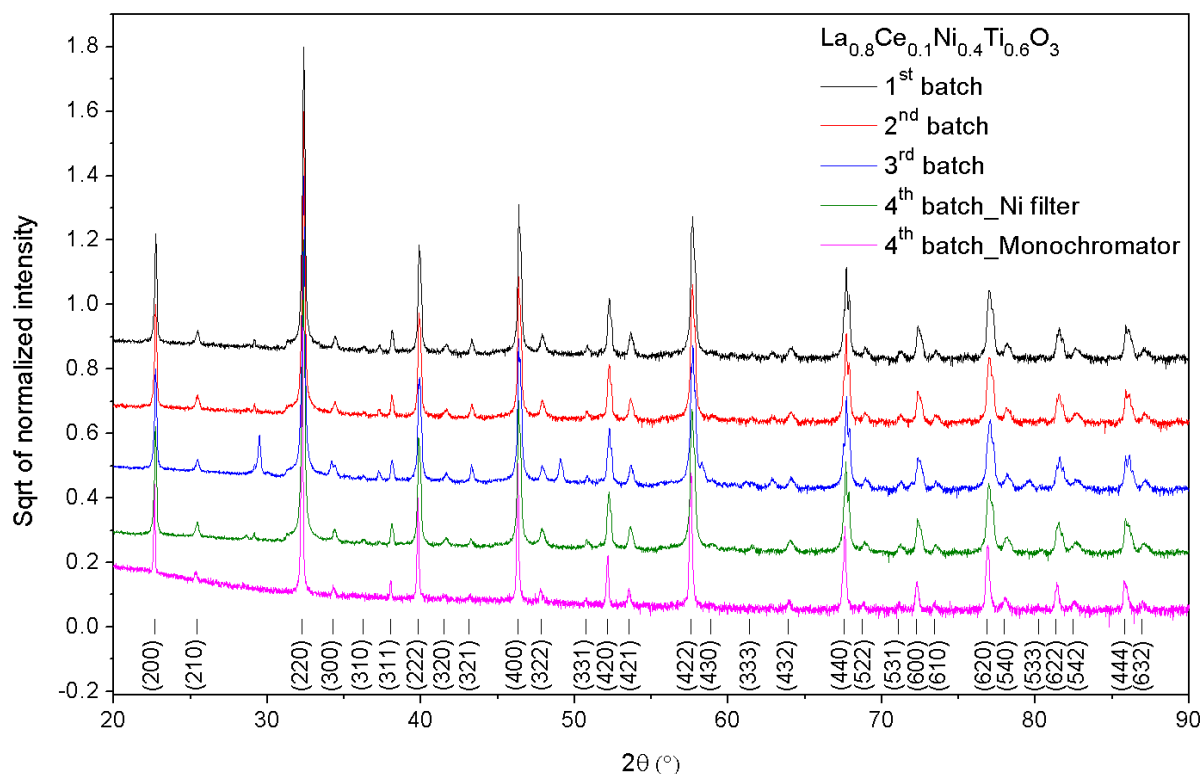
Figure 7- 12 Powder XRD patterns of $La_{0.8}Ce_{0.1}Ni_{0.4}Ti_{0.6}O_3$ prepared from different batches. The 1st batch sample was prepared via conventional solid-state method, and the 2nd batch sample was obtained by re-sintering the sample from 1st batch. The 3rd and 4th batch samples were prepared via modified solid-state method which employed ultrasonic probe for precursor mixing, and different dispersants (ATLOX LP-1 and Hypermer KD1) were used, respectively. Two different XRD instruments that employed Ni filter and monochromator were used to scan the 4th batch sample, respectively. Theoretical positions for reflections are also labelled.

The formation of secondary phases means that some metal cations preferentially segregated from the main phase of perovskite and formed separated phases, which led to the deviation of the perovskite composition from the nominal stoichiometry as originally designed. As mentioned before, the B-site cation exsolution is heavily dependent on the stoichiometry of the perovskite, hence it must be precisely controlled and secondary phases need to be avoided. Therefore, the previously prepared sample (1st batch) was ball milled and pressed into pellet again to be re-sintered (1400 °C, 6 h) as described in subchapter 3.2.1, attempting to mix the powder more thoroughly and facilitate more solid-state reactions to form homogeneous perovskite phase and

remove secondary phases. However, according to the XRD result of the re-sintered $La_{0.8}Ce_{0.1}Ni_{0.4}Ti_{0.6}O_3$ (2nd batch) shown in Figure 7-12 (red line), the extra reflections of secondary phases still appeared at the same positions where they were observed for the 1st batch sample, which indicates that secondary phases cannot be transformed into the perovskite phase solely by re-sintering the sample.

The formation of secondary phases could also be confirmed in SEM, as shown in Figure 7-13. No obvious secondary phases could be seen in the image obtained under secondary electron (SE) mode (Figure 7-13(a)). However, by switching to the back-scattered electron (BSE) mode (Figure 7-13(b and c)), obvious brightness contrast can be observed on the surface of the sample, indicating that the sample was compositionally inhomogeneous, as the intensity of BSE signals is dependent on the weight of the elements in the material as previously introduced in subchapter 3.1.2. Some small grains were found to be darker than the surrounding areas as labelled with boxes in Figure 7-13(b), implying that these grains were rich in some lighter elements such as Ni and Ti. Also, small spherical particles were found in the pits on the surface of the sample, and clearly these small particles were isolated from the main phase of perovskite and hence were secondary phases as well. The inhomogeneous composition of the sample became more obvious after it was treated in 5% H_2/Ar (1100 °C, 5 h) as Ni was reduced as shown in Figure 7-13(d and e). Instead of dispersing uniformly on the sample surface, the Ni particles were preferentially located on some small areas and grain boundaries, which implies that these positions contained abundant Ni cations that could be reduced to form Ni particles. As a result, the concentration of Ni in the main grains of perovskite was lowered and hence almost no Ni particle could be exsolved on these grains.
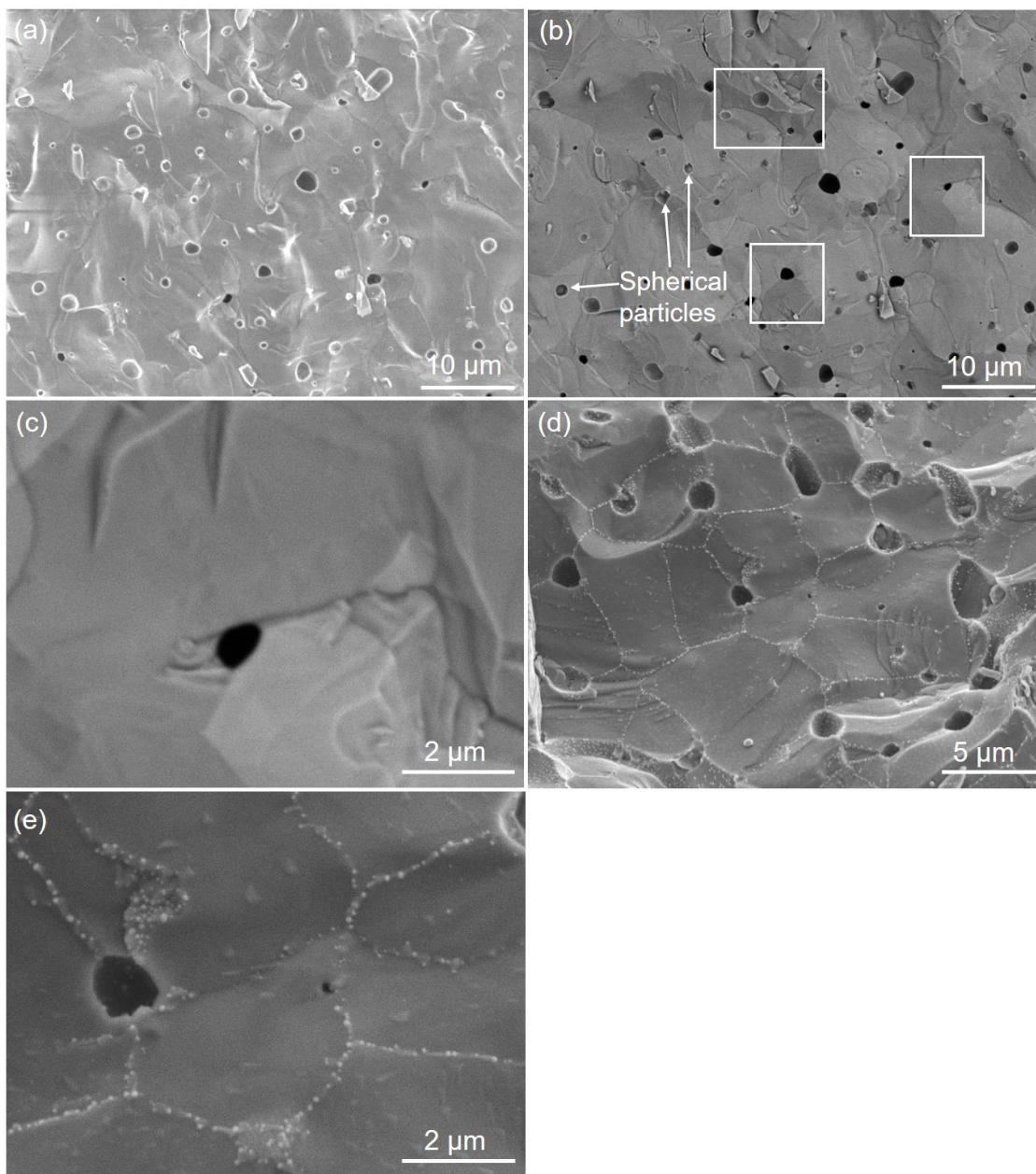
Figure 7- 13 SEM images of the 2nd batch of the $La_{0.8}Ce_{0.1}Ni_{0.4}Ti_{0.6}O_3$ sample: (a) as-prepared (SE); (b and c) as-prepared (BSE); (d and e) after being reduced in 5% H_2/Ar at 1100 °C for 5 hours (SE).

Therefore, the preparation method must be further improved. Inadequate mixing of the metal precursors was thought to be the cause of the inhomogeneous phase compositions. In the conventional solid-state method, the mixing of precursors is conducted by applying ball milling. However, it was found that the solid suspension resulted from the ball milling was not stable and the solids would precipitate to the bottom of the cup during the evaporation of acetone, which could possibly result in the layered settling of precursors due to their different densities. It was also found that some solids were strongly adhered to both the wall of the ball mill cup and the zirconia

balls that were difficult to recover, which might change the overall composition of the perovskite if some precursors were preferentially lost in this step. Therefore, to solve this, a modified solid-state method was employed as described in subchapter 3.2.2, in which the precursors were mixed under sonication by using ultrasonic probe. Under sonication, solids of precursors could be broken down into fine powders to be uniformly dispersed in acetone. Also, the subsequent step of acetone evaporation was conducted under continuous stirring to avoid powder precipitation. Hence, more homogeneous mixing of precursors could be achieved. Another advantage of using sonication is that the mixing process took place in the same beaker in which the precursors were initially weighed and the recovery of powders from the beaker was simple, so the loss of precursors during the mixing process could be minimized. By using this modified solid-state method, the 3rd batch of La$_{0.8}$Ce$_{0.1}$Ni$_{0.4}$Ti$_{0.6}$O$_3$ sample was prepared, and its XRD result can also be found in Figure 7-12 (blue line). However, the result shows that the 3rd batch sample had even more extra reflections as compared to the previous ones, and the extra reflections appearing at 29.5 °, 37.3 °, 49.1 °, 58.3 °, 62.9 ° and 79.7 ° were identified by HighScore Plus to be some cerium oxides and mixed oxides of La and Ni. Moreover, at the reflection positions of perovskite, two or three peaks could be seen to overlap, indicating multiple perovskite phases with different compositions might form. All these results show that the modified solid-state method did not work well at the first time. By applying sonication, the metal precursors should be mixed more uniformly and hence the final product should be more homogeneous, but the fact was that multiple impurities were seen in the product. This might be ascribed to the improper dispersant, as the dispersion of precursors was affected not only by the ultrasonic waves but also by the action of dispersant. However, the dispersant used previously (ATLOX LP-1) might not be capable to disperse precursors uniformly in solution, because it has poor solubility in the solvent (acetone). Therefore, it was replaced by another dispersant (Hypermer KD1) that is highly soluble in acetone and hence should improve the mixing performance for the precursors.

The modified solid-state method was repeated (for the 4th batch sample) by using the new dispersant Hypermer KD1. The final step of sintering was also modified by prolonging the sintering duration to 20 hours to enable more solid-state reactions to form perovskite phase, while the sintering temperature was reduced slightly to 1390 °C to avoid undesired reactions between the sample pellets and the alumina boat during the longer sintering process. The XRD results of the 4th batch of La$_{0.8}$Ce$_{0.1}$Ni$_{0.4}$Ti$_{0.6}$O$_3$

can be found in Figure 7-12. The diffraction pattern of the 4th batch sample was much cleaner as compared with the previous ones, and most of the extra reflections which were observed for the previous batches did not appear this time, indicating that the formation of secondary phases was effectively suppressed by using the modified solid-state method. Only some small extra reflections (at 29.1 ° and 31.2 °) were seen, which could be ascribed to the use of Ni filter as discussed before. This was confirmed by re-scanning the sample in a more advanced XRD instrument at University of Liverpool which could monochromatize X-rays better by using the single crystal monochromator as introduced in subchapter 3.1.1. The diffraction pattern of the 4th batch sample obtained from Liverpool (the purple line in Figure 7-12) shows that the extra reflections (at 29.1 ° and 31.2 °) which were previously observed were absent this time, confirming that these reflections are not secondary phases but some remaining signal of $K\beta$ and the changes of the diffraction background due to the use of the Ni filter in our XRD instrument. Moreover, the signals of $K\alpha2$ were also eliminated in the instrument at Liverpool by using their monochromater, which allowed for the better analysis of the XRD result, and it was found that all the reflections in the diffraction pattern belong to the perovskite phase, indicating the high purity of the product. The improved phase purity was also confirmed by BSE images (Figure 7-14), as no obvious contrast was observed on the sample surface at all the magnifications, indicating the homogeneous compositional distribution in the material. Combining the results of XRD and BSE, it can be concluded that the single-phase perovskite ($La_{0.8}Ce_{0.1}Ni_{0.4}Ti_{0.6}O_3$) could be prepared by using the modified solid-state method, and this method could also be used for other perovskite compositions in this study henceforth.
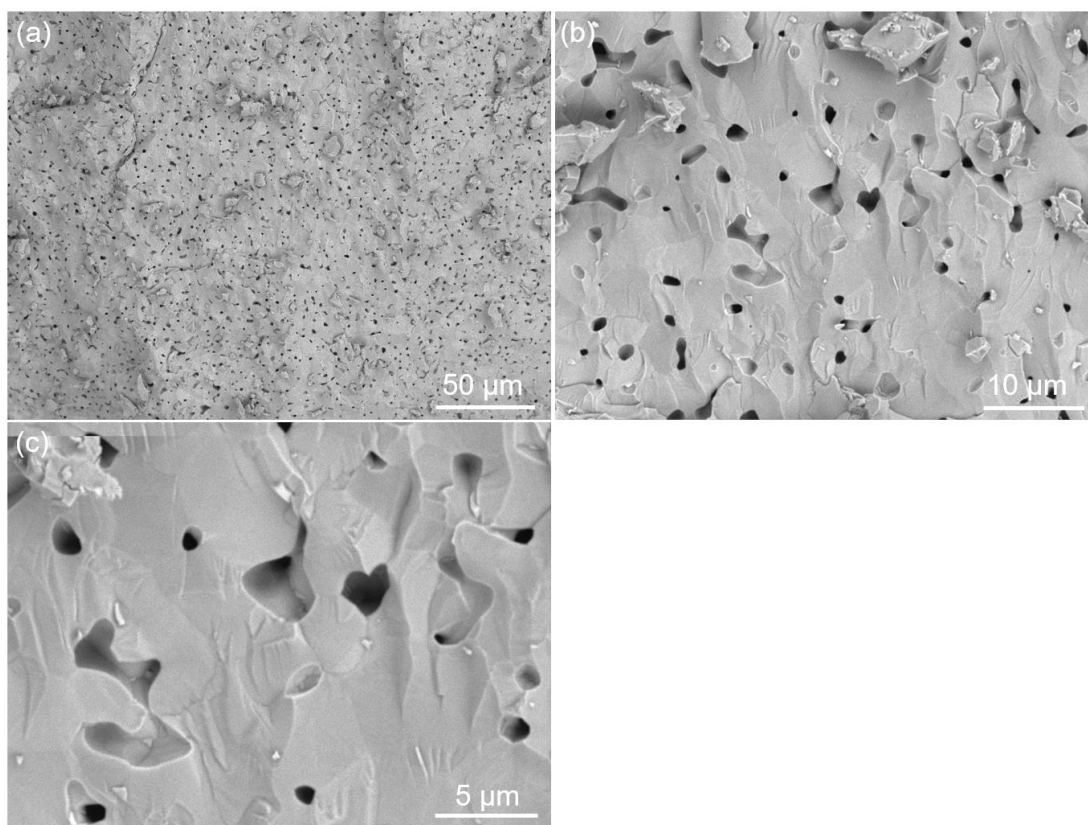
Figure 7- 14 SEM images (BSE) of the 4th batch of $La_{0.8}Ce_{0.1}Ni_{0.4}Ti_{0.6}O_3$ (prepared via the modified solid-state method) at different magnifications.

By using the method described in subchapter 7.2.2, the structure of the as-prepared perovskite $La_{0.8}Ce_{0.1}Ni_{0.4}Ti_{0.6}O_3$ was determined. Regarding the primitive peaks of the perovskite, it was found that peaks of (400) and (222) were broadened while no obvious splitting (or broadening) was observed for (hh0) peaks ((220) and (440)), and hence the overall symmetry of $La_{0.8}Ce_{0.1}Ni_{0.4}Ti_{0.6}O_3$ could be determined to be orthorhombic. Besides, superlattice reflections of (ooo), (oeo) and (eeo), i.e. (311), (321) and (221) respectively, were all found to be present, which suggested a highly distorted structure with both in-phase and out-of-phase tilting. Combining the information obtained above, the most likely space group for the perovskite $La_{0.8}Ce_{0.1}Ni_{0.4}Ti_{0.6}O_3$ could be determined as *Pnma*.

Rietveld refinement was conducted to validate the selected *Pnma* space group (here the setting of *Pbnm*, the same space group as *Pnma*, was used). As shown in Figure 7-15, the data points from XRD were well fitted in the Rietveld refinement, which confirmed the space group *Pnma* for $La_{0.8}Ce_{0.1}Ni_{0.4}Ti_{0.6}O_3$. The perovskite structure was created via CrystalMaker (Figure 7-16), which shows a highly distorted structure as anticipated before. It can be found that significant out-of-phase tilting happened around both x and y axes, and in-phase tilting was seen around the z axis.
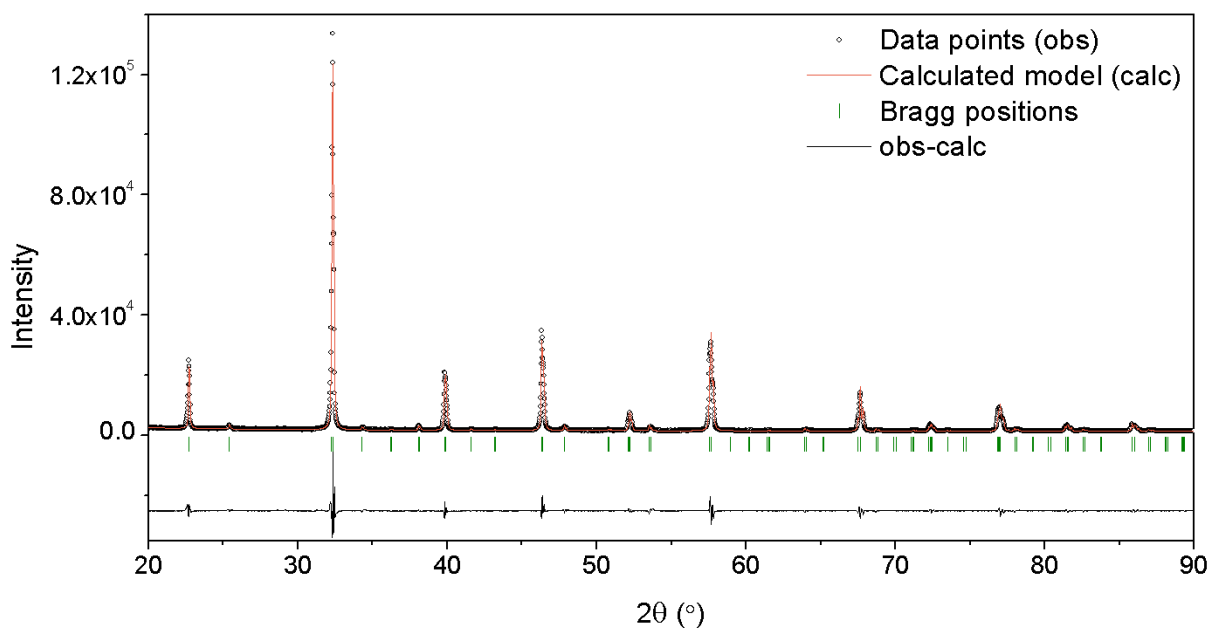
Figure 7- 15 Rietveld refinement of $La_{0.8}Ce_{0.1}Ni_{0.4}Ti_{0.6}O_3$.
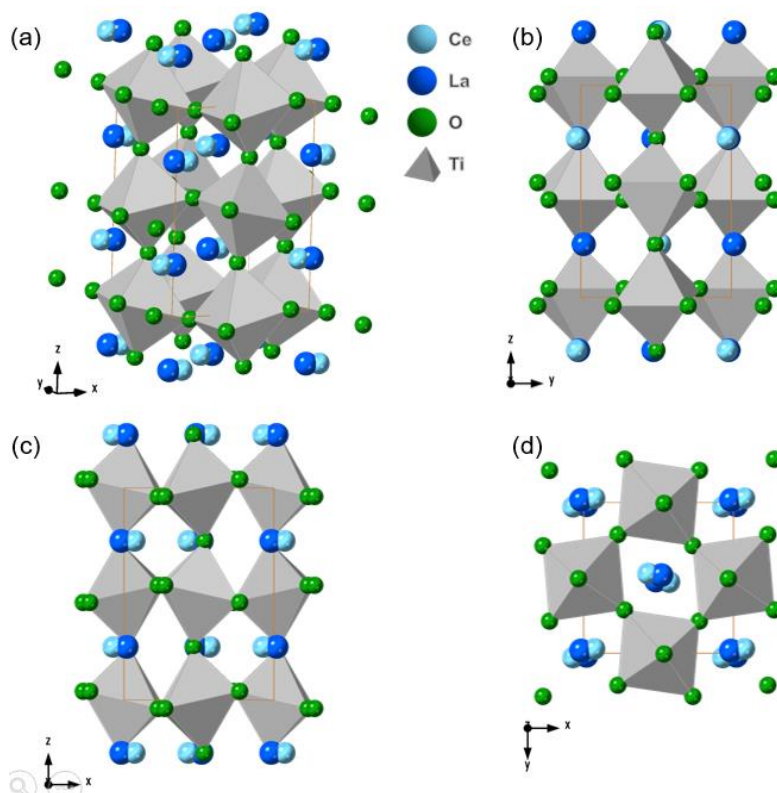
Figure 7- 16 Crystal structure of $La_{0.8}Ce_{0.1}Ni_{0.4}Ti_{0.6}O_3$ showing the perspective view (a) and the projection along x axis (b), y axis (c) and z axis (d), respectively. The A-sites are occupied by Ce and La, representing the partial substitution on A-sites. For simplicity, Ni cations are not shown in the structure.

7.2.4 $La_{0.43}Ca_{0.37}Ni_{0.06}Ti_{0.94}O_3$

The perovskite $La_{0.43}Ca_{0.37}Ni_{0.06}Ti_{0.94}O_3$ was also prepared for the experiment of in situ observation of exsolution process in ETEM as mentioned before. The preparation was also carried out by using the same modified solid-state method as used for $La_{0.8}Ce_{0.1}Ni_{0.4}Ti_{0.6}O_3$ above. All the metal precursors used for the preparation of $La_{0.43}Ca_{0.37}Ni_{0.06}Ti_{0.94}O_3$ were the same as before, except CeO_2 that was replaced by $CaCO_3$ for Ca. By following the same preparation method as above, the as-prepared sample after being sintered at 1390 °C for 20 hours was scanned in XRD (Figure 7-17). It shows that the phase of $La_{0.43}Ca_{0.37}Ni_{0.06}Ti_{0.94}O_3$ prepared via the modified solid-state method was highly pure, as all the peaks appearing in the diffraction pattern belonged to the perovskite phase and no obvious reflections for secondary phases were observed.
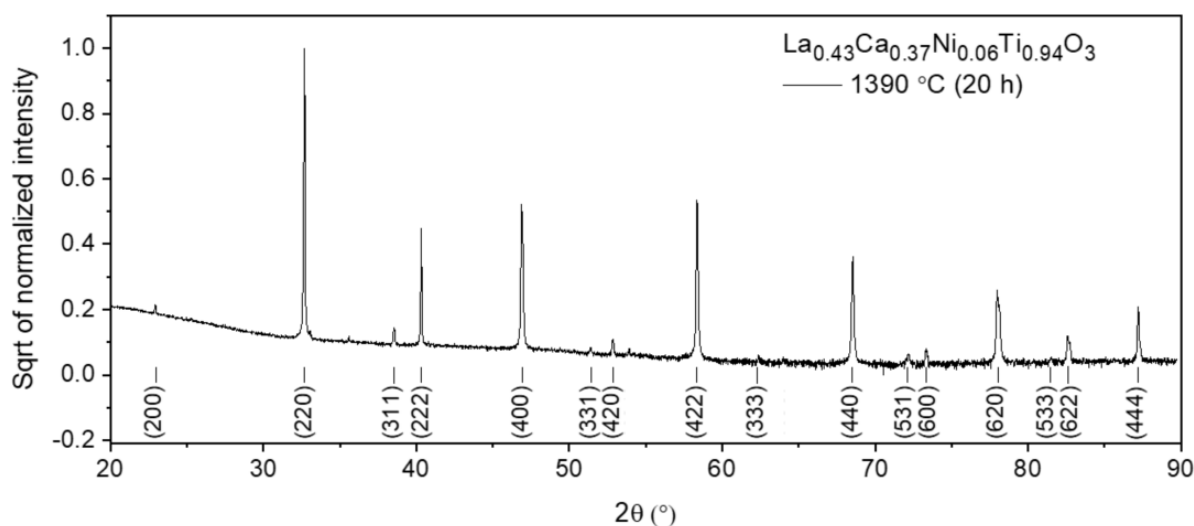
Figure 7- 17 Powder XRD pattern of the $La_{0.43}Ca_{0.37}Ni_{0.06}Ti_{0.94}O_3$ sample (sintered at 1390 °C for 20 h). Theoretical positions for reflections are also labelled.

The crystal structure of the $La_{0.43}Ca_{0.37}Ni_{0.06}Ti_{0.94}O_3$ sample was then determined. For the primitive peaks of the perovskite phase, it was found that the peaks of (400) and (444) were obviously broadened, while the (hh0) peaks ((220) and (440)) appeared to be single peaks with no obvious splitting or broadening, therefore the overall symmetry of $La_{0.43}Ca_{0.37}Ni_{0.06}Ti_{0.94}O_3$ should be selected as orthorhombic. When superlattice reflections were checked, only (ooo) peaks (such as (311) and (331)) were clearly observed while no obvious reflections of (ooe) and (eeo) as well as all their other permutations were found, so the structure should only have some out-of-phase tilting. Therefore, the most likely space group was determined to be orthorhombic *Imma* for $La_{0.43}Ca_{0.37}Ni_{0.06}Ti_{0.94}O_3$. The selected space group was confirmed in the Rietveld refinement (here *Ibmm*, another setting of *Imma*, was used), as the data points were

well fitted with the calculated model as shown in Figure 7-18. The structure of the perovskite $La_{0.43}Ca_{0.37}Ni_{0.06}Ti_{0.94}O_3$ is presented in Figure 7-19. It can be found that out-of-phase tilting happened around x and y axes while there was no obvious tilting observed around the z axis.
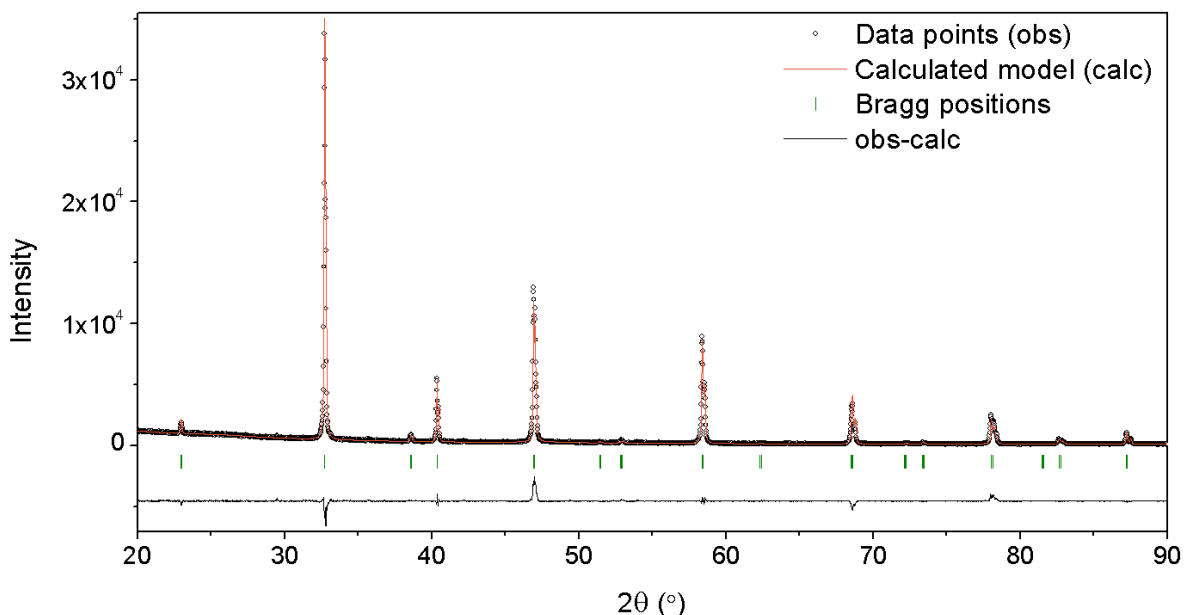
Figure 7- 18 Rietveld refinement of $La_{0.43}Ca_{0.37}Ni_{0.06}Ti_{0.94}O_3$.
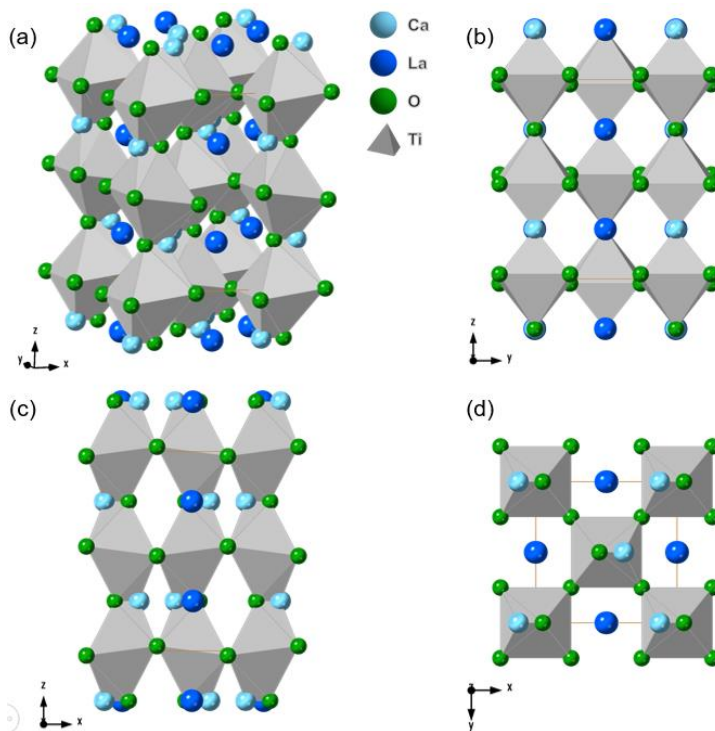
Figure 7- 19 Crystal structure of $La_{0.43}Ca_{0.37}Ni_{0.06}Ti_{0.94}O_3$ showing the perspective view (a) and the projection along x axis (b), y axis (c) and z axis (d), respectively. The A-sites are occupied by Ca and La, representing the partial substitution on A-sites. For simplicity, Ni cations are not shown in the structure.

7.2.5 $La_{0.43}Ca_{0.37}Rh_xTi_{1-x}O_3$ with modified microstructure

Once $La_{0.43}Ca_{0.37}Ni_{0.06}Ti_{0.94}O_3$ was successfully prepared, it was tried to substitute Ni in this composition with different levels of Rh and subsequently exsolve Rh from perovskites. The Rh-substituted perovskites were also prepared in the modified solid-state method, but the conditions used in some preparation procedures (especially the sintering step) were changed mainly due to the two reasons as described below.

Firstly, the microstructure of the perovskite needs to be modified to promote the exsolution of Rh. Actually, exsolving noble metals from dilute substitution systems can be difficult both thermodynamically and kinetically, because the noble metal ions are expected to have strong interaction with the perovskite lattice and this will increase the thermodynamic requirements for exsolution [268]. Additionally, the dilute concentration also means that exsolvable ions need to travel a long distance from the bulk to the surface, so this diffusional process will have larger influence on the extent of exsolution. To solve this problem, the microstructure of the perovskite needs to be modified to reduce the grain size, so it is easier for noble metal ions in the bulk to reach the surface and consequently be exsolved. The grain size of the perovskite can be reduced directly by lowering the phase formation temperature (sintering temperature) during synthesis, as normally larger grains are prone to form at higher temperatures.

Secondly, using the lower sintering temperature is also an inevitable choice to substitute noble metals into perovskite lattice. The oxides of certain noble metals are known to spontaneously convert to the corresponding metals at temperatures of ~1150 °C [269]. For instance, Rh_2O_3 was used as the Rh precursor in the preparation, and the changes of Gibbs free energy of Rh_2O_3 converting to metallic Rh can be found from thermodynamic database, as shown in Figure 7-20. It can be anticipated that the change of Gibbs free energy will become negative at the temperatures above ~1126 °C, and then Rh_2O_3 will convert to Rh spontaneously. If this happens during the phase formation step of perovskite, instead of being accommodated into the perovskite lattice, the newly formed metallic Rh will become secondary phases isolated from the perovskite structure.
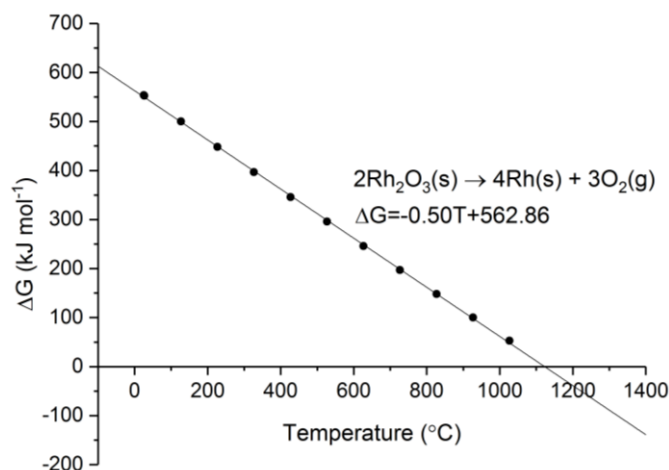
Figure 7- 20 Changes of Gibbs free energy of the reaction of Rh_2O_3 converting into Rh and O_2 as a function of temperature.

Therefore, the modified solid-state method must be further improved by changing the sintering conditions for the Rh-substituted perovskites. Different sintering conditions were investigated, including high temperature with short duration and low temperature with long duration, and the undoped perovskite composition $La_{0.4}Ca_{0.4}TiO_3$ (referred to as Rh0 henceforth) was used to show if pure perovskite phase could be formed by using these sintering conditions. Additionally, the perovskite Rh0 would also be tested in the later catalytic experiments to show the activity of the perovskite support only. The XRD results of Rh0 samples prepared by using different sintering conditions are shown in Figure 7-21, and it can be found that all three samples showed good purity of the perovskite phase and there is no obvious difference between these samples. This indicates that the perovskite phase can be well formed when sintered at 1100 °C for 24 hours. Combining the results above, 1100 °C and 24 h dwell time are likely to be the optimum conditions for the sintering step in the synthesis, as the relatively low temperature could reduce the grain size of the produced perovskite as well as preventing Rh_2O_3 converting to Rh metal.
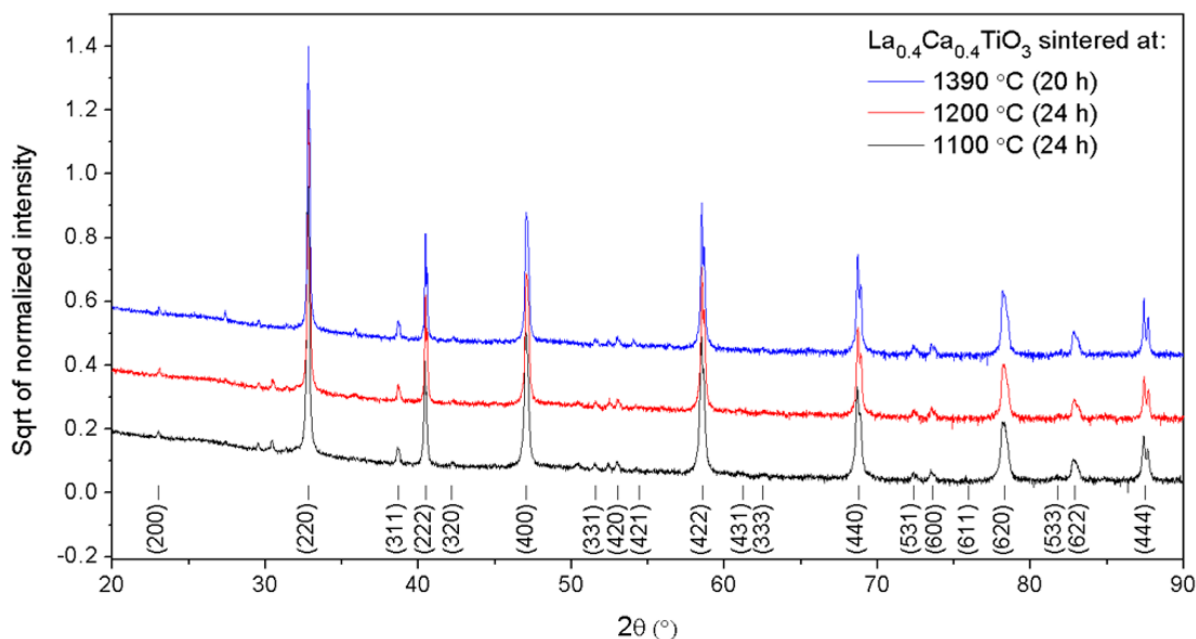
Figure 7- 21 Powder XRD patterns of the $La_{0.4}Ca_{0.4}TiO_3$ samples which were sintered at 1390 °C, 1200 °C and 1100 °C, respectively. Theoretical positions for reflections are also labelled.

By using the new sintering conditions (1100 °C and 24 h), a series of perovskite compositions ($La_{0.43}Ca_{0.37}Rh_xTi_{1-x}O_3$) which contain only dilute concentrations of Rh were prepared. The values of x were taken as 0.01, 0.03 and 0.06 (hence the corresponding samples will be called Rh1, Rh3 and Rh6), respectively, which means that Rh occupies 1 at%, 3 at% and 6 at% on the B-sites of perovskite (or equivalently 0.6 wt%, 1.8 wt% and 3.6 wt% in the total material). The XRD results of the as-prepared Rh1, Rh3 and Rh6 are shown in Figure 7-22 in which the undoped Rh0 is also included as the reference. It was found that the XRD patterns of these samples were similar, except for some slight peak shifts that varied with the substitution level of Rh, indicating the changes of the cell parameter with the insertion of different amounts of Rh in the perovskite lattice. Moreover, there was no significant reflection of secondary phases that could be identified, indicating the preparation method worked successfully for all these compositions.
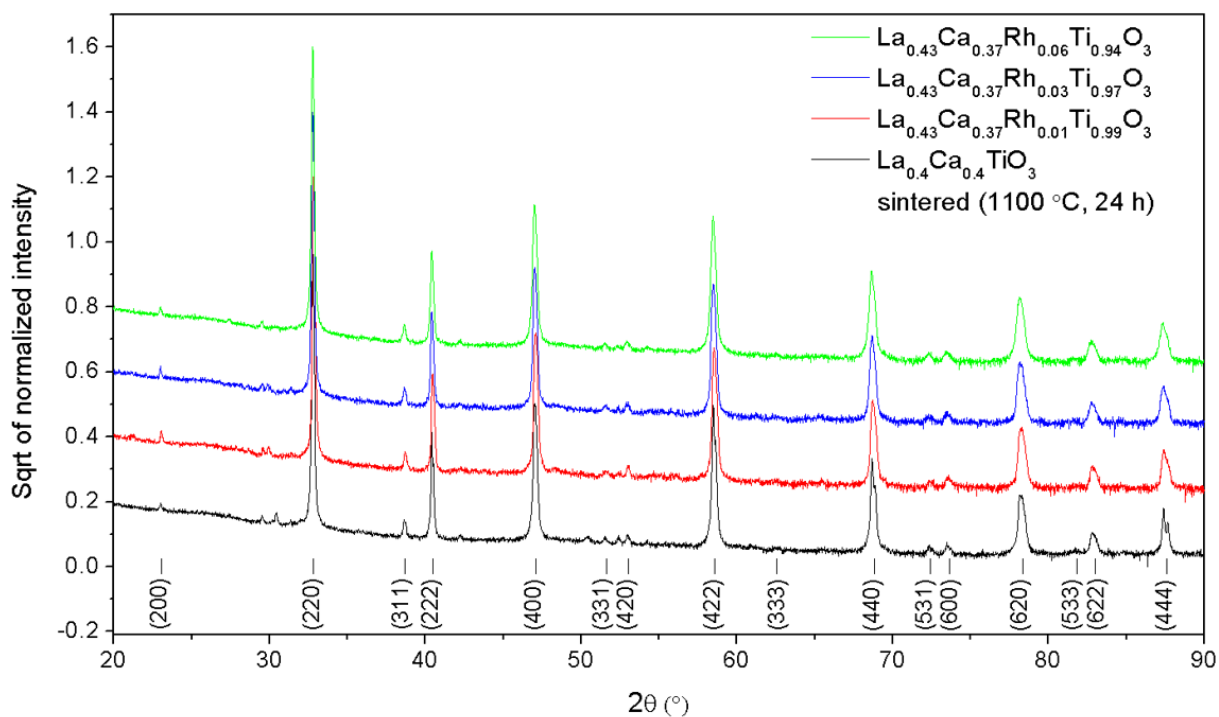
Figure 7- 22 Powder XRD patterns of the $La_{0.43}Ca_{0.37}Rh_xTi_{1-x}O_3$ samples (x=0.01, 0.03 and 0.06) which were sintered at 1100 °C for 24 hours, and comparison with the $La_{0.4}Ca_{0.4}TiO_3$ sample sintered under the same conditions. Theoretical positions for reflections are also labelled.

By checking the splitting (or broadening) of the primitive peaks and the appearance of the superlattice reflections (as summarized in Table 7-1), it was found that all the perovskites prepared in this section (Rh0, Rh1, Rh3 and Rh6) showed almost the same crystal structures: splitting (or broadening) of (h00) and (hhh) peaks (such as (400) and (222)) was observed for all the samples, while none of the (hh0) peak was found split or broadened; for superlattice reflections, only (ooo) peaks were present while all the (ooe) and (eeo) reflections were absent. Therefore, the most likely space group was anticipated to be orthorhombic *Imma* for all the perovskites prepared in this section, and this space group was confirmed in the Rietveld refinement (here the setting of *Ibmm* was used) for each sample as shown in Figure 7-23. Besides, it was discussed in subchapter 7.2.4 that $La_{0.43}Ca_{0.37}Ni_{0.06}Ti_{0.94}O_3$ also has the same structure. This means that accommodating small amounts of Rh or Ni on the B-sites in the original perovskite ($La_{0.4}Ca_{0.4}TiO_3$) did not have significant effects on the lattice and hence the structure was almost retained. Because the structure of the perovskites prepared here is very similar as that of $La_{0.43}Ca_{0.37}Ni_{0.06}Ti_{0.94}O_3$ that has been demonstrated before in Figure 7-19, it will not be repeated here.

Table 7- 1 Determining the crystal structures of $La_{0.4}Ca_{0.4}TiO_3$ and $La_{0.43}Ca_{0.37}Rh_xTi_{1-x}O_3$ by checking the primitive and superlattice peaks in their XRD patterns.

Composition	$La_{0.4}Ca_{0.4}TiO_3$	$La_{0.43}Ca_{0.37}Rh_xTi_{1-x}O_3$		
	-	X=0.06	X=0.03	X=0.01
(h00) split/broaden	√	√	√	√
(hhh) split/broaden	√	√	√	√
(hh0) split/broaden	-	-	-	-
Symmetry	Orthorhombic			
(ooo)	√	√	√	√
(ooe)	-	-	-	-
(eeo)	-	-	-	-
Tilting	Out-of-phase			
Anticipated space group	*Imma*			
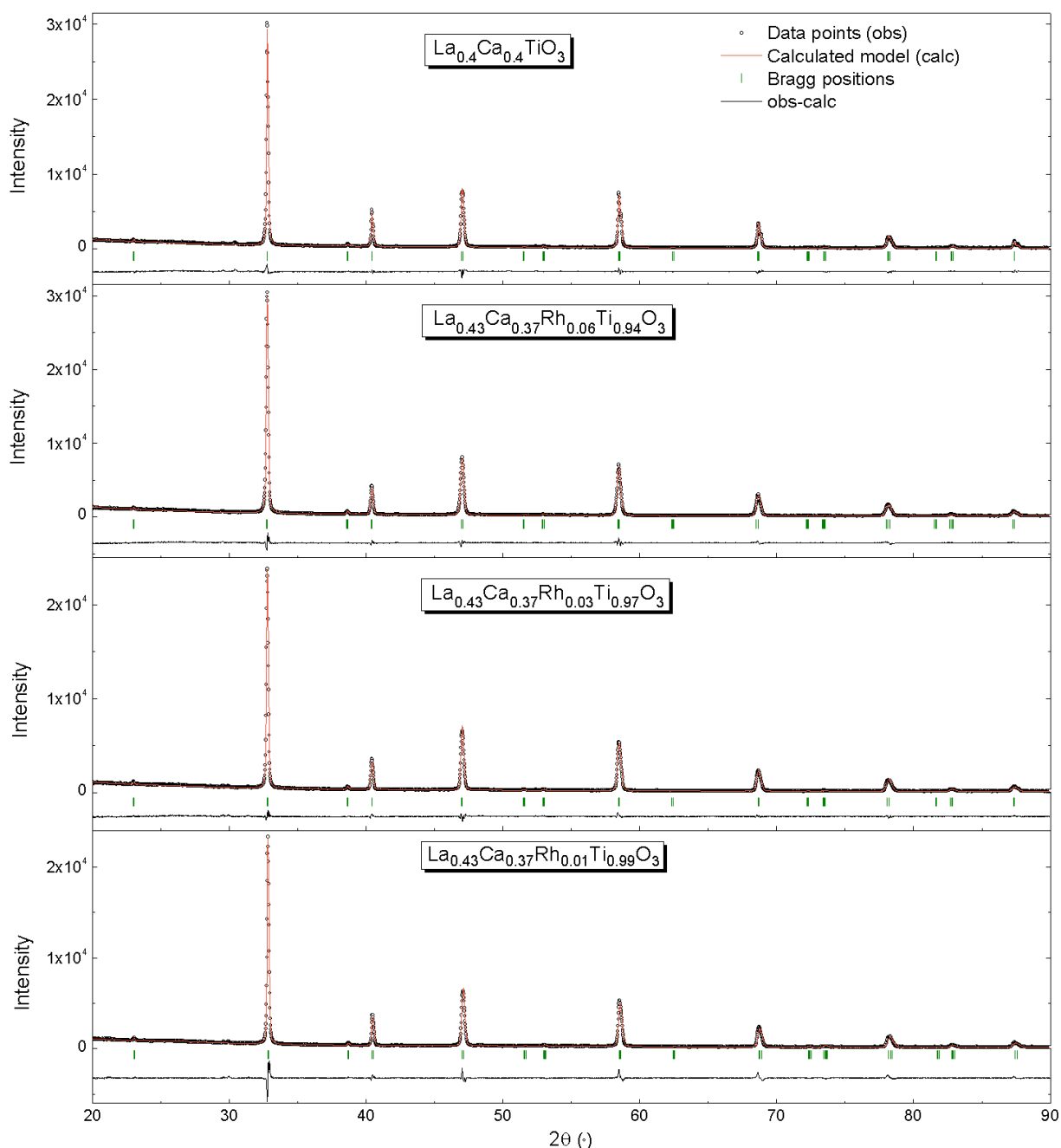
Figure 7- 23 Rietveld refinements of $La_{0.4}Ca_{0.4}TiO_3$ and $La_{0.43}Ca_{0.37}Rh_xTi_{1-x}O_3$.

In spite of the similar crystal structure, the perovskites Rh1, Rh3 and Rh6 contain different concentrations of Rh ions in their lattice as illustrated in Figure 7-24. It can be found that in the lattice of perovskite Rh1, the amount of Rh ions is indeed very dilute and they could interact quite strongly with the lattice, which would consequently make the exsolution of Rh difficult to happen.
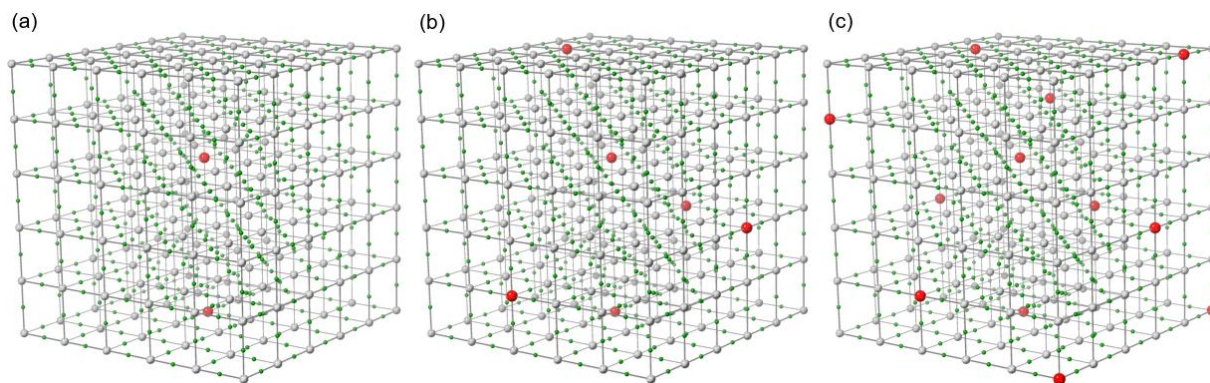
Figure 7- 24 Illustration of different substitution levels of Rh in perovskites of $La_{0.43}Ca_{0.37}Rh_xTi_{1-x}O_3$ (x=0.01, 0.03 and 0.06) in (a), (b) and (c), respectively. Grey, green and red balls represent Ti, O and Rh ions, respectively. For simplicity, A-site cations are not shown in the structure.

Based on the results of Rietveld refinement, the pseudocubic cell parameters for these perovskites (a_p) can be calculated as:

$$a_p = \sqrt[3]{\frac{V}{4}}$$

Equation 7-9

where V is the volume of the perovskite unit cell obtained from Rietveld refinement. The cell parameter can be plotted as a function of the substitution concentration of Rh on the B-sites (Figure 7-25(a)), with very small errors, indicating the high quality of data refinement. It was found that the cell parameters of perovskite Rh0, Rh3 and Rh6 followed a linear relationship, while the sample Rh1 was out of this relationship and its cell parameter was smaller as compared with the other samples, which might imply different oxidation states of Rh in these perovskites. It seems that Rh was substituted at similar oxidation state (probably +3/+4) in perovskite Rh3 and Rh6, and hence their cell parameter would increase linearly with the Rh substitution level. However, the drop of the cell parameter for Rh1 implies that Rh ions were substituted with a higher oxidation state (probably +4) and hence smaller size in the lattice. In order to support the conclusions drawn above, these perovskites were also analysed by X-ray photoelectron spectroscopy (XPS) which revealed the oxidation states at the perovskite surface. Firstly, the core level spectra of La, Ca, Ti and O are shown in Figure 7-25(b), and there was no obvious difference that can be found in these spectra, implying the unaltered oxidation state and coordination environment of these elements in the materials analysed. Regarding the core level spectra of Rh (Figure 7-25(c)), the intense peak appearing at the binding energy of ~309.5 eV could be caused by both

Rh^{3+} and Rh^{4+} depending on their coordination environment according to previous report [270], so it cannot tell the exact oxidation state of Rh. However, a small peak appearing at ~307.7 eV are found for both Rh3 and Rh6, which can be an indication of Rh^{3+} in the Rh$_2$O$_3$ environment according to the literature [271], but this peak seems to be absent for Rh1. To get more evidence of the oxidation state of Rh, the valence band spectra were checked, as Greiner et al. reported that the valence band spectra of transition-metal oxides are affected by d-band occupancies [272]. Based on the valence band spectra shown in Figure 7-25(d), a significant fraction of Rh shows the oxidation state of +3 in both Rh3 and Rh6, while all the Rh in Rh1 seems to be in the +4 state. Therefore, all the evidence provided above shows the higher Rh oxidation state (+4) in Rh1, and this might indicate the stronger interaction between Rh ions and the perovskite lattice in the highly dilute system, which forced the oxidation state of Rh to be closer to that of the host cation Ti which is stable at +4 in the lattice.
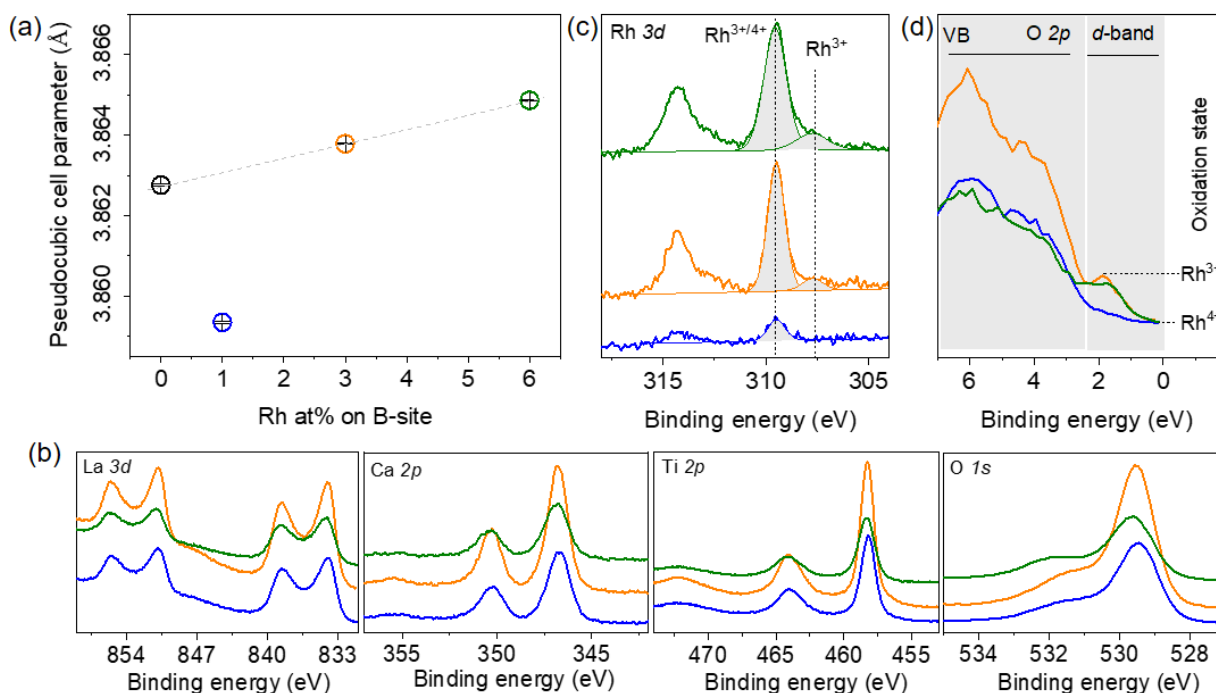
Figure 7- 25 Changes of cell parameter and oxidation states with the substitution level of Rh. (a) Pseudocubic unit cell parameter as a function of Rh substitution on the B-sites. (b) Core level spectra of La, Ca, Ti and O in different perovskites. (c) Core level and (d) valance band spectra of Rh.

The microstructure of the prepared perovskites was obtained by SEM (exemplified by Rh6 in Figure 7-26). It can be found that by reducing the sintering temperature during synthesis, highly porous perovskites were produced, and the grain size of these perovskites was ~500 nm which was much smaller as compared to the perovskites

prepared via the conventional solid-state method where the grain size can be ~50 µm. As mentioned before, the smaller grain size and higher porosity can not only promote more Rh ions to diffuse to the surface and get exsolved, but also benefit the performance in heterogeneous catalysis.
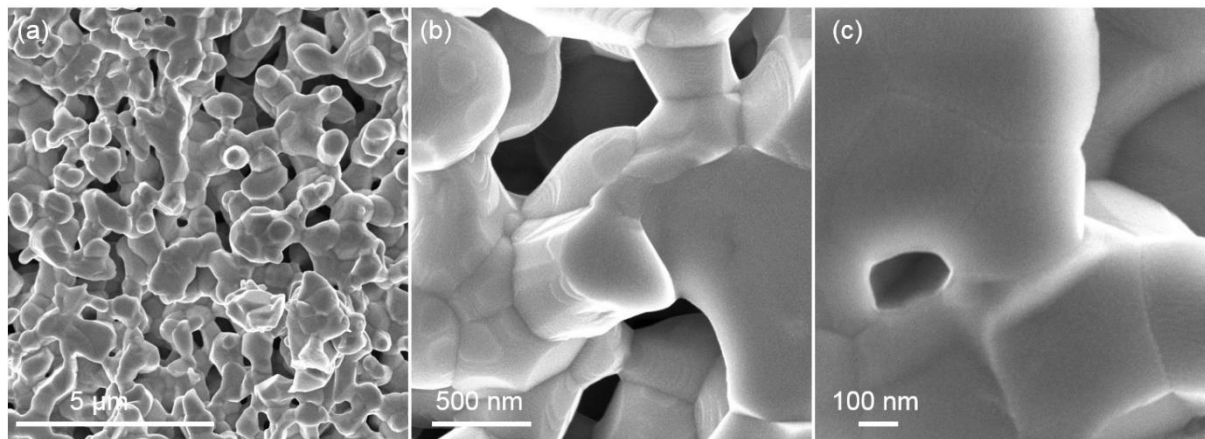
Figure 7- 26 Microstructure (SEM) of the perovskites sintered at 1100 °C (exemplified by $La_{0.43}Ca_{0.37}Rh_{0.06}Ti_{0.94}O_3$) to show their porosity and grain size.

To conclude, by modifying the conventional solid-state method and some key conditions in the procedures, single-phase perovskites with various compositions (including the Rh-substituted ones) can be successfully prepared. More importantly, this modified solid-state method allows for the precise control over the stoichiometry to change the concentration of Rh in the perovskite, and the high porosity and small grain size can be achieved as well. Within the perovskites prepared, the Ni-based perovskites were mainly used in the mechanistic study of the exsolution process in situ in ETEM. For the Rh-based perovskites, efforts were made to promote more exsolution of Rh and control the particle characteristics by controlling different parameters, aiming to improve their catalytic activity for the model reaction of CO oxidation. These investigations will be discussed in the following subchapters.

7.3 Mechanistic study of nanoparticle exsolution via in situ observation in ETEM

In order to further tune the properties of the exsolved materials to improve their catalytic activity and stability, the better understanding of the mechanism of the exsolution process is desired. To obtain the insight into the changes happening on the perovskite surface during exsolution, the state-of-the-art environmental transmission electron

microscope (ETEM) was used, which allowed for the in situ observation of the formation process of individual nanoparticles with ultra-high spatial and temporal resolution. The in situ observation did not only reveal the atomic-scale process of the particle nucleation and growth, but also demonstrated the formation process of the unique socketed interface between the exsolved particles and the perovskite support. The high-resolution data not only showed these phenomena qualitatively, and more importantly, it allowed for the quantitative analysis to obtain deeper understanding of the processes by fitting the data with some theoretical models in literature [268, 273]. Moreover, it was also demonstrated that the shape of the exsolved particles as well as the nanointerfaces between the exsolved particles and their underlying oxide can be modified by controlling the atmosphere during the exsolution process.

7.3.1 Designs of in situ observation of exsolution

As mentioned before, two types of Ni-based perovskites with different concentrations of exsolvable ions were prepared for the in situ observation experiments of exsolution. One is the low Ni substituted composition $La_{0.43}Ca_{0.37}Ni_{0.06}Ti_{0.94}O_3$ in which Ni only occupies 6 at% of the B-sites in the perovskite lattice. The other one is the high Ni substituted $La_{0.8}Ce_{0.1}Ni_{0.4}Ti_{0.6}O_3$ that contains 40 at% Ni on the B-sites. These two compositions are representative for a wide range of the exsolved structures and the respective applications reported in literature.

The exsolved materials have been investigated in different applications, and normally the required particle sizes can vary between 5 and 50 nm [274]. In order to observe the formation of metal nanoparticles in this size range, TEM would be the appropriate technique, not only because it can provide atomic-scale images of the material, but also due to its "see-through" (perspective) ability as it employs an electron beam to pass through a small area of the specimen for imaging as introduced in Chapter 3, which allows for the simultaneous observation of the particle, the perovskite support and their interface. During the observation in TEM, the edges of the grains (Figure 7-27(a)) should be focused because the observing region must be thin enough to allow the electron beam to pass through. More importantly, the sample needs to be oriented along a major crystallographic axis, hence the atoms can align well in the images and the data obtained will be more meaningful. Moreover, the conventional TEM is operated under vacuum and at normal temperatures, while here the images need to be acquired under gas environments and at elevated temperatures, which poses

obstacles for maintaining the high resolution and avoiding drift and misalignment of the sample during the heating steps [275]. The latest generation ETEM (TITAN G2 80-300 kV from FEI) equipped with an objective Cs aberration corrector and a double tilt holder was used, and the system can be operated under the gas pressure up to 20 mbar and at temperatures up to 1300 °C [105]. The high-performance nano-chips (from DENSolutions) were used to stabilize the sample to reduce the effect of thermal drift during heating. 4K videos of the exsolution process were recorded at a spatial resolution of 0.09 nm in TEM mode and a time resolution of ~50 ms (20-30 frames per second).

7.3.2 Formation of the socketed interface

Firstly, the formation of the unique socketed interface between the exsolved particles and the perovskite support was studied. The reduction of the powdered sample ($La_{0.43}Ca_{0.37}Ni_{0.06}Ti_{0.94}O_3$) was conducted in situ in ETEM, by using the conditions (20 mbar H_2 and at 900 °C) which are representative for many applications. As the observing region must be thin enough, a target region at the sample edge as labelled in Figure 7-27(b) was selected and several small areas in it were monitored during exsolution. The structural changes observed in a representative area are shown in Figure 7-27(c) as a function of time, and Figure 7-28 shows some key dimensions of the exsolved particle and the perovskite at their socketed interface which changed with time. The nucleation stage of the particle was not recorded in this reduction as it occurred very fast, and hence at the time labelled as t = 0 s, the exsolved particle has already formed with a considerable size (~1 nm and ~3 nm in apparent height and width, respectively). The particle grew larger gradually with time and ended up with the height and width of ~1.7 and ~4.5 nm, respectively at the time t = 250 s. From the snapshots at different times, it can be found that the particle seems to exsolve isotropically, as the height and the width of the exsolved particle increased almost proportionally as indicated in Figure 7-28(c), which means that the basic structure of the particle was maintained during its growth. Moreover, the particle remained in close crystallographic orientation with respect to the perovskite lattice over time, which might imply some interactions between each other.

It is also noticeable from the snapshots in Figure 7-27(c) that apart from the growth of the particle, the perovskite lattice also changed locally around the particle. The surface of the perovskite around the particle was flat initially at t = 0 s, while the elevation of

the perovskite surface at the point of junction with the particle was observed to occur with the exsolution process. Figure 7-28(b) shows that the perovskite surface rose until t = 99 s when it nearly plateaued to be ~1 nm. The elevation of the perovskite lattice could account for the formation of the socketed interface, mainly due to the two observations as discussed below. Firstly, it has been reported that an exsolved particle is around 30% submerged in the perovskite surface [26], and here the final ratio of the elevation of the perovskite lattice and the particle diameter (width) was very close to that value (27%). Secondly, the growth of the particle (height and width) was tried to be fitted by different theoretical models as previously reported by Gao et al [268]:

$$\text{Strain-limited:} \qquad d_s(t) = d_{s0} \left(\ln\left(1 + \frac{t}{\tau_s}\right) \right)^{\frac{1}{3}} \qquad \text{Equation 7-10}$$

$$\text{Reactant-limited:} \quad d_r(t) = d_{r0} \left(1 - exp\left(-\frac{t}{\tau_r}\right) \right)^{\frac{1}{3}} \qquad \text{Equation 7-11}$$

$$\text{Diffusion-limited:} \qquad d_d(t) = d_{d0} \left(\frac{t}{\tau_d} \right)^{\frac{1}{6}} \qquad \text{Equation 7-12}$$

where d, t and τ denote particle dimension (at a given time and at equilibrium), time and time constant, respectively. These models were established based on three potential factors which may limit the rate of particle growth during the exsolution process [268], including: the strain which is related to the formation of the particle and the interaction between the particle and the perovskite support; the supply of the reactant (the exsolvable ions, Ni in this case) which is dependent on the substitution concentration of metals in perovskite; and the diffusion of these exsolvable ions from the bulk in perovskite to the surface. As shown in Figure 7-28(d), the kinetic data of the particle growth can be well fitted by the reactant- and strain-limited models, which might imply that the particle growth was limited by the supply of exsolvable ions and the strain. Considering the observed elevation of the perovskite lattice, it could generate significant strain effect that might confine the growth of the particle during exsolution. Therefore, the results above indicate that the socket was formed in parallel with the growth of the particle, which could be caused by the local structural change of the perovskite lattice.

From Figure 7-27(c), it was also found that neither the socket nor the particle pinned to it seemed to move or drift throughout the exsolution process, even that two more particles were exsolved in nanoscale proximity of the initially exsolved one, which can

be observed after t = 66 s. This indicates the high stability of the socket structure as well as the strong interactions between the particle and the perovskite support, and they together could explain the strong anchorage of the exsolved particles to the support, even at the temperature of 900 °C.
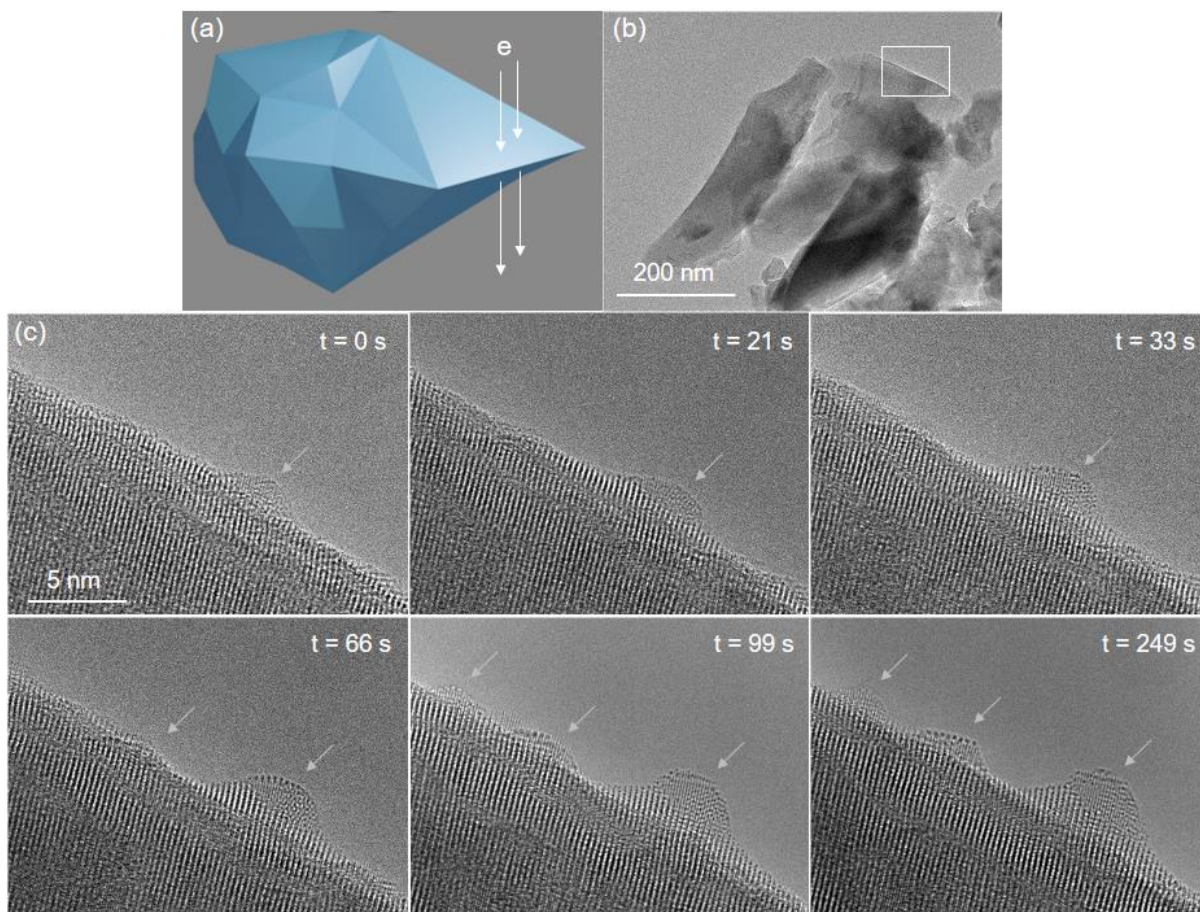
Figure 7- 27 Particle growth and the formation of the socketed interface on $La_{0.43}Ca_{0.37}Ni_{0.06}Ti_{0.94}O_3$ under H_2. (a) Schematic demonstration of a sample particle in a suitable orientation and its edge is selected for TEM imaging. (b) TEM image showing the target region on the edge of a perovskite grain for observation of the particle exsolution. (c) Snapshots of a selected area at different times, showing the structural changes during the exsolution under H_2 at 900 °C.
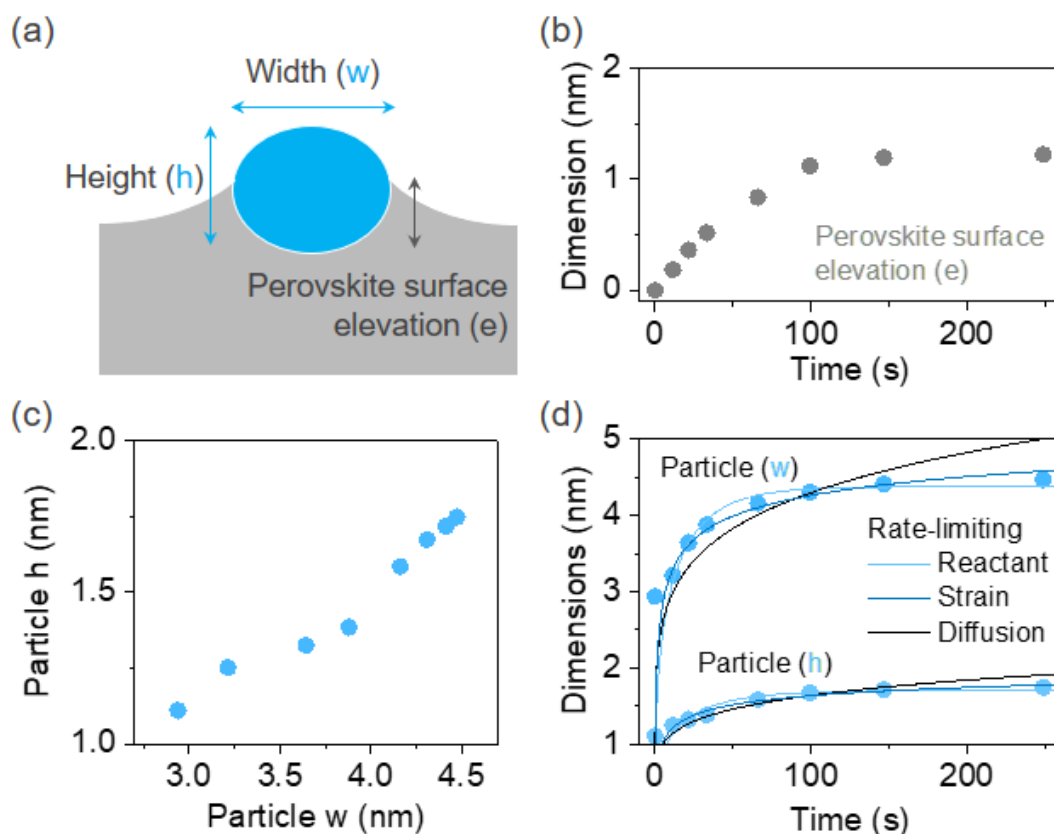
Figure 7- 28 Analysis of the changes of the particle and perovskite based on the snapshots in Figure 7-27. (a) Schematic demonstration of the socketed interface between the exsolved particle and the perovskite, annotated with key dimensions which change with time. (b) Evolution of the elevation of the perovskite lattice in the region adjacent to the exsolved particle with time. (c) Plot of the particle height vs width at different dimensions when particle grows. (d) Evolution of the particle height and width with time, fitted by different models to identify the rate-limiting factor for the particle growth.

The results discussed above were obtained from the low substituted system ($La_{0.43}Ca_{0.37}Ni_{0.06}Ti_{0.94}O_3$), hence the growth of the particle finished at a very early stage due to the limited exsolvable ions. Here the higher substituted system ($La_{0.8}Ce_{0.1}Ni_{0.4}Ti_{0.6}O_3$) was tested as well, to investigate if the particle can still be firmly anchored to the socket at the later stage of particle growth and when there are more particles or reactants exsolved from the perovskite. A lamella (Figure 7-29(a)) was obtained from the $La_{0.8}Ce_{0.1}Ni_{0.4}Ti_{0.6}O_3$ sample by using the FIB extraction and it was quickly heated to cause some fractures in the lamella (Figure 7-29(b)), which allowed us to monitor several grains to simultaneously track multiple particles within the relatively narrow field of view. The sample was heated in situ in H_2 atmosphere at 650 °C and the overviews of a big selected area before and after the reduction can be found in Figure 7-29(c) which indicates that abundant particles were exsolved in

nanoscale proximity of each other. Two smaller areas (A1 and A2) were selected in which multiple particles were tracked at different times during the later stages of the particle growth. The selected area A1 (Figure 7-29(d)) shows that the 7 tracked particles were all pinned to their original positions but just grew ~40% larger in size (Figure 7-29(f)) before and after 10 and 30 min of elapsed time. Evolution of the tracked particles in the other area A2 was recorded at a higher magnification (Figure 7-29(e)), which also shows no movement or drift of the particles, although the particle growth in this area seems to stabilize faster as compared to A1. These observations indicate that the exsolved particles are still immobile on the perovskite surface during the later stages of the particle growth, which is consistent with the findings from the early stages as shown above, even though stronger particle-particle interactions may exist because of the higher concentration of particles.
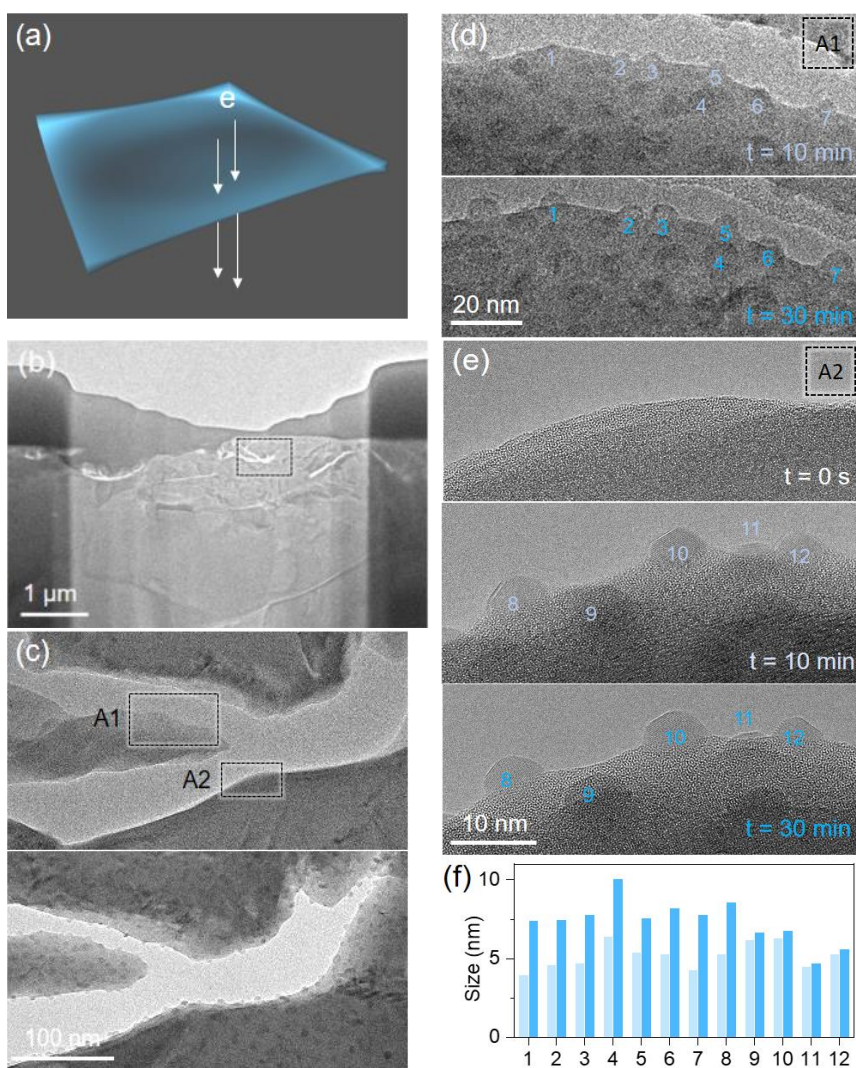
Figure 7- 29 Tracking particle anchorage on $La_{0.8}Ce_{0.1}Ni_{0.4}Ti_{0.6}O_3$ under H_2. (a) Schematic demonstration of a lamella of the perovskite sample obtained by using FIB extraction, in a suitable orientation for TEM imaging. (b) TEM image showing the perovskite lamella which has fractures. (c) Selected area of the lamella before and

after the exsolution under H_2 at 650 °C. (d) Selected area (A1) of the lamella, showing the particle growth at different times, with the tracked particles labelled. (e) Selected area (A2) of the lamella, showing perovskite surface before exsolution and the particle growth at different times during exsolution, with the tracked particles labelled. (f) Sizes of the tracked particles at early (light blue) and later (blue) growth stages, respectively.

Different mechanisms of the particle formation process during the exsolution have been proposed to explain the formation of the unique socketed particle-perovskite interface. In a widely accepted mechanism, the exsolvable ions would form a metal nucleus within the oxide matrix, and it would grow into a nanoparticle of a critical size which would then move towards the surface and be expelled from the perovskite lattice (Figure 7-30(a)) [276]. The movement of the particle pre-formed in the bulk to the surface could explain the formation of the socket and the partly immersion of the particle in the oxide, but contradictorily we did not observe any particle moving within the perovskite lattice towards the surface throughout the particle growth process. Moreover, it has been shown that the particle nucleation would be more difficult to occur in the bulk of the oxide as compared to on its surface, because of the high energy barrier arising from the strain and the oxide lattice reconstruction around the particle within the oxide [268, 276]. All the observations of the particle growth process shown above indicate that the particles nucleate near the surface of the perovskite, and then they grow larger epitaxially and isotropically at the initial points where they nucleated without moving or drifting. In parallel to the particle growth, the perovskite lattice rises synchronously around the particles, probably because the particles grow partly in the oxide and hence gradually pushing the perovskite lattice to rise laterally, which could explain the formation of the socketed interface between the exsolved particle and the perovskite support.
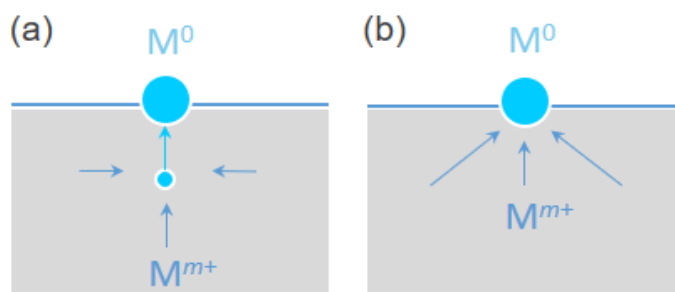
Figure 7- 30 Possible mechanisms for metal exsolution. (a) exsolvable ions nucleate just under the free surface to grow particle to a critical size and then it is expelled out of the perovskite lattice remaining partly immerged in the perovskite; (b) exsolvable ions diffuse to the perovskite surface where they get reduced and form a nucleus which is then grown larger by the following ions.

7.3.3 Determining exsolution dynamics via direct visualization of particle nucleation and growth

As shown in the last section, when the perovskites (both the high substituted and the low substituted compositions) were reduced in H_2 atmosphere in situ in ETEM, the very first stage of the exsolution when the particle started to nucleate and grow occurred too fast to be recorded in videos. It is well known that the reducing atmosphere can facilitate the exsolution process. Therefore, here attempts were made to replace the commonly used reducing atmosphere with the vacuum environment in order to slow down the exsolution process so that the nucleation and the initial growth stages of the exsolved particle could be visualized in situ in ETEM. The low substituted composition $La_{0.43}Ca_{0.37}Ni_{0.06}Ti_{0.94}O_3$ was used, as the low concentration of Ni^{2+} ions could also make the exsolution process slower. The sample was reduced in vacuum at 900 °C in ETEM, and the results indicate that such conditions were capable to trigger the metal exsolution from the perovskite, which will be shown below.

Figure 7-31(a) shows one of the Ni nanoparticles obtained from the reduction in vacuum as mentioned above. It can be found that, unlike the approximately spherical particles exsolved under the H_2 atmosphere, this particle exsolved under the vacuum environment had a highly faceted shape. The high resolution of the TEM result allowed for clear visualization of the crystal structures of both the Ni nanoparticle and the perovskite as well as the details of their interface (Figure 7-31(b)). Firstly, according to the structure and the lattice spacing of the Ni crystal (Figure 7-31(a and b)), this particle exsolved under vacuum still seems to be metallic Ni, and the exposed facets of this particle were (111), (11-1) and (100) as labelled in Figure 7-31(a). Also, this particle was still partially immerged in the perovskite lattice and there seems to be epitaxial relationship between them, as Figure 7-31(a) shows that some part of the Ni metal lattice was interwoven with the perovskite lattice under the surface. The epitaxial relationship between the exsolved particle and the host oxide has been reported before for the exsolution under H_2 atmosphere [26], and here the highly clear alignment between the lattices of these two phases confirmed the similar particle-oxide interactions when the exsolution was carried out under vacuum (Figure 7-31(b)). Similar to the Ni crystal as mentioned above, the orientation of the perovskite crystal can also be identified based on its lattice spacing, and hence the 3D models can be built (Figure 7-31(c and d)) to show the lattice information revealed by Figure 7-31(a and b), respectively. The orientation relationship shown here is consistent with some

previous reports in which they found that ions prefer to diffuse along the [110] orientation within the perovskite [26, 248].
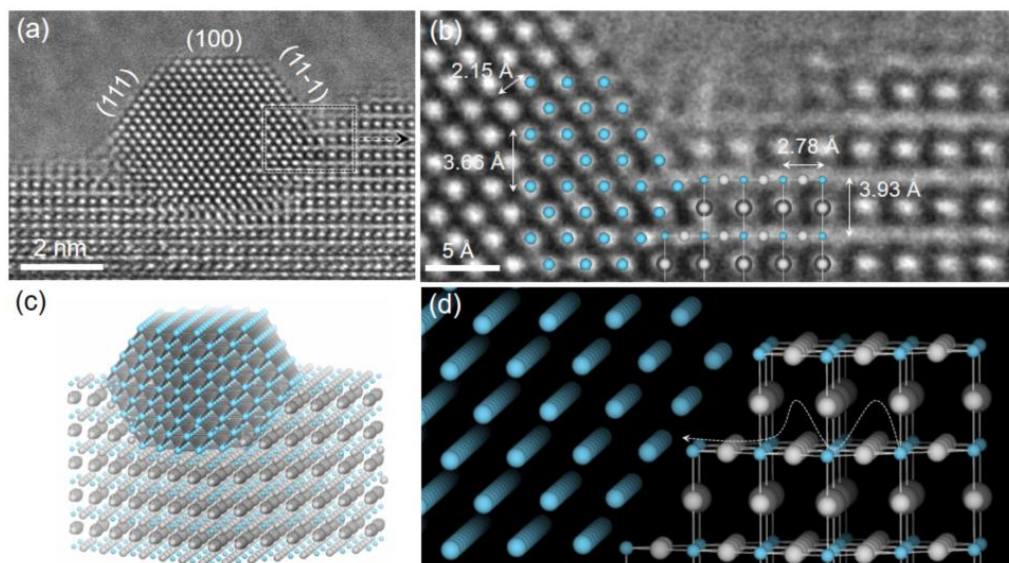
Figure 7- 31 Particle-perovskite interface alignment. (a) TEM image of Ni nanoparticle exsolved from $La_{0.43}Ca_{0.37}Ni_{0.06}Ti_{0.94}O_3$ in ETEM, under vacuum at 900 °C. (b) Details of the interface between Ni nanoparticle and perovskite, with an overlay showing the Ni metal and perovskite lattices in their respective orientations. (c) 3D model built based on the crystallographic relationships highlighted in (a) and (b). (d) Details of the 3D model which highlights the diffusion pathway of Ni^{2+} in the perovskite lattice towards Ni nanoparticle.

As expected, the exsolution process was slowed down by reducing the low substituted composition in the vacuum atmosphere, so the nucleation and the early stage of particle growth were recorded in the selected area. Selected snapshots (Figure 7-32(a)) of the chosen area show the evolution of the particle at different times during the exsolution process. The dimensional data (width and height) of the particle were extracted from these TEM snapshots and are shown in Figure 7-32(b) as a function of time (logarithmic scale). No nanoparticle or nucleus was observed initially (t = 0 s), but the nucleation process took place extremely fast, within 0.2 s. Moreover, the subsequent growth was also fast and the particle grew to around 1 nm within 0.4 s, after which a plateau was observed where the particle growth stagnated for around 10 s. Then the particle growth restarted and its rate seemed to accelerate between 10 and 100 s until reaching another plateau. The plots in Figure 7-32(b) indicate that the growth of the particle was not a continuous process during the exsolution, but it kept switching alternately between the periods of hiatus and the period of sudden and fast growth. Despite this, it was found that the particle still grew isotropically as its overall shape was almost retained (nearly constant ratio between the particle height and width

150

as shown in Figure 7-32(c)) throughout the exsolution process, which is consistent with the observation under H_2 atmosphere as discussed above.
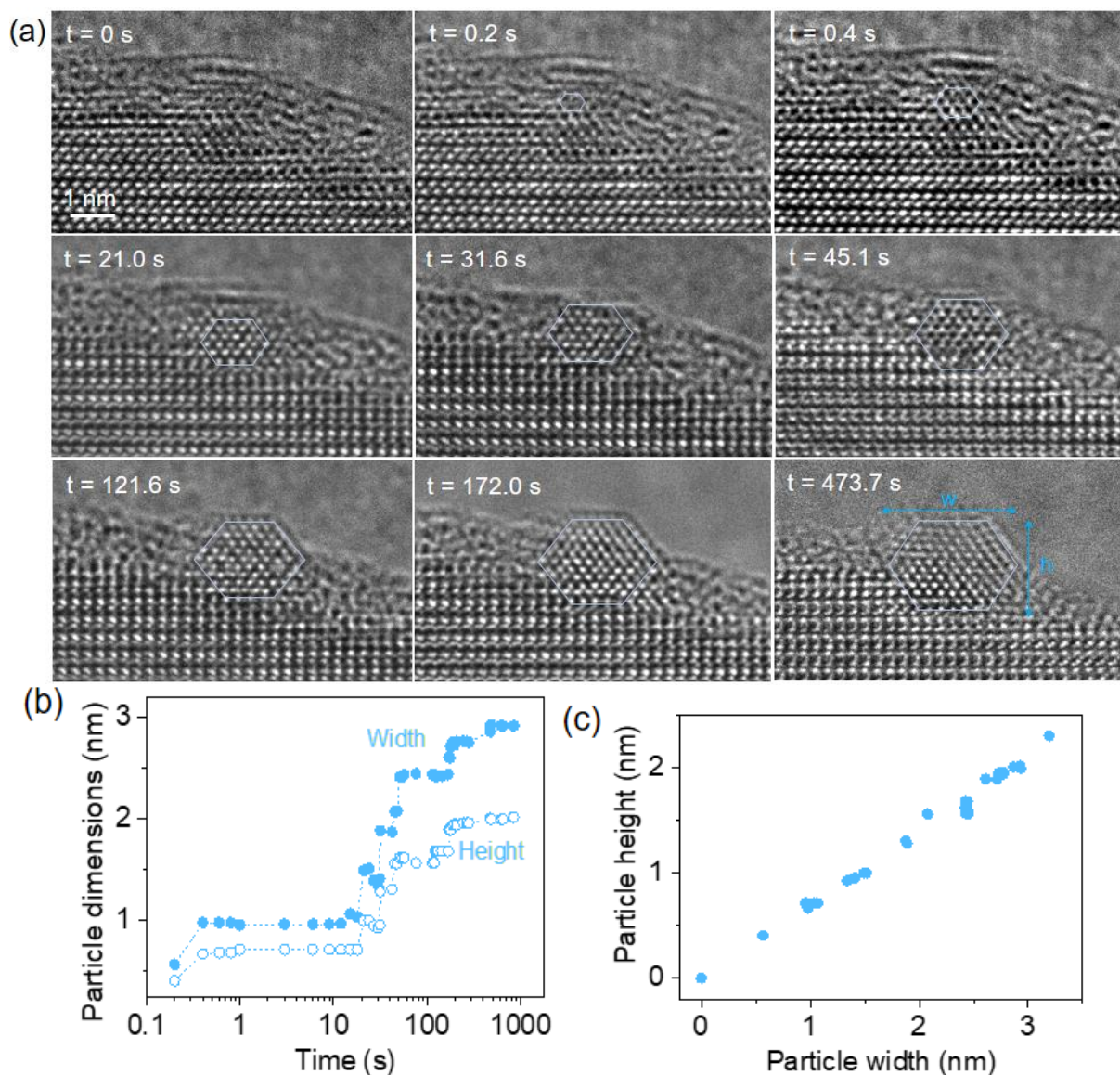
Figure 7- 32 Visualization of particle nucleation and growth during exsolution. (a) TEM snapshots showing the exsolution of Ni nanoparticle from $La_{0.43}Ca_{0.37}Ni_{0.06}Ti_{0.94}O_3$, at different times, during the in situ reduction in ETEM under vacuum at 900 °C. The contours were added to highlight the growth of the nanoparticle. (b) Evolution of the particle dimensions (width and height) with time, based on the TEM images selectively shown in (a). (c) Plot of the particle height vs width at different dimensions, based on the data shown in (b).

Knowing the orientation of the Ni particle from Figure 7-31 and the isotropic nature of the particle growth, 3D models of the particle at different times can be built based on the dimensional data from Figure 7-32, following the steps as introduced here. A model of cubic crystal of Ni metal was imported into CrystalMaker to serve as the starting material for reconstruction, and it was rotated to the same orientation as that was observed for the Ni particle in Figure 7-31 (orientation can be determined by crystal

structure and lattice spacing). As a starting material, the cubic model must be larger than the actual particle in Figure 7-32, hence the number of cells involved in the cubic model was adjusted to ensure that its dimension exceeded the size (width) of the actual particle. The three exposed facets of Ni particle have been shown in Figure 7-31(a), hence two sets of these planes were inserted at both the top and the bottom of the cubic model symmetrically. These planes formed the contour of the particle, and by moving their positions, the height and width of the particle inside the contour can be adjusted to the dimensions given in Figure 7-32(b). Finally, the atoms outside the contour were removed, leaving the 3D model of the particle.

The 3D models at some key stages are shown in Figure 7-33(a), and from which the number of the exsolved Ni atoms in the particle at the respective stages can be estimated (Figure 7-33(b)). The evolution of the number of the exsolved Ni atoms in that particle was fitted with theoretical models derived from Equation 7-10, 7-11 and 7-12 as shown before, aiming to identify the limiting factors for the particle growth during the exsolution. Figure 7-33(b) shows that the particle growth data was best fitted by the reactant-limited model, followed by the strain-limited model, and hence the particle growth was likely to be limited by the locally available concentration of exsolvable ions and the strain from the perovskite lattice due to the confined nature of exsolved particles. However, it is surprising to find that ion diffusion, which was expected to be the rate limiting step due to the relatively low diffusion of ions, did not appear to be the major factor which limited the growth of the exsolved particle at this temperature. The depth within the perovskite from which exsolvable ions were drawn to form the particle of ~3 nm is shown as a function of time in Figure 7-33(c) and it is of the order of 10 nm. The particle and the relative volume of the perovskite needed to contribute ions to form that particle are shown in Figure 7-33(d). Comparatively speaking, the depth from which the ions were exsolved is considerable, as Figure 7-33(d) shows that ions do need to diffuse across a few tens of layers of perovskite unit cells to be exsolved. The relation between the exsolved particle size and the exsolution depth is consistent with the results in literature that reported that for ~30 nm particles exsolution does not use ions from the depth further than around 100 nm within perovskite [26, 253]. These results suggest that it is important to reduce the grain size of exsolved materials to maximise the exsolution process. For instance, to exsolve particles of ~30 nm, it would be good to use perovskite with the grain size no larger than 200 nm, hence all volume in perovskite can contribute to exsolution.
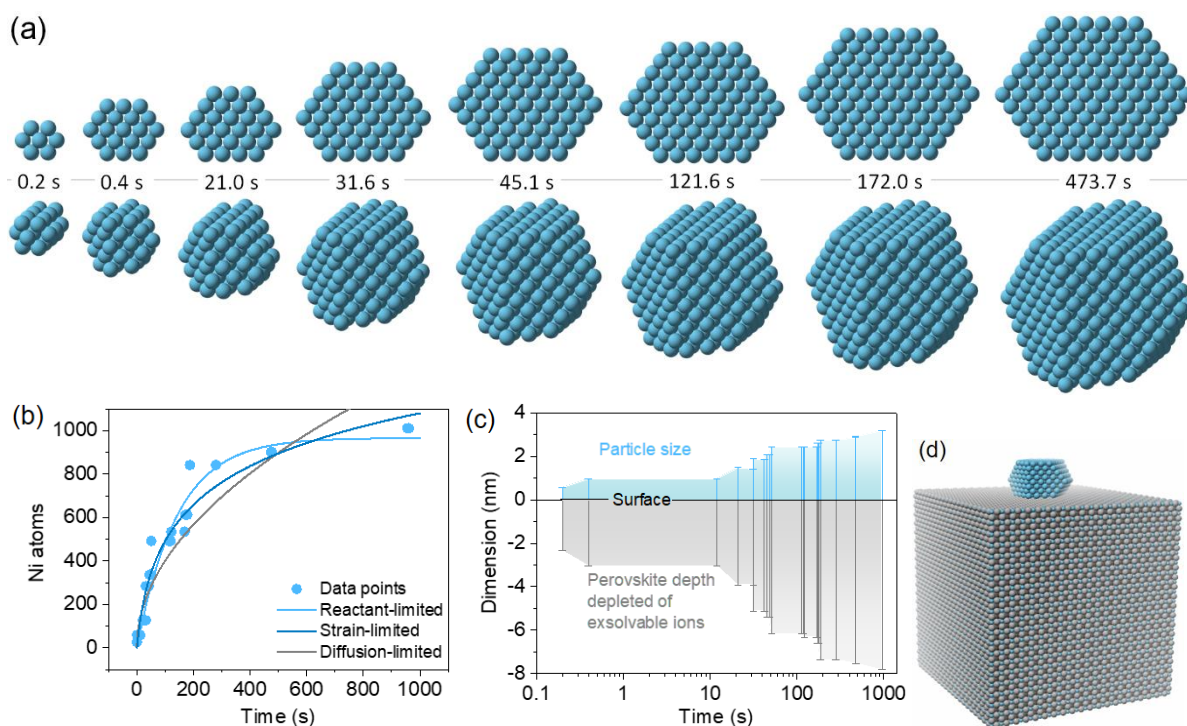
Figure 7- 33 Mechanistic insight into exsolution at the atomic scale. (a) 2D and 3D models of the exsolved Ni nanoparticle at different times during the reduction, built based on the TEM data shown in Figure 7-32. (b) Plot of the number of Ni atoms involved in the exsolved nanoparticle at different times, calculated based on the models selectively shown in (a), and the plot is fitted by different models to identify the rate-limiting factor for the particle growth. (c) Plot of the size (width) of the exsolved nanoparticle and the corresponding depth within the perovskite which has been depleted of Ni^{2+} ions. (d) 3D model showing the final stage of the exsolved nanoparticle and the corresponding volume of perovskite which is required to contribute to the growth of this nanoparticle.

7.3.4 New exsolved nanostructures

It was found from the results above that the particles exsolved in situ in ETEM under the H_2 atmosphere showed the approximately spherical or ellipsoidal shape (as shown in Figure 7-27 and 7-29), which was consistent with most observations of the exsolved particles reported in the literature. Nevertheless, Figure 7-31 showed that the particle exsolved under vacuum in ETEM had a highly faceted shape, which was distinctive from the ones exsolved under the H_2 atmosphere. Interestingly, the particles exsolved under vacuum still seem to disperse homogeneously at different locations on the perovskite (e.g. an atomically flat surface, or near the edges of terraces), similar as the analogues exsolved under H_2 atmospheres. Moreover, particles exsolved under vacuum at different positions on the perovskite surface are shown in Figure 7-34(a) and it was found that all these particles had the same shape and the same orientation

153

with respect to the perovskite surface. It indicates that by changing the atmosphere under which the exsolution is conducted, homogeneous metal nanoparticles can be grown from the perovskite and the shape of the particles can be controlled by the atmosphere. Figure 7-34(b) shows another example for this premise, where $La_{0.8}Ce_{0.1}Ni_{0.4}Ti_{0.6}O_3$ was reduced in the 5% CO atmosphere at 900 °C for 10 h. It was found that the particles exsolved under the CO atmosphere were approximately cubic-shaped and they dispersed quite homogeneously as well.
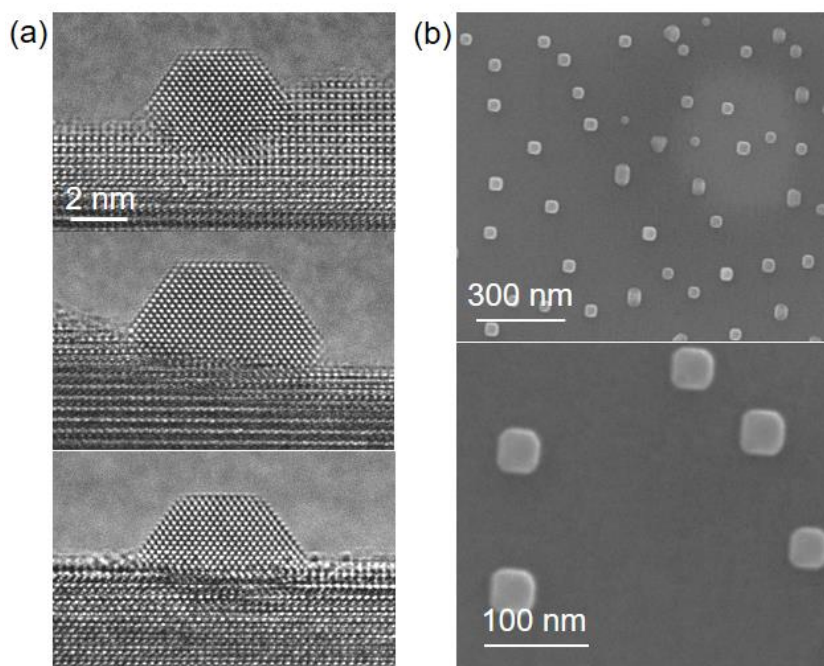
Figure 7- 34 Shape of the exsolved particles controlled by reduction atmosphere. (a) Particles exsolved from different areas of $La_{0.43}Ca_{0.37}Ni_{0.06}Ti_{0.94}O_3$ under vacuum at 900 °C in ETEM, showing the faceted shape. (b) Particles exsolved from $La_{0.8}Ce_{0.1}Ni_{0.4}Ti_{0.6}O_3$ under 5% CO atmosphere at 900 °C for 10 h, showing the approximately cubic shape.

Additionally, some atmospheres may also lead to novel heterostructures. For instance, Figure 7-35(a) shows the perovskite $La_{0.8}Ce_{0.1}Ni_{0.4}Ti_{0.6}O_3$ reduced in the atmosphere of slightly humidified H_2 at 1000 °C for 10 h. It was found that there was an oxide appendage (probably La_2TiO_5 according to the XRD in Figure 7-35(b)) forming adjacent to each exsolved particle, hence forming the new heterostructures, which might also alter the interfacial relationship between the particles and the perovskite support.
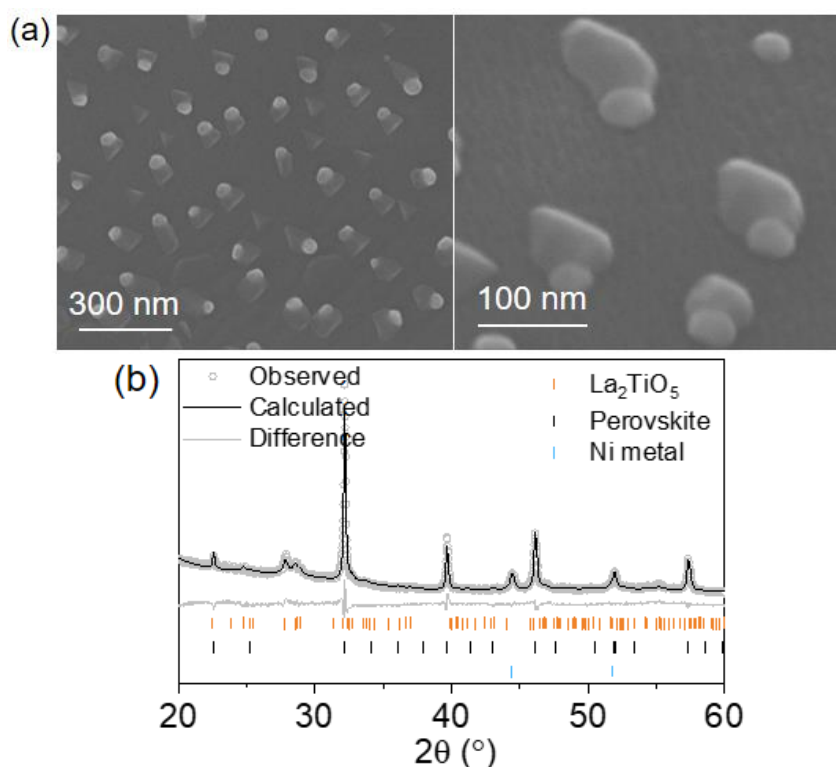
Figure 7- 35 Formation of heterostructures via exsolution. (a) Ellipsoid-shaped particles on the ad-grown oxide (La_2TiO_5), exsolved from $La_{0.8}Ce_{0.1}Ni_{0.4}Ti_{0.6}O_3$ under 2.5% H_2O/5% H_2 atmosphere at 1000 °C for 10 h. (b) XRD result of the sample shown in (a).

These results show the great potential to further tailor the exsolved materials. As mentioned previously, some reactions are structure-sensitive, and hence the exsolved materials can show their advantage in tuning the particle shape by controlling the reduction atmosphere. Moreover, the formation of the metal-metal oxide heterointerfaces also provides more possibilities for catalysis. Although the catalytic activity brought by these new exsolved nanostructures was not further investigated in this thesis, it is worth being focused in the future studies.

7.3.5 Key findings for the mechanistic study of exsolution in ETEM

In this subchapter, it was demonstrated that by using the state-of-the-art environmental TEM, the particle nucleation and growth process as well as the formation of the socketed interface can be observed in situ at an atomic scale, under gas atmosphere and at temperature. Moreover, the high resolution also allows for the quantitative analysis of the TEM data, which provides more insights into the exsolution process.

Firstly, it was found that the exsolved particles would grow epitaxially and isotropically at the initial position near the perovskite surface where they nucleated, and in parallel

the surrounding perovskite lattice would also rise around the particles and gradually form the socket which strains the particle to limit its growth. Secondly, by conducting the exsolution under vacuum environment, the nucleation and the early stages of particle growth can be monitored. According to the quantitative analysis, during the early stages of particle growth, the exsolution seems to happen in a stepwise manner rather than continuously, which uses the ions diffusing from the adjacent region of a few nanometers within the perovskite. It was also found that during these stages, the exsolution process seems to be mainly limited by the availability of exsolvable ions rather than the diffusion of ions. Hence, in order to trigger more ions to get exsolved, the grain size of the material should be reduced.

It was also demonstrated that the atmosphere for the exsolution process has significant effects on the exsolved nanostructures. It can not only control the shape of the exsolved metal particles, but may also lead to the novel metal-metal oxide heterointerfaces. These diverse but controllable nanostructures could endow the exsolved materials with more possibilities to tune their catalytic properties.

7.4 Efficient use of Rh via exsolution

The subchapter above has demonstrated the mechanisms of the formation of socketed particles during exsolution process, and the particle growth seems to be limited by the availability of exsolvable ions near the perovskite surface. These insights provided important guidance for the material design to exsolve noble metals. For example, as demonstrated before, the preparation method was modified to reduce the grain size of perovskites, aiming to facilitate more ions in the bulk to exsolve on the surface. Actually exsolving noble metals has been reported before by other groups, but the perovskite compositions they used contain relatively high concentrations of noble metals [236, 238, 277], which makes these catalysts neither economical nor practical to be used at large scales. That is why perovskite compositions with dilute substitution levels of noble metal (Rh) were designed for exsolution in this study. However, the metal exsolution from the highly dilute composition might be challenging, due to the stronger interactions between the metal ions and the perovskite lattice, as mentioned before. Hence, in this subchapter, attempts were made to control different parameters, such as the substitution level, the reduction time and temperature, in order to promote more Rh to exsolve from the perovskite and also to control the particle characteristics, which could lead to improved catalytic activity of noble metal catalysts.

7.4.1 Effect of substitution level of Rh on exsolution

As mentioned in subchapter 7.2.5, a series of perovskites with different substitution levels of Rh (Rh1, Rh3 and Rh6 for $La_{0.43}Ca_{0.37}Rh_xTi_{1-x}O_3$ (x=0.01, 0.03 and 0.06)) were successfully prepared. Here, the effects of the substitution level on the exsolution of Rh were investigated. The as-prepared perovskites were crushed and sieved to get powders with the size of 80-160 μm. This size range of powders was used for all the tests in this study, and it will not be repeated henceforth. Then the sieved samples of Rh1, Rh3 and Rh6 were reduced in 5% H_2/Ar at 900 °C for 10 hours (with the heating and cooling rates of 5 °C min^{-1}) by using the reduction setup introduced in Chapter 3, and the microstructures of the samples after the reduction are shown in Figure 7-36.
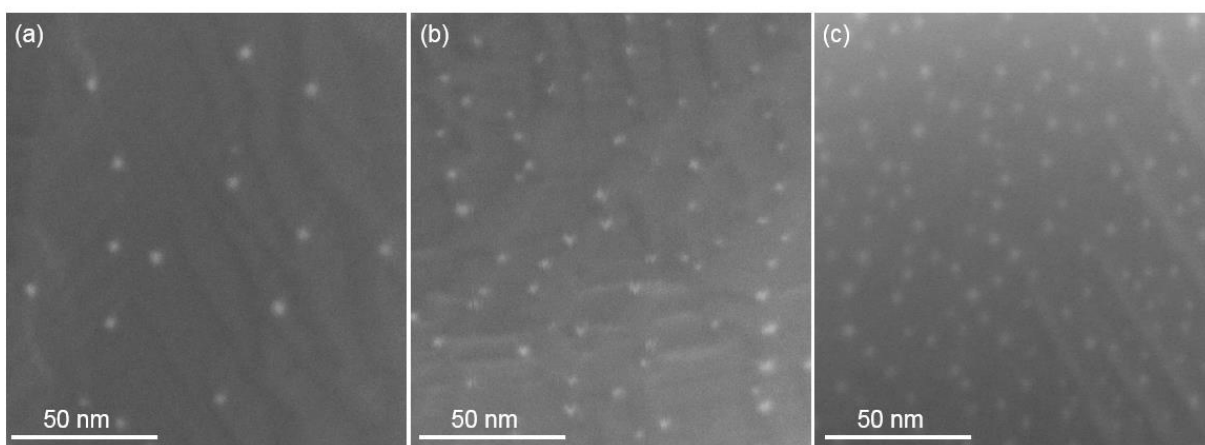
Figure 7- 36 SEM images of perovskites $La_{0.43}Ca_{0.37}Rh_xTi_{1-x}O_3$ after the reduction in 5% H_2/Ar at 900 °C for 10 hours: (a) x=0.01, (b) x=0.03, and (c) x=0.06.

It is easy to notice the changes of the size and population of the exsolved Rh particles with the substitution level of Rh in Figure 7-36. The size and population of the particles contained in Figure 7-36 were calculated based on pixel contrast from the SEM images in the software Mathematica, following the procedure which was previously reported [253]. The analysis results of the particles in the SEM images above can be found in Figure 7-37. It was found that with the higher Rh concentration in the perovskite, the average size of exsolved particles decreased while the particle population increased.
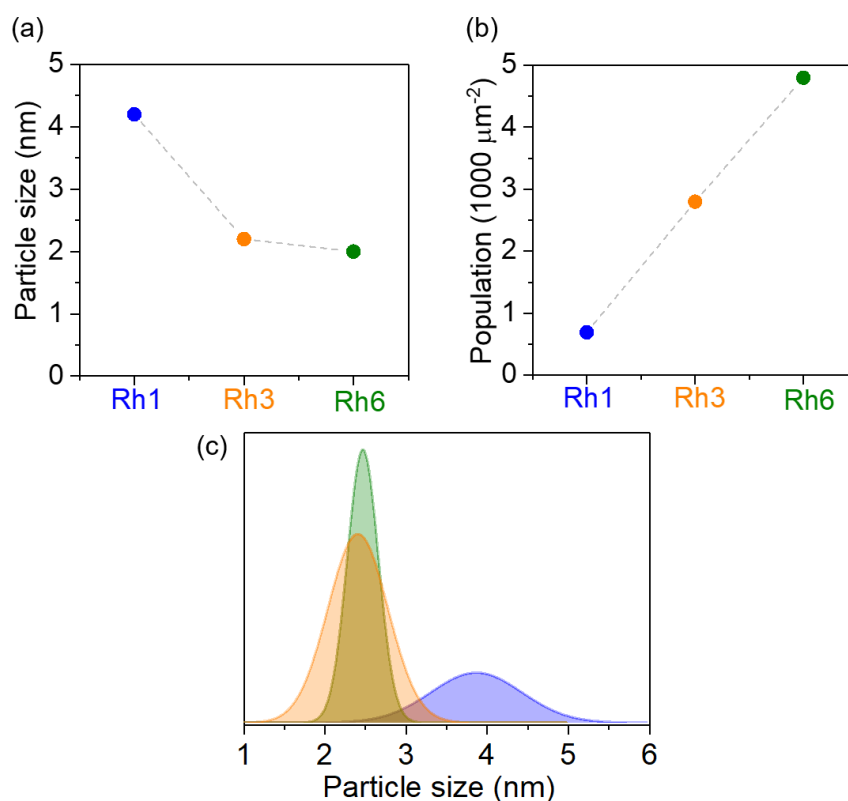
Figure 7- 37 Analysis of Rh particles exsolved from perovskites Rh1, Rh3 and Rh6 after the reduction in 5% H_2/Ar at 900 °C for 10 hours: (a) particle size, (b) particle population, and (c) particle size distribution.

The opposite changes of the particle size and population with the substitution level of Rh can be understood based on the theory of particle nucleation and growth and it is also related to the availability of exsolvable Rh ions in each perovskite composition. To form a Rh cluster of 1 nm (Figure 7-38(a)), about 1400, 467 and 233 unit cells from the perovskites Rh1, Rh3 and Rh6 are required, respectively, to contribute Rh ions for the growth of that Rh cluster (Figure 7-38(b)). In other words, the radius of the region within the perovskite lattice from which Rh ions need to be exsolved to form the 1 nm cluster is about 3.4, 2.4 and 1.9 nm for Rh1, Rh3 and Rh6, respectively (Figure 7-38(c)). In the lattice with high Rh substitution levels, exsolvable ions disperse close to each other and hence these ions would show more tendency to accumulate to form nuclei, which would lead to higher particle populations instead of large particles. On the contrary, in lower substitution systems, exsolvable ions need to migrate for much longer distances to form even one nucleation point, which increases the nucleation barrier. Hence, these ions would be more prone to grow the existing nuclei, and that is why the formation of larger particles but lower population is favored in lower substitution systems.
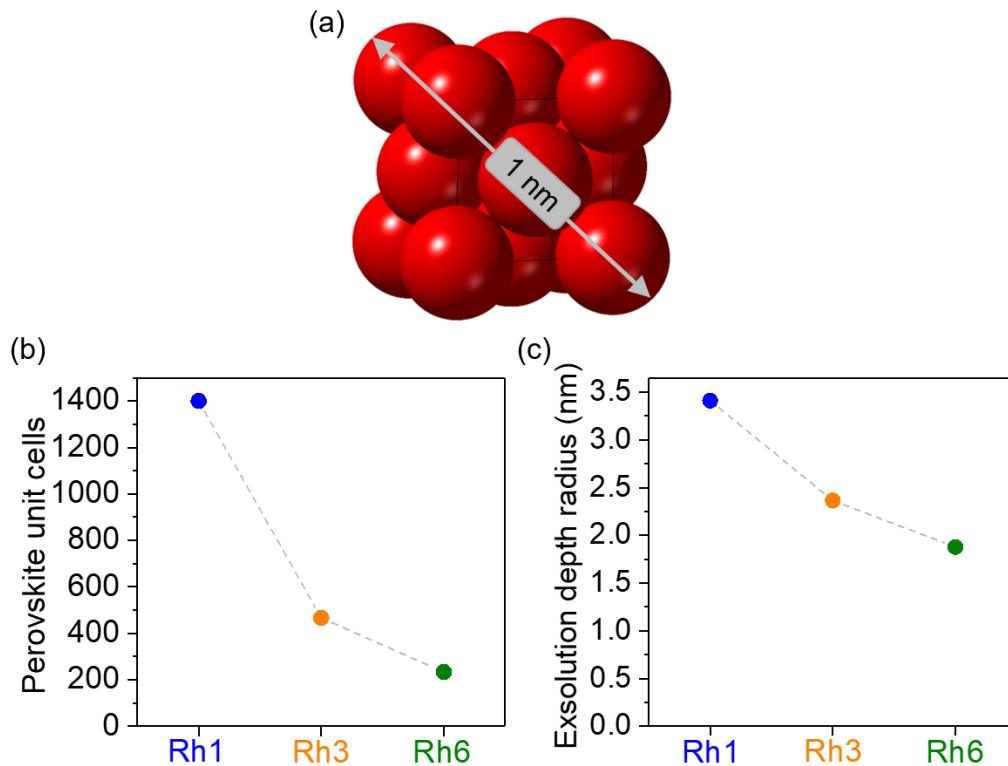
Figure 7- 38 (a) Crystal model showing a 1 nm metal cluster. (b) Numbers of perovskite unit cells required in different substitution systems to form a 1 nm metal cluster. (c) Depths of exsolution required in different substitution systems to form a 1 nm metal cluster.

Moreover, the size distributions of the exsolved particles are shown in Figure 7-37(c), and all these size distributions were found to follow a near-gaussian shape. However, the size distribution was narrower for the particles exsolved from the higher substitution system, and on the contrary the lower substitution systems generated less uniform particles. This might be ascribed to the different concentrations of Rh ions in these systems as well. As discussed above, Rh ions disperse in close proximity in the high substitution system and hence they are more likely to nucleate homogeneously, which would lead to more uniform particle size at the end. While for the lower substitution system, Rh ions would prefer to grow the existing nuclei, which would increase the chances for the size differentiation of the individual particles during the growth process.

Exsolution of Rh would be further studied by using the most dilute perovskite (Rh1), as this could potentially lead to more efficient use of Rh, although it might also be more challenging.

7.4.2 Effect of reduction time on exsolution

As mentioned above, the most dilute composition Rh1 was selected to be further studied, and firstly the effect of the reduction duration on the Rh exsolution was investigated. The sample was reduced in 5% H_2/Ar at 900 °C for different durations (0, 10 and 30 hours, respectively), where the 0-hour reduction means to cool down the system immediately when the desired temperature is reached. The microstructures of the as-reduced samples are shown in Figure 7-39.
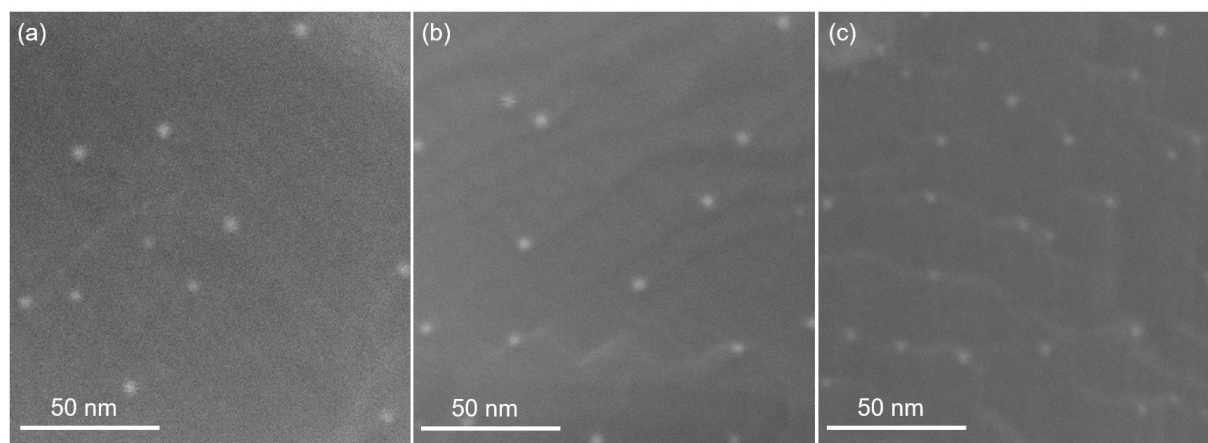
Figure 7- 39 SEM images of perovskite $La_{0.43}Ca_{0.37}Rh_{0.01}Ti_{0.99}O_3$ after the reduction in 5% H_2/Ar at 900 °C for different durations: (a) 0 hour, (b) 10 hours, and (c) 30 hours.

It was found that during the isothermal period after the temperature reached 900 °C, there was no significant change of the particle size with the prolonged reduction time, while the particle population increased a lot during this period, and these observations were confirmed by the particle analysis results as shown in Figure 7-40. Particle analysis shows that the average size of the exsolved particles only changed from ~4.5 nm to ~3.5 nm when the dwell time at 900 °C was increased from 0 to 30 hours. However, the particle population increased by nearly five times from ~250 μm^{-2} to ~1300 μm^{-2}. Moreover, Figure 7-40(c) shows that the particle size distribution became more homogeneous with the increasing reduction duration, and the peak of the particle size distribution also shifted to lower values indicating that the longer reduction duration would preferentially generate additional smaller particles as compared to the initially formed ones, which could explain the reduced average particle size with the longer reduction duration. All the results above could provide some insight into the particle formation process during the exsolution: in the first stage during the temperature rising and the early isothermal periods, some nuclei form and they would grow into relatively large particles; while in the later stage under isothermal conditions,

more Rh ions from the deeper layers within the perovskite diffuse to near the surface for exsolution, and they would preferentially form additional particles with smaller sizes. Unlike the samples prepared via deposition techniques where metal particles would agglomerate at high temperatures over time, here more particles are formed via exsolution.
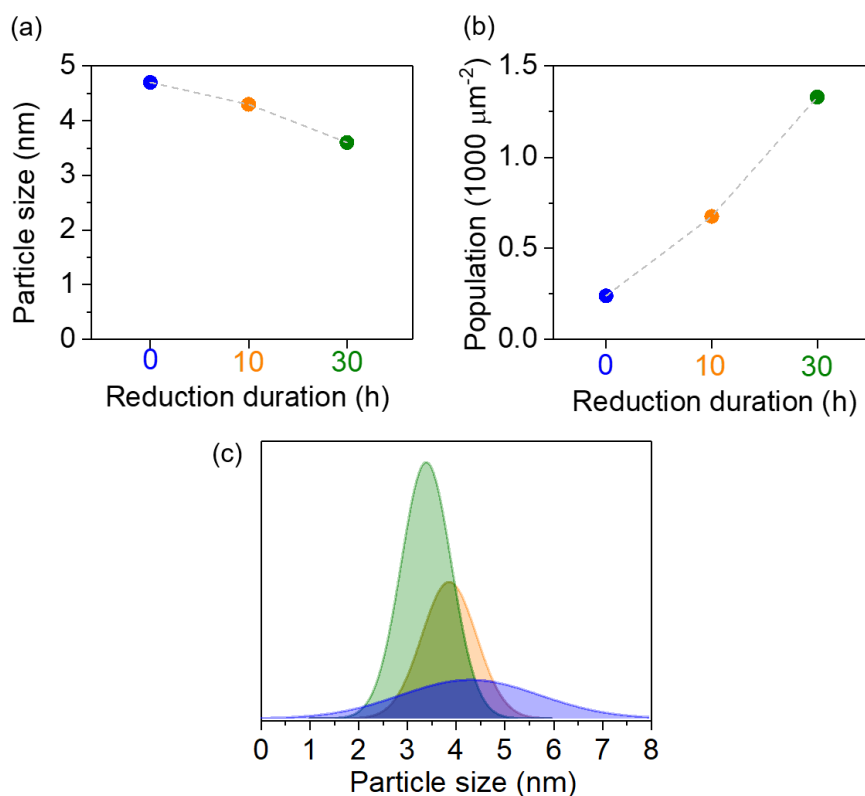
Figure 7- 40 Analysis of Rh particles exsolved from perovskite La$_{0.43}$Ca$_{0.37}$Rh$_{0.01}$Ti$_{0.99}$O$_3$ after the reduction in 5% H$_2$/Ar at 900 °C for different durations. (a) Particle size, (b) particle population, and (c) particle size distribution.

7.4.3 Effect of reduction temperature on exsolution

It is expected that the metal exsolution can be significantly influenced by the reduction temperature as it determines the driving force for the bulk diffusion of the exsolvable species and the reduction, and hence the effects of the reduction temperature were investigated. The perovskite Rh1 was reduced in 5% H$_2$/Ar for 10 hours but at different temperatures varying between 500 and 1000 °C, and the microstructures of the as-reduced samples are shown in Figure 7-41.
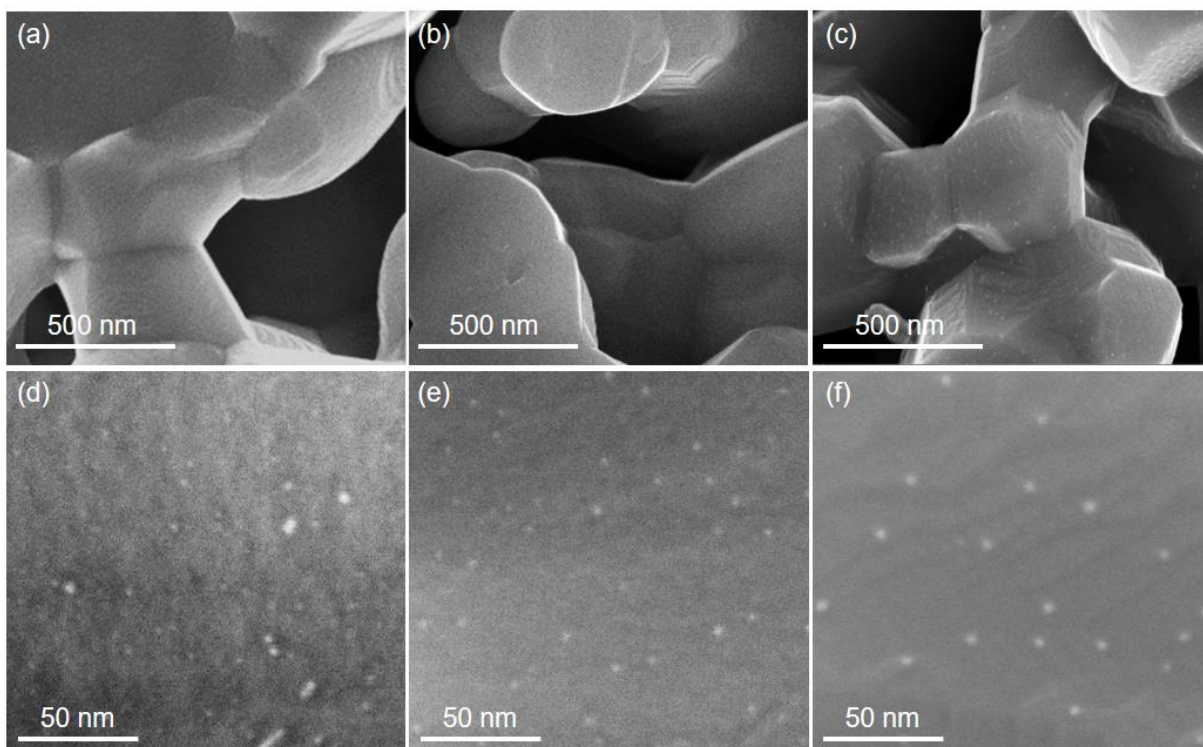
Figure 7- 41 (a-c) lower-magnification SEM images of perovskite $La_{0.43}Ca_{0.37}Rh_{0.01}Ti_{0.99}O_3$ after the reduction in 5% H_2/Ar at 500, 600 and 900 °C, respectively. (d-f) Details of perovskite $La_{0.43}Ca_{0.37}Rh_{0.01}Ti_{0.99}O_3$ after the reduction in 5% H_2/Ar at 500, 600 and 900 °C, respectively.

The analysis of particles (Figure 7-42) allows us to look inside the effects of reduction temperature on the exsolved particles. It can be noticed that the plots of both the average particle size and the population show a plateau at 700 °C in Figure 7-42(a and b), and hence the plots can be divided into two temperature regions, namely the low temperature region (500-700 °C) and the high temperature region (700-1000 °C), respectively. Firstly, in the low temperature region (500-700 °C), there was no obvious change of the particle size (~2 nm), while the particle population increased gradually from ~1500 μm^{-2} at 500 °C to ~2500 μm^{-2} at 700 °C, which might be ascribed to the limited reducibility of Rh ions at the low temperature. In the exsolution process, there are two important steps, which are the diffusion of exsolvable ions and the reduction. For the normal rhodium oxide, it can be reduced readily at relatively low temperatures (~300 °C), but if Rh is incorporated into the titanate, its reducibility would drop and hence a relatively higher temperature would be required to trigger the reduction [278]. Here the reducibility of Rh might be lowered as it was substituted in the highly dilute perovskite lattice, which means that a higher reduction temperature would be required. Therefore, the exsolution might be limited by the reduction at 500 °C, and when the reduction rate became faster with the increasing temperature, additional nucleation

could occur, which led to the higher particle population. However, in the high temperature region (700-1000 °C), the particle size increased from ~2 nm at 700 °C to ~5 nm at 1000 °C, while the particle population dropped from ~2500 μm^{-2} to ~500 μm^{-2} at the same time. Therefore, these results indicate that nucleation is favored at low temperatures while the particles are more prone to grow larger at high temperatures, which is consistent with the nucleation/growth theory [268]. Moreover, it was found that the size distribution of the particles exsolved at higher temperatures was less homogeneous as compared with the ones exsolved at lower temperatures (as shown in Figure 7-42(c)). It was observed that a considerable amount of particles seems to nucleate during the temperature rising period according to Figure 7-39 and 7-40. For the low-temperature reduction, fewer particles would nucleate during the temperature rising period due to the relatively short duration for this period. On the contrary, for the high-temperature reduction, the longer time required for heating up means that more particles would nucleate in this stage, while the newly exsolved ions in the later isothermal stage would not only grow the existing particles but also nucleate to form more particles, which would result in the big deviation of the sizes of the final particles. This could account for the broader particle size distributions by using the higher reduction temperatures.
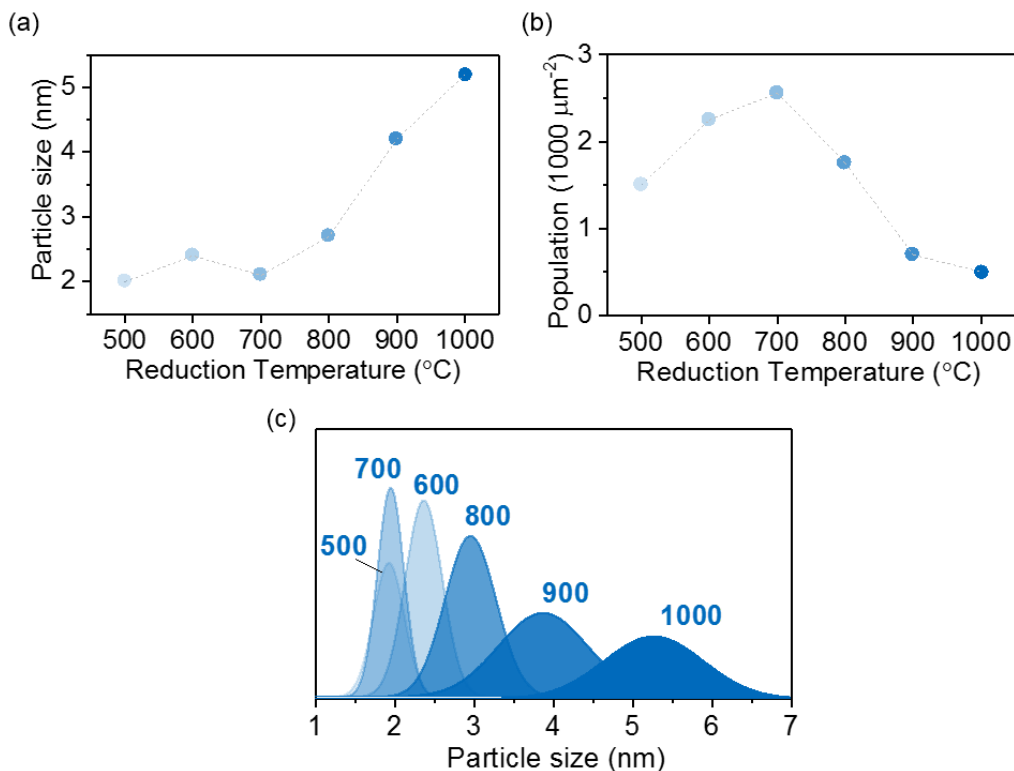
Figure 7- 42 Analysis of Rh particles exsolved from perovskite $La_{0.43}Ca_{0.37}Rh_{0.01}Ti_{0.99}O_3$ after the reduction in 5% H_2/Ar for 10 hours at different temperatures: (a) particle size, (b) particle population, and (c) particle size distribution.

7.4.4 Extent of exsolution as a function of substitution level, reduction time and temperature

As shown above, the effects of different parameters including the Rh substitution level in perovskite, the reduction time and temperature on the exsolution of Rh nanoparticles have been investigated, but the exact extent of the Rh exsolution obtained under each condition has not been revealed. Here, the amount of Rh metal exsolved from a unit surface area of the perovskite (N_{Rh}, Rh atom per surface area (μm^{-2})) was calculated (Figure 7-43(a-c)), based on the particle size and population obtained under each condition:

$$N_{Rh} = \frac{4\pi \cdot \rho_{Rh} \cdot N_a}{3 \cdot A_{Rh}} \sum_i f_i \cdot \left(\frac{d_i}{2}\right)^3 \qquad \text{Equation 7-13}$$

where ρ_{Rh} and A_{Rh} are the density and atomic weight of Rh metal, respectively, N_a is the Avogadro's constant, and f_i is the fraction of the particles (per area of perovskite, μm^{-2}) with the diameter of d_i (nm). For instance, the amounts of Rh metal exsolved from perovskites with different substitution levels are shown in Figure 7-43(a). Seemingly, Rh6 exsolved the highest amount of Rh ($\sim 5 \times 10^6$ μm^{-2}) as it had the highest substitution level of Rh among the three samples here, but it is surprising to find that the amounts of Rh exsolved from Rh1 and Rh3 were similar ($\sim 2 \times 10^6$ μm^{-2}), indicating that Rh1 can use the noble metal more efficiently than Rh3. Moreover, Rh6 contained 6 times as many Rh atoms in the lattice as Rh1, but the amount of Rh finally exsolved from Rh6 was only around 2-fold higher as compared with Rh1, which indicates that the amount of the exsolved metal does not increase proportionally with the substitution level. Therefore, the results above indicate that employing Rh1 could allow for more efficient use of Rh.

Regarding Rh1, the amount of the exsolved metal also varied with the reduction conditions. Figure 7-43(b) shows that a considerable amount of Rh atoms N_{Rh} ($\sim 10^6$ μm^{-2}) has already exsolved from the perovskite during the temperature rising period in the reduction, and by prolonging the dwell time at 900 °C from 0 to 10 h, the amount of the exsolved Rh increased about two-fold to $\sim 2.1 \times 10^6$ μm^{-2}. However, no significant increase of the amount of the exsolved Rh was obtained by further increasing the dwell time from 10 to 30 h, which indicates that the major percentage of the exsolution of Rh takes place in the early stages of the reduction process and then an equilibrium may be reached gradually where no more Rh can be exsolved. Also, Figure 7-43(c) reveals the monotonic increase of the amount of the exsolved Rh within the reduction

temperature range between 500 and 1000 °C, where the value of N_{Rh} increased from only ~0.5 × 10⁶ μm⁻² at 500 °C to ~ 3 × 10⁶ μm⁻² at 1000 °C. Combining the effects of the reduction time and temperature, it seems that reducing the sample Rh1 at the high temperature (1000 °C) for 10 h can facilitate the highest extent of Rh exsolution, which means the most efficient use of the noble metal through exsolution from the view of atomic utilization. However, the amount of the exsolved Rh metal may not be the only factor that affects the catalytic activity, but other catalyst properties such as particle characteristics may also have some influences, hence different samples will be tested in the model reaction of CO oxidation in the following sections to investigate the affecting factors for the catalytic activity.
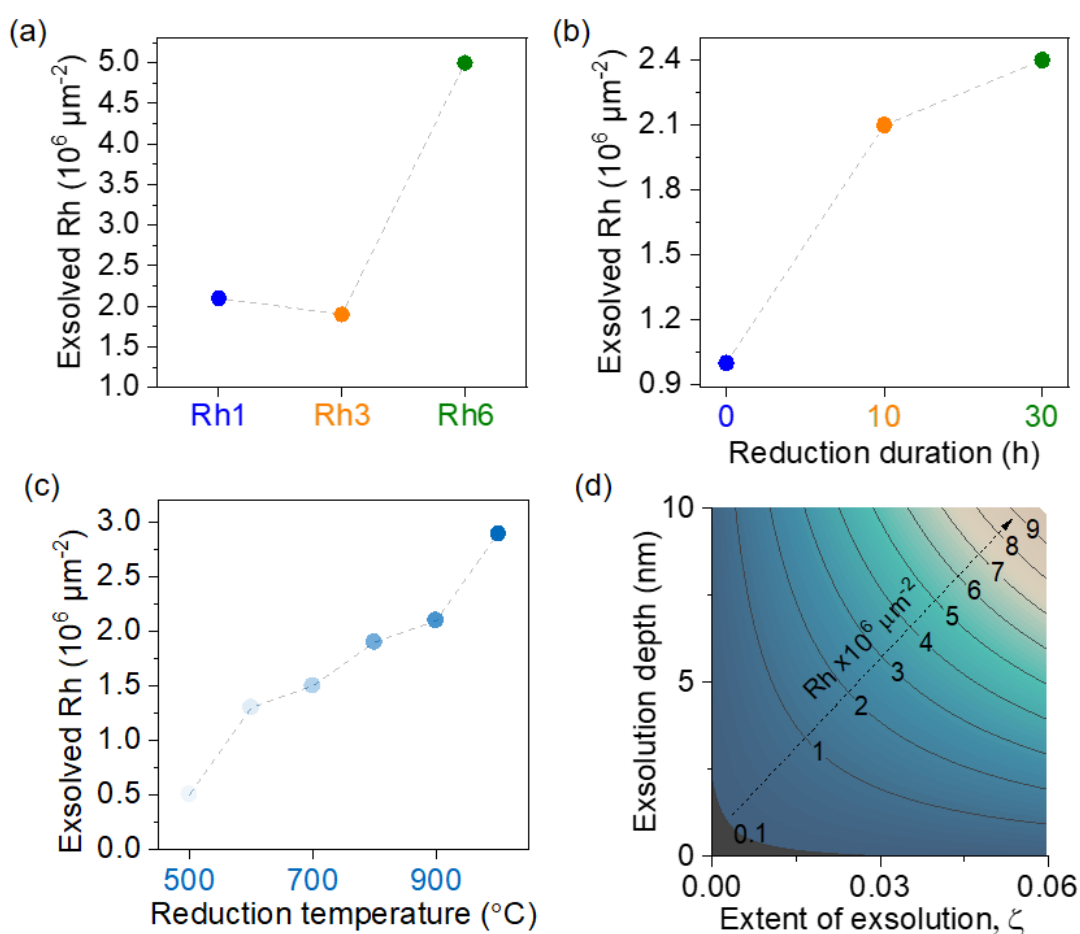
Figure 7- 43 Amount of Rh atoms which exsolved in 5% H₂/Ar per surface area of the perovskite support (N_{Rh}) varying with (a) substitution level in perovskite, (b) reduction time at 900 °C and (c) reduction temperature. (d) 2D plot of N_{Rh} as a function of the exsolution depth within perovskite and the extent of exsolution from the corresponding region (ζ).

In addition, given the amount of the exsolved Rh atoms, the average depth (D_{Rh}) of the region within the perovskite where the exsolution has occurred as well as the degree

of the exsolution from the corresponding region (ζ, mol Rh per mol of perovskite, $La_{0.43}Ca_{0.37}Rh_{x-\zeta}Ti_{1-x}O_3$) can be calculated as:

$$D_{Rh} = \frac{N_{Rh} \cdot a_p^3}{\zeta}$$

Equation 7-14

where a_p is the pseudocubic perovskite cell parameter. Hence the correlation between the exsolution depth (D_{Rh}) and exsolution degree (ζ) can be shown in Figure 7-43(d). The values of the D_{Rh} and ζ can reflect the efficiency of the noble metal through the exsolution. For the perovskite Rh1, the highest amount of Rh ($\sim 3 \times 10^6$ μm^{-2}) can be exsolved when it is reduced at 1000 °C (Figure 7-43(c)). There are two possible extreme cases. First, in the exsolution region, all the Rh ions have been depleted for exsolution, hence $\zeta = x = 0.01$. In this case, the required depth of the exsolution region would be smaller than 20 nm, and considering that the grain size of the perovskite is around 500 nm, the extent of the exsolution seems to be quite limited. On the other hand, if the whole volume within the perovskite grain takes part in the exsolution, the depth of exsolution would be ~250 nm (half the grain size), and the corresponding degree of exsolution (ζ) in this case would be less than 0.001. Both cases suggest that there is still a lot of room for the improvement of the efficiency of noble metals, by increasing the extent of metal exsolution from perovskite. Towards these two extreme cases, two potential methods can be suggested to trigger more metal to exsolve from the perovskite. The first method is to further reduce the grain size of the perovskite to <50 nm, which could allow for the exsolution from a larger fraction of the bulk within the perovskite and also provide more surface area for exsolution. The second method is to improve the degree of exsolution from the perovskite, which could be achieved by modifying the perovskite stoichiometry to increase the mobility of metal ions in the lattice.

7.4.5 Catalytic activity of exsolved Rh system in CO oxidation

It has been shown above that Rh nanoparticles can be exsolved from the highly dilute composition, and their characteristics (size and population) can be controlled via the reduction time and temperature. Here the samples of Rh1 that were reduced at different temperatures (for 10 h) hence possessing different Rh particle characteristics, were tested in the CO oxidation reaction, aiming to investigate the effects of these particle characteristics on the catalytic activity. The catalytic tests of these samples

were carried out using the slightly oxidizing conditions (P_{CO}=0.6 kPa, P_{O_2}=1.0 kPa and F_t=450 mL min^{-1}), as a function of temperature (light-off experiments), and the results are summarized in Figure 7-44. The activities of these samples can be compared in terms of the temperatures at which they achieve 5% and 50% conversion of CO (T_5 and T_{50}, respectively) and also based on the kinetic behaviors they show below T_5 (Figure 7-44).

Catalytic tests were also conducted on the other two samples in order to show the activity of the perovskite support only, with the first one being the undoped perovskite (Rh0) as introduced previously and the second one being the Rh substituted perovskite but without being exsolved (hence unexsolved Rh1). Figure 7-44(a) indicates that the undoped perovskite (Rh0) was nearly inert as no measurable reaction rate (minimum measurable limit to be 3 x 10^{-4} µmol CO_2 s^{-1}) was detected by 400 °C and only less than 0.1% of CO was converted at the highest temperature in the test (~500 °C). The unexsolved Rh1 showed some activity as it converted ~5% CO at ~500 °C, but it is still very low. Therefore, these results show that the perovskite mainly serves as a support in the exsolved catalyst and the activity is primarily due to the Rh particles.
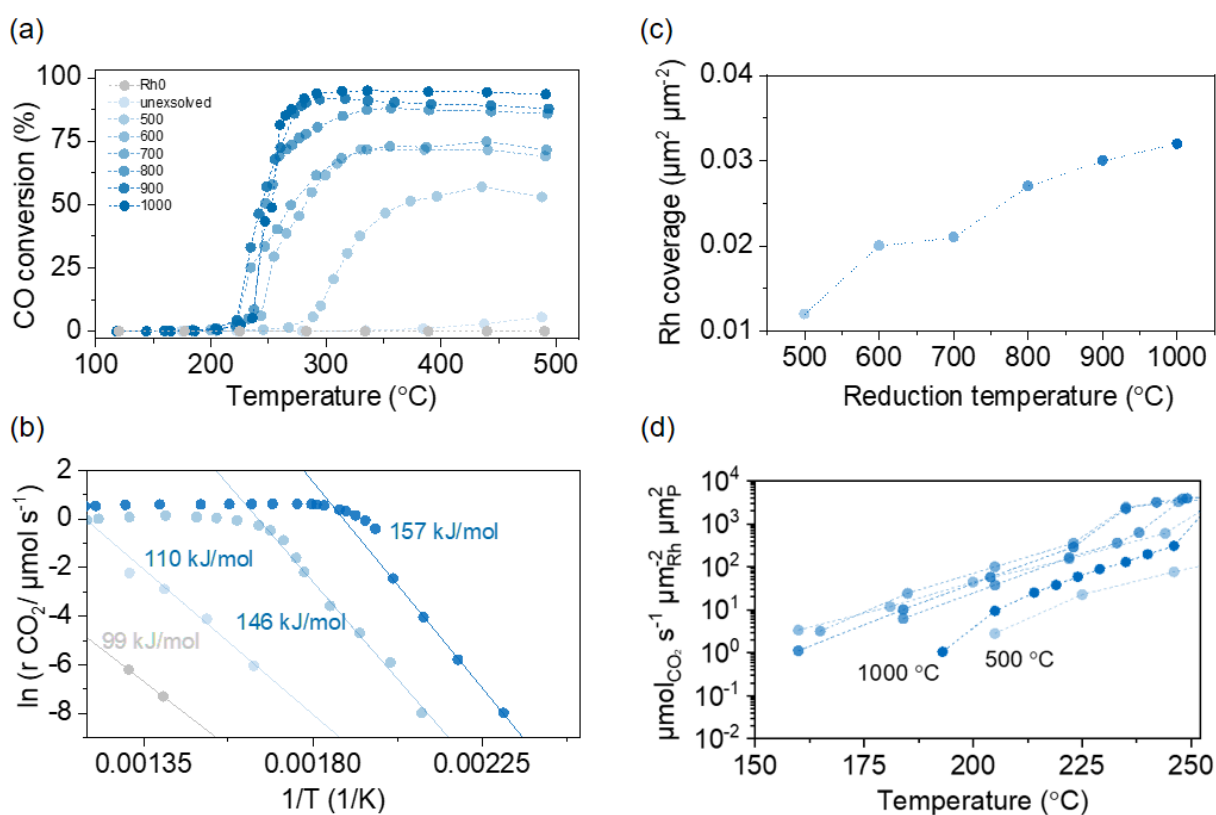
Figure 7- 44 (a) Light-off experiments over La$_{0.43}$Ca$_{0.37}$Rh$_{0.01}$Ti$_{0.99}$O$_3$ reduced at different temperatures for 10 h, in CO oxidation reaction under conditions of P_{CO}=0.6 kPa, P_{O_2}=1.0 kPa and F_t=450 mL min^{-1}. (b) The corresponding Arrhenius plots showing

the activation energies. (c) Rh coverage calculated for the samples reduced at different temperatures. (d) CO_2 production rate divided by Rh metal coverage for the samples shown in (a), as a function of temperature.

Regarding the exsolved samples of Rh1, Figure 7-44(a) shows a rising trend of the catalytic activity with the increasing reduction temperature, and depending on their activities, these samples can be classified into three groups. Firstly, the sample reduced at 500 °C showed the lowest activity. It started to produce the minimum detectable CO_2 at ~270 °C while this temperature for all the other samples was ~200 °C, and it also had a T_{50} value of ~375 °C. Then the second group contains the samples reduced at medium temperatures (600 and 700 °C) that were more active as compared with the previous one, as they showed T_{50} values about 100 °C lower than that of the sample reduced at 500 °C. The last group contains the samples reduced at high temperatures (800-1000 °C) which were more active than the samples discussed above, with the T_{50} values of ~250 °C. The T_5 values of these samples also changed in the similar way as T_{50}, but within a narrower temperature window (220-275 °C). Additionally, the maximum CO conversion achieved by these samples also fell into these three groups as it increased gradually with the reduction temperature.

It should be noticed that the CO conversion shown in Figure 7-44(a) increased gradually between T_5 and T_{50}, with the corresponding temperature window to be around 100, 50 and 30 °C for the samples reduced at low, medium and high temperatures, respectively. This is different from the behavior of conventional noble metal catalysts as shown in Chapter 4, where the temperature window between T_5 and T_{50} was narrower. This difference probably indicates that the interaction between the exsolved Rh particles and the perovskite support might affect the catalytic behaviors of these samples. The activation energies of these samples (calculated by using the kinetic data in the low temperature region) might provide some evidence to the metal-support interactions (Figure 7-44(b)). It was found that the activation energies for these samples varied between 99 and 157 kJ mol^{-1}, and the sample exsolved at the high temperature showed the highest activation energy (157 kJ mol^{-1}) which was consistent with the characteristic values reported for noble metal catalysts on non-reducible supports [279]. This observation makes sense as the reducibility of the perovskite support is expected to be very low because it has already been reduced for a long period during the sample preparation stage to promote the metal exsolution. The higher reduction temperature would cause more reducibility loss for the perovskite, which would result in the higher activation energy as observed here. As mentioned

before, the unexsolved sample Rh1 also showed slight activity even though there should not be any Rh particles dispersing on the surface. Perovskites substituted by some active metals on the B-sites (Rh in this case) have been reported to possess some catalytic activity for reactions including CO oxidation, and the low activation energy obtained for the unexsolved sample here was similar as those reported for other perovskite oxides containing active species [280-282].

By observing the particle characteristics (Figure 7-42) and the corresponding catalytic activity (Figure 7-44(a)), no direct correlation between them could be found. Figure 7-42 shows that between the reduction temperature of 500 and 700 °C, the particle size remained small (~2 nm) and the particle population increased gradually, while at higher temperatures (between 700 and 1000 °C), the particle size kept increasing while the particle population kept decreasing. The small particle size and high particle population demonstrated by the low temperature reduced samples are typically thought to be advantageous for catalysis. However, the catalytic activity observed here actually increased monotonically with the reduction temperature, hence it seems that the activity is not directly affected by the particle characteristics. On the other hand, the samples (Rh0 and unexsolved Rh1) have indicated previously that the activity is mainly contributed by the Rh particles. Hence, the Rh metal coverage, as the particle size and population are factored together, might have a significant influence on the activity. The Rh metal coverage (η_{Rh}, surface area of Rh particles per surface area of support, μm^2 μm^{-2}) was calculated as:

$$\eta_{Rh} = 2\pi \cdot \sum_i f_i \cdot \left(\frac{d_i}{2}\right)^2 \qquad \text{Equation 7-15}$$

where f_i is the fraction of the particles (per area of perovskite, μm^{-2}) with the diameter of d_i (nm). A clear correlation between the catalytic activity and the Rh metal coverage can be found by combining the results in Figure 7-44(a and c), as the samples possessing higher Rh metal coverage on the surface showed higher activity for CO oxidation. However, this correlation was not directly proportional, which indicates that some other factors apart from Rh metal coverage might also affect the activity. This is more obvious as shown in Figure 7-44(d) in which the reaction rates are normalized with respect to η_{Rh}. It was found that when the activity is normalized in this way, most samples showed the similar reactivity within the selected temperature window, while the samples reduced at 500 and 1000 °C showed different reactivity, probably implying different states of Rh particles for these samples. The oxidation state of Rh particles,

for instance, might be one of those factors, which is also related to the particle size to some extent. It was reported that the Rh particles smaller than ~2 nm are more likely to be oxidized and stay stable at the oxidized state, while the Rh particles bigger than ~4 nm can stay at the reduced state [279]. The detailed relation between the oxidation state of Rh and the corresponding activity for CO oxidation is still under debate: some studies showed that metallic particles are active while the oxidized Rh only serves as spectator species as CO is strongly adsorbed on the oxidized sites [283]; some claimed that both the metallic Rh and its support containing Rh^{3+} are active [284]; while some also reported that the thin O-Rh-O trilayer forming on the surface of Rh particles is active while surface further oxidation will cause deactivation [285]. All these hypotheses indicate that the catalyst would be deactivated if Rh is intensively oxidized. The results above indicate that the activity of Rh catalyst for CO oxidation seems to be largely determined by Rh metal coverage, while other factors such as Rh oxidation state might also have some minor influences.

7.4.6 Exsolution vs infiltration

To evaluate the actual applicability of the dilute exsolved Rh catalyst for CO oxidation, the sample Rh1 reduced at 900 °C for 10 h (referred to as $Rh-eABO_3$ henceforth) was compared to the Rh impregnated γ-alumina (referred to as $Rh-iAl_2O_3$) that is widely used in conventional TWCs. The $Rh-iAl_2O_3$ sample contained the same nominal amount of Rh as that was substituted in the perovskite Rh1 (0.6 wt%). The impregnated sample was prepared with the wet impregnation method as introduced in subchapter 3.2.3.

The microstructures of these two samples are shown in Figure 7-45(a and b), which indicate that the γ-alumina-based sample had much higher surface area as compared to the perovskite-based sample (around 100 vs 1 m^2 g^{-1}). Then these samples were tested in the catalytic experiments of CO oxidation using the same conditions as mentioned before, and they showed similar catalytic activity (Figure 7-45(d)) and also similar activation energies (Figure 7-45(e)). It has been shown that only a fraction of the nominally substituted Rh in the perovskite can be exsolved on the surface (Figure 7-43), which would normally result in the lower catalytic activity (as demonstrated in Figure 4-12). However, the fact that the exsolved sample showed similar activity to the impregnated sample indicates that the activity of the exsolved Rh particles was

enhanced. This activity enhancement might be originated from the strained nature of the exsolved Rh particles as previously shown for other exsolved particles [259].

Moreover, the commercial 1 wt% Rh/Al_2O_3 catalyst was also included in Figure 7-45 (d) and (e). It achieved 5% and 50% CO conversions at lower temperatures and its activation energy was also lower, which indicated that its activity was still slightly superior to the exsolved sample. This was not surprising considering that the exsolved sample contained only about half the amount of Rh as the commercial catalyst and the extent of exsolution was quite limited. However, as mentioned before, the exsolved material possesses great potential to be further improved by promoting more Rh to exsolve on the surface. Therefore, the exsolved material is very promising to beat the commercial catalyst and achieve more efficient use of noble metals in the future.
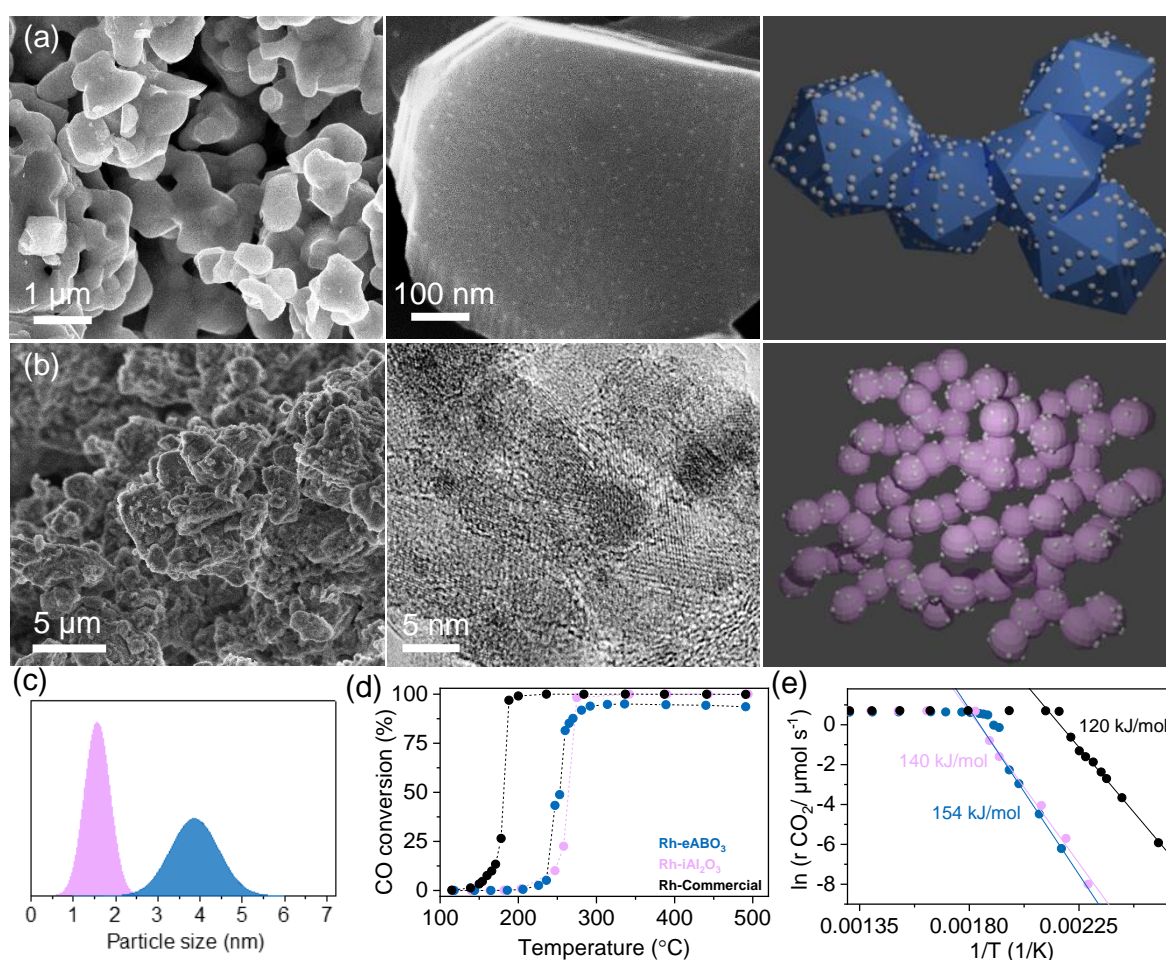
Figure 7- 45 (a) Low-magnification overview (SEM), detail of the sample surface (SEM) showing Rh particles, and schematic demonstration of the Rh exsolved perovskite reduced at 900 °C for 10 h (Rh-eABO₃). (b) Low-magnification overview (SEM), detail of the sample surface (TEM) showing Rh particles, and schematic demonstration of the Rh impregnated alumina (Rh-iAl₂O₃). (c) Size distributions of Rh particles for these samples. (d) Catalytic activity in CO oxidation tested under conditions of P_{CO}=0.6 kPa,

P_{O_2}=1.0 kPa and F_t=450 mL min^{-1}. (e) The corresponding Arrhenius plots showing the activation energies for the samples. The commercial 1 wt% Rh/Al$_2$O$_3$ sample is also included in (d) and (e) for comparison.

7.4.7 Key findings for exsolved noble metal catalysts

Here the exsolution of the noble metal (Rh) from the dilute perovskite system is briefly summarized. In this study, the Ca-based titanate was designed knowing that Ca can promote lower temperature phase formation and ion diffusion that enabled the preparation of the perovskite with relatively small grain size (~500 nm), which could benefit the metal exsolution by reducing the diffusion distance of exsolvable ions to the surface.

The modified perovskite microstructure allowed for the exsolution of Rh nanoparticles from the highly dilute substituted perovskite, and the factors that can affect the characteristics of the exsolved particles were also demonstrated. Regarding the substitution level, particle nucleation is favored at high substitution levels, while particle growth is more prone to occur when the substitution level becomes lower. Also, by prolonging the reduction duration, more Rh ions from the deeper layers within perovskite lattice are able to diffuse to the surface and exsolve to either grow the existing particles or form more particles, which is opposite to the deposited particles that will sinter over time. However, a considerable amount of metal ions seems to exsolve in the early stage of the reduction process and then a plateau would be gradually reached where no more metal can be exsolved. Finally, by increasing the reduction temperature, the population of the exsolved particles increases up to 700 °C and it starts decreasing afterwards, while the particle size increases with the temperature. Moreover, by testing the exsolved materials with different particle characteristics, it was found that the catalytic activity for CO oxidation is mainly determined by a combination of particle size and population factored together through the Rh metal coverage.

It is encouraging to find that the exsolved Rh catalyst exhibits the comparable activity as the state-of-the-art Rh/Al$_2$O$_3$ catalyst with the same nominal Rh loading, even though only about one tenth of the Rh in the perovskite lattice could exsolve at the surface. This implies the enhancement of the activity for the exsolved catalysts probably due to the particle-perovskite interactions, and hence the exsolved catalysts

show the potential to surpass the conventional catalysts if the exsolution process can be further promoted.

7.5 Conclusions

This chapter has demonstrated the comprehensive study of the exsolved materials, from the preparation of the perovskite, to the mechanistic insight into the exsolution process, and finally the exsolution of noble metals for more efficient use in catalysis.

The in situ reduction in ETEM provided important mechanistic insights into the exsolution process. The direct visualization and the quantitative analysis of the TEM results revealed the mechanism of the key steps during the exsolution process including the socket formation and the particle nucleation and growth. It was found that particles would nucleate and grow near the perovskite surface, and the perovskite lattice around the particles would rise in parallel hence forming the socket gradually. Therefore, the particles are strained during the growth process and they are strongly anchored to the socket, which results in the enhanced stability. The particle growth during the exsolution was found to be mainly limited by the availability of the exsolvable ions as it only drained the ions from a few nanometers within the perovskite lattice. This indicated the importance to reduce the grain size of the perovskite when designing the exsolved materials, which was achieved by modifying the preparation method for perovskite. Additionally, new nanostructures can be created by controlling the reduction atmospheres for the exsolution process, which could be the powerful tool to tune the catalytic properties of the exsolved materials.

The mechanistic insight obtained above was employed for designing the exsolved system of noble metals. Perovskites with small grain size allowed for the exsolution of Rh from dilute compositions. The exsolved particle characteristics and the extent of exsolution could be controlled by the parameters such as the substitution level, the reduction time and temperature, and the activity of the exsolved Rh catalysts seemed to be mainly affected by the Rh metal coverage. In spite of the limited extent of exsolution, the exsolved Rh catalyst still showed the similar activity as the conventionally impregnated Rh/Al_2O_3 with the same nominal Rh loading, indicating the great potential of the exsolved catalysts if the extent of exsolution can be increased and also considering their high stability.

Chapter 8: Summary and future work

The primary aim of this study is to design catalyst systems that can provide both the stabilizing effect and the improved activity for noble metal nanoparticles, which could potentially result in lower consumption hence higher efficiency of noble metals in catalysts. Hence, noble metal catalysts with different structures were prepared by using different techniques, and their stability and activity were investigated in CO oxidation reaction.

Firstly, it was clearly demonstrated in the study of spatially controlled nanoparticle pairs, that the particle sintering could happen easily under reaction conditions if metal nanoparticles were only loosely dispersed on the support, which would destroy the designed catalyst system. This highlighted the importance of the stronger interactions between the metal particles and the support to suppress the particle migration and sintering.

Therefore, in order to enhance the particle-support interactions, the metal nanoparticles were attempted to be enclosed into POCs. The POCs were demonstrated to be an effective template to control the particle growth, and hence noble metal nanoparticles (Pd) with uniform particle sizes (~1.6 nm) could be formed. Moreover, the Pd nanoparticles confined by POCs seemed to be stable under the given conditions below ~250 °C, as their catalytic activity was maintained. Despite all these, the catalytic activity exhibited by the POCs confined Pd nanoparticles in CO oxidation was much lower as compared with the state-of-the-art Pd/Al_2O_3 catalyst, which was probably due to the limited accessibility of active sites. Additionally, thermal decomposition (~300 °C) was also an intrinsic disadvantage of POCs-based materials, which limited their applications in high temperature processes.

As full encapsulation could compromise the activity of noble metal nanoparticles, an alternative approach was investigated where noble metal nanoparticles were only partially socketed in the support via redox exsolution from perovskite oxides. The socketed particles of transition metals formed via exsolution have been previously demonstrated to be highly stable, but their formation mechanism has not been revealed yet. Hence, in this study, experiments were carried out in the latest generation ETEM to observe the in situ formation process of the socketed particles for the first time. The high-resolution images from ETEM allowed for both qualitative and

174

quantitative analysis of the data, which provided mechanistic insights into the socket formation, and the metal particle nucleation and growth. Exsolvable ions seemed to nucleate near the perovskite surface and grow larger at the same position where they initially nucleated. The growth of the particle would force the perovskite lattice around it to rise and form the socket gradually. Hence, the particle is strained throughout its growth process and it is strongly anchored to the socket without any movement, which could explain the excellent stability of the exsolved particles. The particle growth during exsolution seemed to be mainly limited by the availability of exsolvable ions, as it only used the ions from a depth of a few nanometers within the perovskite. This highlighted the importance to reduce the grain size of perovskites especially when exsolving from dilute compositions, and the reduced perovskite grain size was achieved by modifying the preparation method. The mechanistic insights were useful to design more efficient exsolved materials for noble metals. Rh nanoparticles were successfully exsolved from dilute compositions, and the particle characteristics could be controlled by parameters like substitution levels, reduction time and temperature. The correlations between the activity and particle characteristics were also investigated, which indicated that the activity for CO oxidation was mainly dependent on the Rh metal coverage (combined effects of particle size and population). In spite of the limited exsolution extent, the exsolved Rh catalyst still exhibited similar activity as that of the state-of-the-art Rh/Al_2O_3 catalyst, indicating that the activity of the exsolved particles was improved probably due to their strained nature.

Generally, this thesis provides valuable principles for designing noble metal catalysts with improved stability and activity. Firstly, noble metal nanoparticles loosely dispersed on the support are unlikely to be stable enough under reaction conditions, hence enhanced particle-support interactions are desired. However, full encapsulation does stabilize nanoparticles, but it might also lead to lowered activity. Partially socketing noble metal nanoparticles in perovskite via exsolution seems to be a promising method to use noble metals more efficiently, as the strained nanoparticles exhibit both enhanced stability and activity.

Moreover, there is still a lot of room for the exsolved materials to improve. Currently only a small part of noble metals substituted in the perovskite lattice can be exsolved at the surface, and the efficiency of noble metals can be further improved if the extent of exsolution could be increased. Two suggestions towards this have been given in the previous chapter, including further reducing the grain size of perovskites and modifying

the perovskite stoichiometry to increase the ion mobility in the lattice. Furthermore, it has been demonstrated that new exsolved nanostructures can be produced by controlling the atmosphere during exsolution, but the activity of these nanostructures has not been investigated in this study. Hence the correlations between the activity and these nanostructures can be studied. Additionally, in this study, the exsolved materials were only tested in CO oxidation, but for the application of automotive exhaust control, their ability to transform HCs and NO_x should also be evaluated.

References

1. Fechete, I., Y. Wang, and J.C. Védrine, *The past, present and future of heterogeneous catalysis.* Catalysis Today, 2012. **189**(1): p. 2-27.
2. Zaera, F., *Nanostructured materials for applications in heterogeneous catalysis.* Chemical Society Reviews, 2013. **42**(7): p. 2746-2762.
3. Can, L. and L. Yan, *Bridging Heterogeneous And Homogeneous Catalysis: Concepts, Strategies, And Applications.* 2014, Weinheim: Wiley-VCH
4. Kettler, P.B., *Platinum Group Metals in Catalysis: Fabrication of Catalysts and Catalyst Precursors.* Organic Process Research & Development, 2003. **7**(3): p. 342-354.
5. Kim, C.H., S.I. Woo, and S.H. Jeon, *Recovery of Platinum-Group Metals from Recycled Automotive Catalytic Converters by Carbochlorination.* Industrial & Engineering Chemistry Research, 2000. **39**(5): p. 1185-1192.
6. Moshfegh, A.Z., *Nanoparticle catalysts.* Journal of Physics D: Applied Physics, 2009. **42**(23): p. 233001.
7. Zhu, Q.L. and Q. Xu, *Immobilization of Ultrafine Metal Nanoparticles to High-Surface-Area Materials and Their Catalytic Applications.* Chem, 2016. **1**(2): p. 220-245.
8. Navalón, S. and H. García, *Nanoparticles for Catalysis.* Nanomaterials (Basel, Switzerland), 2016. **6**(7): p. 123.
9. Xie, X., et al., *Low-temperature oxidation of CO catalysed by Co_3O_4 nanorods.* Nature, 2009. **458**: p. 746-749.
10. Tang, C., et al., *Mesoporous $NiO–CeO_2$ catalysts for CO oxidation: Nickel content effect and mechanism aspect.* Applied Catalysis A: General, 2015. **494**: p. 77-86.
11. Prasad, R. and P. Singh, *A Review on CO Oxidation Over Copper Chromite Catalyst.* Catalysis Reviews, 2012. **54**(2): p. 224-279.
12. Wang, X., et al., *Activation of Surface Oxygen Sites in a Cobalt-Based Perovskite Model Catalyst for CO Oxidation.* The Journal of Physical Chemistry Letters, 2018. **9**(15): p. 4146-4154.
13. Campbell, C.T., S.C. Parker, and D.E. Starr, *The Effect of Size-Dependent Nanoparticle Energetics on Catalyst Sintering.* Science, 2002. **298**(5594): p. 811-814.
14. Trung Tran, S.B., et al., *Iron-doped ZnO as a support for Pt-based catalysts to improve activity and stability: enhancement of metal–support interaction by the doping effect.* RSC Advances, 2018. **8**(38): p. 21528-21533.
15. Campbell, C.T., *The Energetics of Supported Metal Nanoparticles: Relationships to Sintering Rates and Catalytic Activity.* Accounts of Chemical Research, 2013. **46**(8): p. 1712-1719.
16. Munnik, P., P.E. de Jongh, and K.P. de Jong, *Recent Developments in the Synthesis of Supported Catalysts.* Chemical Reviews, 2015. **115**(14): p. 6687-6718.
17. De Rogatis, L., et al., *Embedded Phases: A Way to Active and Stable Catalysts.* ChemSusChem, 2010. **3**(1): p. 24-42.
18. Pinna, F., *Supported metal catalysts preparation.* Catalysis Today, 1998. **41**(1): p. 129-137.
19. Campelo, J.M., et al., *Sustainable Preparation of Supported Metal Nanoparticles and Their Applications in Catalysis.* ChemSusChem, 2009. **2**(1): p. 18-45.
20. Debecker, D.P., et al., *Preparation of $MoO_3/SiO_2–Al_2O_3$ metathesis catalysts via wet impregnation with different Mo precursors.* Journal of Molecular Catalysis A: Chemical, 2011. **340**(1): p. 65-76.
21. Delannoy, L., et al., *Preparation of Supported Gold Nanoparticles by a Modified Incipient Wetness Impregnation Method.* The Journal of Physical Chemistry B, 2006. **110**(45): p. 22471-22478.
22. Akande, A., et al., *Kinetic modeling of hydrogen production by the catalytic reforming of crude ethanol over a co-precipitated $Ni-Al_2O_3$ catalyst in a packed bed tubular reactor.* International Journal of Hydrogen Energy, 2006. **31**(12): p. 1707-1715.

23. Behrens, M., et al., *Understanding the complexity of a catalyst synthesis: Co-precipitation of mixed Cu,Zn,Al hydroxycarbonate precursors for Cu/ZnO/Al$_2$O$_3$ catalysts investigated by titration experiments.* Applied Catalysis A: General, 2011. **392**(1): p. 93-102.

24. Haruta, M., et al., *Low-Temperature Oxidation of CO over Gold Supported on TiO$_2$, α-Fe$_2$O$_3$, and Co$_3$O$_4$.* Journal of Catalysis, 1993. **144**(1): p. 175-192.

25. Deraz, N.M., *The comparative jurisprudence of catalysts preparation methods: I. precipitation and impregnation methods.* J. Ind. Environ. Chem., 2018. **2**(1): p. 19-21.

26. Neagu, D., et al., *Nano-socketed nickel particles with enhanced coking resistance grown in situ by redox exsolution.* Nature Communications, 2015. **6**: p. 8120.

27. Eggenhuisen, T.M., et al., *Fundamentals of Melt Infiltration for the Preparation of Supported Metal Catalysts. The Case of Co/SiO$_2$ for Fischer−Tropsch Synthesis.* Journal of the American Chemical Society, 2010. **132**(51): p. 18318-18325.

28. Serp, P., P. Kalck, and R. Feurer, *Chemical Vapor Deposition Methods for the Controlled Preparation of Supported Catalytic Materials.* Chemical Reviews, 2002. **102**(9): p. 3085-3128.

29. Liang, C., et al., *The two-step chemical vapor deposition of Pd(allyl)Cp as an atom-efficient route to synthesize highly dispersed palladium nanoparticles on carbon nanofibers.* Chemical Communications, 2005(2): p. 282-284.

30. Lopez-Sanchez, J.A., et al., *Facile removal of stabilizer-ligands from supported gold nanoparticles.* Nature Chemistry, 2011. **3**: p. 551.

31. Lin, J.H. and V.V. Guliants, *Supported Copper Catalysts Prepared from Colloidal Copper for the Water-Gas Shift Reaction.* ChemCatChem, 2011. **3**(9): p. 1426-1430.

32. Hatakeyama, Y., K. Onishi, and K. Nishikawa, *Effects of sputtering conditions on formation of gold nanoparticles in sputter deposition technique.* RSC Advances, 2011. **1**(9): p. 1815-1821.

33. Strobel, R., S.E. Pratsinis, and A. Baiker, *Flame-made Pd/La$_2$O$_3$/Al$_2$O$_3$ nanoparticles: thermal stability and catalytic behavior in methane combustion.* Journal of Materials Chemistry, 2005. **15**(5): p. 605-610.

34. Argyle, M. and C. Bartholomew, *Heterogeneous Catalyst Deactivation and Regeneration: A Review.* Catalysts, 2015. **5**(1): p. 145.

35. Bartholomew, C.H., *Mechanisms of catalyst deactivation.* Applied Catalysis A: General, 2001. **212**(1): p. 17-60.

36. Hansen, T.W., et al., *Sintering of Catalytic Nanoparticles: Particle Migration or Ostwald Ripening?* Accounts of Chemical Research, 2013. **46**(8): p. 1720-1730.

37. Bezemer, G.L., et al., *Cobalt Particle Size Effects in the Fischer−Tropsch Reaction Studied with Carbon Nanofiber Supported Catalysts.* Journal of the American Chemical Society, 2006. **128**(12): p. 3956-3964.

38. Van Santen, R.A., *Complementary Structure Sensitive and Insensitive Catalytic Relationships.* Accounts of Chemical Research, 2009. **42**(1): p. 57-66.

39. Papaioannou, E.I., et al., *Role of the Three-Phase Boundary of the Platinum-Support Interface in Catalysis: A Model Catalyst Kinetic Study.* ACS catalysis, 2016. **6**(9): p. 5865-5872.

40. Dai, Y., et al., *The physical chemistry and materials science behind sinter-resistant catalysts.* Chemical Society Reviews, 2018. **47**(12): p. 4314-4331.

41. Cao, A., R. Lu, and G. Veser, *Stabilizing metal nanoparticles for heterogeneous catalysis.* Physical Chemistry Chemical Physics, 2010. **12**(41): p. 13499-13510.

42. Forzatti, P. and L. Lietti, *Catalyst deactivation.* Catalysis Today, 1999. **52**(2): p. 165-181.

43. Flynn, P.C. and S.E. Wanke, *Experimental studies of sintering of supported platinum catalysts.* Journal of Catalysis, 1975. **37**(3): p. 432-448.

44. Moulijn, J.A., A.E. van Diepen, and F. Kapteijn, *Catalyst deactivation: is it predictable?: What to do?* Applied Catalysis A: General, 2001. **212**(1): p. 3-16.

45. Wang, Z.L., et al., *Shape Transformation and Surface Melting of Cubic and Tetrahedral Platinum Nanocrystals.* The Journal of Physical Chemistry B, 1998. **102**(32): p. 6145-6151.

46. Lu, H.M., et al., *Size-, Shape-, and Dimensionality-Dependent Melting Temperatures of Nanocrystals.* The Journal of Physical Chemistry C, 2009. **113**(18): p. 7598-7602.

47. Zou, W. and R.D. Gonzalez, *Stabilization and sintering of porous Pt/SiO₂: a new approach.* Applied Catalysis A: General, 1993. **102**(2): p. 181-200.

48. Zhang, Z.C. and B.C. Beard, *Agglomeration of Pt particles in the presence of chlorides.* Applied Catalysis A: General, 1999. **188**(1): p. 229-240.

49. Sinfelt, J.H., *Supported "bimetallic cluster" catalysts.* Journal of Catalysis, 1973. **29**(2): p. 308-315.

50. Toshima, N. and T. Yonezawa, *Bimetallic nanoparticles—novel materials for chemical and physical applications.* New Journal of Chemistry, 1998. **22**(11): p. 1179-1201.

51. Cao, A. and G. Veser, *Exceptional high-temperature stability through distillation-like self-stabilization in bimetallic nanoparticles.* Nature Materials, 2010. **9**: p. 75-81.

52. Liu, X., et al., *Synthesis of Thermally Stable and Highly Active Bimetallic Au−Ag Nanoparticles on Inert Supports.* Chemistry of Materials, 2009. **21**(2): p. 410-418.

53. Ikeda, S., et al., *Ligand-Free Platinum Nanoparticles Encapsulated in a Hollow Porous Carbon Shell as a Highly Active Heterogeneous Hydrogenation Catalyst.* Angewandte Chemie International Edition, 2006. **45**(42): p. 7063-7066.

54. Song, H., et al., *Hydrothermal Growth of Mesoporous SBA-15 Silica in the Presence of PVP-Stabilized Pt Nanoparticles: Synthesis, Characterization, and Catalytic Properties.* Journal of the American Chemical Society, 2006. **128**(9): p. 3027-3037.

55. Joo, S.H., et al., *Thermally stable Pt/mesoporous silica core–shell nanocatalysts for high-temperature reactions.* Nature Materials, 2009. **8**: p. 126-131.

56. Park, J.N., et al., *Highly Active and Sinter-Resistant Pd-Nanoparticle Catalysts Encapsulated in Silica.* Small, 2008. **4**(10): p. 1694-1697.

57. Dick, K., et al., *Size-Dependent Melting of Silica-Encapsulated Gold Nanoparticles.* Journal of the American Chemical Society, 2002. **124**(10): p. 2312-2317.

58. Wang, X., et al., *Current advances in precious metal core-shell catalyst design.* Science and technology of advanced materials, 2014. **15**(4): p. 043502-043502.

59. Yin, H., et al., *Heterostructured catalysts prepared by dispersing Au@Fe₂O₃ core–shell structures on supports and their performance in CO oxidation.* Catalysis Today, 2011. **160**(1): p. 87-95.

60. Wang, S., M. Zhang, and W. Zhang, *Yolk−Shell Catalyst of Single Au Nanoparticle Encapsulated within Hollow Mesoporous Silica Microspheres.* ACS Catalysis, 2011. **1**(3): p. 207-211.

61. Li, G. and Z. Tang, *Noble metal nanoparticle@metal oxide core/yolk–shell nanostructures as catalysts: recent progress and perspective.* Nanoscale, 2014. **6**(8): p. 3995-4011.

62. Arnal, P.M., M. Comotti, and F. Schüth, *High-Temperature-Stable Catalysts by Hollow Sphere Encapsulation.* Angewandte Chemie International Edition, 2006. **45**(48): p. 8224-8227.

63. Pan, X. and X. Bao, *The Effects of Confinement inside Carbon Nanotubes on Catalysis.* Accounts of Chemical Research, 2011. **44**(8): p. 553-562.

64. Pan, X., et al., *Enhanced ethanol production inside carbon-nanotube reactors containing catalytic particles.* Nature Materials, 2007. **6**: p. 507.

65. Pal, N. and A. Bhaumik, *Mesoporous materials: versatile supports in heterogeneous catalysis for liquid phase catalytic transformations.* RSC Advances, 2015. **5**(31): p. 24363-24391.

66. Huang, W., et al., *Dendrimer Templated Synthesis of One Nanometer Rh and Pt Particles Supported on Mesoporous Silica: Catalytic Activity for Ethylene and Pyrrole Hydrogenation.* Nano Letters, 2008. **8**(7): p. 2027-2034.

67. Wu, P., et al., *Selective oxidation of cyclohexane over gold nanoparticles supported on mesoporous silica prepared in the presence of thioether functionality.* Catalysis Science & Technology, 2011. **1**(2): p. 285-294.

68. Rodríguez-Castellón, E., et al., *Nickel-impregnated zirconium-doped mesoporous molecular sieves as catalysts for the hydrogenation and ring-opening of tetralin.* Applied Catalysis A: General, 2003. **240**(1): p. 83-94.

69.   Li, Z., et al., *Nitrogen-Functionalized Ordered Mesoporous Carbons as Multifunctional Supports of Ultrasmall Pd Nanoparticles for Hydrogenation of Phenol.* ACS Catalysis, 2013. **3**(11): p. 2440-2448.

70.   Schicks, J., et al., *Nanoengineered catalysts for high-temperature methane partial oxidation.* Catalysis Today, 2003. **81**(2): p. 287-296.

71.   Shinjoh, H., Hatanaka, M., Nagai, Y. et al., *Suppression of Noble Metal Sintering Based on the Support Anchoring Effect and its Application in Automotive Three-Way Catalysis.* Top. Catal., 2009. **52**(13): p. 1967-1971.

72.   Deeba, M., R.J. Farrauto, and Y.K. Lui, *Stabilization of platinum on silica promoted with lanthanum oxide and zirconium oxide.* Applied Catalysis A: General, 1995. **124**(2): p. 339-344.

73.   Ozawa, M. and M. Kimura, *Effect of cerium addition on the thermal stability of gamma alumina support.* Journal of Materials Science Letters, 1990. **9**(3): p. 291-293.

74.   Nagai, Y., et al., *Sintering inhibition mechanism of platinum supported on ceria-based oxide and Pt-oxide–support interaction.* Journal of Catalysis, 2006. **242**(1): p. 103-109.

75.   Qian, K., et al., *Anchoring highly active gold nanoparticles on SiO_2 by CoO_x additive.* Journal of Catalysis, 2007. **248**(1): p. 137-141.

76.   Rodríguez-González, V., et al., *Low-Temperature CO Oxidation and Long-Term Stability of $Au/In_2O_3-TiO_2$ Catalysts.* The Journal of Physical Chemistry C, 2009. **113**(20): p. 8911-8917.

77.   Ma, Z., S.H. Overbury, and S. Dai, *$Au/M_xO_y/TiO_2$ catalysts for CO oxidation: Promotional effect of main-group, transition, and rare-earth metal oxide additives.* Journal of Molecular Catalysis A: Chemical, 2007. **273**(1): p. 186-197.

78.   Yan, W., et al., *Ultrastable Au Nanocatalyst Supported on Surface-Modified TiO_2 Nanocrystals.* Journal of the American Chemical Society, 2005. **127**(30): p. 10480-10481.

79.   Behrens, M. and R. Schlögl, *X-Ray and Samll Angle X-Ray Scattering*, in *Characterization of Solid Materials and Heterogeneous Catalysts: From Structure to Surface Reactivity*, M. Che and J.C. Védrine, Editors. 2012, Wiley-VCH: Germany. p. 611-650.

80.   Weller, M.T., *Inorganic Materials Chemistry*. 1994, New York: Oxford University Press.

81.   *Diffraction and the X-Ray Powder Diffractometer*, in *Transmission Electron Microscopy and Diffractometry of Materials*. 2008, Springer Berlin Heidelberg: Berlin, Heidelberg. p. 1-59.

82.   *Basics of xrd*. 2014 [cited 2018 05/05]; Available from: https://www.slideshare.net/ceutics1315/basics-ofxrd-39635155.

83.   Barnes, P., S. Jacques, and M. Vickers. *Powder Diffraction*. 2006 [cited 2018 04/05]; Available from: http://pd.chem.ucl.ac.uk/pdnn/diff2/kinemat2.htm.

84.   Henderson, S. *Optical Components of Basic Powder Diffractometers*. 2016 [cited 2018 05/05]; Available from: http://slideplayer.com/slide/6143092/.

85.   Pecharsky, V.K. and P.Y. Zavalij, *Fundamentals of Powder Diffraction and Structural Characterization of Materials*. 2 ed. 2009: Springer.

86.   Zhou, W. and Z.L. Wang, *Scanning Microscopy for Nanotechnology: Techniques and Applications*. 2007: Springer.

87.   *Scanning Electron Microscopy (SEM)*. ISAAC : Imaging Spectroscopy and Analysis Centre [cited 2018 28/05]; Available from: https://www.gla.ac.uk/schools/ges/researchandimpact/researchfacilities/isaac/services/scanningelectronmicroscopy/.

88.   Joy, D.C., *Helium Ion Microscopy: Principles and Applications*. 2013: Springer.

89.   Postek, M.T., et al., *Helium Ion Microscopy: a New Technique for Semiconductor Metrology and Nanotechnology* in *Frontiers of Characterization and Metrology for Nanoelectronics*, D.G. Seiler, et al., Editors. 2007, American Institute of Physics: Gaithersburg. p. 161-167.

90.   Arey, B.W., V. Shutthanandan, and W. Jiang. *Helium Ion Microscopy versus Scanning Electron Microscopy*. 2010 [cited 2018 08/05]; Available from: https://www.microscopy.org/MandM/2010/arey.pdf.

91. Postek Michael, T. and E. Vladár Andras, *Helium ion microscopy and its application to nanotechnology and nanometrology.* Scanning, 2008. **30**(6): p. 457-462.

92. John, N., et al., *An Introduction to the Helium Ion Microscope.* AIP Conference Proceedings, 2007. **931**(1): p. 489-496.

93. Mondloch, J.E., E. Bayram, and R.G. Finke, *A review of the kinetics and mechanisms of formation of supported-nanoparticle heterogeneous catalysts.* Journal of Molecular Catalysis A: Chemical, 2012. **355**: p. 1-38.

94. Bell, D.C., et al., *Precision cutting and patterning of graphene with helium ions.* Nanotechnology, 2009. **20**(45): p. 455301.

95. Wachs, I.E., *Characterization of catalytic materials.* 1st ed. 2010, New York, N.Y. (222 East 46th Street, New York, NY 10017): New York, N.Y. 222 East 46th Street, New York, NY 10017 : Momentum Press.

96. Thomas, J.M. and C. Ducati, *Transmission Electron Microscopy*, in *Characterization of Solid Materials and Heterogeneous Catalysts: From Structure to Surface Reactivity*, M. Che and J.C. Védrine, Editors. 2012, Wiley-VCH: Germany. p. 655-702.

97. Chaturvedi, S. and P.N. Dave, *Characterization of Nanostructured Catalysts*, in *Microscopy and imaging science: practical approaches to applied research and education*, A. Méndez-Vilas, Editor. 2017, Formatex Research Center: Spain.

98. Fultz, B. and J. Howe, *Transmission Electron Microscopy and Diffractometry of Materials.* Graduate Texts in Physics, ed. W.T. Rhodes, H.E. Stanley, and R. Needs. Vol. 4. 2013: Springer.

99. Yao, N. and Z.L. Wang, *Handbook of Microscopy for Nanotechnology.* 2005: Kluwer Academic Publishers.

100. Creemer, J.F., et al., *Atomic-scale electron microscopy at ambient pressure.* Ultramicroscopy, 2008. **108**(9): p. 993-998.

101. Wagner, J.B., et al., *Exploring the environmental transmission electron microscope.* Micron, 2012. **43**(11): p. 1169-1175.

102. Boyes, E.D. and P.L. Gai, *Environmental high resolution electron microscopy and applications to chemical science.* Ultramicroscopy, 1997. **67**(1): p. 219-232.

103. Upton, B.H., et al., *In Situ Electron Microscopy Studies of the Interaction of Iron, Cobalt, and Nickel with Molybdenum Disulfide Single Crystals in Hydrogen.* Journal of Catalysis, 1993. **141**(1): p. 171-190.

104. Baker, R.T.K. and N.M. Rodriguez, *A Review of the Use of In situ Electron Microscopy Techniques for the Study of Iron-Based Catalysts for Coal Conversion Processes.* Energy & Fuels, 1994. **8**(2): p. 330-340.

105. Serve, A., et al., *Investigations of soot combustion on yttria-stabilized zirconia by environmental transmission electron microscopy (ETEM).* Applied Catalysis A: General, 2015. **504**: p. 74-80.

106. Mekki-Berrada, A. and A. Auroux, *Thermal Methods*, in *Characterization of Solid Materials and Heterogeneous Catalysts : From Structure to Surface Reactivity*, M. Che and J.C. Védrine, Editors. 2012, Wiley-VCH: Germany. p. 747-842.

107. Leofanti, G., et al., *Surface area and pore texture of catalysts.* Catalysis Today, 1998. **41**(1): p. 207-219.

108. Llewellyn, P.L., E. Bloch, and S. Bourrelly, *Surface Area/Porosity, Adsorption, Diffusion*, in *Characterization of Solid Materials and Heterogeneous Catalysts: From Structure to Surface Reactivity*, M. Che and J.C. Védrine, Editors. 2012, Wiley-VCH: Germany. p. 853-879.

109. Brunauer, S., P.H. Emmett, and E. Teller, *Adsorption of Gases in Multimolecular Layers.* Journal of the American Chemical Society, 1938. **60**(2): p. 309-319.

110. Konno, H., *Chapter 8 - X-ray Photoelectron Spectroscopy*, in *Materials Science and Engineering of Carbon*, M. Inagaki and F. Kang, Editors. 2016, Butterworth-Heinemann. p. 153-171.

111. Fillman, L.M. and S.C. Tang, *Thermal decomposition of metal carbonyls: A thermogravimetry-mass spectrometry study.* Thermochimica Acta, 1984. **75**(1): p. 71-84.

112. *XSTREAM Gas Analyser Series Instruction Manual.* 2006 [cited 2018 18/05]; Available from:

http://www2.emersonprocess.com/siteadmincenter/PM%20Rosemount%20Analytical%20Documents/PGA_Manual_X-STREAM_X1_Basic_200607.pdf.

113.   Patel, B.S. and K.D. Patel, *A Review paper on Catalytic Converter for Automotive Exhaust Emission.* International Journal of Applied Engineering Research, 2012. **7**(11): p. 1-5.

114.   Koltsakis, G.C. and A.M. Stamatelos, *Catalytic automotive exhaust aftertreatment.* Progress in Energy and Combustion Science, 1997. **23**(1): p. 1-39.

115.   Herz, R.K., J.B. Kiela, and J.A. Sell, *Dynamic behavior of automotive catalysts. 2. Carbon monoxide conversion under transient air fuel ratio conditions.* Industrial & Engineering Chemistry Product Research and Development, 1983. **22**(3): p. 387-396.

116.   Yentekakis, I.V., et al., *Novel electropositively promoted monometallic (Pt-only) catalytic converters for automotive pollution control.* Topics in Catalysis, 2007. **42**(1): p. 393-397.

117.   González-Velasco, J.R., et al., *Thermal aging of Pd/Pt/Rh automotive catalysts under a cycled oxidizing–reducing environment.* Catalysis Today, 2000. **59**(3): p. 395-402.

118.   Freyschlag, C.G. and R.J. Madix, *Precious metal magic: catalytic wizardry.* Materials Today, 2011. **14**(4): p. 134-142.

119.   Bond, G.C., *The origins of nobility: the special characteristics of the platinum metals.* Platinum Metals Rev., 1979. **23**(2): p. 46-53.

120.   Acres, G.J.K., *Platinum group metal catalysis at the end of this century.* Materials & Design, 1987. **8**(5): p. 258-262.

121.   Li, W.X., C. Stampfl, and M. Scheffler, *Why is a Noble Metal Catalytically Active? The Role of the O-Ag Interaction in the Function of Silver as an Oxidation Catalyst.* Physical Review Letters, 2003. **90**(25): p. 256102.

122.   *Global EV Outlook 2018.* 2018 [cited 2018 31/10/2018]; Available from: https://www.connaissancedesenergies.org/sites/default/files/pdf-actualites/globalevoutlook2018.pdf.

123.   Guillen-Hurtado, N., et al., *Three-Way Catalysts: Past, Present and Future.* Dyna, 2012. **79**(175): p. 114-121.

124.   Farrauto, R.J., L. Dorazio, and C.H. Bartholomew, *Introduction to Catalysis and Industrial Catalytic Processes.* 2016, New Jersey: John Wiley & Sons, Inc.

125.   *EU: cars and light trucks.* Emission Standards 2014 [cited 2018 30/10/2018]; Available from: https://www.dieselnet.com/standards/eu/ld.php#stds.

126.   Kašpar, J., P. Fornasiero, and N. Hickey, *Automotive catalytic converters: current status and some perspectives.* Catalysis Today, 2003. **77**(4): p. 419-449.

127.   Janssen, F.J.J.G. and R.A.v. Santen, *Environmental Catalysis.* Catalytic Science Series, ed. G.J. Hutchings. Vol. 1. 1999, Danvers: Imperial College Press.

128.   Nieuwenhuys, B.E., *The Surface Science Approach Toward Understanding Automotive Exhaust Conversion Catalysis at the Atomic Level*, in *Advances in Catalysis*, W.O. Haag, B.C. Gates, and H. Knözinger, Editors. 1999, Academic Press. p. 259-328.

129.   Cooper, J. and J. Beecham, *A Study of Platinum Group Metals in Three-Way Autocatalysts.* Platinum Metals Rev., 2013. **57**(4): p. 281-288.

130.   Twigg, M.V., *Twenty-Five Years of Autocatalysts.* Platinum Metals Rev., 1999. **43**(4): p. 168-171.

131.   Ravindra, K., L. Bencs, and R. Van Grieken, *Platinum group elements in the environment and their health risk.* Science of The Total Environment, 2004. **318**(1): p. 1-43.

132.   Taylor, K.C. and J.C. Schlatter, *Selective reduction of nitric oxide over noble metals.* Journal of Catalysis, 1980. **63**(1): p. 53-71.

133.   Oh, S.H., et al., *Comparative kinetic studies of CO · O2 and CO · NO reactions over single crystal and supported rhodium catalysts.* Journal of Catalysis, 1986. **100**(2): p. 360-376.

134.   Farrauto, R.J. and R.M. Heck, *Catalytic converters: state of the art and perspectives.* Catalysis Today, 1999. **51**(3): p. 351-360.

135. *Automotive Three-way Catalytic Converter Market 2018.* 2018 [cited 2018 31/10/2018]; Available from: https://incrediblenews24.com/20180828/automotive-three-way-catalytic-converter-market-2018.

136. Carduner, K.R., M.S. Chattha, and H.S. Gandhi, *Phosphorus poisoning of the three-way catalyst studied by 31P NMR.* Journal of Catalysis, 1988. **109**(1): p. 37-40.

137. Cai, H., et al., *Sulfur poisoning mechanism of three way catalytic converter and its grey relational analysis.* Journal of Central South University, 2014. **21**(11): p. 4091-4096.

138. Monroe, D.R., et al., *The Effect of Sulfur on Three-Way Catalysts*, in *Studies in Surface Science and Catalysis*, A. Crucq, Editor. 1991, Elsevier. p. 593-616.

139. Williamson, W.B., et al., *Effects of oil phosphorus on deactivation of monolithic three-way catalysts.* Applied Catalysis, 1985. **15**(2): p. 277-292.

140. Freund, H.J., et al., *CO Oxidation as a Prototypical Reaction for Heterogeneous Processes.* Angewandte Chemie International Edition, 2011. **50**(43): p. 10064-10094.

141. Engel, T. and G. Ertl, *Elementary Steps in the Catalytic Oxidation of Carbon Monoxide on Platinum Metals*, in *Advances in Catalysis*, D.D. Eley, H. Pines, and P.B. Weez, Editors. 1979, Academic Press. p. 1-78.

142. Matsushima, T. and J.M. White, *On the mechanism and kinetics of the CO-oxidation reaction on polycrystalline palladium: I. The reaction paths.* Journal of Catalysis, 1975. **39**(2): p. 265-276.

143. Baxter, R.J. and P. Hu, *Insight into why the Langmuir–Hinshelwood mechanism is generally preferred.* The Journal of Chemical Physics, 2002. **116**(11): p. 4379-4381.

144. Lynch, D.T., *Use of elementary step mechanisms to explain resonant behavior for co oxidation on platinum.* The Canadian Journal of Chemical Engineering, 1984. **62**(5): p. 691-698.

145. Mars, P. and D.W. van Krevelen, *Oxidations carried out by means of vanadium oxide catalysts.* Chemical Engineering Science, 1954. **3**: p. 41-59.

146. Duan, Y., et al., *New insight of the Mars-van Krevelen mechanism of the CO oxidation by gold catalyst on the ZnO(101) surface.* Computational and Theoretical Chemistry, 2017. **1100**: p. 28-33.

147. Hendriksen, B.L.M., S.C. Bobaru, and J.W.M. Frenken, *Oscillatory CO oxidation on Pd(100) studied with in situ scanning tunneling microscopy.* Surface Science, 2004. **552**(1): p. 229-242.

148. Hendriksen, B.L.M. and J.W.M. Frenken, *CO Oxidation on Pt(110): Scanning Tunneling Microscopy Inside a High-Pressure Flow Reactor.* Physical Review Letters, 2002. **89**(4): p. 046101.

149. Gao, F., et al., *CO oxidation trends on Pt-group metals from ultrahigh vacuum to near atmospheric pressures: A combined in situ PM-IRAS and reaction kinetics study.* Surface Science, 2009. **603**(1): p. 65-70.

150. Chen, M.S., et al., *Highly active surfaces for CO oxidation on Rh, Pd, and Pt.* Surface Science, 2007. **601**(23): p. 5326-5331.

151. Santra, A.K. and D.W. Goodman, *Catalytic oxidation of CO by platinum group metals: from ultrahigh vacuum to elevated pressures.* Electrochimica Acta, 2002. **47**(22): p. 3595-3609.

152. Szanyi, J. and D.W. Goodman, *CO Oxidation on Palladium. 1. A Combined Kinetic-Infrared Reflection Absorption Spectroscopic Study of Pd(100).* The Journal of Physical Chemistry, 1994. **98**(11): p. 2972-2977.

153. Allian, A.D., et al., *Chemisorption of CO and Mechanism of CO Oxidation on Supported Platinum Nanoclusters.* Journal of the American Chemical Society, 2011. **133**(12): p. 4498-4517.

154. Barshad, Y. and E. Gulari, *A dynamic study of CO oxidation on supported platinum.* AIChE Journal, 1985. **31**(4): p. 649-658.

155. Pan, Q., et al., *Enhanced CO Oxidation on the Oxide/Metal Interface: From Ultra-High Vacuum to Near-Atmospheric Pressures.* ChemCatChem, 2015. **7**(17): p. 2620-2627.

156. Park, J.Y., et al., *Tuning of Catalytic CO Oxidation by Changing Composition of Rh−Pt Bimetallic Nanoparticles.* Nano Letters, 2008. **8**(2): p. 673-677.

157. Gao, F., et al., *CO Oxidation on Pt-Group Metals from Ultrahigh Vacuum to Near Atmospheric Pressures. 1. Rhodium.* The Journal of Physical Chemistry C, 2009. **113**(1): p. 182-192.

158. Gao, F., et al., *CO Oxidation on Pt-Group Metals from Ultrahigh Vacuum to Near Atmospheric Pressures. 2. Palladium and Platinum.* The Journal of Physical Chemistry C, 2009. **113**(1): p. 174-181.

159. Kalinkin, A.V., A.V. Pashis, and V.I. Bukhtiyarov, *CO oxidation over a Pt-Rh system: 1. Reaction on individual metals.* React. Kinet. Catal. Lett., 2002. **77**(2): p. 255-261.

160. Castner, D.G., B.A. Sexton, and G.A. Somorjai, *Leed and thermal desorption studies of small molecules (H_2, O_2, CO, CO_2, NO, C_2H_4, C_2H_2 AND C) chemisorbed on the rhodium (111) and (100) surfaces.* Surface Science, 1978. **71**(3): p. 519-540.

161. Ertl, G., M. Neumann, and K.M. Streit, *Chemisorption of CO on the Pt(111) surface.* Surface Science, 1977. **64**(2): p. 393-410.

162. Thiel, P.A., J.T. Yates, and W.H. Weinberg, *The interaction of oxygen with the Rh(111) surface a.* Surface Science, 1979. **82**(1): p. 22-44.

163. Conrad, H., et al., *Interaction of NO and O_2 with Pd(111) surfaces. I.* Surface Science, 1977. **65**(1): p. 235-244.

164. Saliba, N.A., et al., *Oxidation of Pt(111) by ozone (O_3) under UHV conditions.* Surface Science, 1999. **419**(2): p. 79-88.

165. McClure, S.M. and D.W. Goodman, *New insights into catalytic CO oxidation on Pt-group metals at elevated pressures.* Chemical Physics Letters, 2009. **469**(1): p. 1-13.

166. Vedyagin, A.A., et al., *Catalytic Purification of Exhaust Gases Over Pd–Rh Alloy Catalysts.* Topics in Catalysis, 2013. **56**(11): p. 1008-1014.

167. Santos, V.P., et al., *Oxidation of CO, ethanol and toluene over TiO_2 supported noble metal catalysts.* Applied Catalysis B: Environmental, 2010. **99**(1): p. 198-205.

168. Somorjai, G.A., K.R. McCrea, and J. Zhu, *Active Sites in Heterogeneous Catalysis: Development of Molecular Concepts and Future Challenges.* Topics in Catalysis, 2002. **18**(3): p. 157-166.

169. Schubert, M.M., et al., *Correlation between CO surface coverage and selectivity/kinetics for the preferential CO oxidation over Pt/γ-Al_2O_3 and Au/α-Fe_2O_3: an in-situ DRIFTS study.* Journal of Power Sources, 1999. **84**(2): p. 175-182.

170. Al Soubaihi, M.R., M.K. Saoud, and J. Dutta, *Critical Review of Low-Temperature CO Oxidation and Hysteresis Phenomenon on Heterogeneous Catalysts.* Catalysts, 2018. **8**(12).

171. Karim, W., et al., *Catalyst support effects on hydrogen spillover.* Nature, 2017. **541**: p. 68.

172. Dong, B., B. Li, and C.Y. Li, *Janus nanoparticle dimers and chains viapolymer single crystals.* Journal of Materials Chemistry, 2011. **21**(35): p. 13155-13158.

173. Parlett, Christopher M.A., et al., *Spatially orthogonal chemical functionalization of a hierarchical pore network for catalytic cascade reactions.* Nature Materials, 2015. **15**: p. 178.

174. Zhu, W., et al., *Monodisperse Au Nanoparticles for Selective Electrocatalytic Reduction of CO_2 to CO.* Journal of the American Chemical Society, 2013. **135**(45): p. 16833-16836.

175. Li, G., et al., *Metal–Organic Frameworks Encapsulating Active Nanoparticles as Emerging Composites for Catalysis: Recent Progress and Perspectives.* Advanced Materials, 2018. **30**(51): p. 1800702.

176. Moon, H.R., D.W. Lim, and M.P. Suh, *Fabrication of metal nanoparticles in metal-organic frameworks.* Chemical Society Reviews, 2013. **42**(4): p. 1807-1824.

177. Dhakshinamoorthy, A. and H. Garcia, *Catalysis by metal nanoparticles embedded on metal-organic frameworks.* Chemical Society Reviews, 2012. **41**(15): p. 5262-5284.

178. Lu, G., et al., *Imparting functionality to a metal–organic framework material by controlled nanoparticle encapsulation.* Nature Chemistry, 2012. **4**: p. 310.

179. Sun, J.K., et al., *Toward Homogenization of Heterogeneous Metal Nanoparticle Catalysts with Enhanced Catalytic Performance: Soluble Porous Organic Cage as a Stabilizer and Homogenizer.* Journal of the American Chemical Society, 2015. **137**(22): p. 7063-7066.

180. Slater, A.G. and A.I. Cooper, *Function-led design of new porous materials.* Science, 2015. **348**(6238).
181. Tozawa, T., et al., *Porous organic cages.* Nature Materials, 2009. **8**: p. 973.
182. Hasell, T. and A.I. Cooper, *Porous organic cages: soluble, modular and molecular pores.* Nature Reviews Materials, 2016. **1**: p. 16053.
183. Barbour, L.J., *Crystal porosity and the burden of proof.* Chemical Communications, 2006(11): p. 1163-1168.
184. Jones, J.T.A., et al., *Modular and predictable assembly of porous organic molecular crystals.* Nature, 2011. **474**: p. 367.
185. Jiang, S., et al., *Porous organic molecular solids by dynamic covalent scrambling.* Nature Communications, 2011. **2**: p. 207.
186. Song, Q., et al., *Porous Organic Cage Thin Films and Molecular-Sieving Membranes.* Advanced Materials, 2016. **28**(13): p. 2629-2637.
187. Tom, H., et al., *Porous Organic Alloys.* Angewandte Chemie International Edition, 2012. **51**(29): p. 7154-7157.
188. Hasell, T., et al., *Porous Organic Cages for Sulfur Hexafluoride Separation.* Journal of the American Chemical Society, 2016. **138**(5): p. 1653-1659.
189. Chen, L., et al., *Separation of rare gases and chiral molecules by selective binding in porous organic cages.* Nature Materials, 2014. **13**: p. 954.
190. Miklitz, M., et al., *Computational Screening of Porous Organic Molecules for Xenon/Krypton Separation.* The Journal of Physical Chemistry C, 2017. **121**(28): p. 15211-15222.
191. Evans, J.D., et al., *Molecular Design of Amorphous Porous Organic Cages for Enhanced Gas Storage.* The Journal of Physical Chemistry C, 2015. **119**(14): p. 7746-7754.
192. Zhang, F., et al., *Multicomponent Gas Storage in Organic Cage Molecules.* The Journal of Physical Chemistry C, 2017. **121**(22): p. 12426-12433.
193. Zhang, Y., et al., *Porous organic cage stabilised palladium nanoparticles: efficient heterogeneous catalysts for carbonylation reaction of aryl halides.* Chemical Communications, 2018. **54**(22): p. 2796-2799.
194. Mondal, B., et al., *Molecular Cage Impregnated Palladium Nanoparticles: Efficient, Additive-Free Heterogeneous Catalysts for Cyanation of Aryl Halides.* Journal of the American Chemical Society, 2016. **138**(5): p. 1709-1716.
195. McCaffrey, R., et al., *Template Synthesis of Gold Nanoparticles with an Organic Molecular Cage.* Journal of the American Chemical Society, 2014. **136**(5): p. 1782-1785.
196. Qiu, L., et al., *Cage-templated synthesis of highly stable palladium nanoparticles and their catalytic activities in Suzuki–Miyaura coupling.* Chemical Science, 2018. **9**(3): p. 676-680.
197. Yang, X., et al., *Encapsulating highly catalytically active metal nanoclusters inside porous organic cages.* Nature Catalysis, 2018. **1**(3): p. 214-220.
198. Little, M.A., et al., *Guest control of structure in porous organic cages.* Chemical Communications, 2014. **50**(67): p. 9465-9468.
199. Bojdys, M.J., et al., *Porous organic cage crystals: characterising the porous crystal surface.* Chemical Communications, 2012. **48**(98): p. 11948-11950.
200. Zhu, G., et al., *Engineering Porous Organic Cage Crystals with Increased Acid Gas Resistance.* Chemistry – A European Journal, 2016. **22**(31): p. 10743-10747.
201. Hasell, T., et al., *Porous Organic Cage Nanocrystals by Solution Mixing.* Journal of the American Chemical Society, 2012. **134**(1): p. 588-598.
202. Glaspell, G., L. Fuoco, and M.S. El-Shall, *Microwave Synthesis of Supported Au and Pd Nanoparticle Catalysts for CO Oxidation.* The Journal of Physical Chemistry B, 2005. **109**(37): p. 17350-17355.
203. Lin, A., et al., *Palladium Nanoparticles Supported on Ce-Metal–Organic Framework for Efficient CO Oxidation and Low-Temperature CO2 Capture.* ACS Applied Materials & Interfaces, 2017. **9**(21): p. 17961-17968.

204. Liang, Q., et al., *Palladium nanoparticles supported on a triptycene-based microporous polymer: highly active catalysts for CO oxidation.* Chemical Communications, 2013. **49**(79): p. 8928-8930.

205. Kim, J.Y., et al., *In situ- generated metal oxide catalyst during CO oxidation reaction transformed from redox-active metal-organic framework-supported palladium nanoparticles.* Nanoscale Research Letters, 2012. **7**(461): p. 1-8.

206. Ye, J.Y. and C.J. Liu, *$Cu_3(BTC)_2$: CO oxidation over MOF based catalysts.* Chemical Communications, 2011. **47**(7): p. 2167-2169.

207. Tanaka, H. and M. Misono, *Advances in designing perovskite catalysts.* Current Opinion in Solid State and Materials Science, 2001. **5**(5): p. 381-387.

208. Neagu, D. and J.T.S. Irvine, *Perovskite Defect Chemistry as Exemplified by Strontium Titanate*, in *Comprehensive Inorganic Chemistry II*, J. Reedijk, Poeppelmeier, K., Editor. 2013, Elsevier. p. 397-415.

209. Goldschmidt, V.M., *Die Gesetze der Krystallochemie.* Naturwissenschaften, 1926. **14**(21): p. 477-485.

210. Travis, W., et al., *On the application of the tolerance factor to inorganic and hybrid halide perovskites: a revised system.* Chemical Science, 2016. **7**(7): p. 4548-4556.

211. Lin, Y.C. and L.K. Hohn, *Perovskite Catalysts—A Special Issue on Versatile Oxide Catalysts.* Catalysts, 2014. **4**(3).

212. Peña, M.A. and J.L.G. Fierro, *Chemical Structures and Performance of Perovskite Oxides.* Chemical Reviews, 2001. **101**(7): p. 1981-2018.

213. Ferri, D. and L. Forni, *Methane combustion on some perovskite-like mixed oxides.* Applied Catalysis B: Environmental, 1998. **16**(2): p. 119-126.

214. Moradi, G.R., F. Khosravian, and M. Rahmanzadeh, *Effects of Partial Substitution of Ni by Cu in $LaNiO_3$ Perovskite Catalyst for Dry Methane Reforming.* Chinese Journal of Catalysis, 2012. **33**(4): p. 797-801.

215. RIOSECO, F., et al., *EFFECT OF Ag ADDITION ON THE THERMAL STABILITY AND CATALYTIC PROPERTIES OF $LaFeO_3$ PEROVSKITE.* Journal of the Chilean Chemical Society, 2010. **55**: p. 44-49.

216. Bo, J., et al., *Oxygen permeation and phase structure properties of partially A-site substituted $BaCo_{0.7}Fe_{0.225}Ta_{0.075}O_{3-\delta}$ perovskites.* Journal of Energy Chemistry, 2014. **23**(2): p. 164.

217. Keav, S., et al., *Structured Perovskite-Based Catalysts and Their Application as Three-Way Catalytic Converters—A Review.* Catalysts, 2014. **4**(3).

218. Zhu, J., et al., *Perovskite Oxides: Preparation, Characterizations, and Applications in Heterogeneous Catalysis.* ACS Catalysis, 2014. **4**(9): p. 2917-2940.

219. Goodenough, J.B., *Electronic and ionic transport properties and other physical aspects of perovskites.* Reports on Progress in Physics, 2004. **67**(11): p. 1915.

220. Pandey, D. and P. Krishna, *Layer stacking in closed packed structures*, in *International Tables for Crystallography*, T. Hahn, Editor. 1989, Kluwer Academic Publishers: Dordrecht.

221. Trolliard, G., et al., *TEM study of cation-deficient-perovskite related $A_nB_{n-1}O_{3n}$ compounds: the twin-shift option.* Journal of Solid State Chemistry, 2004. **177**(4): p. 1188-1196.

222. Thalinger, R., et al., *Water-Gas Shift and Methane Reactivity on Reducible Perovskite-Type Oxides.* The Journal of Physical Chemistry C, 2015. **119**(21): p. 11739-11753.

223. Skinner, S.J., *Recent advances in Perovskite-type materials for solid oxide fuel cell cathodes.* International Journal of Inorganic Materials, 2001. **3**(2): p. 113-121.

224. Jun, A., et al., *Perovskite as a Cathode Material: A Review of its Role in Solid-Oxide Fuel Cell Technology.* ChemElectroChem, 2015. **3**(4): p. 511-530.

225. Bradow, R., et al., *Ruthenium Perovskite Catalysts for Lean NO_x Automotive Emission Control.* Industrial & Engineering Chemistry Research, 1995. **34**(6): p. 1929-1932.

226. Nitin, L., et al., *Perovskite-type catalytic materials for environmental applications.* Science and Technology of Advanced Materials, 2015. **16**(3): p. 036002.

227. Chen, D., et al., *Nonstoichiometric Oxides as Low-Cost and Highly-Efficient Oxygen Reduction/Evolution Catalysts for Low-Temperature Electrochemical Devices.* Chemical Reviews, 2015. **115**(18): p. 9869-9921.

228. Pecchi, G., et al., *Effect of B-site cation on the catalytic activity of La$_{1-x}$Ca$_x$BO$_3$ (B = Fe, Ni) perovskite-type oxides for toluene combustion.* Journal of Chemical Technology & Biotechnology, 2011. **86**(8): p. 1067-1073.

229. Guo, S., et al., *B-Site Metal (Pd, Pt, Ag, Cu, Zn, Ni) Promoted La$_{1-x}$Sr$_x$Co$_{1-y}$Fe$_y$O$_{3-\delta}$ Perovskite Oxides as Cathodes for IT-SOFCs.* Catalysts, 2015. **5**(1).

230. Wang, Z., et al., *Effect of B sites on the catalytic activities for perovskite oxides La$_{.6}$Sr$_{.4}$Co$_x$Fe$_{1-x}$O$_{3-\delta}$ as metal-air batteries catalysts.* Progress in Natural Science: Materials International, 2018. **28**(4): p. 399-407.

231. Libby, W.F., *Promising Catalyst for Auto Exhaust.* Science, 1971. **171**(3970): p. 499.

232. Voorhoeve, R.J.H., L.E. Trimble, and C.P. Khattak, *Exploration of perovskite-like catalysts: Ba$_2$CoWO$_6$ and Ba$_2$FeNbO$_6$ in NO reduction and CO oxidation.* Materials Research Bulletin, 1974. **9**(5): p. 655-666.

233. Voorhoeve, R.J.H., J.P. Remeika, and L.E. Trimble, *Perovskites containing ruthenium as catalysts for nitric oxide reduction.* Materials Research Bulletin, 1974. **9**(10): p. 1393-1404.

234. Voorhoeve, R.J.H., J.P. Remeika, and D.W. Johnson, *Rare-Earth Manganites: Catalysts with Low Ammonia Yield in the Reduction of Nitrogen Oxides.* Science, 1973. **180**(4081): p. 62.

235. Voorhoeve, R.J.H., et al., *Rare-Earth Oxides of Manganese and Cobalt Rival Platinum for the Treatment of Carbon Monoxide in Auto Exhaust.* Science, 1972. **177**(4046): p. 353.

236. Nishihata, Y., et al., *Self-regeneration of a Pd-perovskite catalyst for automotive emissions control.* Nature, 2002. **418**: p. 164-167.

237. Tanaka, H., et al., *Design of the intelligent catalyst for Japan ULEV standard.* Topics in Catalysis, 2004. **30**(1): p. 389-396.

238. Tanaka, H., et al., *Self-Regenerating Rh- and Pt-Based Perovskite Catalysts for Automotive-Emissions Control.* Angewandte Chemie International Edition, 2006. **45**(36): p. 5998-6002.

239. Tanaka, H., et al., *The intelligent catalyst having the self-regenerative function of Pd, Rh and Pt for automotive emissions control.* Catalysis Today, 2006. **117**(1): p. 321-328.

240. Katz, M.B., et al., *Self-Regeneration of Pd–LaFeO$_3$ Catalysts: New Insight from Atomic-Resolution Electron Microscopy.* Journal of the American Chemical Society, 2011. **133**(45): p. 18090-18093.

241. Katz, M.B., et al., *Reversible precipitation/dissolution of precious-metal clusters in perovskite-based catalyst materials: Bulk versus surface re-dispersion.* Journal of Catalysis, 2012. **293**: p. 145-148.

242. Madsen, B.D., et al., *SOFC Anode Performance Enhancement through Precipitation of Nanoscale Catalysts.* ECS Transactions, 2007. **7**(1): p. 1339-1348.

243. Bierschenk, D.M., et al., *Pd-substituted (La,Sr)CrO$_{3-\delta}$–Ce$_{0.9}$Gd$_{0.1}$O$_{2-\delta}$ solid oxide fuel cell anodes exhibiting regenerative behavior.* Journal of Power Sources, 2011. **196**(6): p. 3089-3094.

244. Tsekouras, G., D. Neagu, and J.T.S. Irvine, *Step-change in high temperature steam electrolysis performance of perovskite oxide cathodes with exsolution of B-site dopants.* Energy & Environmental Science, 2013. **6**(1): p. 256-266.

245. Neagu, D., et al., *In situ growth of nanoparticles through control of non-stoichiometry.* Nature Chemistry, 2013. **5**: p. 916.

246. Jalili, H., et al., *New Insights into the Strain Coupling to Surface Chemistry, Electronic Structure, and Reactivity of La$_{0.7}$Sr$_{0.3}$MnO$_3$.* The Journal of Physical Chemistry Letters, 2011. **2**(7): p. 801-807.

247. Lee, W., et al., *Cation Size Mismatch and Charge Interactions Drive Dopant Segregation at the Surfaces of Manganite Perovskites.* Journal of the American Chemical Society, 2013. **135**(21): p. 7909-7925.

248. A. De Souza, R., M. Saiful Islam, and E. Ivers-Tiffée, *Formation and migration of cation defects in the perovskite oxide LaMnO$_3$.* Journal of Materials Chemistry, 1999. **9**(7): p. 1621-1627.

249. Chambers, S.A., et al., *Ultralow Contact Resistance at an Epitaxial Metal/Oxide Heterojunction Through Interstitial Site Doping.* Advanced Materials, 2013. **25**(29): p. 4001-4005.

250. Abild-Pedersen, F., et al., *Mechanisms for catalytic carbon nanofiber growth studied by ab initio density functional theory calculations.* Physical Review B, 2006. **73**(11): p. 115419.

251. Gohier, A., et al., *Carbon nanotube growth mechanism switches from tip- to base-growth with decreasing catalyst particle size.* Carbon, 2008. **46**(10): p. 1331-1338.

252. Papaioannou, E.I., et al., *Sulfur-Tolerant, Exsolved Fe–Ni Alloy Nanoparticles for CO Oxidation.* Topics in Catalysis, 2018.

253. Neagu, D., et al., *Demonstration of chemistry at a point through restructuring and catalytic activation at anchored nanoparticles.* Nature Communications, 2017. **8**(1): p. 1855.

254. Zhu, Y., et al., *Promotion of Oxygen Reduction by Exsolved Silver Nanoparticles on a Perovskite Scaffold for Low-Temperature Solid Oxide Fuel Cells.* Nano Letters, 2016. **16**(1): p. 512-518.

255. Park, B.H. and G.M. Choi, *Ex-solution of Ni nanoparticles in a $La_{0.2}Sr_{0.8}Ti_{1-x}Ni_xO_{3-\delta}$ alternative anode for solid oxide fuel cell.* Solid State Ionics, 2014. **262**: p. 345-348.

256. Hou, N., et al., *A-Site Ordered Double Perovskite with in Situ Exsolved Core–Shell Nanoparticles as Anode for Solid Oxide Fuel Cells.* ACS Applied Materials & Interfaces, 2019. **11**(7): p. 6995-7005.

257. Hosseini, D., et al., *Reversible Exsolution of Dopant Improves the Performance of $Ca_2Fe_2O_5$ for Chemical Looping Hydrogen Production.* ACS Applied Materials & Interfaces, 2019. **11**(20): p. 18276-18284.

258. Zubenko, D., S. Singh, and B.A. Rosen, *Exsolution of Re-alloy catalysts with enhanced stability for methane dry reforming.* Applied Catalysis B: Environmental, 2017. **209**: p. 711-719.

259. Yan, B., et al., *Highly active subnanometer Rh clusters derived from Rh-doped $SrTiO_3$ for CO_2 reduction.* Applied Catalysis B: Environmental, 2018. **237**: p. 1003-1011.

260. Myung, J.H., et al., *Switching on electrocatalytic activity in solid oxide cells.* Nature, 2016. **537**(7621): p. 528-531.

261. Connor, P.A., et al., *Tailoring SOFC Electrode Microstructures for Improved Performance.* Advanced Energy Materials, 2018. **8**(23): p. 1800120.

262. Glazer, A., *Simple ways of determining perovskite structures.* Acta Crystallographica Section A, 1975. **31**(6): p. 756-762.

263. Howard, C.J. and H.T. Stokes, *Structures and phase transitions in perovskites - a group-theoretical approach.* Acta Crystallographica Section A, 2005. **61**(1): p. 93-111.

264. Ball, C.J., et al., *Structures in the System $CaTiO_3$/$SrTiO_3$.* Journal of Solid State Chemistry, 1998. **139**(2): p. 238-247.

265. Howard, C.J. and H.T. Stokes, *Group-Theoretical Analysis of Octahedral Tilting in Perovskites.* Acta Crystallographica Section B, 1998. **54**(6): p. 782-789.

266. Glazer, A., *The classification of tilted octahedra in perovskites.* Acta Crystallographica Section B, 1972. **28**(11): p. 3384-3392.

267. Neagu, D., *Materials and microstructures for high temperature electrochemical devices through control of perovskite defect chemistry,* in *School of Chemistry.* 2013, University of St Andrews: St Andrews.

268. Gao, Y., et al., *From material design to mechanism study: Nanoscale Ni exsolution on a highly active A-site deficient anode material for solid oxide fuel cells.* Nano Energy, 2016. **27**: p. 499-508.

269. Mallika, C., O.M. Sreedharan, and M.S. Chandrasekharaiah, *Determination of the standard Gibbs energy of formation of $Rh_2O_3(s)$ and $IrO_2(s)$ from solid oxide electrolyte electromotive force measurements.* Journal of the Less Common Metals, 1985. **107**(2): p. 203-212.

270. Nefedov, V.I., M.N. Firsov, and I.S. Shaplygin, *Electronic structures of $MRhO_2$, MRh_2O_4, $RhMO_4$ and Rh_2MO_6 on the basis of X-ray spectroscopy and ESCA data.* Journal of Electron Spectroscopy and Related Phenomena, 1982. **26**(1): p. 65-78.

271. Vallet, C.E., et al., *XPS characterization of anodic layers grown on Ir- and Rh-implanted titanium.* Electrochimica Acta, 1993. **38**(10): p. 1313-1320.

272. Greiner, M.T., et al., *Universal energy-level alignment of molecules on metal oxides.* Nature Materials, 2012. **11**(1): p. 76-81.

273. Jo, Y.R., et al., *Growth Kinetics of Individual Co Particles Ex-solved on $SrTi_{0.75}Co_{0.25}O_{3-\delta}$ Polycrystalline Perovskite Thin Films.* Journal of the American Chemical Society, 2019. **141**(16): p. 6690-6697.

274. Irvine, J.T.S., et al., *Evolution of the electrochemical interface in high-temperature fuel cells and electrolysers.* Nature Energy, 2016. **1**: p. 15014.

275. Jinschek, J.R., *Advances in the environmental transmission electron microscope (ETEM) for nanoscale in situ studies of gas–solid interactions.* Chemical Communications, 2014. **50**(21): p. 2696-2706.

276. Oh, T.S., et al., *Evidence and Model for Strain-Driven Release of Metal Nanocatalysts from Perovskites during Exsolution.* The Journal of Physical Chemistry Letters, 2015. **6**(24): p. 5106-5110.

277. Gao, Y., et al., *In situ growth of Pt_3Ni nanoparticles on an A-site deficient perovskite with enhanced activity for the oxygen reduction reaction.* Journal of Materials Chemistry A, 2017. **5**(14): p. 6399-6404.

278. Borer, A.L. and R. Prins, *Temperature-Programmed Reduction and CO Hydrogenation of La_2O_3-Promoted Rh/SiO_2 Catalysts.* Journal of Catalysis, 1993. **144**(2): p. 439-451.

279. Ligthart, D.A.J.M., R.A. van Santen, and E.J.M. Hensen, *Supported Rhodium Oxide Nanoparticles as Highly Active CO Oxidation Catalysts.* Angewandte Chemie International Edition, 2011. **50**(23): p. 5306-5310.

280. Cimino, S., et al., *Methane combustion and CO oxidation on $LaAl_{1-x}Mn_xO_3$ perovskite-type oxide solid solutions.* Applied Catalysis B: Environmental, 2003. **43**(4): p. 397-406.

281. Simonot, L., F.O. Garin, and G. Maire, *A comparative study of $LaCoO_3$, Co_3O_4 and $LaCoO_3$—Co_3O_4: I. Preparation, characterisation and catalytic properties for the oxidation of CO.* Applied Catalysis B: Environmental, 1997. **11**(2): p. 167-179.

282. Ciambelli, P., et al., *$AFeO_3$ (A=La, Nd, Sm) and $LaFe_{1-x}Mg_xO_3$ perovskites as methane combustion and CO oxidation catalysts: structural, redox and catalytic properties.* Applied Catalysis B: Environmental, 2001. **29**(4): p. 239-250.

283. Boubnov, A., et al., *Oscillatory CO Oxidation Over Pt/Al_2O_3 Catalysts Studied by In situ XAS and DRIFTS.* Topics in Catalysis, 2013. **56**(1): p. 333-338.

284. Munuera, G., A. Fernandez, and A.R. Gonzalez-Elipe, *The Role of the Oxygen Vacancies at the Support in the Co Oxidation On Rh/CeO_2 AND Rh/TiO_2 AUTOCATALYSTS*, in *Studies in Surface Science and Catalysis*, A. Crucq, Editor. 1991, Elsevier. p. 207-219.

285. Flege, J.I. and P. Sutter, *In situ structural imaging of CO oxidation catalysis on oxidized Rh(111).* Physical Review B, 2008. **78**(15): p. 153402.